STUDIES OF NATURAL FRACTURES, FAULT ZONE PERMEABILITY, AND A PORE SPACE-PERMEABILITY MODEL

A DISSERTATION
SUBMITTED TO THE DEPARTMENT OF GEOPHYSICS
AND THE COMMITTEE ON GRADUATE STUDIES
OF STANFORD UNIVERSITY
IN PARTIAL FULFILLMENT OF THE REQUIREMENTS
FOR THE DEGREE OF
DOCTOR OF PHILOSOPHY

By
Donald Alan Seeburger
May, 1981

Printed as Stanford Rock Physics Report #11
The Board of Trustees of the Leland
Stanford Junior University
Stanford, California 94305

ABSTRACT

This thesis consists of three sections, with one section on each of the following subjects: 1) in situ fracture distribution, 2) fault zone permeability, and 3) a pore model of permeability and bulk modulus. While not directly related, each of these deals with the distribution of pore space in crustal rocks and the transport properties of that pore space. The work has potential applications in such fields as oil and gas exploration, nuclear waste disposal, and earthquake studies.

The results of a study of the natural fracture distribution encountered in boreholes are presented in the first section. The ten wells studied were drilled in three areas of the United States: five near Palmdale, California; three near Hollister, California; and two near Monticello Reservoir, South Carolina. All but one of the wells were drilled in granitic rock. Seven wells were drilled to depths of 200-250 m, while three were drilled to depths of about 1 km. The distribution and orientation of fractures in these wells were determined using an ultrasonic borehole televiewer. The number of fractures observed was relatively independent of depth. Steeply dipping fractures were found throughout the wells. Statistically significant fracture orientations could not be related simply to the measured orientation of the regional stress field. The data appear to indicate that local rather than regional effects often control the distribution and orientation of natural fractures. Therefore, it is often not possible to predict the fracture distribution and orientations that would be encountered in a well simply from an analysis of the tectonic stress field and the regional geology.

The second section consists of an examination of the characteristics of fluid flow around fault zones. Faults are often described as conduits or barriers to fluid flow; many times a single fault is required to be both a barrier and a conduit. In cases for which faults appear to act as both barriers and conduits, the required permeability is highly anisotropic; high permeability is found parallel to the fault plane in the hanging wall and the permeability perpendicular to the fault plane is low. Several direct observations of fault zone structure are cited. It is generally found that a throughgoing fault plane or fracture zone exists in the hanging wall of a fault zone and that relatively fine grain, low porosity "gouge" zone exists in the footwall. Based upon general relations between porosity, sorting, pore and grain size, and permeability, the structural characteristics of the observed fault zones are consistent with the permeability distribution near faults. These conclusions appear to be generally valid for all types of rocks. As a result, faults should not be considered as two-dimensional, planar features, but as three dimensional features whose structure may determine the permeability and pore fluid distribution in situ. The permeability and porosity distribution could be of importance to petroleum migration and the generation and maintenance of high pore pressures.

In section three, a network model of pore space from which permeability and bulk modulus can be calculated as a function of confining pressure is presented. Pores are modeled as straight conduits of circular, elliptic, or tapered section. Flow through each conduit is modeled using Poiseuille flow. Permeability is

modeled by considering a regular system of interconnected conduits and applying network theory. Permeability as a function of confining pressure and the effect of porosity on the bulk modulus are determined by the elastic properties associated with the individual pore shapes. The permeability and bulk modulus characteristics of the network are similar to those found in laboratory experiments. In particular, it is found that for rocks like sandstone the bulk modulus is affected most by easily deformed, fine, thin cracks while permeability is controlled by larger stiff, round pores. In contrast, for rocks like granite and tight sandstones, both permeability and bulk modulus are controlled by easily deformed thin cracks. The results of this work indicate that network theory has many applications to the study of porous media, particularly when interactions of physical properties are considered. This work is a first step toward a complete pore space model, one which adequately predicts the rock response to any physical stimulus.

TABLE OF CONTENTS

PART I. THE DISTRIBUTION OF NATURAL FRACTURES AND JOINTS AT DEPTH IN CRYSTALLINE ROCK

PART II. PERMEABILITY AND FAULT ZONE STRUCTURE

PART III. A PORE SPACE MODEL FOR PERMEABILITY AND BULK MODULUS

APPENDIX

THE DISTRIBUTION OF NATURAL FRACTURES AND JOINTS AT DEPTH IN CRYSTALLINE ROCK

ABSTRACT

This paper presents the results of studies of the natural fracture distribution encountered in ten test wells drilled in three areas of the United States. Seven of the wells were drilled to depths of 200-250 m, while three were drilled to depths of about 1 km. Using an ultrasonic borehole televiewer, fracture depths, strikes, and dips were determined. Steeply dipping fractures were found throughout each of the wells and, in general, few horizontal fractures were observed. The number of fractures observed did not decrease markedly with increasing depth. Statistically significant fracture orientations which were basically invariant with depth were found for each well. No simple relation between these preferred fracture orientations and the orientation and relative magnitudes of the current regional stress fields was observed. For wells in the western Mojave Desert, California, possible relations between the orientation of fractures and the current regional stress field were found, but for wells near Hollister, California, and Monticello Reservoir, South Carolina, the observed fracture orientations are a product of the complex geologic histories of the areas and do not seem to be related to the current stress field. As found in the wells in the western Mojave Desert and near Hollister, there is no tendency for the intensity of fracturing to increase near the San Andreas fault.

INTRODUCTION

The upper crust of the earth is composed of fractured rock. Fractures are found on all scales from microfractures with dimensions of microns to lineaments with dimensions of kilometers. These fractures exert a profound effect upon the physical properties of rock. Laboratory and theoretical fracture studies have been extensive. Fractures have been found to affect the strength of rock (e.g. Brace, 1960), the velocity of elastic waves (e.g. Nur, 1971; Hadley, 1976), and the effective elastic moduli (e.g. Walsh, 1965; Budiansky and O'Connell, 1976). The permeability and distribution of pore fluids in crystalline rocks are primarily determined by the density and distribution of fractures (e.g. Snow, 1968; Brace, 1979). A knowledge of the in situ fracture distribution is thus of great importance for characterization of the upper crust. But systematic subsurface observations of fractures have been few. Most such observations have been made in tunnels and mines where the stress field and fracture pattern may have been considerably altered during operations. For example, McGarr (1971) and McGarr et al. (1979) studied the relation of fracture occurrence and rock bursts in deep mines. Fracture orientations were observed to be affected by the presence of the tabular excavations, and burst fractures were observed to occur where natural fractures were unusually sparse. Overbey and Rough (1971) compared fracture orientations measured at surface outcrops and from aerial photographs with those found in oriented cores and impression packer surveys of hydraulically fractured intervals in eastern Ohio. They found a fair degree of correlation between natural and induced fractures at depth and major fracture trends measured at the surface. The data discussed by Overbey and Rough (1971) are significant in that both the existence and the orientation of the fractures were determined; most borehole studies have been concerned with only the presence of fractures (e.g. Shanks et al., 1976).

In this paper we present the results of in situ fracture studies performed in test wells drilled in three different regions: five wells were in the Mojave Desert near Palmdale, California, three were near Limekiln Valley, south of Hollister, California, and two wells were at Monticello Reservoir, northwest of Columbia, South Carolina. The wells were continuously logged using an ultrasonic borehole televiewer (described below) and the fracture orientations and distribution as a function of depth were determined.

The fracture patterns were compared to the orientation and nature of the measured current regional stress field and the historic stress field as deduced from regional structural geology. From this comparison, the possible mechanisms of fracture formation which could be responsible for the current observed fracture distribution were considered. Using several holes in one region, an idea of the horizontal and vertical distributions of fractures in situ can be obtained and the results compared to theoretical predictions and other field measurements of natural fracture distributions. The results of this study should indicate whether the distribution and orientation of fractures in situ can be predicted from either the current stress field or the stress history of a region and whether the fracture distribution at depth can be predicted simply by the downward extrapolation of the near surface fracture systems.

A brief discussion of the mechanics of fracture formation is warranted in order to interpret the significance of the fractures encountered in these wells. Theories of fracture genesis can be divided into four basic groups.

1) Observed fractures and joints appear to be primarily extension fractures which form in planes perpendicular to the direction of least compression (see Engelder and Geiser, 1980). Such fractures are predicted to occur, for example, to accommodate lateral expansion associated with isostatic uplift (Price, 1976; Haxby and Turcotte, 1976). If an isostatically uplifted mass of rock subtends the same arc as it moves outward, there will be a decrease in the lateral stress as a result of overburden removal and Poisson's effect, of lateral expansion, and of thermal contraction. Fractures formed by such a mechanism would be near vertical, tensile, or extension, fractures.

2) The second group we consider is shear failure due to compressive stresses. The characteristic of shear fractures is shearing displacement along the fracture surface. Fractures which form as a result of shear failure may occur in conjugate pairs with an angle of about 30^{0} between the direction of maximum compressive stress and the shear planes. For the case of shear fractures

associated with wrench faults, Wilcox et al. (1974) point out that often only one of the conjugate pair becomes a well-developed fracture set.

3) Fracturing due to residual stress is a third mechanism to be considered (see Engelder, 1979). Residual stresses are "locked in" stresses associated with the previous history of the rock. Natural fracturing due to residual stress effects would generally be tensile in nature, caused by a reduction of confining stress. As in the case of other extension fractures, fracture planes would be predicted to occur perpendicular to the direction of least compressive stress in the rock.

4) A fourth mechanism of fracture formation is natural hydraulic fracturing (Secor, 1965). If pore pressures locally exceed the least compressive stress, extension fractures will propagate in a plane perpendicular to the least principal stress.

5) A final type of fracture, or joint, is that which is generated or extended by near-surface weathering-type processes. Such fractures are expected to be found in decreasing numbers with increasing depth and to be more random in orientation than those mentioned above.

In general, the number of fractures observed in this study should be greatest near the surface where confining pressures are low. For tensile fractures, simple elasticity theory predicts that the increase of confining pressure with depth would tend to close existing fractures and inhibit the formation of new fractures. Increasing confining pressure would also tend to close shear fractures although crushed rock or gouge might prohibit this. Also, the creation of shear fracture systems may not be very depth dependent in the upper several kilometers of the crust.

Caution must be exercised in using any failure criterion to predict fracture orientations within a body of rock. The fracture orientations predicted by simple theory are those which would occur in a uniform isotropic material. Real materials may contain flaws or discontinuities which affect the failure mechanism. For shear failure, the Coulomb law (see Jaeger and Cook, 1969) predicts the orientation of only the first fracture or set of fractures. As soon as the first fracture forms, the stresses in its vicinity are markedly changed, and the Coulomb law is inadequate to predict further fracturing of the material. Similarly, in the case of tensile fracture formation, the degree to which a given fracture can relieve tensile stresses will control the occurrence of secondary fractures. The stresses near a fracture may not then be predicted simply by a knowledge of the boundary stresses.

Clearly, the major complication in attempting to analyze the mechanism of fracture formation in the upper crust is the uncertainty of the geologic history of the rock mass. Rocks may undergo repeated tectonic loadings with resultant folding, fracturing, and faulting. Each tectonic cycle may add its own distinct fracture set, or preexisting fracture sets may be modified. The fractures or joints which are observed today reflect the entire deformational history of the rock. The existence of fracture sets which cannot be explained on the basis of the current stress field is not unexpected. As examples, Tchalenko and Ambraseys (1970), Freund (1974), and Wilcox et al. (1974) found from field mapping and clay model experiments that the orientations of fractures near faults may change with time and deformation; and Hodgson (1971) found little correlation of joints with fold axes in his field mapping of the Comb Ridge area of the Colorado Plateau.

TECHNIQUE

The borehole televiewer (manufactured by Simplec Manufacturing Co. under license of Mobil Oil Corp.) is a rotating acoustic transducer emitting pulses focused in a 3^{o} beam at a rate of 180 times per second (Zemanek et al., 1970). The transducer rotates at 3 revolutions per second and moves vertically in the hole at a speed of 2.5 cm/sec. The amplitude of the reflected signal is plotted as brightness on a three-axis oscilloscope as a function of the beam azimuth and vertical position in the hole. The scope trace is triggered at magnetic north by a flux gate magnetometer in the tool. Essentially the smoothness of the borehole wall is mapped. Where the smoothness of the borehole wall is perturbed by a planar feature such as a fracture, a dark sinusoidal pattern is seen (see Figure 1). Resolution of the tool depends upon hole diameter, wall conditions, reflectivity of the formation, and acoustic impedance of the well bore fluid. The wall condition is the most important factor as a rough well bore makes detection of fine features quite difficult. Except for highly fractured intervals, the conditions in the Mojave and Monticello wells were nearly ideal and all fractures with apertures of more than a few mm were probably detected. The conditions in the Limekiln Valley wells were highly variable. In heavily fractured, poor picture-quality intervals, only a subset of the total fracture population could be analyzed.

As an example, Figure 2 presents televiewer pictures of a 15.2 m vertical section of well displayed in two sections. The interval from about 0 to 4 m in Figure 2 is one in which numerous single fractures are found. From about 4 to 7 m there is a relatively unfractured interval, while from about 7 to 10 m is an interval in which a few distinct, parallel fractures are found. Knowing the well diameter the dip of these fractures may be calculated by measuring the peak to trough amplitude of the sinusoids. The fracture strike is taken to be in the direction of the midpoint between peak and trough (Figure 1). The test wells were drilled with a diameter of approximately 15 cm so that the circumference (horizontal scale) is about 50 cm. Thus, there is greater than 3:1 horizontal exaggeration in the pictures and as a result, fractures with dips of less than 5° appear to be horizontal. Apparently low dipping fractures (such as those in the first few meters of Figure 2) actually dip at least $10\text{-}15^{\circ}$.

Televiewer surveys were run in each well from total depth (TD) to the top of the water column or the bottom of casing; in either case, usually to within several meters or tens of meters, of the surface. Only those features for which the sinusoidal signature could be resolved were picked as fractures.

There are two major limitations in the analysis of fracture orientation from televiewer data. First, with the televiewer, only the orientation of a small portion of a fracture plane is actually observed. On a large scale, many fractures may appear planar, but when restricted to viewing only small portions of the entire fracture, variations of strike and dip by as much as 10^o may be apparent. Thus, in trying to determine preferred fracture orientation, data from televiewer surveys may result in more scatter and lower levels of statistical significance for preferred orientations than would be found in surveys which consider larger portions of the fractures. The second problem is that nearly vertical fractures are not often intersected by vertical wells. Thus, there is a bias in the method as vertical fractures are not sampled.

In order to evaluate the distribution of fracture orientations, poles to fracture planes for all dipping fractures in each well were plotted on a lower hemisphere, equal area projection. To obtain an estimate of the statistical significance of these pole groupings (and thus to arrive at an estimate of the preferred fracture orientations), orientation-density diagrams were prepared using a method described by Kamb (1959). The pole densities were contoured in intervals of 2σ, where σ is the standard deviation of the total number of points in a given area under random sampling. The expected density, E, for no preferred orientation is 3σ. The standard deviation and the sampling area used in preparing these diagrams are both determined by a statistical relation based upon the number of poles plotted. The number of poles, N; the sample area, A, given as a fraction of the total area of the hemisphere; the expected density, E; and the standard deviation, σ, are given for each plot. Observed densities that differ from E (3σ) by more than two or three times the standard deviation (i.e., $> 6\sigma$) are likely to be significant, particularly if the higher densities are clustered in one section of the diagram. An example of the method is presented in Figure 3; the number of poles (N) is 165, the sample area (A) is .05, the expected density (E) is 8.6, and the standard deviation (σ) is 2.9. As shown in Figure 3b, the only statistically significant pole concentrations in Figure 3a are two clusters with mean strikes and dips of about N20°W, 63°SW, and N52°W, 55°NE.

DATA AND INTERPRETATION

In this section the results of the borehole fracture surveys are presented. Plots of the number of fractures as a function of depth, lower-hemisphere equal-area stereographic pole projections, and orientation-density diagrams are presented for each well. The data are then interpreted in light of what is known of the regional geology and stress field. The detailed structural history of the rock at the well sites is generally not well known. When further information from either field geology or the fracture data is lacking, it is assumed that the fractures currently observed are oriented as they were at the time of their formation. In addition, no analysis of the timing of fracture genesis can be made from the televiewer data. The interpretation of the fracture orientation data is limited by these constraints.

MOJAVE DESERT WELLS

Five wells were drilled in the western Mojave desert as part of an in-situ stress measurement program along the locked portion of the San Andreas fault in southern California. The sites lie along the part of the fault that last ruptured in the 1857 Fort Tejon earthquake (Sieh, 1978). Throughout the western Mojave desert, Tertiary formations rest unconformably upon a surface of pre-Tertiary crystalline rocks that underwent deep erosion during late Cretaceous and early Tertiary time (Dibblee, 1967). In middle to late Miocene time the Mojave block was deformed primarily by normal faulting along northwest trending faults (Dibblee, 1967). Geologic and paleomagnetic studies indicate that as much as 10% north-south shortening of the wedge between the Garlock and San Andreas faults may have occurred during the Pliocene and Quaternary (Burke and Ponti, 1979). This shortening has been accommodated by strike-slip faulting on northwest striking faults, thrust faulting on east-west trending faults, folding, and possible block rotation. The nature of the deformation is consistent with an applied north-south compression. Geodetic measurements (Savage and Prescott, 1979; Lisowski and Savage, 1979; Prescott and Savage, 1976; Thatcher, 1976) indicate that present deformation in the western Mojave near Palmdale has a direction of maximum shortening of N10^{o}-15^{o}W and a direction of maximum extension of about N75^{o}-80^{o}E. This deformation field is basically consistent with the in situ stress field orientations determined by hydraulic fracturing in two of the wells considered in this study (Zoback et al., 1980).

Four of the wells in the western Mojave desert comprise a north-northeast trending profile running across the San Andreas fault from the foothills of the San Gabriel Mountains near Valyermo to Adobe Mountain in the western Mojave desert (Figure 4).

Well 1 was drilled on the north limb of a large syncline 2 km southwest of the San Andreas fault and between the San Andreas and Punchbowl faults (Figure 4). Well 1 is the only well in this study not drilled in crystalline rock. The results are presented here for completeness. The axis of the syncline strikes N70^{o}W and plunges to the west. At the well site the dip of the north limb was approximately 45^o-50^o to the southwest. The well was drilled to a depth of 245 m, entirely through the upper Miocene Punchbowl formation. Here the Punchbowl formation consists of massive, cross-bedded, coarse terrestrial sandstone with large lenses of pebble and cobble conglomerate (Noble, 1954). At surface outcrops the formation is relatively unfractured, although there are bedding plane fractures spaced at 1 to 3 m intervals and some vertical joints with locally varying attitudes, spaced at 3 to 7 m intervals (Sbar et al., 1979).

Wells 2, 4, 5, and XTLR were drilled at buttes located 4, 22, 34, and 4 km, respectively, northeast of the San Andreas fault (Figure 4). These wells were drilled entirely in quartz monzonite to depths of 257, 230, 239, and 869 m respectively. The quartz monzonite buttes are part of the suite of Mesozoic intrusives which form the basement of much of the western Mojave. Horizontal and steeply dipping fractures and joints were observed in outcrops at these sites. The buttes are apparently composed of slightly more siliceous material than the surrounding basement, and are thus more resistant to erosion (D.B. Burke, pers. comm.).

The rock penetrated by the Mojave wells was found to be highly fractured. Figure 5 contains frequency plots showing the number of fractures per meter as a function of depth for each well and Figure 6 contains plots of the cumulative number of fractures in each well as a function of depth. The number of fractures observed in well 1, drilled in sandstone, is significantly less than that observed in the wells drilled in quartz monzonite. The number of fractures per meter is not uniform throughout each well. Fractures often occur in relatively dense clusters, as at about 55 and 115-125 m in Mojave 4 (Figure 5). These fractured intervals appear in Figure 6 and steeper portions of the cumulative fracture curve. The cumulative fracture curve for Mojave 2 appears to flatten somewhat at depths greater than 160 m, implying a decrease in the fracture density. In the other wells, the curves indicate that the fracture density may be decreasing with depth below 150-200 m, but there is only a very moderate trend to lower fracture density with depth. Also, note that in the upper 150 meters the number of fractures encountered in Mojave 2, 4, and 5 are similar. The data show no tendency for the fracture density to increase as the San Andreas fault is neared.

Poles to all of the dipping fractures are shown in Figure 7a. Figure 7b contains the orientation-density plots derived from the pole distributions. At least two significant maxima are observed in the density plots for each well. For all wells, the secondary maxima are significant at only the 6σ level. For wells 2 and 4 the primary maxima also barely exceed the 6σ level.

In Mojave 1 the predominant fracture set ($> 10\sigma$) strikes N20-30°W and dips 35-40° to the southwest. A second cluster ($> 6\sigma$) with fractures striking slightly east of north is also present. Bedding planes, which would strike about N70°W and dip about 45-50°SW, were not observed. In Mojave 2 a broad cluster ($> 6\sigma$) of northwesterly striking, southwest dipping ($\sim 50^{\circ}$) fractures are found. In Mojave 4, possible conjugate fracture sets trending N35-55°E and dipping 50-60° to the northwest and southeast are found at the 6σ level. Most fractures in Mojave 2 and 4 appear to be randomly oriented, with minor significant maxima. In contrast, in Mojave 5 a fracture set striking about N80°E and dipping steeply ($\sim 60^{\circ}$) to the southeast is extremely pronounced ($> 16\sigma$). A second set of fractures ($> 6\sigma$) is also observed in Mojave 5 striking northwest and dipping to the northeast. Note that the majority of observed fractures dipped from 40° to 70°. Very few horizontal fractures were observed in these wells: 3 in Mojave 1, 2 in Mojave 2, 3 in Mojave 4, and 4 in Mojave 5.

The pole distribution for Mojave 5 (Figure 7a) may be interpreted as a girdle. A girdle is a concentration of points along a great circle. If the points are poles to planes, as they are here, the planes are in a statistically cylindrical zone about an axis which is perpendicular to the great circle forming the girdle (see Dennis, 1972). For Mojave 5, this axis has an approximate trend of S60°E and plunges about 50° to the southeast.

Fractures occurring below a depth of 137 m were analysed separately to test for depth dependence in the fracture orientation. Poles and density plots for the fractures found in these intervals are shown in Figure 8. A comparison of Figures 7 and 8 shows that each of the maxima present below 137 m also appears when fractures in the entire well are considered. Thus, the fracture patterns in the deeper intervals are basically subsets of the patterns found throughout the wells.

An approximately 1 km deep hole, well XTLR, was drilled at the same site as Mojave 2. The results of fracture studies performed in this well are shown in Figures 9 and 10. From Figure 9 it can be seen that the quartz monzonite was highly fractured throughout the logged section of the well (to about 870 m). Note that only a slight decrease of fracturing with depth was observed. The greatest decrease in fracture density was found at about 140 m, as in the shallow wells. There is, however, no strong trend to relatively unfractured rock with depth, in contrast to what might be expected due to increasing confining pressure.

One significant (> 14σ) cluster of poles was found in well XTLR striking N5-25°W and dipping about 60°SW. A comparison of Figures 7 and 10 shows that the fracture orientations found in Mojave 2 and XTLR are nearly the same. With the increased depth and number of fractures in XTLR, the level of significance of this pole cluster increased substantially.

Deep measurements of the stress field in XTLR indicate that the minimum horizontal stress is the minimum principal stress below a depth of about 300 m. Below this depth strike-slip faulting would be preferred. To test whether the change from a thrust-type environment to a strike-slip environment affected the fracture orientations, the distribution of those fractures found below 300 m in XTLR was considered (Figure 11). One significant (> 14σ) cluster was found. The orientation of this cluster is indistinguishable from the preferred fracture orientation found above 300 m, in the entire well, and from Mojave 2. The level of significance for this fracture orientation is greatest when the deep fracture data is included. The primary effect seen in the near surface intervals seems to be the addition of randomly oriented fractures which served to decrease the significance of the shallow interval clusters.

INTERPRETATION

Let us now consider the mode of origin of the fracture systems encountered in these wells based on the relation of the fracture orientations and the orientation of the regional stress field and the geologic history of the area. The fracture clusters found in the wells near the San Andreas fault have grossly similar strikes and dips. This could mean that these fractures formed under similar conditions. This is important when one considers 1) that well 1 was drilled in a Miocene sandstone while wells 2 and XTLR were drilled in Cretaceous quartz monzonite, and 2) the fact that well 1 and wells 2 and XTLR are on opposite sides of the San Andreas fault and were thus further separated in the past. In wells 1, 2, and XTLR, particularly in the deep intervals, the fracture poles cluster about orientations which are approximately parallel to the direction of maximum compression. It appears that these fractures are being held open, like tensile features, by the north-south compressional regional stress field. In the shallow intervals, the strikes of fracture planes represented by pole clusters ranges from subparallel to the direction of maximum compression (N10°-30°W) to subparallel to the San Andreas fault (∼ N65°W). Those fractures subparallel to the San Andreas fault could be open as a result of surface irregularities and debris associated with shear motion on fracture planes. Both of these possibilities imply that the current fracture orientation is related to the tectonic stress field and not to surface effects.

The fracture clusters shown in Mojave 4 are quite different from those found in wells closer to the San Andreas fault, and could represent a conjugate set of reverse faults striking to the northeast. The stress field theoretically necessary to cause motion on such fractures would have an axis of maximum compression which deviates by about 30^o in a counterclockwise sense from the present orientation. Garfunkel (1974) predicted counterclockwise rotations of up to 40^o for fault blocks in the Mojave desert during the Cenozoic. So, it is possible that these are shear planes which have rotated, but this cannot, of course, be stated with certainty.

In Mojave 5, a fracture set with a mean strike of about $N80^oE$ and a dip of 60^oE is dominant throughout the entire well. These fractures could be currently active reverse faults generated as a result of the regional roughly north-south compression.

Hydrofracture stress measurements in the shallow Mojave wells indicate that both horizontal stresses are greater than the lithostat (Zoback et al., 1980), and therefore thrust-type stress environment may be responsible, at least in part, for the orientations of the near surface fractures; but the magnitudes of the stresses appear to be too low to be responsible for the formation of the currently observed fracture systems.

As a whole, the fractures found in the Mojave wells appear to owe their existence to tectonic stresses rather than to near surface effects. This seems to be borne out on the basis of the orientation of the fractures with respect to the tectonic stress field, as discussed above, and by two other observations: 1) the fracture frequency does not decrease markedly with depth, and 2) the fracture orientations are not depth dependent, even where the relative magnitudes of the principal stresses change, as in well XTLR.

MONTICELLO RESERVOIR, SOUTH CAROLINA

Two approximately one km deep wells were drilled near Monticello Reservoir, Fairfield County, South Carolina (Figure 12). The well sites are in an area underlain by a complex series of almandine-amphibolite facies, metamorphic rocks, and granitic intrusives of the Charlotte Belt lithologies of the Piedmont Province (Dames and Moore, 1974). These consist of interlayered and folded gneisses, amphibolite, and schist, all of which have been intruded by plutons of granite to granodiorite composition. The following description of the geologic history of the region has been synthesized from the work of Overstreet and Bell (1965), Fisher et al. (1970), and Dames and Moore (1974).

Most of the metamorphic rocks presently exposed to the Piedmont were originally deposited as a thick sequence of shale, siltstone, volcanic tuff, etc., in the "Appalachian Geosyncline" between 250 and 600 million years ago. Episodes of folding, regional metamorphism, and igneous intrusion apparently followed each of three long sedimentation intervals. At the end of the final depositional period, the previously formed metamorphic rocks and the unmetamorphosed sediments experienced regional metamorphism. During this time the Piedmont was uplifted, accompanied by fracture deformation, folding, and the intrusion of discordant plutons. Also during this period, which correlates with the end of the Paleozoic, thrust faulting occurred on a major scale in the southern Appalachians.

By mid-Triassic much of the Piedmont had been worn down to a broad peneplain which truncated the exposed complex rock structures. Subsequent re-elevation of the region was accompanied by the formation of northeast-southwest trending structural troughs. These troughs are generally parallel to regional northeast-southwest trending Appalachian structures. Further uplift in late Triassic or early Jurassic time was accompanied by the emplacement of numerous northwest-southeast trending diabase dikes intruded along preexisting fractures. After another erosional cycle, during which the Piedmont was again reduced to a peneplain, continental uplift elevated the region now occupied by the Appalachians and adjacent Piedmont areas. Since the Jurassic, the region has undergone weathering, erosion, and deposition without any major tectonic disturbances.

The two wells, Monticello 1 and 2, were drilled to depths of 1100 and 1203 m, respectively, as part of a program to study induced seismicity at Monticello Reservoir. Both wells were drilled in intrusive granodiorite bodies of late Paleozoic age. The drill site for Monticello 1 was located on the top of a broad ridge west of the center of the reservoir. Monticello 2 was drilled within one km downstream of the dam which impounds the reservoir. The two wells are about 5 km apart.

Borehole televiewer records were obtained for the total depth of each well. The well conditions were excellent and the recorded data quality was generally very good.

The results of the fracture surveys are presented in Figures 13 and 14. Figure 13 shows the number of fractures as a function of depth in each well. Figure 14 shows poles to fracture planes and orientation-density plots.

The data show that the state of natural fracturing in the two wells is significantly different. The total number of fractures in Monticello 2 is approximately three times that in Monticello 1 (Figure 13). Fractures in Monticello 1 were found to occur mostly in discrete intervals, such as at 140, 190, 300, and 580 m, within relatively unfractured rock. In contrast, the granodiorite encountered in Monticello 2 was highly fractured, particularly from the surface to about 275 m and from about 460 to 510 m. Due to the highly fractured nature of the rock, small discrete fracture zones, as found in Monticello 1, are not as apparent in Monticello 2. The lowest fracture density in Monticello 2 is found from about 510 to 750 m and is similar to the fracture density found in Monticello 1 at the same depth. Below 750 m, a slight increase in the fracture density is observed in Monticello 2. It is interesting to note that the slope of the cumulative fracture curve for Monticello 2 in the intervals 275-460 m and 750 m - TD are about the same and the segments are nearly colinear. In the interval from 460-750 m the strain was apparently accommodated in the densely fractured zone at 460-510 m. As a result, the fracture density from 510 to 750 m is the lowest found in this well.

Twenty-six of the 147 fractures in Monticello 1 and 65 of the 439 fractures in Monticello 2 were horizontal. This is by far the highest density of horizontal fractures of any of the data sets. Horizontal fractures were found throughout each well; however, about half of each total was found in the upper 300 m of the well (Figure 15). In both wells, several horizontal fractures were found at depths greater than 1 km. In addition, the density of horizontal fractures is relatively high in Monticello 2 in the interval 400-500 m. The presence of these horizontal fractures may be due to decreased confining stresses as a result of the post-Jurassic erosional history of the area.

The orientation density plot for Monticello 1 (Figure 14) shows two small significant maxima (contours > 6σ) with approximate orientations of strike N45°E, dip 60°E and strike N50°W, dip 25°W. For Monticello 2, there is one extremely dense cluster of poles (maximum contour > 12σ) with a strike of about N5°E and dip 70°E.

In addition to the major differences in fracture orientation found within a horizontal distance of only 5 km, there were major differences in fracture orientation vertically in each well. In Monticello 1 this difference is shown in Figure 16 in which orientation-density plots are shown for the intervals surface-305 m, 305-610 m, and 610 m - TD. In the upper zone (surface 305 m) one significant cluster with northwest strike and southwest dip is apparent, a subset of the cluster found when all fractures encountered in the well were considered. In the middle zone (305-610 m), a northeast striking, southeast dipping cluster is apparent. This cluster is also apparent when all fractures are considered. In the pole density plot for the bottom third of the well (610 m - TD), the distribution is seen to be essentially random. In Monticello 2 (Figure 17) the fractures in the upper zone form two significant clusters (> 6σ): one striking approximately north-south and dipping to the east, and one striking east northeast and dipping gently to the southeast. In the lower interval (610 m - TD) there is a dense cluster (> 16σ) of fractures striking north-south and dipping steeply to the east. This north-south striking set is prominent when the fractures as a whole are considered. The fracture cluster found in the interval 305-610 m has a strike which differs by about 60^0 from that found in the rest of the hole. This group of fractures is the west-northwest trending, northeast dipping set responsible for the extended lobe on the density plot for the entire well (Figure 14).

Secor (1980) presents the results of joint studies made at surface outcrops near Monticello Reservoir. At outcrops within a few kilometers of the well sites fracture distributions similar to those found in both Monticello 1 and 2 were found. Secor concluded that there was little regional consistency to the orientation of the major joint sets. The marked difference we have observed in the two wells seems to support this conclusion. Surface fractures were also studied on the cleared bedrock surface at the site of the Virgil C. Summer Nuclear Station (Dames and Moore, 1974). This site is about 6 km southeast of the Monticello 1 site and 1 km east of Monticello 2. Poles to 247 fractures with no observed shear displacement across their faces and to 85 fractures which exhibited either shear displacement or hydrothermal alteration were plotted (Dames and Moore, 1974). In both cases, a pole density maximum occurred for planes striking about N44°E, dipping more than 60°SE. This orientation is very similar to one of the maxima found in Monticello 1. However, other maxima in the surface data, such as a northeast trending, northwest dipping set, are not apparent in data from either well. There is no surface indication of the pronounced north-south trending, eastward dipping set of fractures which is found in Monticello 2, but as shown in Figure 16, this fracture set is most pronounced at depths greater than 600 m.

Dames and Moore (1974) note that the northeast trend of fractures they observed is parallel to local regional trends. However, the rapid variation of fracture orientations in both the horizontal and vertical directions as shown by the study of Secor (1980) and the well data seem to exclude the possibility that all of the fractures were caused by the same regional stress field. The current local stress field has been determined by in-situ stress measurements using the hydrofracture technique (Zoback, 1980) and from earthquake focal mechanisms (Talwani et al., 1978). In Monticello 1 and 2, the difference in magnitude between the two horizontal principal stresses is relatively small except at shallow depth where the greatest horizontal principal stress is substantially greater than the vertical stress. As discussed by Zoback (1980), this vertical stress profile is indicative of conditions conducive to thrust-type faulting in the upper 300 m or so if appropriately oriented fracture planes are present. Seismologic studies confirm that the reservoir induced earthquakes which have been recorded in this area are apparently occurring at depths of less than 1 km (Talwani et al., 1978). The earthquakes appear to occur in clusters and apparently do not define linear fault planes. Events in the different clusters all have slightly different composite focal mechanisms. Most earthquakes are of the thrust type. A comparison of focal mechanisms for earthquakes close to the Monticello 1 site (Figure 18) with the shallow fracture orientations in the well shows fairly good agreement of possible fault planes and significant groupings of natural fractures (Figure 14, after Zoback, 1980). A comparison of pole densities in the upper third of Monticello 2 (34-305 m) with composite focal mechanisms for earthquakes occurring near that well site also shows a good correlation with one of the possible fault planes. Thus, the shallow earthquakes at Monticello Reservoir seem to be associated with shear motion on pre-existing fractures such as those encountered in these wells.

It has been noted that the fracture distribution in the interval 305-610 m in Monticello 2 is markedly different than that found above and below. The majority of the fractures found in this interval were located in a highly fractured interval centered at a depth of about 500 m (Figure 13). Pore pressure measurements made in the well revealed a zone of artesian pressures from above 394 m to somewhere above 591 m. The presence of the artesian zone suggests that impoundment has raised the pore pressure in an aquifer represented, perhaps, by the distinct fracture set found in the interval 305-610 m. The distinct orientation and hydrologic characteristics could be an indication that this fracture set has an origin different from that of the fracture sets seen in the shallow and deep intervals of the well. Thus it is possible that the fractures encountered in Monticello 2 are an example of superimposed fracture sets which may have formed under different stress regimes at different times.

INTERPRETATION

In neither well is there an appreciable decrease in the number of observed fractures with depth. The measured in-situ stress field and the shallow nature of the seismicity seem to indicate that deviatoric stresses are small at depths greater than a few hundred meters. These facts would seem to indicate that shear stresses associated with the current stress field are not responsible for the formation of the current fracture patterns. Dames and Moore (1974) concluded that near surface fractures upon which there has been shear displacement or hydrothermal mineralization were concentrated along older features. As noted previously, the rapid change of fracture orientation from well to well and from outcrop to outcrop (Secor, 1980) seems to preclude a fracture origin due simply to the historic regional stress field. It would seem, then, that the fractures encountered in these two wells owe their existence to local stress effects, whether from local amplification of the regional stress field due to variable rock properties or as a result of local structural or thermal processes not yet known in detail. It is not possible to determine here whether the mode of fracture formation was of predominately shearing or tensile nature.

LIMEKILN VALLEY, CALIFORNIA

Fracture studies have been performed in three wells drilled near the creeping section of the San Andreas fault in central California. These wells were drilled to depths of about 220 m in Cretaceous quartz monzonite of the Gabilan Range. The wells were located 2, 4, and 14 km west of the San Andreas Fault (Figure 19).

The Gabilan Range is part of the Coast Ranges province of central California. (For a detailed summary of the geology of this area, see Page (1966) and Compton (1966)). The structural and stratigraphic history of the Coast Ranges province has been quite complex. In the Tertiary, folding, high angle reverse faulting, thrusting, and strike-slip faulting in the Coast Ranges have been more or less simultaneous. All of these types of deformation have affected Plio-Pleistocene deposits in one area or another, implying that all have been at least locally active in the Quaternary. The Gabilan Range itself is a broad granitic complex enclosing numerous large metamorphic relics. Its length is about 75 km in a northwest-southeast direction, with a maximum width of about 15 km. It is bounded on the east by the San Andreas fault and on the north, west, and south by Cenozoic clastic sedimentary rocks. As a whole, the Gabilan Range appears relatively undeformed, although there is evidence of small scale folding and lineation.

Televiewer picture quality was generally good in wells LKB and LKC, but well LKD was so intensely fractured that the overall data quality is relatively poor. The fracture density (number of fractures per meter) is greater in these wells than in any of the other wells studied (compare Figures 6, 16, and 20). LKC, the least fractured of the Limekiln wells is more densely fractured than Mojave 4 and Monticello 2, the most densely fractured wells in the other two data sets. Only in LKC is there a possible indication that the number of fractures is decreasing with depth. There is no relation between proximity to the San Andreas fault and the density of fracturing in these wells. LKD, the well furthest from the fault, encountered the most fractures, while LKB, the well closest to the fault, lies between LKC and LKD in fracture density.

Poles to dipping fracture planes and orientation-density plots for each well are presented in Figure 21. The fractures encountered in the Limekiln wells seem to belong to a few well-developed fracture systems as, in each case, the maximum contour on the density plot is at least 10σ. In well LKB, located 2 km west of the San Andreas fault, two significant clusters of poles are observed. The most significant cluster ($> 16\sigma$) has a mean strike of about N60^{o}W and a dip of 60^{o}W. The secondary cluster ($> 10\sigma$) has an approximate mean strike of N65^{o}E and dip of 55^{o}E. It is possible that the two maxima are part of a girdle, with the perpendicular to the trend of the girdle having an approximate trend of S10^{o}E and plunge 55^{o}SE. There are also two clusters in the orientation-density plot for well LKC which is located 4 km from the

San Andreas fault. The most significant cluster ($> 10\sigma$) has an approximate mean strike of N20°W and dip 65°W, while the secondary cluster ($> 6\sigma$) has an approximate mean strike of N50°W and dip 55°E. The fracture population picked for LKD is only a subset of the total population due to the intense fracturing and resultant data quality problems. Three clusters are apparent on the orientation-density plot for well LKD, located 14 km from the fault. The most significant cluster ($> 14\sigma$) has an approximate mean strike of N10°E and dip of 60°W. The two lesser clusters ($> 8\sigma$) have approximate orientations of N5°W, dip 65°E and N40°E, dip 65°E; these two clusters may not be statistically distinct. Orientation-density plots for the upper 110 m and 110 m - TD for each well are shown in Figure 22. A comparison of the fracture orientations in the shallow and deep sections with those of the entire well indicates that the orientations are consistent through- out each entire well.

INTERPRETATION

The magnitude of the in-situ stress field was measured in several intervals in each of these wells using the hydrofracture technique (Zoback et al., 1980). Unfortunately, the orientation of the stress field was determined only in well LKC, where the direction of maximum horizontal compression was found to be about north-south. This orientation of the horizontal components of the stress field is compatible with right lateral shear on the San Andreas fault which trends approximately N40°W in the Coast Ranges province of central California. The maximum and minimum horizontal stresses measured in each of these wells were always greater than the vertical stress, which would imply that thrust-type shearing could be favored in near surface rock (Zoback et al., 1980).

Geodetic measurements of strain across the San Andreas fault (Thatcher, 1979; Savage and Burford, 1973) have been modeled by the motion of relatively rigid blocks. There has been no evidence or strain accumulation on either side of the fault system, so that the relative motion appears to be accommodated by slip accumulation in a very narrow zone centered on the San Andreas fault. Such motion is consistent with a roughly north-south regional compression. However, triangulation studies carried out by Burford (1965), and an analysis of fold trends (Page, 1966) indicate that the direction of maximum shortening is N35°-40°E. Also, earthquake focal mechanisms indicate general north-south compression, but with considerable scatter (Zoback and Zoback, 1980). Gawthrop (1977), in a study of the seismicity of the central coastal region of California, found that the least horizontal principal stress was oriented about N60°W. This conclusion was based upon an average of 30 events, with approximately equal numbers of strike-slip and thrust events. The direction of maximum compression varied from N10°W to N60°E, with an average of about N30°E, close to the direction inferred from fold orientations.

As in the Monticello wells, the fracture orientations vary considerably from well to well. In well LKB, the pole maxima may represent conjugate shear sets lying on a girdle. Considering their dips, these fractures probably represent dip-slip shear features. If they are like reverse faults, the indicated direction of maximum compression is about N80°W, which is inconsistent with any of the measured regional stress fields. If the fractures are like normal faults, the indicated direction of maximum extension would be N80°W. This possibility is inconsistent with the observation in this region that the in-situ stress field at shallow depth favors thrusting, and in deeper intervals favors strike-slip faulting. Thus, the orientation of the fractures in LKB does not bear a direct relation to the current regional stress field.

By considering the scatter in the orientation-density diagram for LKC, it is possible to conclude that the two maxima represent a conjugate set of shear fractures. However, the data do not rule out a tensile origin for at least one of the groups. If the maxima do represent a shear set, a direction of either maximum compression or extension of about N35°E is indicated. No observations of the stress field favor normal faulting, so that, from the fracture pattern, a direction of maximum compression of about N35°E is indicated. This is approximately the direction of maximum compression axes found from focal mechanisms.

The fracture pattern in well LKD seems to be indicative of a conjugate set of shear fractures striking about N10°E, the set dipping to the west dominating. Again, from the fracture pattern this shear set could be a result of N80°W compression, as the magnitude of measured stresses seems to exclude extension. As in

LKB, the orientation of the fractures in LKD does not bear a direct relation to the current regional stress field.

The directions of maximum compression derived from the fracture orientations in wells LKB and LKD are nearly identical. It was noted earlier that the pole maxima in LKB may be part of a girdle. If the poles to the fracture planes in LKB are rotated about small circles through the angle required to give the girdle a 90^0 dip, then the effects of a possible structural plunge may be removed (see Dennis, 1972; Billings, 1972). (A rotation of $50\text{-}60^0$ about a horizontal axis is required to give the girdle in LKB a 90^0 dip.) The resulting orientation-density plot for LKB is very similar to that found for LKD. This may be an indication that the fractures found in LKB and LKD were originally formed under similar conditions and that there has been considerable post-fracturing deformation of these blocks of the Gabilan Range.

The Limekiln Canyon wells were drilled in a relatively stable block in a region which has a very complex geologic history. The fractures found in these wells were strongly oriented, yet these orientations were not consistent from well to well. No simple regional stress field can be proposed which can explain the observed distribution of fractures. As is possible for each of the data sets, and may be best shown in wells LKB and LKD, any inconsistency between the fracture orientations and the regional stress field may be due to post-fracturing deformation.

SUMMARY AND CONCLUSIONS

In this paper, observations of the natural fracture distributions found in ten wells from three different regions of North America have been presented. All but one of these wells were drilled in granitic rock. Fractures were numerous in all wells. The lowest fracture density was found in Mojave 1, drilled in sandstone 2 km from the San Andreas fault. The highest fracture density was found in LKD, drilled in quartz monzonite 14 km from the San Andreas fault in central California.

Fractures were found throughout every well. There is a slight tendency for the fracture density to decrease with depth (see Figures 6, 9, 13, and 20). From laboratory experiments and simple elasticity theory on the effect of confining pressure on crack closure, fracture density would have been expected to decrease more rapidly with depth than was observed. Factors such as surface roughness and debris, not usually important in laboratory and theoretical developments, may be responsible for the fractures remaining open to depths of more than 1 km with only a minor decrease in fracture density.

In addition to orientation information, an estimate of the apparent fracture aperture at the borehole could be made from the televiewer data. Observed apparent apertures ranged from a few millimeters to several centimeters. The size of the apparent apertures was found to be roughly independent of depth.

Most fractures were steeply dipping. Few horizontal fractures were observed in any of the wells. Vertical fractures are not well sampled by vertical boreholes, and thus do not make a contribution to the fracture populations observed in these wells.

At least one statistically significant concentration of poles to the observed fracture planes was found in every well. These significant pole concentrations were generally found throughout each entire well.

Preferred fracture orientations found in the wells were compared to the regional stress field and structure. In no area was there a simple, genetic relationship between all of the fracture sets and the regional stress field or structure. However, in the Mojave wells it appears that there may be relationships between the current, measured stress field and many of the fractures which are observed. In the Monticello wells extremely local conditions appear to control fracture distribution and response. The Limekiln wells are examples of cases in which local fracture patterns appear distinct, but there is some evidence that much of the difference is due to post-fracture deformation of the rock. Many factors, from changing mineralogy to local structural effects to the superposition of several unrelated fracture sets over geologic time could be responsible for the complex fracture patterns observed in each area.

The measured shear stresses in these wells are currently low (less than 100 bars) (Zoback et al., 1980; Zoback, 1980), even in unfractured intervals. If such low shear stresses are representative of the stress state under which these fracture sets were formed, extensive development of shear sets would not be expected and most of the fractures would be of tensile origin. It is interesting to note, however, that in several cases the pole clusters in the orientation density plots could be interpreted as indicative of the presence of conjugate shear fracture sets. Whether these clusters are due to the fractures having formed in shear, or to the results of shear motion on favorably oriented, pre-existing tensile fractures, or to processes not involving shear stresses cannot be determined here. From the televiewer data it is impossible to determine whether the fracture sets are of shear or tensile origin, or whether any shear deformation has occurred across the fractures subsequent to their creation.

In most of the wells considered the fracture orientations did not vary with depth. Thus, knowledge of the shallow fracture orientations in a well may be a good indicator of the orientation at depth. This is not always true as, for example, the fracture orientations found in the artesian zone of Monticello 2 were markedly different from those found in the rest of the well. Also, as highly fractured intervals were often found throughout the wells studied, a decrease in the fracture density in one interval does not indicate that a more densely fractured interval is not located at greater depth.

The Mojave and Limekiln Canyon wells were located close to the San Andreas fault, which might be expected to affect the fracture distributions. For example, Friedman (1969) studied the macro- and microfracture distributions from cores recovered from wells drilled near the Oak Ridge fault, a major reverse fault in the Ventura basin. Friedman concluded that conjugate shear sets of fractures had developed, with one set parallel to the fault plane. He also concluded that the abundance of microfractures increases with proximity to the fault and is independent of the depth of burial. The Mojave and Limekiln wells closest to the San Andreas fault were 2 km away from it. It is possible that closer to the fault the fracture orientations may parallel the San Andreas (Friedman's (1969) data generally came from within a half kilometer of the mapped subsurface location of the Oak Ridge fault). However, the data presented here show that there is no tendency for the fracture planes to align themselves with the San Andreas fault, nor is there an increase in fracture density as the fault is approached.

Thus far this study has taken the measured fracture distribution as a known and an attempt has been made to try to determine the regional conditions which would be resonsible for such distributions. The reverse question could also be asked - knowing the structural history and the regional stress field could one predict the fracture distribution to be found in a well at a given site? In the case of lineaments, one might expect a good correlation between stress field, regional geology, and lineament orientation (see Hodgson, 1961). Lineaments are fairly widely spaced, however, and are not likely to be extensively sampled by wells (Kowalik and Gold, 1976). The data presented here indicate that fractures on a smaller scale than lineaments are not simply related to regional processes and their distribution may be controlled by local factors. The use of an approach based upon simple fracture mechanics in a homogenous medium to predict fracture orientations seems not to be justified on the basis of the data presented here. It thus appears unlikely that fracture orientations in a well can always be predicted with certainty simply from a knowledge of the regional stress field and the geologic history of the area.

REFERENCES

Billings, M.P., Structural Geology, 606 pp., Prentice-Hall, Inc., Englewood Cliffs, 3rd ed., 1972.

Brace, W.F., An extension of Griffith theory of fracture to rocks, J. Geophys. Res., 65, 3477-3480, 1960.

_____, Permeability of crystalline and argillaceous rocks: status and problems, Int. J. Rock Mech. Min. Sci., in press.

Budiansky, B. and R.J. O'Connell, Elastic moduli of cracked solids, Int. J. Solids Structures, 12, 81-97, 1976.

Burford, R.O., Strain analysis across the San Andreas fault and Coast Ranges of California, Paper presented at second symposium, Commission on recent crustal movements, Aulanko, Finland, August 1965.

Burke, D.B. and D.J. Ponti, Ongoing crustal deformation in the western Mojave region of south-central California (abs.), Geol. Soc. Amer. annual mtg., 1979.

Cloos, E., Lineation, a critical review and annotated bibliography, Geol. Soc. Amer. Mem. 18, 1946. Supplement, review of literature, 1942-52, 1953.

Compton, R.R., Granitic and metamorphic rocks of the Salinian block, California Coast Ranges, in Geology of Northern California, E.H. Bailey, ed., Cal. Div. Mines Geol. Bull. 190, 277-287, 1966.

Dames and Moore, Supplemental geologic investigation Virgil C. Summer Nuclear Station - unit one Fairfield County, South Carolina for South Carolina Electric and Gas Company, 61 pp. + figures, 1974.

Dennis, J.G., Structural Geology, 532 pp., Ronald Press, New York, 1972.

Dibblee, T.W., Jr., Areal geology of the western Mojave Desert, California, U.S. Geol. Surv. Prof. Paper 522, 153 pp., 1967.

Engelder, T., The nature of deformation within the outer limits of the central Appalachian foreland fold and thrust belt in New York state, Tectonophysics, 55, 289-310, 1979.

Engelder, T., and P. Geiser, On the use of regional joint sets as trajectories of paleostress fields during the development of the Appalachian Plateau, New York, J. Geophys. Res., 85, 6319-6341, 1980.

Fisher, G.W., F.J. Pettijohn, J.C. Reed, Jr., K.N. Wemer, eds., Studies of Appalachian Geology: Central and Southern, 460 pp., Interscience Publications, New York, 1970.

Freund, R., Kinematics of transform and transcurrent faults, Tectonophysics, 21, 93-134, 1974.

Friedman, M., Structural analysis of fractures in cores from Saticoy field, Ventura County, California, AAPG Bull., 53, 367-389, 1969.

Garfunkel, Z., Model for the late Cenozoic tectonic history of the Mojave Desert, California, and for its relation to adjacent regions, Geol. Soc. Amer. Bull., 85, 1931-1944, 1974.

Hadley, K., Comparison of calculated and observed crack densities and seismic velocities in Westerly granite, J. Geophys. Res., 81, 3484-3494, 1976.

Haimson, B.C., Near surface and deeper hydrofracturing stress measurements in the Waterloo quartzite (abs.), EOS, Trans. Amer. Geophys. Union, 59, 329, 1978.

Haxby, W.F., and D.L. Turcotte, Stresses induced by the addition or removal of overburden and associated thermal effects, Geology, 4, 181-184, 1976.

Hickman, S. and M.D. Zoback, Bulk permeability measurements in fractured crystalline rock, in preparation, 1981.

Hodgson, R.A., Regional study of jointing in Comb Ridge-Navajo Mountain area, Arizona and Utah, Amer. Assoc. Petrol. Geol. Bull., 45, 1-38, 1961.

Jaeger, J.C. and N.G.W. Cook, Fundamentals of Rock Mechanics, 515 pp., Chapman and Hill, London, 1969.

Jahns, R.H., Tectonic evaluation of the Transverse Ranges province as related to the San Andreas fault system, Proc. of Conference on Geologic Problems of San Andreas Fault System, Stanford Univ. Publ. Geol. Sci., 13, 149-170, 1973.

Johnson, A.M., Physical Processes in Geology, 577 pp., Freeman, Cooper and Co., San Francisco, 1970.

Kamb, W.B., Ice petrofabric observations from Blue Glacier, Washington, in relation to theory and experiment, J. Geophys. Res., 64, 1891-1910, 1959.

Kowalik, W.S. and D.P. Gold, The use of landsat -1 imagery in mapping lineaments in Pennsylvania, Proc. First International Conference on the New Basement Tectonics, Utah Geol. Soc., 236-249, 1976.

Kranz, R.L., Crack growth and development during creep of Barre granite, Int. J. Rock Mech. Min. Sci., 16, 23-36, 1979.

Lisowski, M. and J.C. Savage, Strain accumulation from 1964 to 1977 near the epicentral zone of the 1976-1977 earthquake swarm southeast of Palmdale, California, Bull. Seism. Soc. Amer., 69, 751-756, 1979.

McGarr, A., Violent deformation of rock near deep-level, tabular excavations-seismic events, Bull. Seism. Soc. Amer., 61, 1453-1466, 1971.

McGarr, A., D.D. Pollard, N.C. Gay, and W.D. Ortlepp, Observations and analysis of structures in exhumed mine-induced faults, in Proceedings of Conference VIII: Analysis of Actual Fault Zones in Bedrock, U.S. Geol. Surv. Open File Rep. 79-1239, 101-120, 1979.

Noble, L.F., The San Andreas fault zone from Soledad Pass to Cajon Pass, California, Calif. Div. Mines Geol. Bull., 170, 37-38, 1954.

Nur, A., Effects of stress on velocity anisotropy in rock with cracks, J. Geophys. Res., 76, 2022-2034, 1971.

Overbey, W.K. and R.L. Rough, Prediction of oil- and gas-bearing rock fractures from surface structural features, U.S. Dept. of Interior, Bureau of Mines, Report of Investigations 7500, 14 pp., 1971.

Overstreet, W.C. and H. Bell III, The crystalline rocks of South Carolina, U.S. Geol. Surv. Bull. 1183, 126 pp., 1965.

Page, B.M., Geology of the Coast Ranges of California, Geology of Northern California, E.H. Bailey, ed., Cal. Div. Mines Geol. Bull. 190, 255-276, 1966.

Prescott, W.H. and J.C. Savage, Strain accumulation on the San Andreas fault near Palmdale, California, J. Geophys. Res., 81, 4901-4908, 1976.

Price, N.J., Fault and joint development in brittle and semi-brittle rocks, 176 pp., Pergamon Press, 1966.

Savage, J.C. and R.O. Burford, Geodetic determination of relative plate motion in central California, J. Geophys. Res., 78, 832-845, 1973.

Savage, J.C. and W.H. Prescott, Geodimeter measurements of strain during the southern California uplift, J. Geophys. Res., 84, 171-177, 1979.

Sbar, M.L., T. Engelder, R. Plumb, and S. Marshak, Stress pattern near the San Andreas fault, Palmdale, California, from near surface in-situ measurements, J. Geophys. Res., 84, 156-164, 1979.

Secor, D.T., Role of fluid pressure in jointing, Am. Journ. Sci., 263, 633-646, 1965.

_____, Geological studies in an area of induced seismicity at Monticello Reservoir, South Carolina, First technical report to U.S. Geol. Surv., Contract No. 14-08-0001-19124, 1980.

Shanks, R.T., B.S. Kwon, M.R. DeVries, and P.A. Wichman, A review of fracture detection with well logs, Soc. Pet. Eng. Ann. Mtg., 1976, paper SPE 67159.

Sieh, K.E., Slip along the San Andreas fault associated with the great 1857 earthquake, Bull. Seism. Soc. Amer., 68, 1421-1448, 1978.

Snow, D.T., Rock fracture spacings openings, and porosities, J. Soil. Mech. and Foundations Div., Proc. ASCE, SM 1, 73-91, 1968.

Talwani, P., D. Stevenson, J. Sanber, B.K. Rastogi, A. Drew, J. Chiang, and D. Amick, Seventh technical report to U.S. Geol. Surv., Contract no. 14-08-0001-14553, 1978.

Tchalenko, J.S. and N.N. Ambraseys, Structural analysis of the Sasht-e Bayaz (Iran) earthquake fractures, Geol. Soc. Amer. Bull., 81, 41-60, 1970.

Thatcher, W., Episodic strain accumulation in southern California, Science, 194, 691-695, 1976.

________, Systematic inversion of geodetic data in central California, J. Geophys. Res., 84, 2283-2295, 1979.

Walsh, J.B., The effect of cracks on the compressibility of rock, J. Geophys. Res., 70, 381-389, 1965.

Wilcox, R.E., T.P. Harding, and D.R. Seeley, Basic wrench tectonics, AAPG Bull., 57, 74-96, 1973.

Zemanek, J., E.E. Glenn, L.J. Norton, and R.L. Caldwell, Formation evaluation by inspection with the borehole televiewer, Geophysics, 35, 254-269, 1970.

Zoback, M.D., In-situ study of the mechanism of reservoir triggered earthquakes in the southeastern United States, submitted to Proc. of Research Conference on intra-continental earthquakes, Ohrid, Yugoslavia, September, 1979.

Zoback, M.D., H. Tsukahara, and S. Hickman, Stress measurements at depth in the vicinity of the San Andreas fault: Implications for the magnitude of shear stress at depth, J. Geophys. Res., 85, 6157-6173, 1980.

Zoback, M., J. Roller, J. Svitek, and D. Seeburger, Hydraulic fracturing stress measurements and natural fracture studies near the San Andreas fault in southern California, Proc. Conference on the magnitude of Deviatoric Stresses in the Earth's Crust and Upper Mantle, 301-320, 1980.

Zoback, M.L. and M.D. Zoback, State of stress in the coterminus United States, J. Geophys. Res., 85, 6113-6156, 1980.

FIGURE CAPTIONS

Figure 1 Isometric sketch of fracture or bedding plane intersecting borehole at moderate dip angle, and corresponding Borehole Televiewer log (after Zemanek et al. (1969), Fig. 7).

Figure 2 Televiewer pictures for 15.2 m of well in two 7.6 m sections. Top of sequence is at upper left, bottom at lower right. Numerous fractures are present, shown as dark sinusoidal bands.

Figure 3 a) Lower hemisphere equal-area sterographic projection of fracture poles encountered in well LKC.

b) The corresponding orientation-density diagram. The standard deviation, $\sigma = 2.9$, and the sampling area, $A = .05$, are determined by the number of fractures, $N = 165$, using the method of Kamb (1959). A random distribution of poles would yield pole densities between 2σ and 4σ. Pole densities greater than 6σ represent statistically significant preferred fracture orientations. Two significant pole clusters are shown here: a north-northwest striking southwest dipping cluster with maximum contour of 10σ, and a northwest striking, northeast dipping cluster with maximum contour of 6σ.

Figure 4 Map showing location of wells in the western Mojave desert, California. Well 1 is about 2 km southwest of the San Andreas fault, and was drilled entirely through the Miocene Punchbowl sandstone. Wells 2, 4, 5, and XTLR are 4, 22, 34, and 4 km, respectively, northeast of the San

Andreas fault. All were drilled in Mesozoic quartz monzonite which is part of the suite of Mesozoic intrusives which form the basement of much of the western Mojave.

Figure 5 Frequency plot of the number of fractures per meter as a function of depth in the Mojave wells 1, 2, 4, and 5. Note that fractures were found throughout each well.

Figure 6 Cumulative number of fractures plotted as a function of depth for the Mojave wells. The sandstone encountered in Mojave 1 is significantly less fractured than the granite encountered in wells 2, 4, and 5. In general, only a slight decrease in the number of fractures with increasing depth is observed.

Figure 7 Lower hemisphere, equal-area diagrams for Mojave 1, 2, 4, and 5.

a) Poles to all dipping fractures in the entire well.

b) Orientation-density diagrams for all dipping fractures. Significant fracture orientations (contours $> 6\sigma$) were found for each pole population. Maximum contours ranged from 6σ in well 4 to 16σ in well 5. Note that there is no significant fracture orientation common to all four populations, even though all were sampled within 35 km of the San Andreas fault. There is no single, simple relationship between these preferred fracture orientations and the regional stress field.

Figure 8 Lower hemisphere, equal-area diagrams for Mojave 1, 2, 4, and 5.

a) Poles to all dipping fractures below 137 m.

b) Orientation-density diagrams for all dipping fractures below 137 m. Significant fracture orientations were found for each pole population. Each significant fracture orientation observed in the deeper intervals was also significant when the entire well was considered. The density maxima in wells 2 and 4 are barely significant. Well 5 has the only population for which the maximum contour exceeds 6σ.

Figure 9 a) Frequency plot of number of fracture plotted as a function of depth for well XTLR.

b) Cumulative number of fractures plotted as a function of depth for XTLR.

The number of fractures is almost uniformly distributed with depth, with only a slight tendency to fewer fractures with increasing depth.

Figure 10 a) Poles to all dipping fractures in the entire well.

b) Orientation-density diagrams for all dipping fractures. The maximum contours (14σ) indicate that the preferred fracture orientation strikes north-northwest and dips steeply to the southwest. This pole distribution compares favorably, particularly in the deeper interval, with that found in Mojave 2, which was drilled at the same site as XTLR. The strike of this significant fracture orientation is parallel to the direction of the maximum regional compressive stress, possibly implying that these fractures are being held open like tensile features.

Figure 11 Lower hemisphere, equal-area diagrams for XTLR.

a) Poles to all dipping fractures below 300 m.

b) Orientation-density diagrams for all dipping fractures below 300 m.

The fracture distribution in well XTLR below 300 m is substantially the same as that found throughout the entire well. In situ stress measurements indicate that the vertical principle stress is the minimum principal stress above 300 m, and that the minimum horizontal stress is the minimum principal stress below 300 m. No significant change in fracture orientations was observed due to the change from a thrust-type environment to a strike-slip environment.

Figure 12 Map showing location of wells near Monticello Reservoir, Fairfield County, South Carolina. Both wells were drilled in intrusive granodiorite bodies of late Paleozoic age in the Charlotte Belt.

Figure 13 a) Frequency plot of number of fracture plotted as a function of depth for Monticello 1 and 2.

b) Cumulative number of fractures in Monticello 1 and 2 plotted as functions of depth.

The number of fractures encountered in Monticello 2 was about three times that encountered in Monticello 1, which was relatively unfractured. There is little indication in these wells of a decrease in the number of fractures with increasing depth. Numerous fractured zones were found in these wells, the largest of which was centered at a depth of about 475 m in Monticello 2.

Figure 14 Lower hemisphere, equal-area diagrams for Monticello 1 and 2.

a) Poles to all dipping fractures.

b) Orientation-density diagrams for all dipping fractures.

Although located only five kilometers apart, the fracture patterns found in these wells are very different. The maximum contours for Monticello 1 are 6σ for two small areas, while one pole cluster with a maximum contour of 12σ was found in Monticello 2. There is an approximately 45° difference in strike between that of the largest cluster in Monticello 1 and that in Monticello 2.

Figure 15 Cumulative number of horizontal fractures plotted as a function of depth for Monticello 1 and 2. About half of the horizontal fractures in each well were found at depths above 300 m. Several horizontal fractures were also found at depths of about 1 km in both wells and in the highly fractured intervals between about 400-500 m in Monticello 2.

Figure 16 Orientation-density diagrams for Monticello 1 for the intervals surface-305 m, 305-610 m, and 610 m-TD. Different fracture distributions are found in each of these intervals; shallow dipping, northwest striking fractures in the upper interval, southwest dipping and northeast striking fractures in the intermediate interval, and a random distribution in the lower interval.

Figure 17 Orientation-density diagrams for Monticello 2 for the intervals surface-305 m, 305-610 m, and 610 m-TD. In the upper interval two significant pole maxima are found at the 6σ level. One of the maxima is part of the north-south striking set found when the fracture population of the entire well was considered (Figure 14). The second shallow dipping group shows up as a slight ($> 4\sigma$) concentration in Figure 14. In the intermediate interval a strong northwest striking, northeast dipping set is found; this set is responsible for the extended lobe in Figure 14. Most of the fractures in this interval are found in the densely fractured zone at about 500 m depth. In the bottom interval the north-south striking fracture set is very prominent; there is little evidence below 600 m for the northwest striking set of the intermediate interval.

Figure 18 Comparison of orientation-density diagrams for shallow intervals of Monticello 1 and 2 and poles to probable fault planes found from local focal mechanisms. Note that the poles to the fault planes lie near or within significant fracture pole concentrations.

Figure 19 Map showing location of wells near Hollister, California. Wells LKB, LKC, and LKD are 2, 4, and 14 km southwest of the San Andreas fault, respectively. These wells were drilled in Cretaceous quartz monzonite.

Figure 20 a) Frequency plot of number of fractures per meter plotted as a function of depth for wells LKB, LKC and LKD. b) Cumulative number of fractures plotted as a function of depth. In general, these wells encountered more densely fractured rock than any of the others in this study. Again, there is only a slight tendency for the number of fractures to decrease with depth. Also, there is no tendency for the number of fractures to increase near the San Andreas fault.

Figure 21 Lower hemisphere, equal-area diagrams for LKB, LKC and LKD.

a) Poles to all dipping fractures.

b) Orientation-density diagram for all dipping fractures. In each well dense pole concentrations were found. Note that, again, there is no significant fracture orientation common to each of the populations.

Figure 22 Lower hemisphere, equal-area diagrams for LKB, LKC and LKD.

a) Orientation-density diagram for the interval surface-110 m.

b) Orientation-density diagram for the interval 110 m-TD. The fracture orientations found in these wells tend to be relatively consistent with depth.

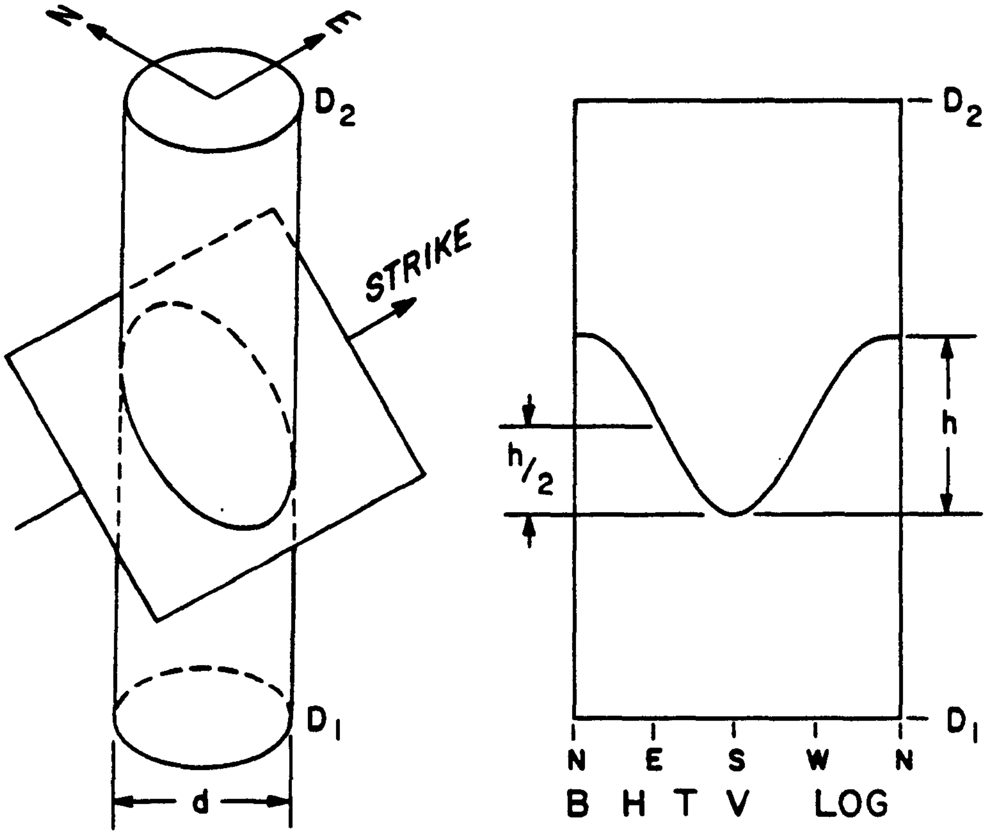

Strike : Orientation of midpoint between peak and trough (at $h/2$)

Dip : $\tan^{-1} h/d$

FIGURE 1

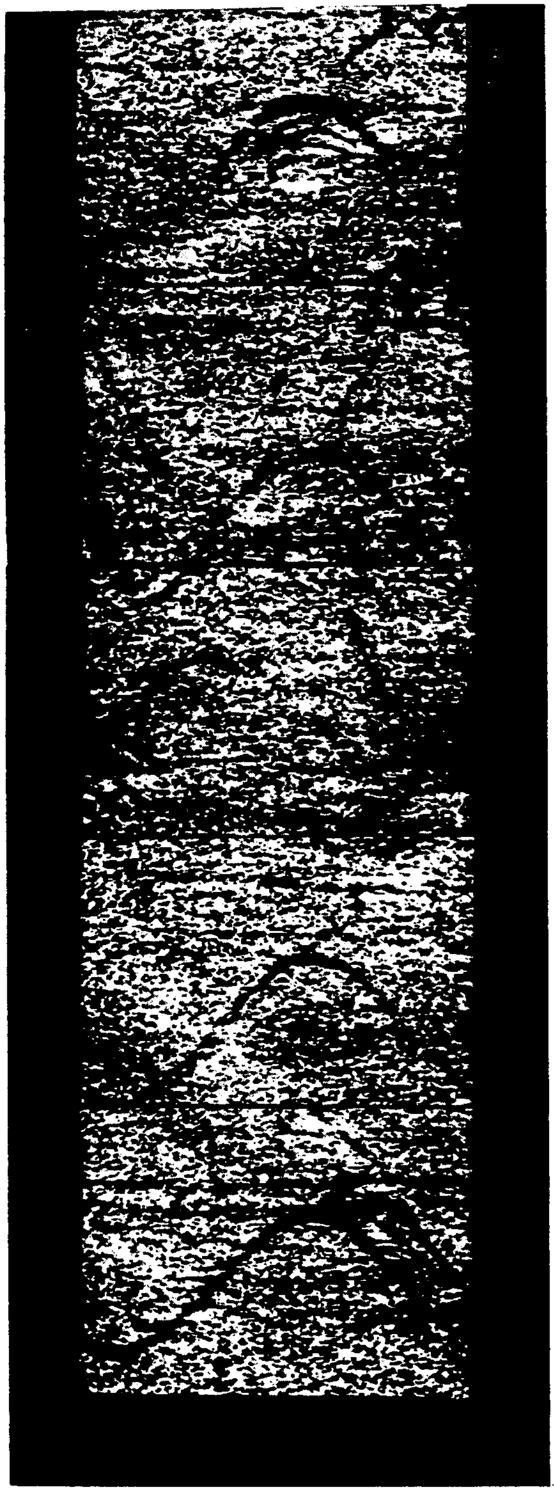

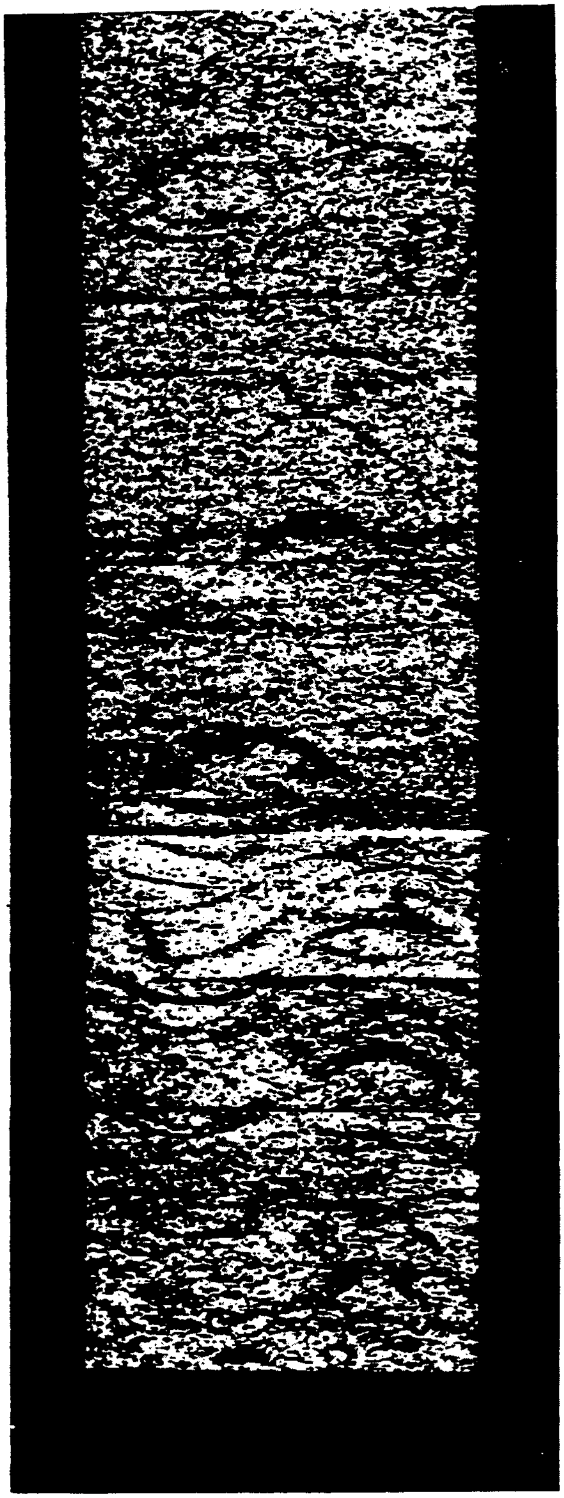

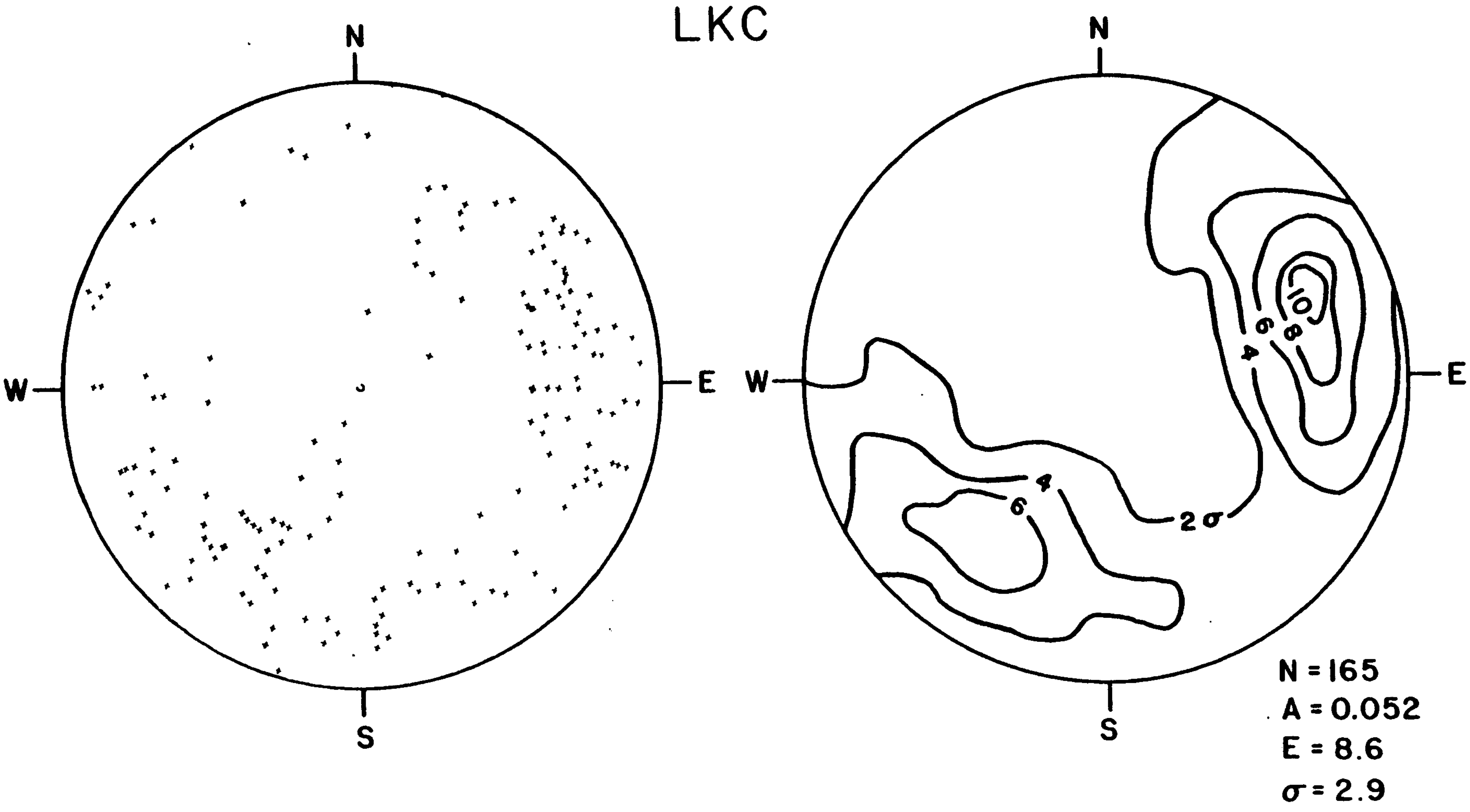

FIGURE 3

FIGURE 4

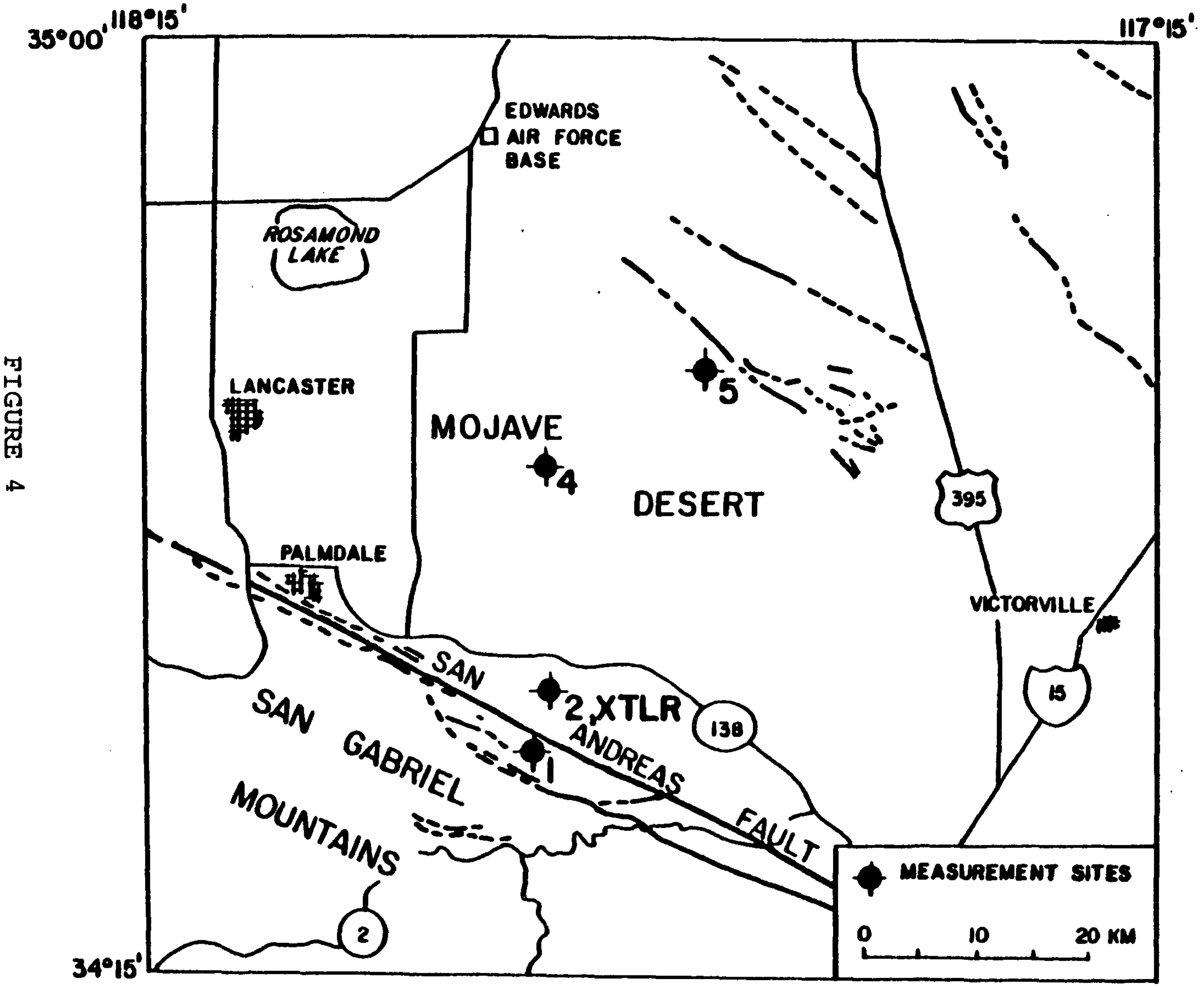
35°00'
118°15'
117°15'
34°15'
EDWARDS AIR FORCE BASE
ROSAMOND LAKE
LANCASTER
MOJAVE
DESERT
4
5
395
PALMDALE
VICTORVILLE
15
SAN ANDREAS FAULT
2 XTLR
1
138
SAN GABRIEL MOUNTAINS
2
MEASUREMENT SITES
0
10
20 KM

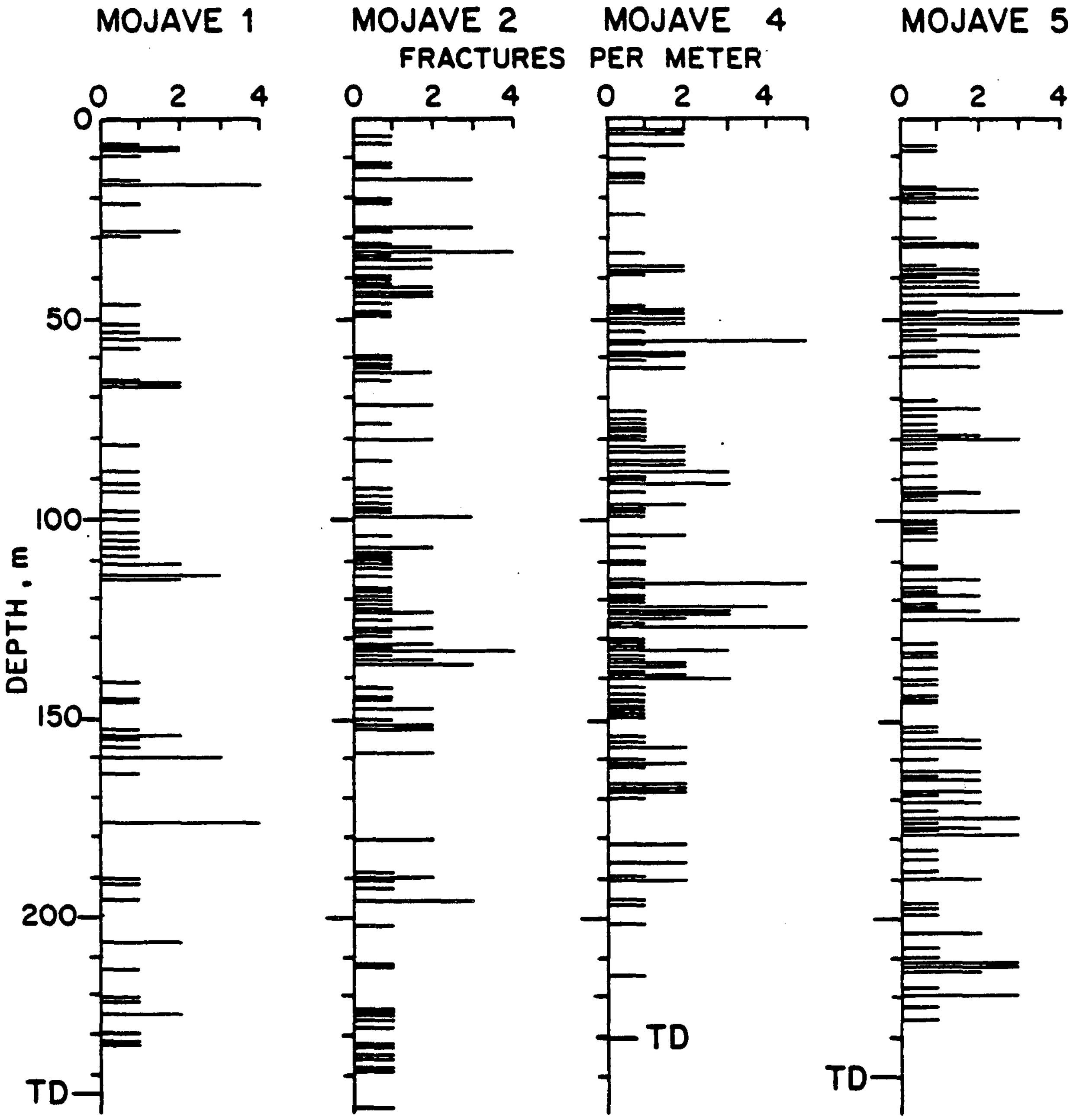
MOJAVE 1
MOJAVE 2
MOJAVE 4
MOJAVE 5
FRACTURES PER METER
0
2
4
DEPTH, m
0
50
100
150
200
TD

FIGURE 5

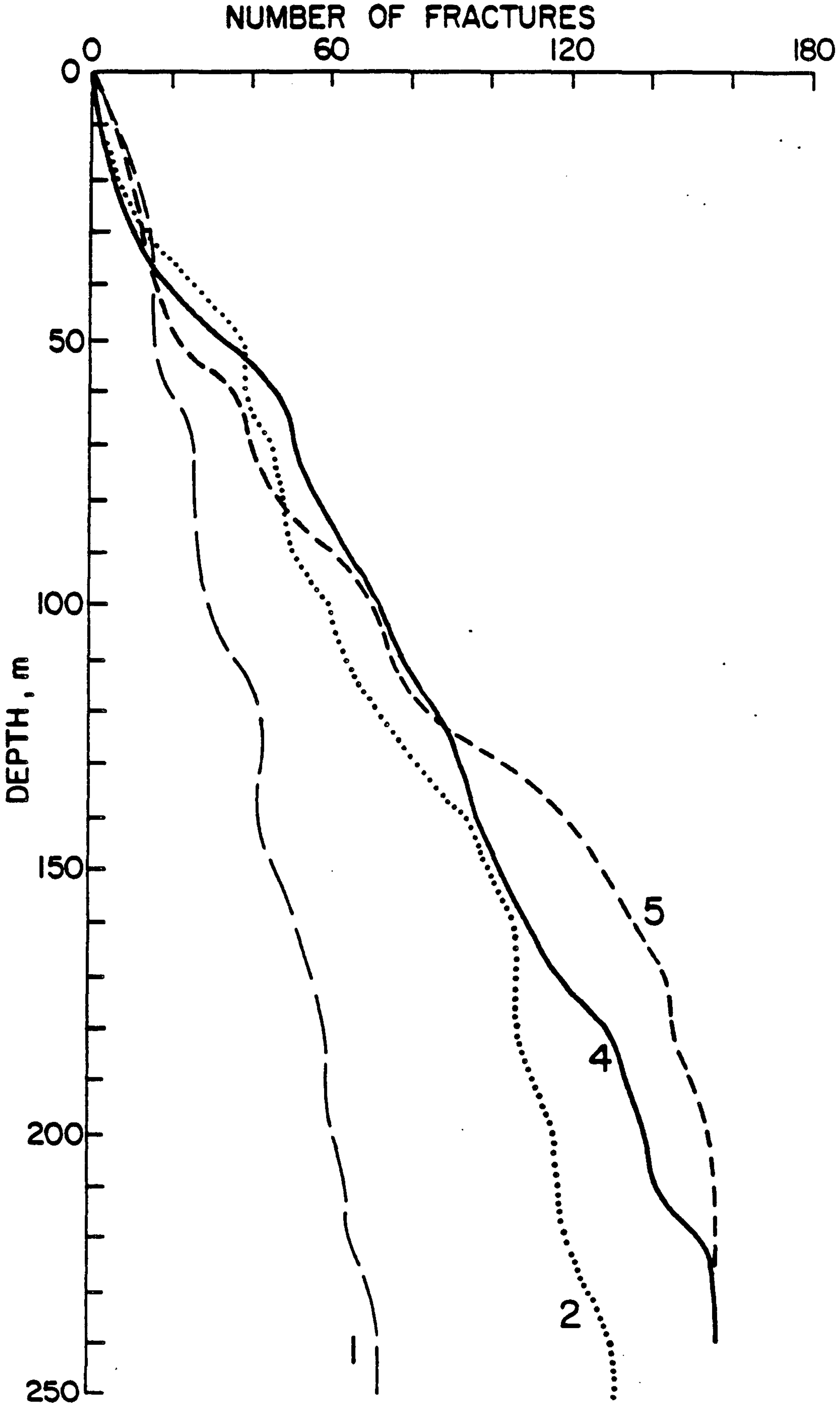
NUMBER OF FRACTURES
0
60
120
180
0
50
100
150
200
250
DEPTH, m
1
2
4
5

FIGURE 6

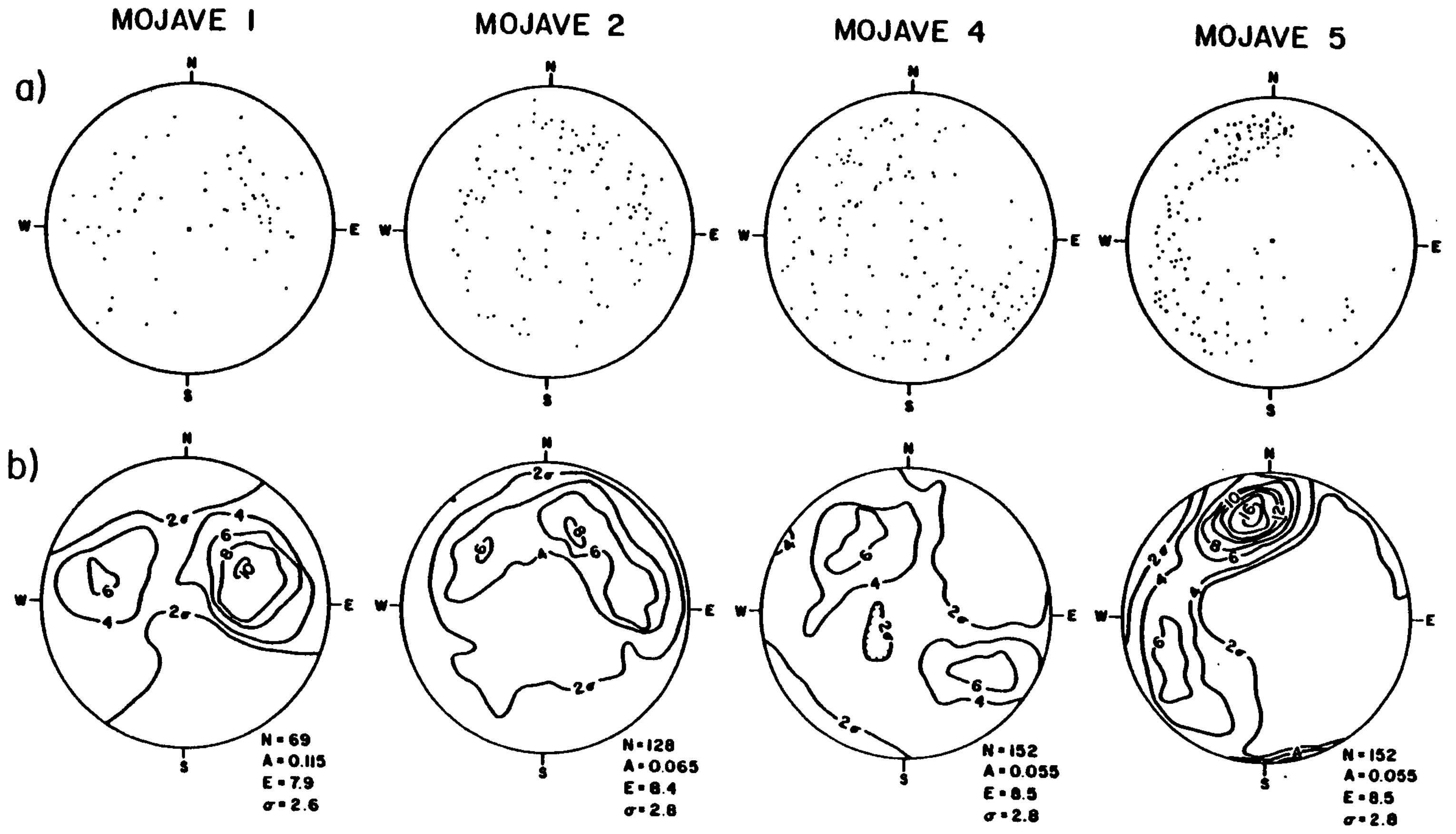
MOJAVE I
MOJAVE 2
MOJAVE 4
MOJAVE 5
a)
b)
N
S
W
E
2σ
4
6
8
10
12
16
N=69
A=0.115
E=7.9
σ=2.6
N=128
A=0.065
E=8.4
σ=2.8
N=152
A=0.055
E=8.5
σ=2.8
N=152
A=0.055
E=8.5
σ=2.8

FIGURE 7

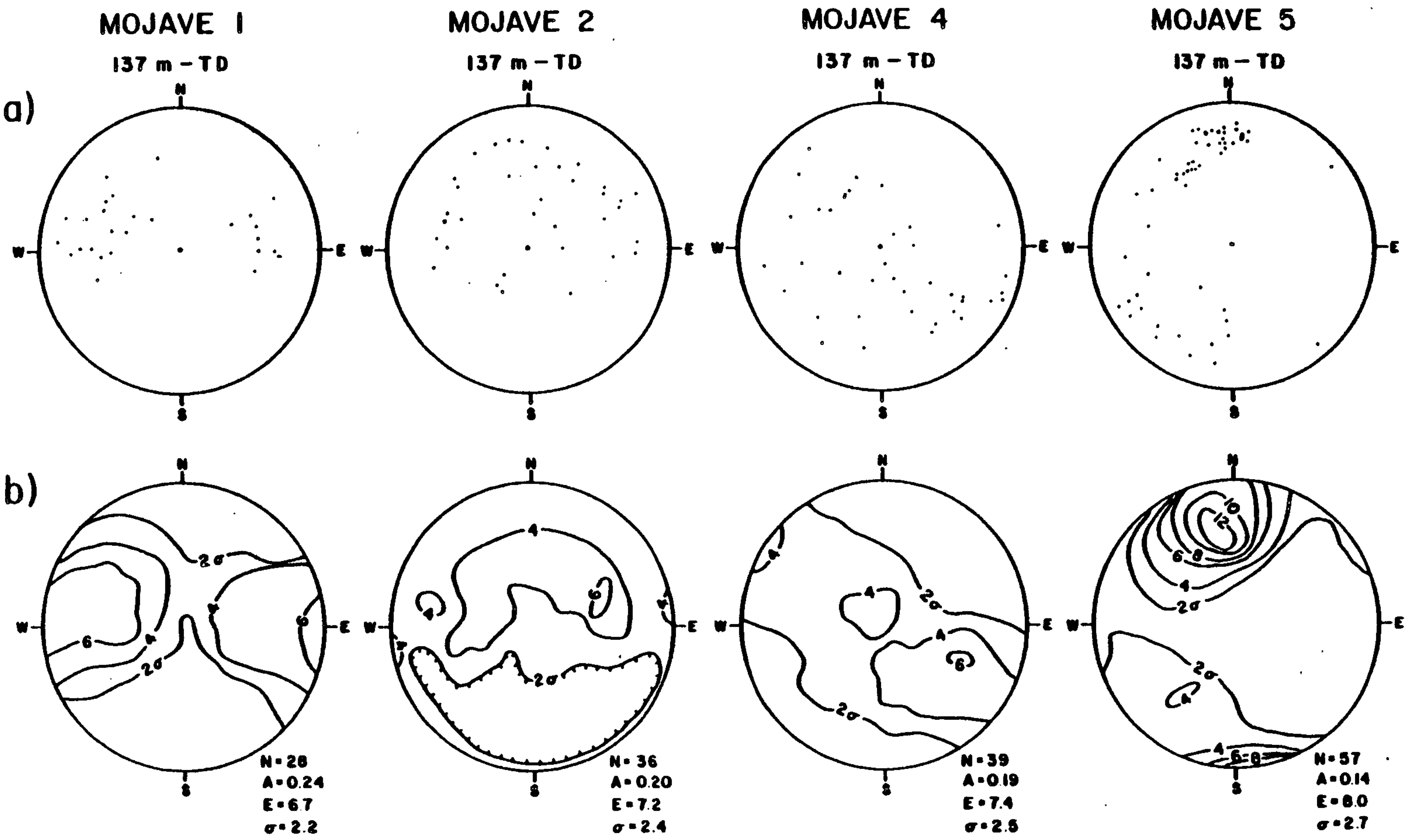
MOJAVE 1
137 m - TD
MOJAVE 2
137 m - TD
MOJAVE 4
137 m - TD
MOJAVE 5
137 m - TD
a)
b)
N
S
E
W
2σ
4
6
8
10
12
N=28
A=0.24
E=6.7
σ=2.2
N=36
A=0.20
E=7.2
σ=2.4
N=39
A=0.19
E=7.4
σ=2.5
N=57
A=0.14
E=8.0
σ=2.7

FIGURE 8

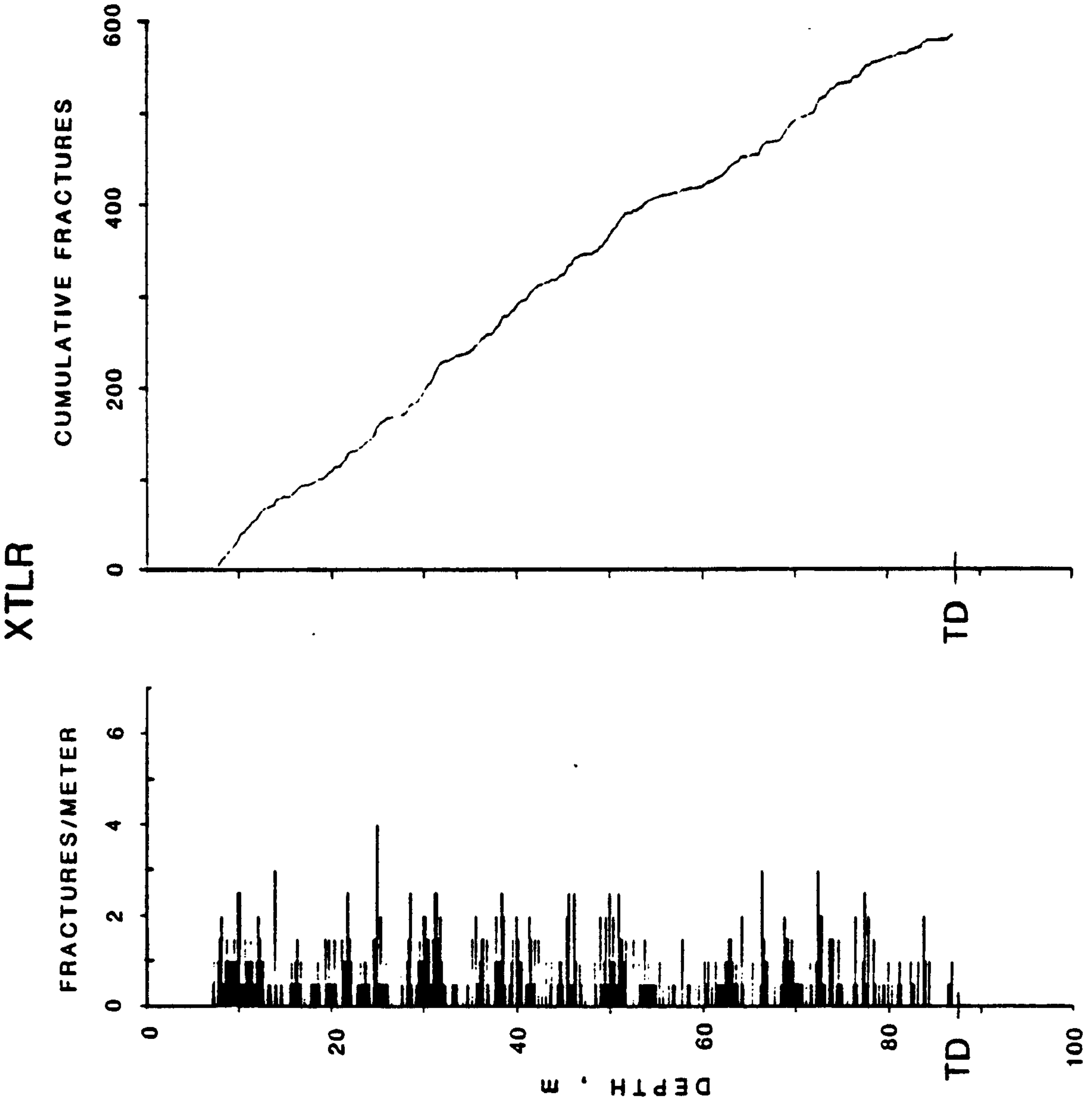
XTLR
CUMULATIVE FRACTURES
0
200
400
600
TD
FRACTURES/METER
0
2
4
6
0
20
40
60
80
100
TD
DEPTH, m

FIGURE 9

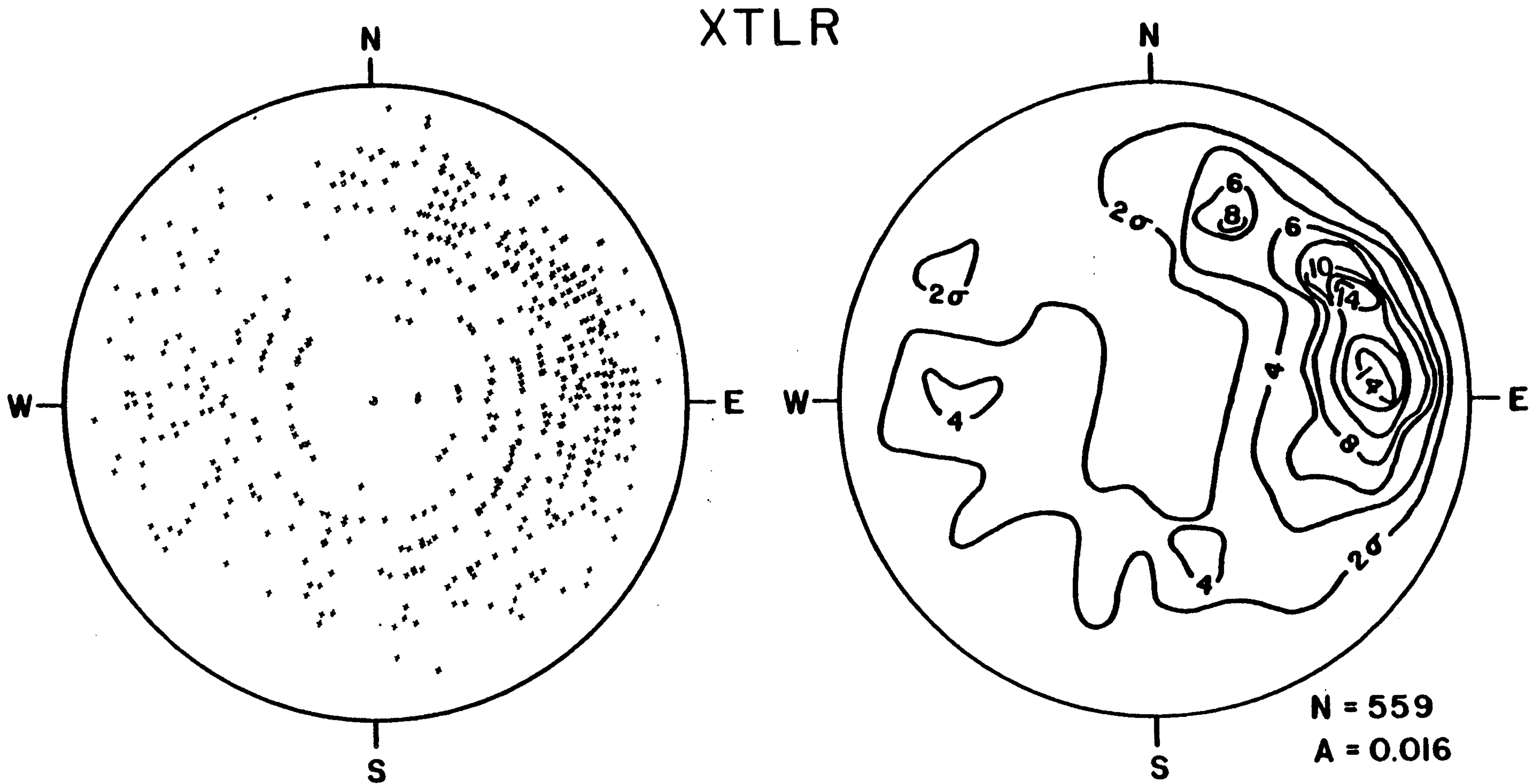

N = 559
A = 0.016
E = 9.0
σ = 3.0

FIGURE 10

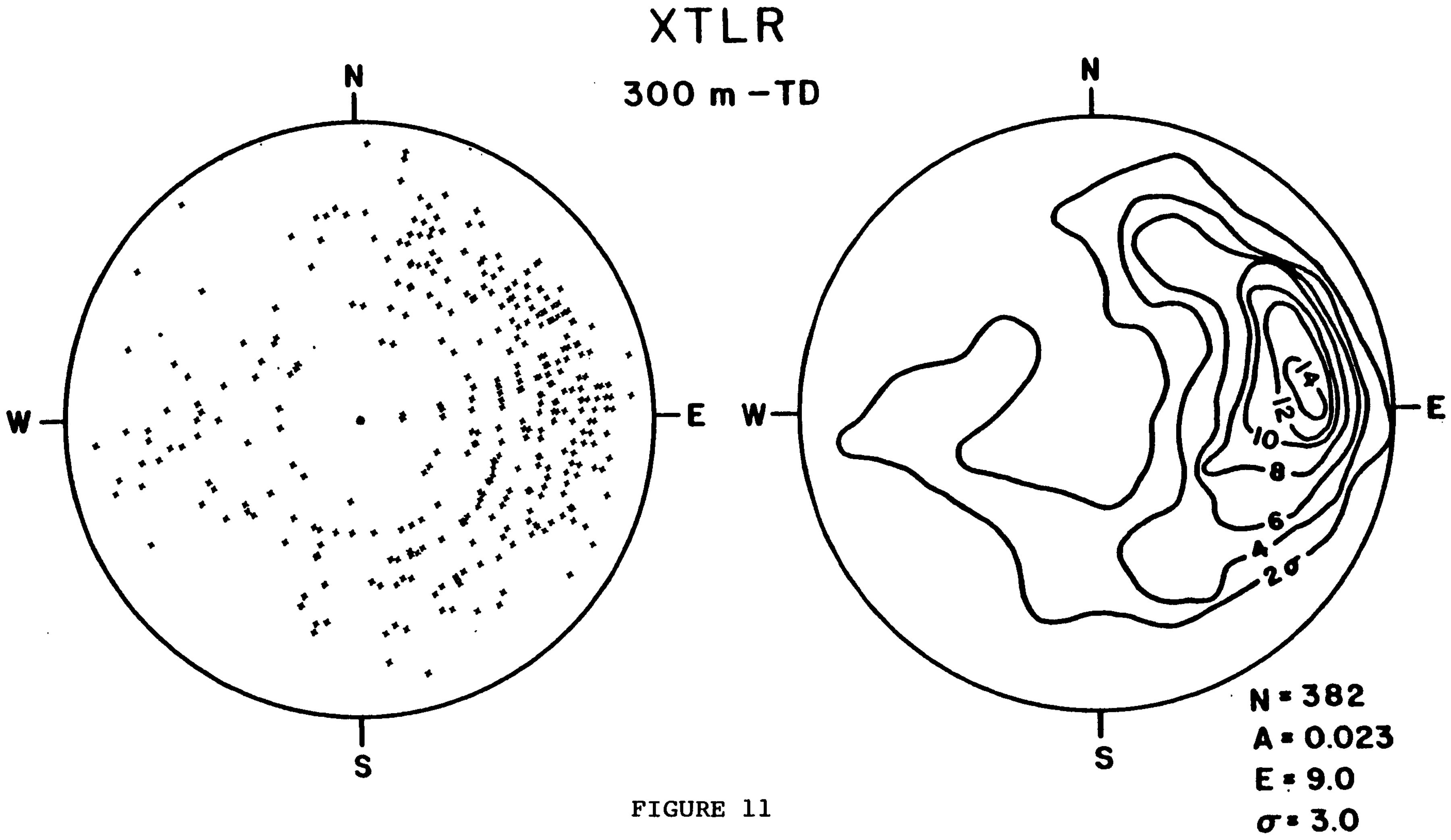

FIGURE 11

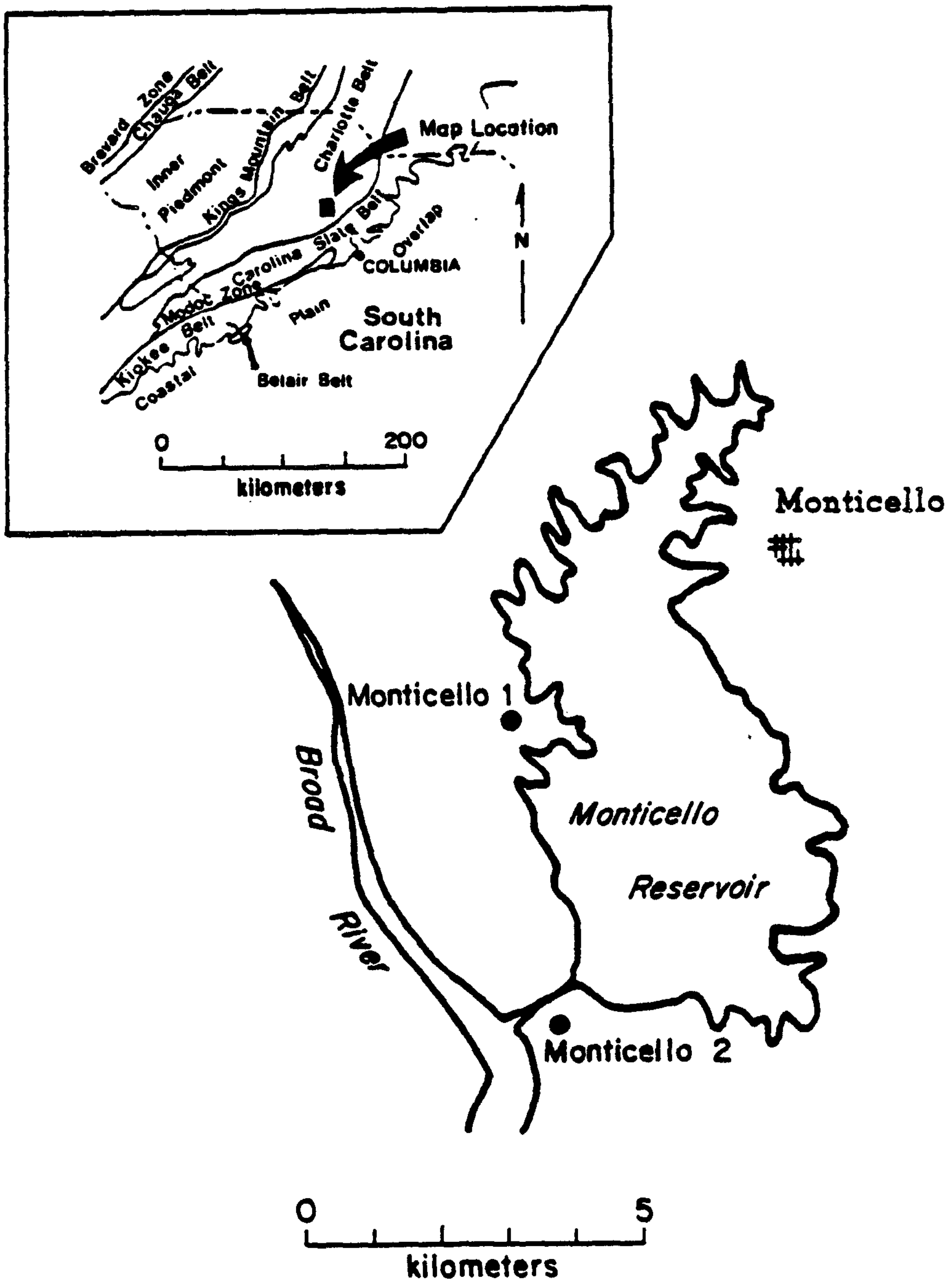
Brevard Zone
Chauga Belt
Inner Piedmont
Kings Mountain Belt
Charlotte Belt
Map Location
Carolina Slate Belt
Overlap
COLUMBIA
N
Modoc Zone
Kiokee Belt
Plain
Coastal
Belair Belt
South Carolina
0
200
kilometers
Monticello
Monticello 1
Broad River
Monticello Reservoir
Monticello 2
0
5
kilometers

FIGURE 12

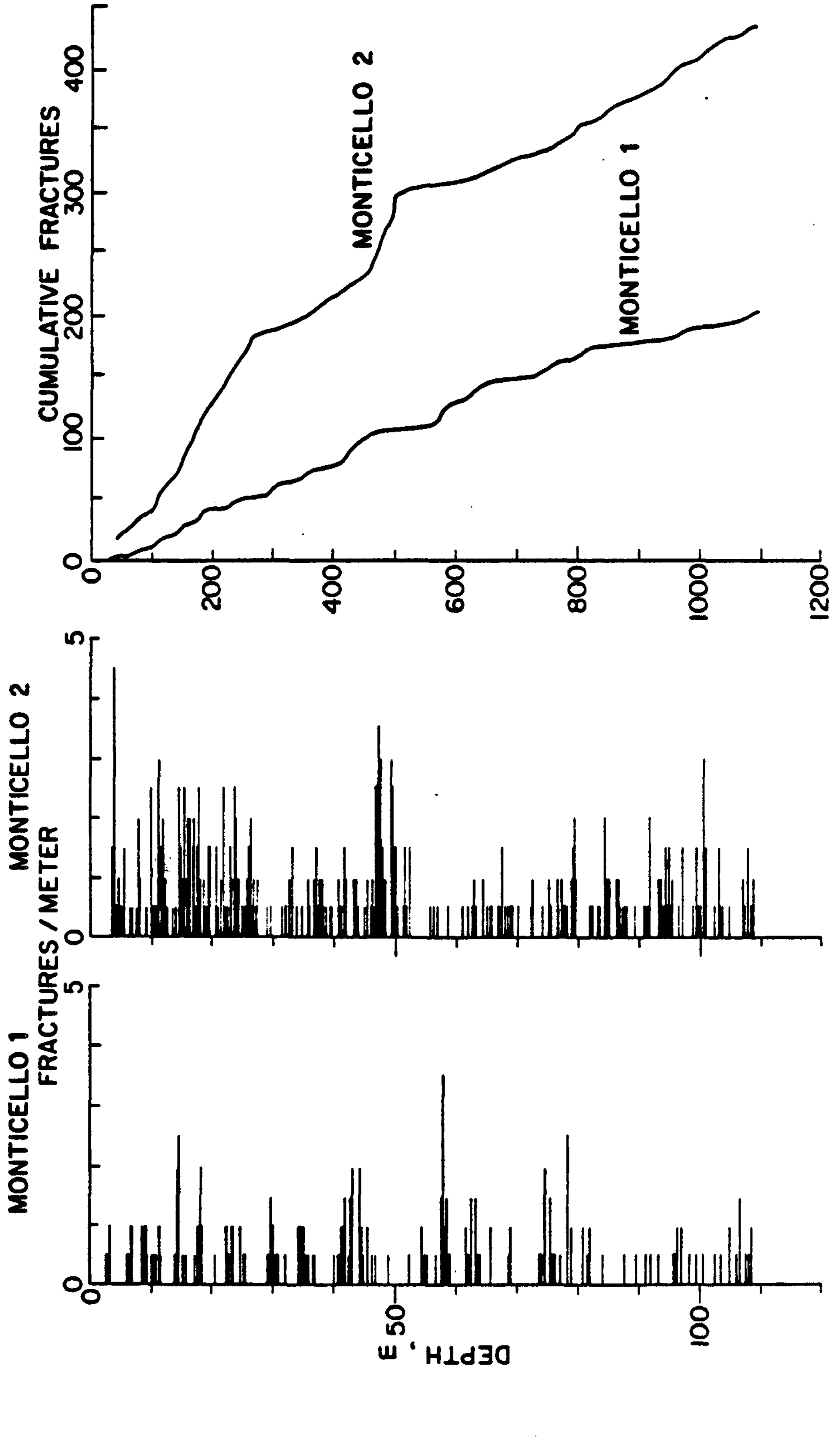
MONTICELLO 1
FRACTURES / METER
MONTICELLO 2
0
5
0
5
DEPTH, m
0
50
100
CUMULATIVE FRACTURES
0
100
200
300
400
MONTICELLO 2
MONTICELLO 1
0
200
400
600
800
1000
1200

FIGURE 13

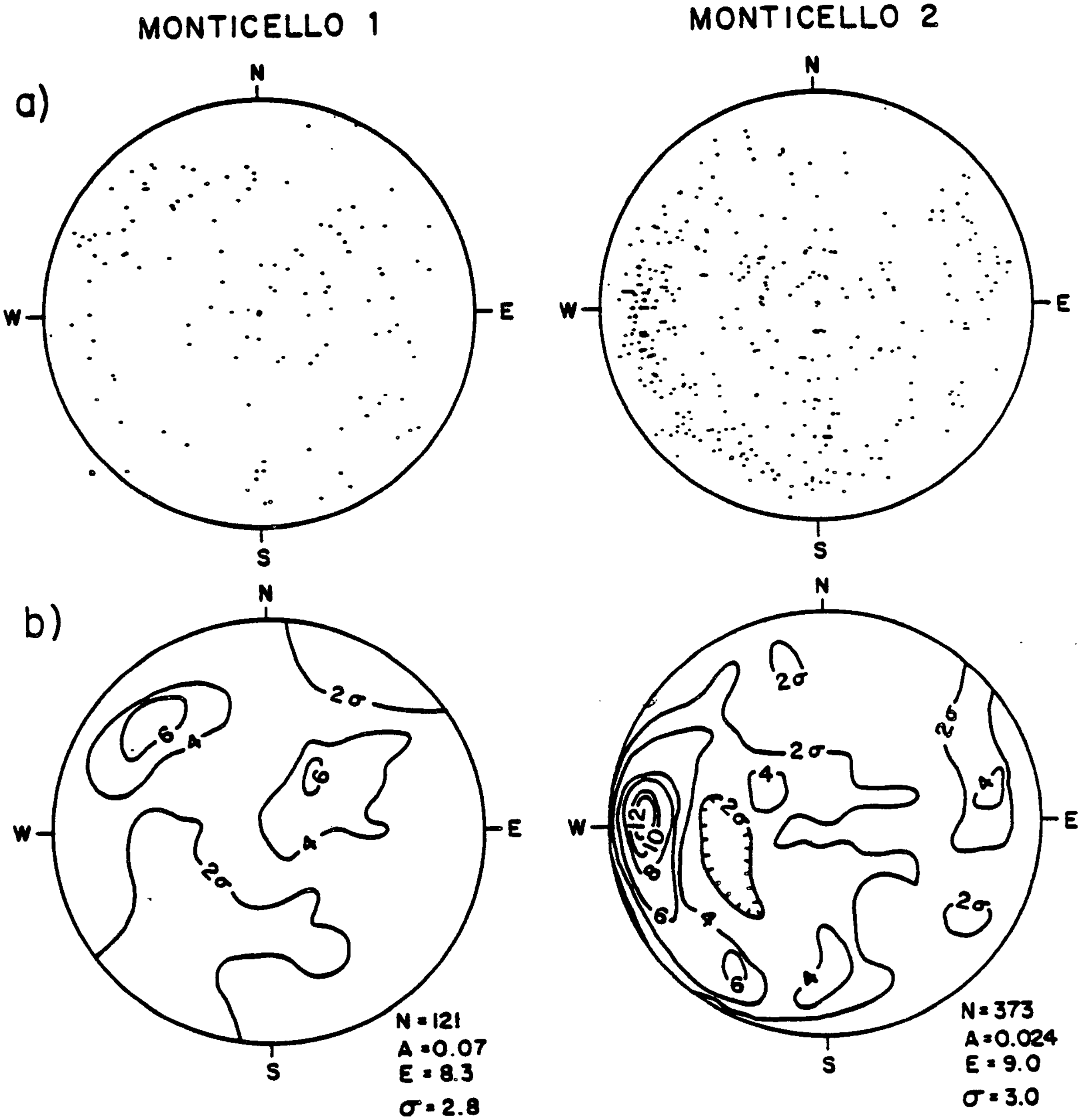
MONTICELLO 1
MONTICELLO 2
a)
b)
N
S
W
E
2σ
4
6
8
10
12
N = 121
A = 0.07
E = 8.3
σ = 2.8
N = 373
A = 0.024
E = 9.0
σ = 3.0

FIGURE 14

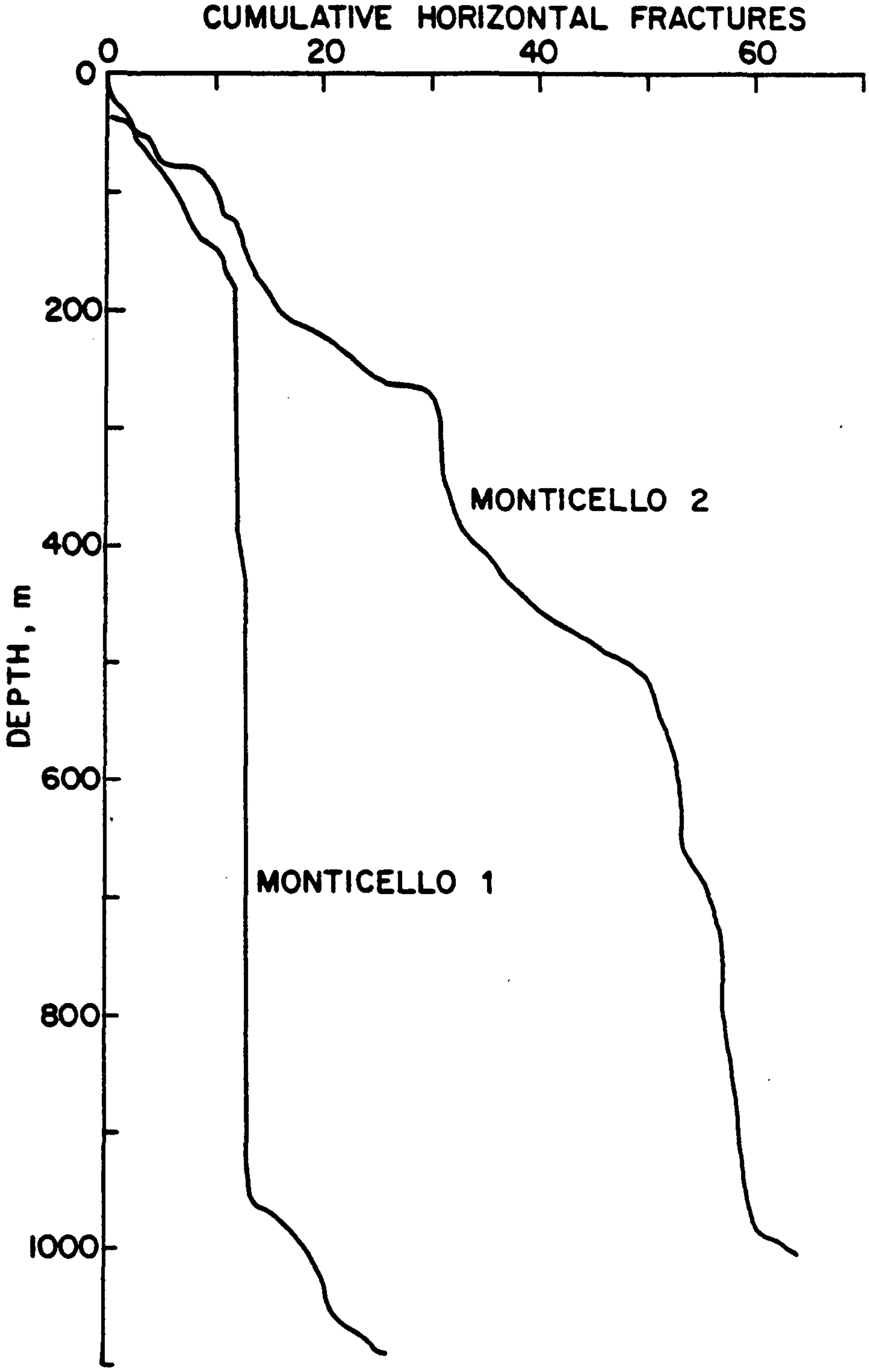
CUMULATIVE HORIZONTAL FRACTURES
0
20
40
60
0
200
400
600
800
1000
DEPTH, m
MONTICELLO 2
MONTICELLO 1

FIGURE 15

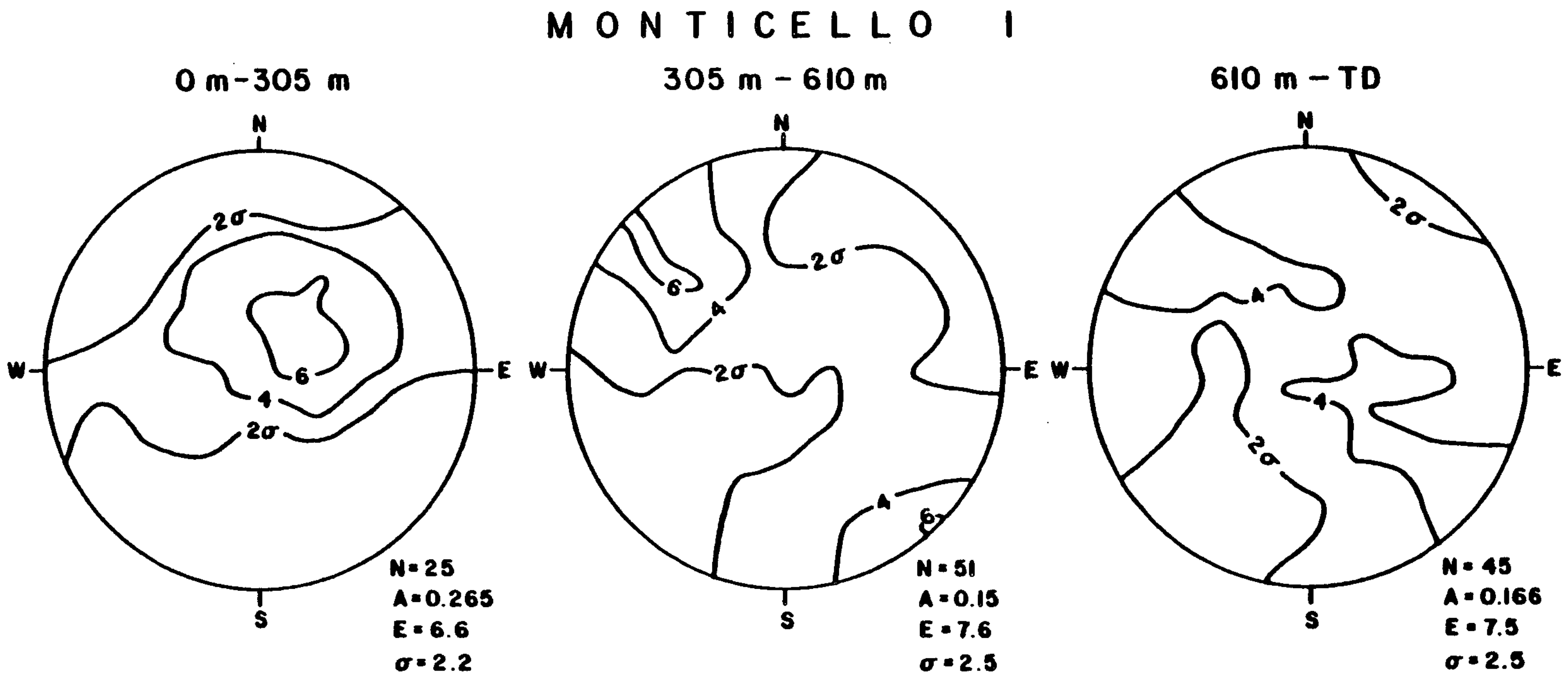
MONTICELLO I
0 m-305 m
305 m - 610 m
610 m - TD
N
S
E
W
2σ
4
6
N=25
A=0.265
E=6.6
σ=2.2
N=51
A=0.15
E=7.6
σ=2.5
N=45
A=0.166
E=7.5
σ=2.5

FIGURE 16

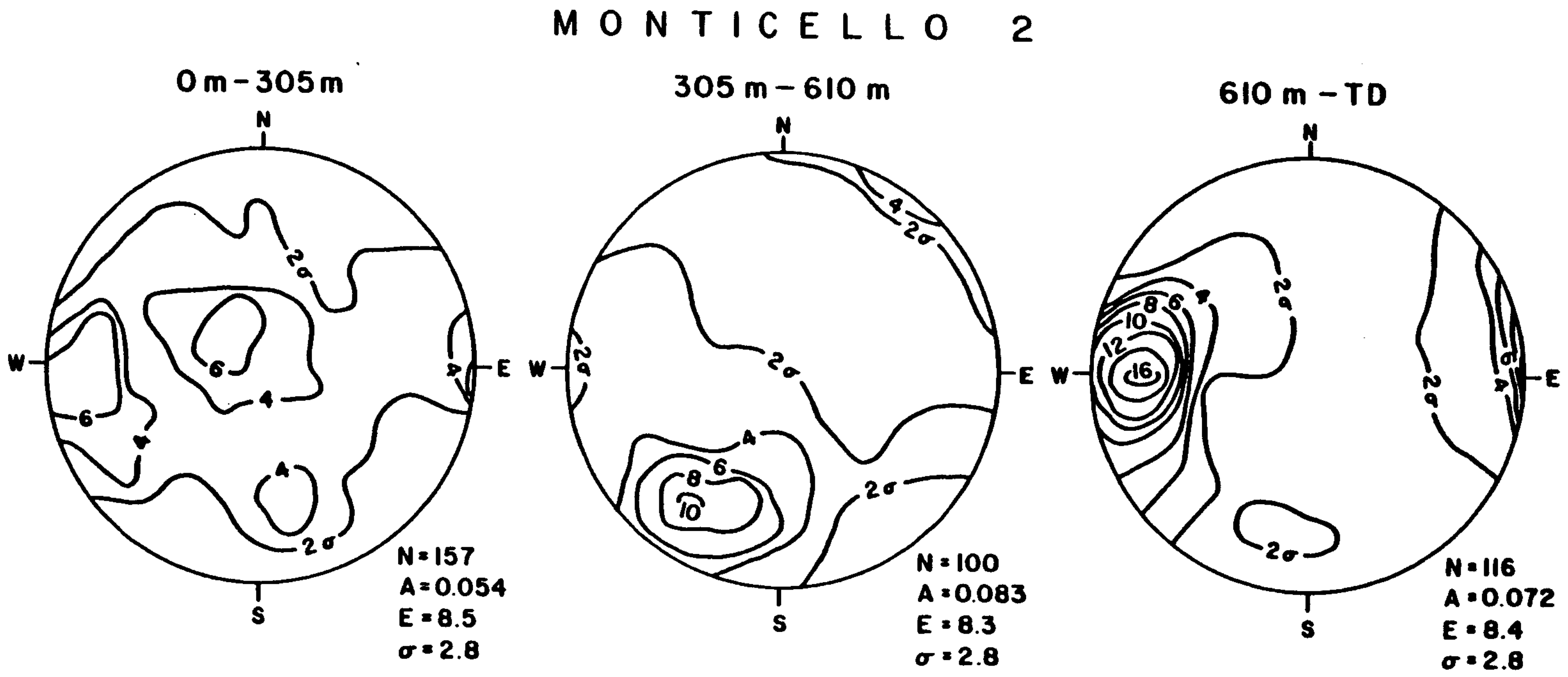
MONTICELLO 2
0m-305m
305m-610m
610m-TD
N
S
W
E
2σ
4
6
N=157
A=0.054
E=8.5
σ=2.8
8
10
N=100
A=0.083
E=8.3
σ=2.8
12
16
N=116
A=0.072
E=8.4
σ=2.8

FIGURE 17

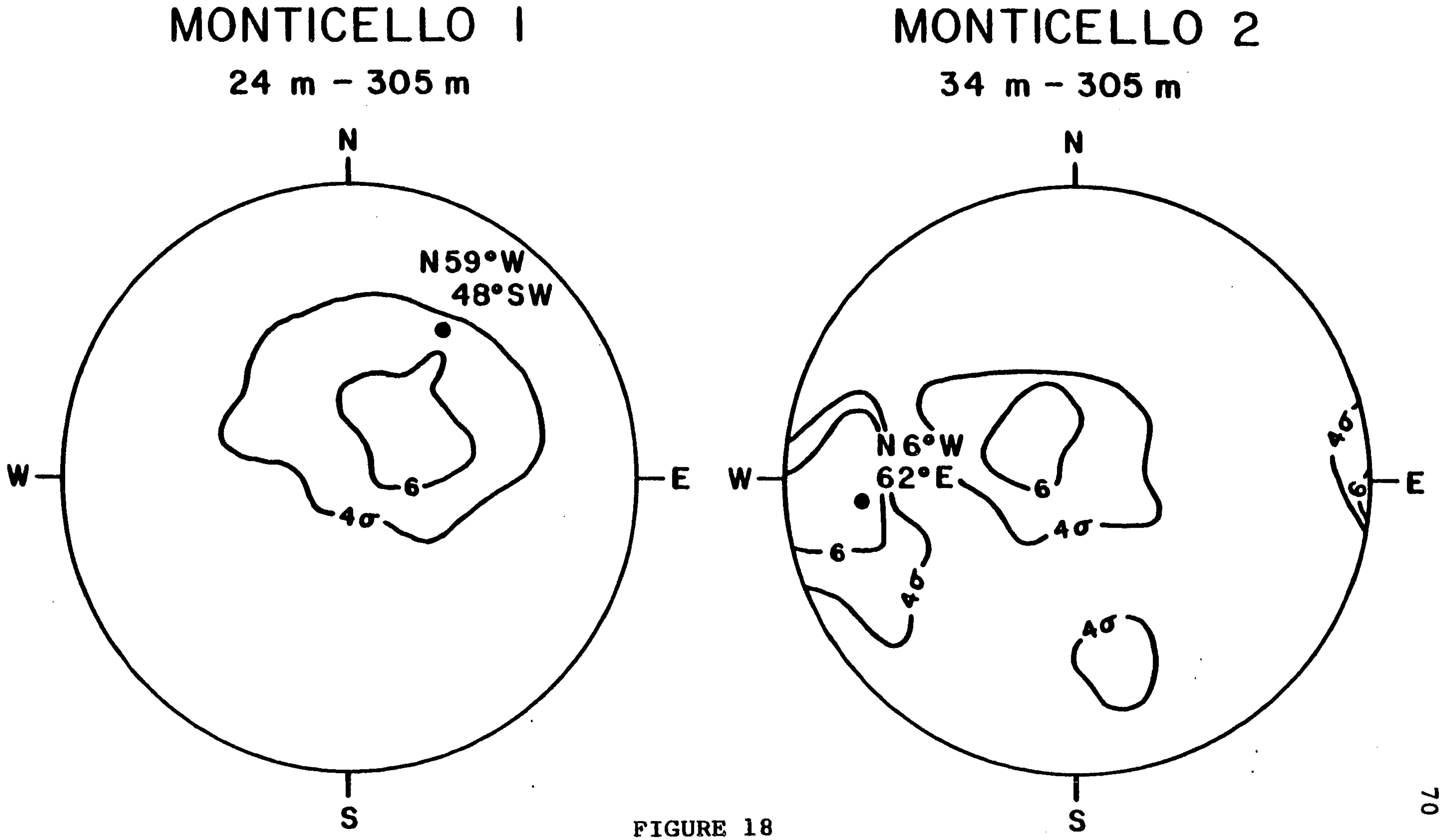
MONTICELLO I
24 m – 305 m
N
W
E
S
N59°W
48°SW
6
4σ
MONTICELLO 2
34 m – 305 m
N
W
E
S
N6°W
62°E
6
4σ
6
4σ
4σ
4σ
6

FIGURE 18

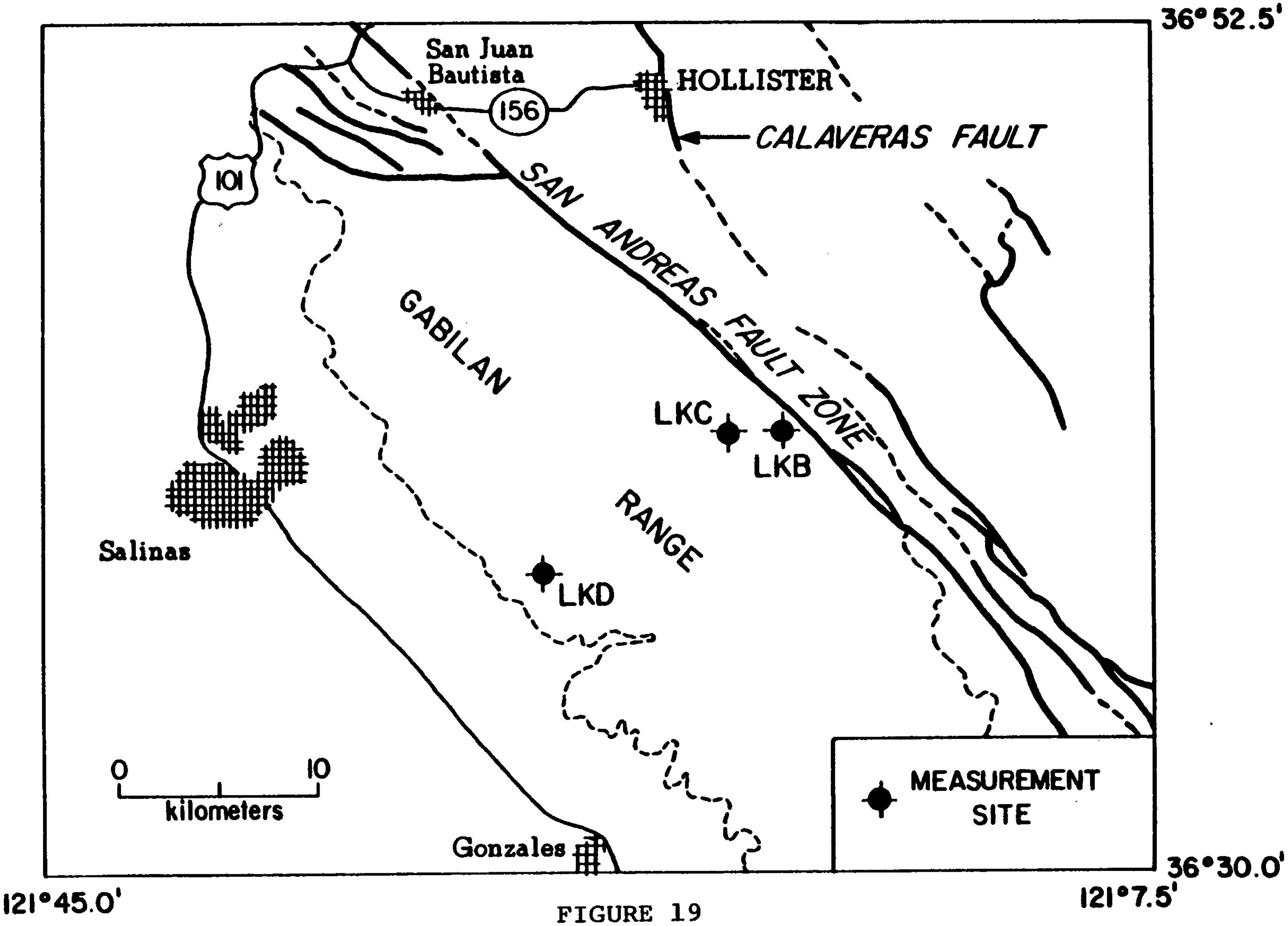
36°52.5'
San Juan
Bautista
156
HOLLISTER
CALAVERAS FAULT
101
SAN ANDREAS FAULT ZONE
GABILAN
RANGE
LKC
LKB
LKD
Salinas
0
10
kilometers
Gonzales
MEASUREMENT
SITE
36°30.0'
121°45.0'
121°7.5'

FIGURE 19

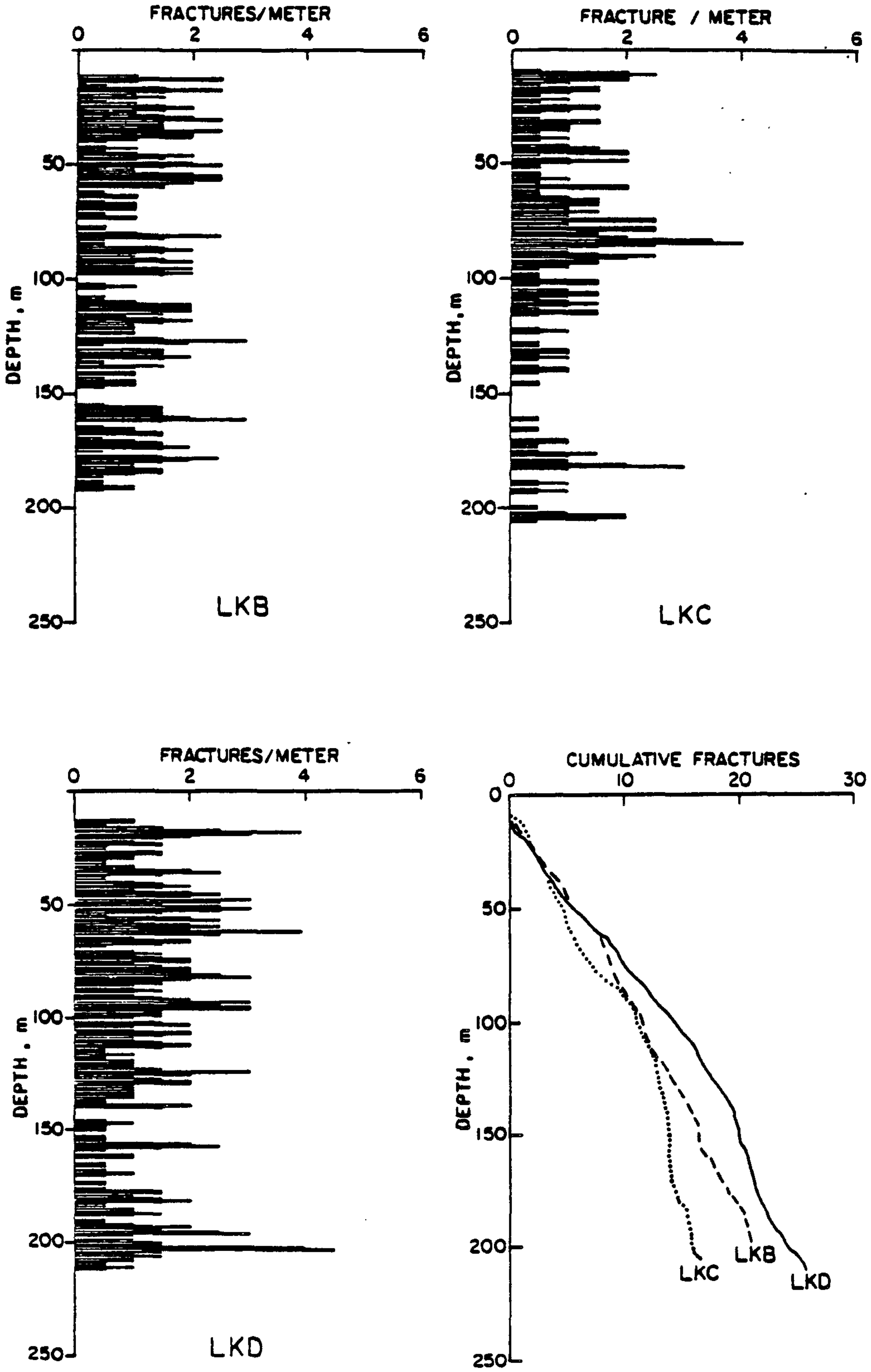
FRACTURES/METER
0
2
4
6
DEPTH, m
50
100
150
200
250
LKB
FRACTURE / METER
0
2
4
6
DEPTH, m
50
100
150
200
250
LKC
FRACTURES/METER
0
2
4
6
DEPTH, m
50
100
150
200
250
LKD
CUMULATIVE FRACTURES
0
10
20
30
DEPTH, m
0
50
100
150
200
250
LKC
LKB
LKD

FIGURE 20

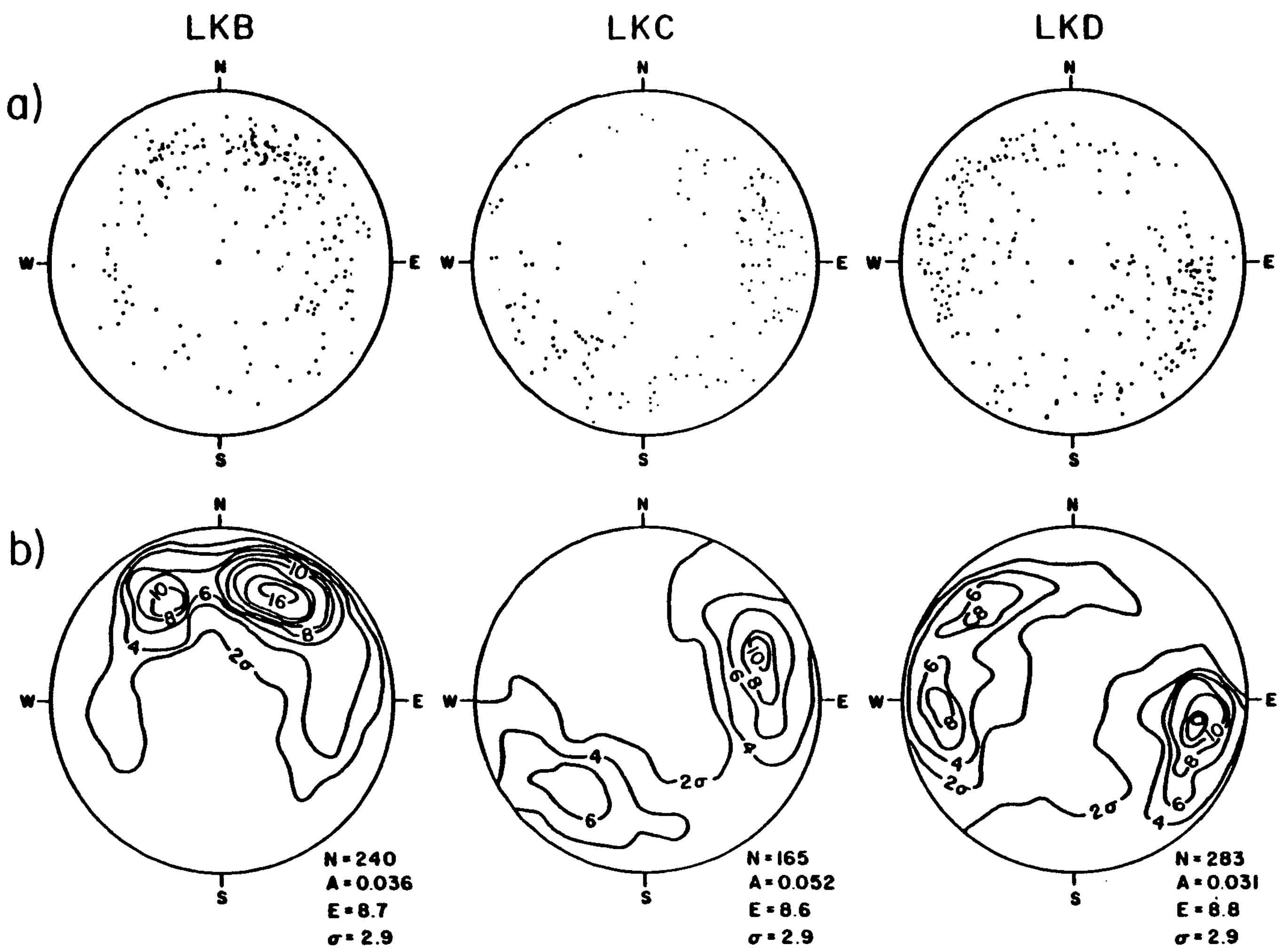
LKB
LKC
LKD
a)
b)
N
S
W
E
2σ
4
6
8
10
16
N=240
A=0.036
E=8.7
σ=2.9
N=165
A=0.052
E=8.6
σ=2.9
N=283
A=0.031
E=8.8
σ=2.9

FIGURE 21

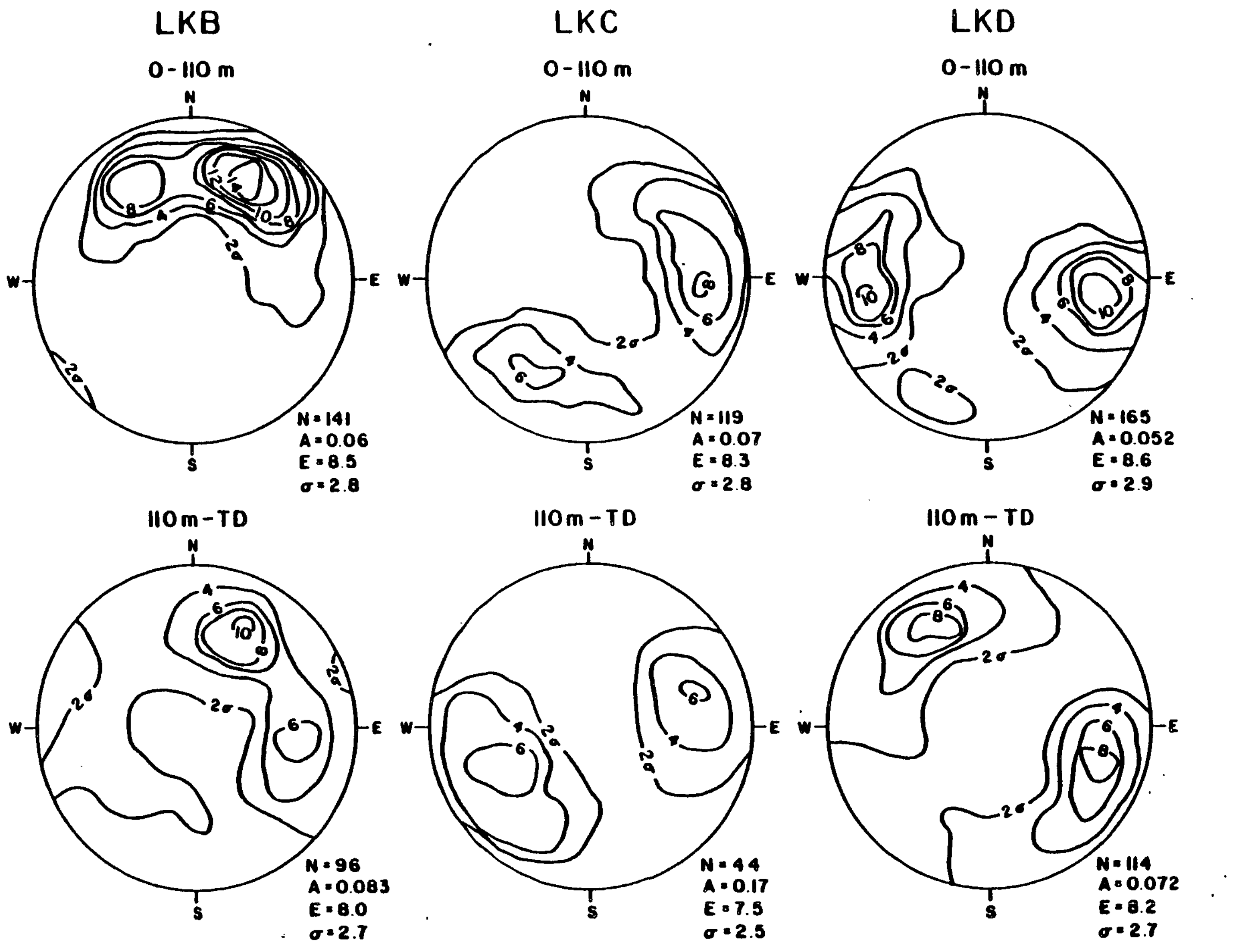
LKB
LKC
LKD
0-110 m
0-110 m
0-110 m
N
W
E
S
14
12
10
8
6
4
2σ
N=141
A=0.06
E=8.5
σ=2.8
N=119
A=0.07
E=8.3
σ=2.8
N=165
A=0.052
E=8.6
σ=2.9
110m-TD
110m-TD
110m-TD
N=96
A=0.083
E=8.0
σ=2.7
N=44
A=0.17
E=7.5
σ=2.5
N=114
A=0.072
E=8.2
σ=2.7

FIGURE 22

PERMEABILITY AND FAULT ZONE STRUCTURE

ABSTRACT

A critical review of the permeability characteristics in the upper crust reveals that in the volume around a fault there is an anisotropic permeability distribution which differs from that of the surrounding rock. The most commonly observed permeability anisotropy has high permeability parallel to the fault zone and low permeability across it. The high permeability zone is most often found on the hanging wall side of the fault zones, with the low permeability zone on the footwall side. Consideration of the structural factors which affect permeability leads to the conclusion that the high permeability zone is a result of increased fracturing and porosity, while the low permeability zone is a result of porosity reduction, grain size reduction, and a lessening of the degree of sorting in fault zone material. A comparison of this predicted structure with that observed in mines and encountered by wells finds relatively good agreement between the two. Highly fractured zones, which would be relatively permeable, are found parallel to fault zones and very often in the hanging wall side of the zone. Low permeability "gouge" zones are very often found on the footwall side of the fault zone. Both the permeability data and direct observations indicate that fault zones have an anisotropic, three-dimensional structure. This structure can have major effects on such processes as hydrocarbon migration and the development of high pore pressures during the faulting cycle.

INTRODUCTION

The flow and distribution of pore fluids in situ is a subject of both scientific and economic interest. Through the effective stress law (Hubbert and Rubey, 1959), the important role of pore fluids in physical processes is predicted. Pore fluids also play an important role in in situ geochemical processes. Pore fluid movement has been called upon to explain temporal changes in geophysical phenomena (e.g. Nur and Booker, 1972; Lachenbruch, 1980). Finally, distribution and ease of production determine the economic viability of oil, gas, ore, and water accumulations.

With the knowledge that pore fluid flow and distribution play an important role in physical and economic processes, it is appropriate to study some of the factors which affect these parameters. In this paper a review of the observations of pore fluid flow and distribution near faults will be presented. Many direct and indirect observations of fluid flow and distribution near faults have been made in such varied fields as ground water and oil field development, tunneling, surface field geology, and mining. Most of these measurements are made within one or two kilometers of the surface, although mining observations may be indicative of depths of at least 5 km and oil wells have been drilled to more than 10 km.

A knowledge of the structures commonly found in fault zones and their effect on fluid flow is of importance to the understanding of such problems as hydrocarbon migration and earthquake mechanisms. Structural elements such as faults and fracture zones may explain much of the variation of in situ flow and pore pressure (e.g. Brace, 1979). Direct field observations of fault zone structure will be cited and the permeability distribution inferred from these observations will be compared to that actually found in the subsurface. The resulting fault zone permeability model is consistent with observed flow paths near many faults in sedimentary, igneous, and metamorphic rocks.

DARCY'S LAW

Most rocks are to some degree porous, and beneath shallow depths their pores are usually filled with fluid. The empirical relationship for the flow of this fluid through interconnected pore space in response to potential differences is given by Darcy's law (Hubbert, 1940). In its tensor form, Darcy's law is (Biot, 1955; Bear et al., 1968)

$$\underline{q} = -\underline{\underline{K}}\nabla h$$

where $\underline{q}$ is the volume flow per unit area; $h = p + \rho g z$ is the fluid potential where p is applied pressure, ρ is fluid density, g is the acceleration of gravity, and h is the distance from the datum level; and $\underline{\underline{K}}$ is the hydraulic conductivity. Darcy's law has been shown to be appropriate for flows with a Reynolds number of less than 1, which is appropriate for almost all naturally occurring subsurface flow.

$\underline{\underline{K}}$ is a symmetric second order tensor (Biot, 1955). There exist in general three mutually orthogonal axes, the principal directions of $\underline{\underline{K}}$, for which the off-diagonal elements are zero. The trace of $\underline{\underline{K}}$, $K_{11} + K_{22} + K_{33}$, is an invariant. In the case of $K_{11} = K_{22} = K_{33}$, with $K_{ij}=0$, i = j, $\underline{\underline{K}}$ is an isotropic tensor and the general Darcy's law reduces to the original scalar law.

The components of the hydraulic conductivity are functions of both the porous solid and the pore fluid. This relationship has been expressed as (Hubbert, 1940)

$$K = \frac{k}{\mu}$$

where k is the (intrinsic) permeability of the matrix and μ is the fluid viscosity. k is controlled by the flow paths through the rock and the interaction of the fluid phases and matrix present. In an isothermal system, μ is essentially independent of position, so that the variations of K are only due to variations of k. Thus, $\underline{\underline{k}}$ is also a symmetric tensor.

Much work has been done trying to correlate permeability with parameters such as porosity and resistivity (Brace, 1977), which are easily measured in situ. These methods have shown some success when used on data from laboratory samples and from similar sedimentary lithologies in the field. However, no functional relationship between permeability and any other factor, such as porosity, which is applicable for all naturally occurring flow paths has yet been formulated.

Many researchers have investigated the various parameters which influence the intrinsic permeability (Kozeny, 1927; Fair and Hatch, 1933; Rose, 1945; Ryder, 1948). These studies have shown that permeability decreases with decreasing porosity, grain size, fracture density, and degree of sorting. In addition, Fair and Hatch

(1933) found that permeability decreases with increasing angularity of grains. Zoback and Byerlee (1975), Nur et al. (1980) and Walls (1980) found permeability to be affected by changes in confining pressure and clay content. Summers et al. (1978) found that permeability may be temperature and/or time dependent.

In the case of fractured rock, intrinsic permeability is not a well-defined parameter (Snow, 1972). The volume flow rate through fractured rock is a function of the cube of the fracture aperture (Snow, 1968). Thus, the measured permeability of fractured rock is generally much higher than that for similar but unfractured rock. If the rock is extensively fractured, an effective permeability for an equivalent porous rock may be used (Castillo, 1972). However, for a rock with only a few important fluid conducting fractures, the indicated effective permeability may be sample size or location dependent.

With a knowledge of the factors which affect permeability, e.g. porosity, grain size, sorting, and fracture density; observations of fluid flow and distribution near faults can be used to infer the structure of the matrix. Similarly, from direct observations of fault zone structure and material, the flow and distribution of fluids may be estimated.

OBSERVATIONS OF FLUIDS NEAR FAULT ZONES

A fault zone is a distinct structual element in which the parameters which affect fluid flow and distribution may be markedly different than those found in the parent rock outside of the zone.

In theories and observations of in situ fluid flow, fault zones have been called upon to perform two seemingly contradictory roles; that of barrier to fluid flow, and that of conduit. In this section typical observations which lead to these conclusions will be reviewed.

FAULT ZONES AS BARRIERS

Several factors may account for fault zones appearing as barriers to subsurface flow. Among these factors are (Davis and DeWiest, 1966): 1) fault action may tend to pulverize rock in the fault zone, creating a relatively impermeable gouge; 2) faulting may juxtapose permeable and impermeable formations; 3) elongated and flat clasts may tend to be rotated parallel with the fault surface to reduce the permeability perpendicular to the fault; and 4) deposition of minerals along the fault surface may reduce the permeability. For multiphase fluid flow, barriers to one or more fluid phases may be due to preferential wetting of the matrix by one fluid phase (Smith, 1966). A barrier to subsurface flow is indicated by abrupt lateral changes in water table elevation, fluid pressure, fluid type, or fluid salinity.

That faults may be barriers to flow has been recognized by hydrogeologists for many years. Many faults, such as the Raymond Hill Fault near Pasadena, California, were first discovered because they created barriers to subsurface flow (Bryant, 1978). Where ground water resources have been extensively developed, faults are often observed to divide the ground water basin into distinct subbasins with their own water tables and production histories. Examples of such fault controlled subbasins are found in the Livermore Valley (Figure 1) and Coachella Valley ground water basins in California (California Department of Water Resources, 1964, 1966, 1974). In these basins, water table offsets of up to 70 m (260 feet) (across the Mission Creek fault in the Coachella Valley ground water basin) are observed. Fault gouge is thought to play a major role in providing barriers to flow as juxtaposition of permeable and impermeable beds and mineralization are not always probable factors.

In hydrocarbon production, faults in the reservoir rocks have been found to wholly or partly form the trap for many oil and gas accumulations. Most pools found in structural traps are modified by faults. Most oil and gas accumulations trapped by faults are found in the footwall side of normal faults (Levorsen, 1967).

Hydrocarbon trapping by faults is indicated by abrupt lateral variations in gas-oil and oil-water contacts, pore pressure, and production characteristics. In the Kala field, Baku district of the USSR, faults form the boundaries for separate pools, distinguished by differing oil-water contacts (Figure 2) (Levorson, 1967). Five major faults divide the Wilmington Oil Field, California into six fault blocks (Gilluly and Grant, 1949; Long Beach Department of Oil Properties, 1970). Each fault block possesses its own characteristics as to oil-water contact, quantity of oil produced, and pressures within producing zones. Evamy et al. (1978) reported that for each major fault block in the Niger Delta, the petroleum maturation and migration histories were distinct, implying separate fluid systems since the beginning of the petrogenic cycle, possibly as early as the Eocene. As a further example, faults are important trapping elements for gas accumulations in the Lower Devonian Oriskany sand in northern Pennsylvania and southern New York (Finn, 1948). Finn (1948) noted that the "fault separating the West End Harrison pool from the East End Harrison pool has a very small amount of displacement, but it is sufficient to separate the producing areas. Production apparently continues in both pools to the fault plane, the fault acting only as a means of preventing migration from one to the other."

Ground subsidence and faulting due to fluid withdrawal also illustrate the role of faults as barriers to fluid flow (Reid, 1973; Holzer, 1976). Kreitler (1976) noted that land subsidence due to fluid extraction in the Houston, Texas area appears to be fault controlled. He stated that "faults in the Houston-Galveston area appear to act as fluid barriers. Fluid production on one side of a fault causes pressure declines and aquifer or reservoir compaction on that side of the fault and not on the other. This differential sediment compaction is translated to the surface as differential land subsidence or fault movement." An example of fault controlled subsidence measurements is presented in Figure 3. The producing horizons of the oil and gas fields considered by Kreitler (1976) extend to depths of more than 2500 m, implying that faults may act as barriers to at least such depths.

Fault zones are not always observed to be barriers to fluid flow. Wasson (1948) observed that in certain Gulf Coast areas trapping appears to be accomplished only by the juxtaposition of permeable and impermeable strata. In a recent study, Smith (1979) concluded that trapping in sand-shale sequences is generally determined by the amount of slip which has occurred on the fault. If the net slip has not been larger than the thickness of the formation, fault trapping was rarely observed. This seems to imply that a certain amount of motion is required to insure the creation of a gouge zone of great enough thickness and lateral extent to be a barrier.

The observations presented so far have been primarily from sedimentary rock. The number of pore fluid observations in crystalline rock is less than that for sediments. However, similar observations have been made in crystalline rock. For example, Price (1961) found that in the basalt flow aquifers of the Walla Walla area, Washington, fault zones act as barriers to the lateral movement of ground water.

FAULT ZONES AS CONDUITS

In apparent contradiction to the observations just presented, when exploring for fluids in crystalline rock, fault zones are preferred locations for well sites. This is generally due to the increased supplies which may be obtained from the fractured rock associated with fault zones. Meier and Petersson (1951) described tests where yields from wells located in fault zones in gneiss in

Sweden were five to eight times the yield from wells in similar but unfaulted rocks. The yields found in these wells indicate that the effective permeability near faults in crystalline rock may be relatively large. Similar results have been reported for the crystalline rocks of Idaho (Littleton and Crosthwaite, 1957; Stevens, 1960). Ward (1946) has reported an instance in South Australia where the flowing ground water was confined to a fractured fault zone in which mineral deposition had occurred (Figure 4).

The rising hot waters which reach the surface as thermal springs frequently use fault zones as conduits. A study of the distribution of thermal springs (Waring, 1965), reveals a close correlation of thermal spring locations and fault zones. Lowell (1974) calculated that the depth of circulation of water in thermal springs in the southeastern United States may be 1.5 to 2.0 km. Thus fault zones may provide paths for fluid migration to depths of at least this magnitude.

Newhouse (1942) presented many examples of ore bodies whose location and distribution are determined by fault zones. The majority of these ore bodies were emplaced by liquids at depths of at least several kilometers. Ore bodies discussed are generally found emplaced along faults, particularly in areas where the fault trend is not planar. The fractures associated with faults and gouge material present are controlling factors in the distribution of ore bodies which were emplaced as liquids.

In theories of hydrocarbon development and accumulation, faults are often postulated as providing conduits for oil and gas migration (e.g. Schowalter, 1979; McAuliffe, 1979). Surface evidence for such migration is found in the oil seeps associated with faults in such areas as the Ventura Basin-Santa Barbara Channel area, California (McCullogh, 1934), the Maracaibo basin, Venezuela (Miller et al., 1955), and the oil, bitumen, and gas seepages in the Lower Fars "Salt Zone" in Iraq (Dunnington, 1955). In the Serendipity Gas Seep area, south Texas offshore, extensive gas seeps are presumed to be related to the presence of faults (Watkins and Worzel, 1978). In the Big Horn Basin of Wyoming, Stone (1967) has postulated that faults have acted as conduits for vertical oil migration to account for observed local oil-water contact irregularities.

Previously, the role of faults as hydrocarbon trapping elements in the Niger Delta has been mentioned. Trapping was observed to occur in accumulations found on the footwall side of the fault (Evamy et al., 1978; Weber et al., 1978). However, flow along these same faults is also presumed to occur. According to Weber et al. (1978), the main reason for assuming that fluid flow along these faults has taken place is that in downthrown blocks "the intersection of the top of the reservoirs and the faults appear to be at the spillpoints of many accumulations" (Figure 5). Faults playing such dual roles are observed to depths of more than 3 km in the Niger Delta.

The observations briefly summarized here indicate that flow near faults may be facilitated by the fracturing and increased porosity (dilatency?) associated with a fault. In contrast, there are many observations which indicate that flow across fault zones is minimal.

The conclusion that faults in the Niger Delta have acted as seals since the Eocene and the observation that faults which juxtapose the same or similar formations may act as seals indicates that the structure of fault zones rather than the temporary juxtaposition of permeable and impermeable beds or cross-fault pressure differences is responsible for many faults acting as seals. Both high and low fault zone permeability often appear to be due to the structure of the fault zone. What is more, the observations of Weber et al. (1978) are examples in which single faults exhibit both high and low permeabilities, with high permeability zones parallel to the fault plane, particularly on the hanging wall side, and low permeability perpendicular to the fault zone. If this permeability anisotropy is due to fault structure, the implications are that the fault zone itself is structurally anisotropic. In particular, the zones of high permeability could be due to well connected fractured zones or high porosity, large pore, zones while the zones of low permeability could be due to zones of relatively low porosity, small grain size, poor sorting, or decreased fracture density.

DIRECT FAULT ZONE OBSERVATIONS

In the previous examples we have seen that faults may act as barriers to, and conduits for, subsurface fluid flow, It has been shown that both roles may be played by the same fault. In this section field observations of fault zone materials and structures which may affect fluid flow are reviewed, with an attempt made to explain the observed fault zone permeability characteristics.

Fault zones may be directly observed in tunnels and mines, and at the surface where repeated action has left a fault trace or where erosion or excavation has exposed a previously buried feature. A commonly observed feature of fault zones which could affect fluid flow is fault gouge. Louderback (1942) described a section across a fault zone as showing a "complex succession of fault fractures, often ranging in magnitude and sense of dip, crush belts, brecciated belts, thoroughly sheared belts, and gouge belts." In tunnels cut across the Hayward fault in California he described the most extreme cataclastic belt as having the character of a thoroughly ground-up gouge clay. The characteristic of clays and clay sized particles in fault gouge that is important to fluid flow is their small grain size. As noted earlier, permeability decreases with decreasing grain size for rocks with similar porosities. Materials such as clays and gouge may have fairly large porosities, but their permeabilities should be very low (Shi et al., 1980). Thus gouge, or grain size reduction due to shearing, may be, at least in part, responsible for fault zones appearing as barriers to fluid flow.

Aydin (1977, 1978; Aydin and Johnson, 1978) studied faults in the Entrada and Navajo sandstones of southeastern Utah. The Entrada sandstone, of Late Jurassic age, is composed of members of white, cross-bedded sandstone and of red or brown silty sandstone, siltstone, and shale. The Early Jurassic Navajo sandstone is composed mainly of white, cross-bedded sandstone. Grains in both sandstones are primarily quartz and feldspar. Both sandstones are commonly cemented by calcite; siliceous and pelitic cements are locally present. The Entrada sandstone is friable whereas the Navajo sandstone is firmly cemented.

Aydin recognized three forms of fault in these sandstones: 1) deformation bands, 2) zones of deformation bands, and 3) slip surfaces. Deformation bands are small faults with shear displacements on the order of a few millimeters distributed across the bands. In the outer portion of the band, the matrix, including pores and matrix material, deforms. The inner portion of the band is about 0.5 mm thick. In this zone sand grains fracture and further consolidation takes place (Figure 6). The resulting deformation band has "much smaller grain size, poorer sorting, and lower porosity than the original parent sandstone" (Aydin, 1977). The difference in grain size and sorting is illustrated in Figure 7. The porosity in undeformed Entrada and Navajo sandstones averages 25 and 24 percent, respectively. For deformation bands in these rocks Aydin found the average porosity to be 10 and 6 percent, respectively.

A zone of deformation bands is formed by two or more deformation bands adjacent to each other which share the same average strike and dip. Slip surfaces are through going, locally planar surfaces of discontinuity of displacement. Slip surfaces may accommodate displacements on the order of several meters. Aydin found that slip surfaces always form on either border of a region of highly concentrated deformation bands in a well-developed zone (Figure 8). Microscopic studies of thin sections containing slip surfaces in

Entrada sandstone show that there is intense granulation within an area of 1 to 3 mm width adjacent to the slip surface (Figure 9). Aydin estimated that the porosity immediately adjacent to the slip surface was less than 1 percent.

The permeability within a deformation band should be less than in an undeformed rock since the porosity, grain size, and degree of sorting have all been reduced. Near a slip surface, where the porosity and grain size have been even further reduced, the permeability should be quite small. The capillary displacement pressure for deformation band material should be quite large, particularly next to slip surfaces. Structural analysis of fault zones in Entrada and Navajo sandstone shows that flow through such zones will be small relative to that through undeformed rock under the same conditions.

In the examples presented by Aydin (Figures 8, 10), slip surfaces were found on the hanging wall side of normal faults. On the footwall side of the slip surface, nearly impermeable deformation bands were present, while the hanging wall side of the slip surface consisted of essentially undeformed country rock. Flow to the slip surface from the hanging wall block would be unimpeded. Slip surfaces, as discontinuities in the formation, may provide paths for flow in directions parallel to the surface of discontinuity.

Weber et al. (1978) noted that there was a zone of dilatation or pore increase on the downthrown side, and compaction or pore decrease on the upthrown side of faults formed in ring-shear apparatus experiments and along small natural shear faults. They concluded that such a system could facilitate fluid movement along the downthrown (hanging wall) side of faults. They also noted that in synsedimentary faults at Frechen, West Germany, the fault zones were asymmetric in their configuration wherever observed. At Frechen, the fine-grained material in the fault zones was distributed in a manner consistent with trapping on the footwall side and vertical flow in the hanging wall side of normal faults. These observations are also consistent with ore body emplacement (Newhouse, 1942), where the majority of ore bodies are found in the hanging wall block, apparently due to migration up the fault zone.

Anisotropic in situ permeability and pore fluid distribution was clearly shown in the San Jacinto Tunnel of the Colorado River Aqueduct near Banning, California (Thompson, 1966). This tunnel was drilled through primarily Cretaceous granitic rock, with at least one section of Paleozoic or older metamorphics. Twenty one northwest striking faults intersecting the tunnel course were mapped at the surface. The attitude of the faults as mapped at the surface proved to be consistent to depths of greater than 300 m. Thompson (1966) noted that large quantities of water were found in open interconnected fractures and joints in the hanging (northeast) wall of the northwest-striking faults. In the hanging wall the degree of fracturing increased toward the fault zone, from relatively unfractured to highly fractured rock. As the tunnels approached the fault zone from the hanging wall, water was found in hard but somewhat fractured rock. As the heading neared the fault the number of open fractures and the volume of inflow increased. By the time the footwall, where gouge and crushed material were present, was reached,

> "...the hydrostatic head had generally been reduced to the extent that little difficulty was encountered in driving through the soft, faulted material characteristic of the actual planes of slippage. Conversely, when headings were being advanced from the southwest side of the northeasterly dipping faults (through their footwalls) large flows of water under very high pressures were freed instantaneously..."

(Thompson, 1966). The high fluid pressues mentioned are due to the total, unrelieved, hydrostatic head.

The large volumes of water under high hydrostatic pressure found in the fractured zones are indicative of an extensive, interconnected fracture system associated with the fault zone. It is also important to note that the gouge zones are identified as the zones in which slippage takes place. Here again, the highest permeability and porosity occurs on the hanging wall side of the fault zone, and the inhomogeneous distribution of permeability and pore fluids was nearly identical for every fault encountered.

Wallace and Morris (1979) studied faults in mines, principally in the Coeur d'Alene mining district of Idaho. They concluded that faults have a definite three dimensional, rather than planar, character. They found that faults are "generally constituted of one or more clay-like gouge zones in a matrix of sheared and foliated rock bordered by highly fractured rock." The gouge material is commonly saturated with water and is described as "resembling modeling clay". Many gouge zones developed at the margin of fault zones, while others developed within complex faulted zones. Fractures associated with the faults are commonly conduits for water and in the past served as channelways for hydrothermal solutions. Faults were also seen to act as barriers to fluid flow. An example was cited in which a water table difference of 50 m was encountered, even though the fault cut normally permeable quartzite. Of particular importance is the observation that there was no striking difference in the fault zone characteristics found to a current depth of 2.5 km. Considering the environment of ore deposition near these faults, it seems likely that they were buried as deeply as 5 km at the time of their formation and are thus representative of faulting to such depths.

Most direct fault zone observations are made at or close to the earth's surface. Regions which have undergone uplift and erosion may provide opportunities to study features which at one time were located several kilometers below the surface, but considerable alteration may accompany such motion and could make interpretation of fluid flow paths difficult. Thus, direct access to deep fault zones, particularly in crystalline rock, is extremely limited. Reflection seismology, however, provides a means to study deep fault zones indirectly. For example, Lynn (1979, and Lynn et al., 1979) studied migrated data from the COCORP (Consortium for Continental Reflection Profiling) seismic reflection profile of the southeastern Wind River Mountains, Wyoming. In this data, both the Pacific Creek thrust and the Wind River thrust are seen as strong seismic reflectors. Coherent reflections from the Wind River thrust have been interpreted to depths of as great as 32 km. As crystalline basement rocks occur on both sides of the fault at depth, it is unlikely that the juxtaposed blocks have significantly different seismic impedences. This suggests (as argued by Lynn, 1979) that the fault zone, itself, is the source of the impedence contrast causing the reflections.

In the upper 10 to 15 km, where brittle processes dominate, severe fracturing and the development of gouge would be expected. Logs of wells which intersect the fault zone at depths of about 2 km report "granite wash" - highly fractured water saturated crystalline rock (Lynn, 1979). Lynn (1979) noted that the fault zone reflections appeared to be due to low velocities in the fault zone, itself. The fracturing and possible presence of clays or clay size particles could well give the fault zone a significantly lower velocity than surrounding undeformed rock (Wang et al., 1978). Below 10 to 15 km, where ductile deformation is presumed to occur, the fault zone reflections may be due to strong velocity effects that may be found in mylonites (Jones, 1981).

The conclusion to be drawn from the deep crustal reflection data is that fault zones have a distinct structure which is apparent throughout the region of brittle deformation and, apparently, through much of the region of plastic deformation. The low fault zone velocity (Lynn, 1979) is consistent with the observation that a fractured or dilatant zone is found in fault zones in the near surface. This observation is an indication, but not a proof, that the structure of fault zones, as described above, may extend throughout the region of brittle deformation.

The size of fault zones is highly variable. There is only a very general increase in fault zone width with increasing offset. The fault zones studied by Aydin (1977) ranged from a few millimeters to about a meter in width. Wallace and Morris (1979) found a rough correlation of fault zone width and displacement in faults observed in deep mines. Fault zones on which several kilometers of displacement have occurred tend to be one hundred or more meters wide, while those which show only a few hundred meters of displacement are only a few meters wide. Gouge zones ranged in width from 20 to 30 meters to about 0.1 m. The Wind River thrust, with over 25 km of displacement, has a fault zone thickness, as interpreted from the COCORP data, of over 1 km throughout much of its length.

IMPLICATION FOR HYDROCARBON MIGRATION

A hydrocarbon migration model for normal fault environments can be formulated based upon the observed fault zone structures in the Entrada and Navajo sandstones. These fault zones are characterized by a layer of mechanically altered material. This layer has been called a zone of deformation bands by Aydin, and correlates to "fault gouge" often reported in the geological, geophysical, and mining literature. As mentioned above, the matrix properties of this gouge zone are such that permeability is much lower than in undeformed rock. At the edge of fault zones in sandstone, slip surfaces may be present. For normal faults, it appears that slip surfaces may occur more often on the hanging wall side of the fault zone. Accompanying this slip zone there may be a zone of dilatation. As a result, flow parallel to the fault may be quite good.

Fault zones will affect hydrocarbon migration and accumulation only if they are continuous on the scales required for trapping and vertical migration. Aydin's work has shown that there is a general increase in the thickness of the deformed zone with increasing displacement, from a single deformation band to a zone of deformation bands to a slip surface and concentrated zone of deformation bands. Presumably the lateral extent of the deformed zones also increases as the displacement increases. Smith (1979) found the displacement on the order of the thickness of the reservoir bed was necessary for fault sealing in the Gulf Coast salt basin. It thus appears that a certain amount of displacement, which may be dependent on the structure and type of the original, unfaulted rock, is required before a fault zone may become an important element in hydrocarbon migration.

As shown in Figure 11, hydrocarbon accumulation and migration may be determined by fault zone structure. Hydrocarbons would tend to be trapped by the deformed zones and would migrate along slip surfaces and neighboring dilatational zones. For normal faults, most accumulations should be found in the footwall block with the deformed zone separating the slip surface and the reservoir rock. In the downthrown side, fault trapping would not usually be observed due to vertical migration of hydrocarbons along the fault trend. For oil trapped in structural accumulations in the downthrown block, the spillpoint should be at the intersection of the reservoir and the fault.

In practice, trapping against the hanging wall side of faults is rarely observed while trapping against the downthrown side is fairly common (Leversen, 1967). Vertical migration along fault zones is usually postulated in theories of hydrocarbon migration (e.g. Schowalter, 1979). Considerable evidence for such vertical migration is presented by surface oil and gas shows related to faults (e.g. McCollough, 1934; Miller et al., 1955; Watkins and Worzel, 1978).

As an example, consider the oil accumulations in the Escravos Beach field, Nigeria, illustrated in Figure 5. For most of the accumulations in this field, trapping is against the upthrown flank of a growth fault. In the downthrown blocks, where reservoir rock intersects a growth fault the hydrocarbon-water contacts are near the intersection of the top of the reservoir and the fault. In these accumulations any volume of oil in the structural closure has presumably migrated up the fault zone. Only where trapping is altered by the presence of an overpressured zone is there a significant accumulation of oil trapped against a fault in the downthrown block. These observations from the Escravos Beach field and those of Evamy et al. (1978) for other fields in the Niger Delta area are consistent with the hydrocarbon distribution predicted by the migration model developed here.

IMPLICATIONS FOR EARTHQUAKE PROCESSES

In situ pore pressure and permeability can have enormous effects on earthquake processes. Hubbert and Rubey (1959) used the effective stress law to illustrate the potential role high pore pressure could have in reducing the magnitude of stresses required for faulting. Bredehoeft and Hanshaw (1968) analyzed the hydrologic characteristics of rocks containing high pore pressure and concluded that the maintenance of high pore pressure depends critically on permeability. Rocks of nanodarcy permeability are required to maintain pore pressure at high levels for geologic times. Brace (1979) found that in situ permeability of crystalline rock is relatively high and tentatively suggested that the average crustal permeability is of the order of 10 md. Brace (1979) concluded that this high value of permeability seems to exclude the possibility of pore pressure much greater than hydrostatic occurring in terrains of outcropping crystalline rocks. From the data he presented, a hot pluton environment or a blanket of low permeability, clay-rich rocks appear necessary for the maintenance of high pore pressure.

Recently, Lachenbruch (1980) proposed a model of thermally induced pore pressures which arise during faulting. The model predicts that dynamic friction could be reduced to 10% of its original value if fault zone permeability were less than 0.1 μd. However, if the fault zone permeability were greater than 100 md, thermally induced pore pressures should have a negligible effect on frictional stress. Lachenbruch also noted that the fault zone permeability is a relatively unknown quantity.

Although no direct permeability measurements were made in the fault zones discussed earlier, order of magnitude estimates can be based upon their sealing properties. In the Niger Delta, faults have acted as seals since the Eocene. In many areas, faults are seals in gas reservoirs with sands juxtaposed against sands. The sealing ability of faults in sedimentary basins seems to approximate that of the cap rocks of the reservoir. Typical values of fault zone permeability would then range from 10^{-5} to 10^{-9} darcies (Brace, 1979). If the "gouge" zone of fault zones in crystalline rock has permeability characteristics similar to those in sedimentary rocks, and examples of sealing fault in crystalline rock have been found (see above), then permeabilities in parts of fault zones in crystalline rock may also be as low as 10^{-5} to 10^{-9} darcies. This value of permeability is considerably less than the 100 md maximum required for thermally induced pore pressures to be effective in reducing dynamic friction (Lachenbruch, 1980). Also permeabilities of 10^{-9} darcy are of the order required for high pore pressure maintenance (Brace, 1979). It is thus possible that high pore pressures could be maintained for times appropriate for recurrent faulting in, and trapped behind, low permeability fault zones.

The possible presence of high permeability in directions parallel to the fault zone, as indicated by the examples given earlier, is also of interest. Simpson (1976) and Bell and Nur (1978) note that the in situ permeability controls the rate of pore pressure diffusion, which is particularly important in cases of induced seismicity. A high permeability fault zone would mean that the delay time between loading and the increase of subsurface pore pressure would be relatively small, and the increase in pore pressure would originally be concentrated along the fault zone. A key to undersanding induced seismicity may thus be found in studying the details of in situ permability along fault where induced seismicity has, or has not, occurred.

The role of very low permeability rock in maintaining high pore pressures in situ has been mentioned above. Another possible source of high pore pressure in fault zones is tectonic stress, which can create a transient high pore pressure (Hanshaw and Zen, 1965; Bredehoeft and Hanshaw, 1968). The transient pore pressure increase would be rapidly dissipated in the relatively permeable unfaulted rock, and would be very rapidly dissipated in high permeability zones associated with faults. The high pore pressure would be relatively concentrated in the low permeability "gouge" zone of the fault. In such a fault zone the effective stress would be low in the gouge zone, possibly to the extent that unstable sliding may take place at very low shear stresses. In the description of in situ fault zones given by Thompson (1966) note that the actual slippage was observed to have occurred in "soft, faulted material". A zone of low permeability in the fault zone provides a mechanism with which shear strain accompanying instability can be localized without specifying a particular constitutive relation, such as the strain softening model of Rudnicki (1977). The low permeabilities inferred for fault zones and the fact tht the permeability of low permeability rock tends to be very sensitive to the state of stress (Jones and Owens, 1980; Brace et al., 1968) makes a model of faulting with high pore pressures concentrated in fault zones very appealing. A parallel observation, noted by Hubbert and Rubey (1959), is that thrust faults often follow evaporites, in which the permeability is generally low.

Fault zones with the structures discussed in the first section of the paper have a distinct permeability anisotropy. This anisotropy, and the structures which cause it, imply that high pore pressures may become concentrated along fault zones. If this is so, the stresses required for faulting would be low. This would go a long way to resolving the conflict between the interpretations of seismic data (Brune, 1970), direct measurements of crustal stresses (Zoback et al., 1980), and the absence of heat flow anomalies around fault zones (Lachenbruch and Sass, 1973) which all indicate that stresses related to faulting are low, with the high stresses inferred from the experiments done on frictional sliding of rocks (Stesky and Brace, 1973).

If, in fact, a zone of low permeability material is a characteristic of fault zones, it is unlikely that any increased pore pressure in such a zone could be observed in a regional pore pressure monitoring program. Such a pressure monitoring program would be able to see only the small transient pore pressures induced by tectonic strain in the relatively permeable unfaulted rock. This also means that pore presure monitoring in low permeability fault zone material would be sensitive to very localized strain, thus requiring large numbers of monitoring positions to gain a regional picture of strain accumulation along fault zones.

CONCLUSIONS

Field examples which illustrate the role of fault zones on fluid flow and distribution have been presented. It has been shown that fault zones are often barriers to fluid flow. It has also been shown that fault zones may act as channels for fluid flow, and that many faults have been observed to exhibit both characteristics. These characteristics have been observed in all types of rock: sedimentary, igneous, and metamorphic, and they have been observed as deep as the maximum depths to which each particular type of observation has been made. The examples have shown that permeability and fluid distribution may be heterogeneously distributed in faulted rock and there may be consistent relationships between the orientation of the fault zone and the permeability and porosity distribution.

The distribution of permeability and porosity yields information on the structure of fault zones. The fact that faults may act as barriers to fluid flow implies that the fault zone material has either low porosity, small grain size, poor sorting, low fracture density, or any combination of these factors. These conclusions are consistent with the observations made on the structure of fault gouge and may give some indication as to the extent to which gouge is distributed. Fault zones as conduits for flow are indicative of relatively high porosity or fracture density in some volume of the fault zone and the continuity of faults from one area to another.

The behavior of fluids near faults has many tectonic and economic implications. Based upon the observations presented here, fault zones in sedimentary sequences are commonly composed of fine grain, poorly sorted, possibly low porosity material whose presence and structure is due to the physical process of faulting. This fault zone material should have a very low permeability based upon its matrix characteristics. As a result, fault zones are effective hydrocarbon trapping agents. At the edge of fault zones, where slip planes commonly occur, the continuous slip surface and the neighboring dilatant zone may provide a path for vertical hydrocarbon migration. As a result, hydrocarbon accumulations in normal fault environments show consistent relationships, with trapping against faults in the footwall block and with hydrocarbon-water contacts (spillpoints) in the hanging wall block at the intersection of the top of the reservoir and the fault plane.

It is significant that the fault zone permeability model here is consistent with actual oil field data and does not require the presence of an alternating sand and shale or clay sedimentary sequence. As a result, the model presented here should be appropriate for a much wider range of environments than other models which require impermeable clay or shale formations to be smeared along the fault plane.

For the faulting process, the fact that faults provide conduits for fluid flow would seem to imply that any pore pressure build-up and maintenance must occur in porous, nearly impermeable material in the fault zone itself. Such materials would be shales, clays or gouges. If this low permeability fault zone material is common along active faults, then the thermally induced pore pressure mechanism discussed by Lachenbruch (1980) will facilitate movement during faulting. Also, high pore pressures in a limited volume of low permeability rock would result in a limited region of low effective stress in which a faulting instability would occur with stresses considerably less than those predicted from simple friction models.

In the case of reservoir induced seismicity, pore pressure changes should be most rapid along existing permeable fault zones. The presence of a highly permeable fault zone greatly affects the final stress state due to reservoir loading and pore pressure diffusion.

The observations presented here have been interpreted to yield a simple model of fault zone permeability and structure. Not all faults exhibit such a simple structure or permeability distribution, but the observations presented here appear to be so consistent for a great many faults that lacking further, detailed data, they are assumed to provide a valid first estimate of in situ conditions in fault zones. Many factors, however, may serve to complicate the analysis of actual systems. Important factors to be considered include the timing of deposition, faulting and fluid movement;

superimposed periods of tectonic activity; geochemical alteration and precipitation; permeability variations in the aquifers and along the fault, pore pressure and temperature distributions; and the three dimensional nature of the aquifer and fault zone. A complete analysis of processes occurring around faults will be possible only when the three-dimensional structure and characteristics of the fault zone are understood.

REFERENCES

Aydin, A., Faulting in sandstone, Ph.D. dissertation, Stanford Univ., 246 pp., 1977.

Aydin, A., Small faults formed as deformation bands in sandstone, PAGEOPH, 116, 913-930, 1978.

Aydin, A. and A.M. Johnson, Development of faults as zones of deformation bands and as slip surfaces in sandstones, PAGEOPH, 116, 931-942, 1978.

Bear, J., D. Zaslavsky, and S. Irmay, Physical Principles of Percolation, UNESCO, 1969.

Bell, M.L. and A. Nur, Strength changes due to reservoir-induced pore pressure and stresses and it application to Lake Oroville, J. Geophys. Res., 83, 4468-4483, 1978.

Biot, M.A., Theory of elasticity and consolidation for a porous anisotropic solid, J. Appl. Phys., 26, 182-185, 1955.

Brace, W.F., Permeability from resistivity and pore shape, J. Geophys. Res., 82, 3343-3349, 1977.

Brace, W.F., Permeability of crystalline and argillaceous rocks: status and problems, Int. J. Rock Mech. Min. Sci., in press, 1979.

Bredehoeft, J.D. and B.B. Hanshaw, On the maintenance of anomalous fluid pressure, Geol. Soc. Amer. Bull., 79, 1097-1106, 1968.

Brune, J.N., Tectonic stress and the spectra of seismic shear waves from earthquakes, J. Geophys. Res., 75, 4997-5009, 1970.

Bryant, W.A., The Raymond Hill Fault, Calif. Geol., 31, 127-142, 1978.

California Department of Water Resources, Livermore and Sunol Valleys, evaluation of ground water resources, appendix A: geology, Bull. 118-2, 79 pp., 1966.

California Department of Water Resources, Evaluation of ground water resources: Livermore and Sunol Valleys, Bull. 118-2, 153 pp., 1974.

Castillo, E., Mathematical model for two-dimensional percolation through fissured rock, in Proceedings of symposium on percolation through fissured rock, Intl. Soc. Rock Mech. and Int. Assoc. Eng. Geol., T1-D, 1-7, 1972.

Davis, S.N. and R.J.M. DeWiest, Hydrogeology, John Wiley and Sons, 463 pp., 1966.

Dunnington, H.V., Generation, migration, accumulation, and dissipation of oil in northern Iraq, in Habitat of Oil, Am. Assoc. Petrol. Geol., 1194-1251, 1955.

Evamy, B.D., J. Haremboure, P. Kamerling, W.A. Knapp, F.A. Molloy, and P.H. Rowlands, Hydrocarbon habitat of tertiary Niger Delta, Amer. Assoc. Petrol. Geol. Bull., 62, 1-39, 1978.

Fair, G.M. and L.D. Hatch, Fundamental factors governing the streamline flow of water through sand, J. Amer. Water Works Assoc., 25, 1551-1565, 1933.

Finn, F.H., Geology and occurrence of natural gas in Orianskany sandstone in Pennsylvania and New York, Bull. Amer. Assoc. Petrol. Geol., 33, 303-335, 1948.

Gilluly, J. and U.S. Grant, Subsidence in the Long Beach harbor area, California, Bull. Geol. Soc. Amer., 60, 461-530, 1949.

Hanshaw, B.B., and E. Zen, Osmotic equilibrium and overthrust faulting, Geol. Soc. Amer. Bull., 76, 1379-1386, 1965.

Holzer, T.L., Ground failure in areas of subsidence due to ground-water decline in the United States, in Land Subsidence Symposium, Proceedings of the second international symposium on land subsidence, Int. Assoc. Hydro. Sci., Pub. 121, 423-433, 1976.

Hubbert, M.K., The theory of ground-water motion, J. Geol., 48, 785-944, 1940.

Hubbert, M.K. and W.W. Rubey, Role of fluid pressure in mechanics of overthrust faulting, I, Bull. Geol. Soc. Amer., 70, 115-166, 1959.

Jones, F.O. and W.W. Owens, A laboratory study of low permeability gas sands, J. Pet. Tech., 1631-1640, 1980.

Jones, T.D., Seismic velocities in tectonically altered rocks, Stanford Rock Physics Progress Report, 10, 120-152, 1981.

Kozeny, J., Wasserkraft und wasser wirtschaft, 22, 96 pp., 1927.

Kreitler, C.W., Faulting and land subsidence from ground-water and hydrocarbon production, Houston-Galveston, Texas, in Proceedings of the second international symposium on land subsidence, Int. Assoc. Hydro. Sci., Pub. 121, 435-446, 1976.

Lachenbruch, A.H., Frictional heating, fluid pressure, and the resistance to fault motion, J. Geophys. Res. 85, 6097-6112, 1980.

Lachenbruch, A.H. and J.H. Sass, Thermo-mechanical aspects of the San Andreas fault system, in Proceedings of the Conference on the Tectonic Problems of the San Andreas Fault System, 192-205, Stanford University Press, Stanford, Ca. 1973.

Levorsen, A.I., Geology of Petroleum, W.H. Freeman and Co., San Francisco, Ca., 724 pp., 1967.

Littleton, R.T. and E.G. Crosthwaite, Ground-water geology of the Bruneau-Grand View area Owhyhee County, Idaho, U.S. Geol. Surv. Water Supply Paper 1460-D, 147-198, 1957.

Long Beach Department of Oil Properties, The subsidence story, 4 pp., 1970.

Louderback, G.D., Faults and earthquakes, Bull. Seism. Soc. Amer., 32, 305-330, 1942.

Lowell, R.P., Circulation in fractures, hot springs, and convective heat transport on mid-ocean ridge crests, Geophys. J.R. Astr. Soc., 40, 351-365, 1975.

Lynn, H.B., Migration and interpretation of deep crustal seismic reflection data, Ph.D. thesis, Stanford University, 158 pp., 1979.

Lynn, H.B., L. Gagnon, E. Kjartansson, and D.A. Seeburger, Migrations and interpretation in laterally varying media, Wind River thrust, Wyoming (abstract), Soc. Expl. Geophys. ann. mtg., 1979.

McAuliffe, C.D., Oil and gas migration-chemical and physical constraints, Amer. Assoc. Petrol. Geol. Bull., 63, 761-781, 1979.

McCullough, E.H., Structural influence on the accumulation of petroleum in California, in Problems of Petroleum Geology, Amer. Assoc. Petrol. Geol., 735-760, 1934.

Meier, O. and S.G. Petersson, Water supply in the Archaean bedrocks of Sweden, Int. Assoc. Sci. Hydro., Assemblee Generalé de Bruxelles, 1951, v. 2, 224-227, 1951.

Miller, J.B., K.L. Edwards, P.O. Wolcott, H.W. Anisgard, R. Martin, and H. Andregg, Habitat of oil in the Maracaibo Basin, Venezuela, in Habitat or Oil, Amer. Assoc. Petrol. Geol., 601-640, 1955.

Newhouse, W.H., ed., Ore deposits as related to structural features, Princeton University Press, 280 pp., 1942.

Nur, A. and J.R. Booker, Aftershocks caused by pore fluid flow? Science, 175, 885-887, 1972.

Nur, A.M., J.D. Walls, K. Winkler, J. DeVilbiss, Effects of fluid saturation on waves in porous rock and relations to hydraulic permeability, SPEJ, 20, 450-458, 1980.

Price, C.E., Artificial recharge through a well tapping basalt aquifers, Walla Walla area, Washington, U.S. Geol. Surv. Water-Supply Paper 1594-A, 33 pp., 1961.

Reid, W.M., Active faults in Houston, Texas, Ph.D. dissertation, Univ. Texas at Austin, 122 pp., 1973.

Rose, H.E., An investigation into the laws of flow of fluids through beds of granular materials, Proc. Inst. Mech. Eng., 153, 141-148, 1945.

Rubey, W.W. and Hubbert, M.K., Role of fluid pressure in mechanics of overthrust faulting, II., Bull. Geol. Soc. Amer., 70, 167-206, 1959.

Rudnicki, J.W., The inception of faulting in a rock mass with a weakened zone, J. Geophys. Res., 82, 844-854, 1977.

Ryder, H.M., Permeability: absolute, effective, measured, World Oil, 128, 173-177, 1948.

Schowalter, T.T., Mechanics of secondary hydrocarbon migration and entrapment, Amer. Assoc. Petrol. Geol. Bull., 63, 723-760, 1979.

Shi, L.Q., C. Morrow, D. Moore and J. Byerlee, Permeability of fault gouges under confining pressure and shear stress (abstract), EOS, Trans. Amer. Geophys. Union, 61, 1120, 1980.

Simpson, D.W., Seismicity changes associated with reservoir loading, Eng. Geol., 10, 123-150, 1976.

Smith, D.A., Theoretical considerations of sealing and nonsealing faults, Amer. Assoc. Petrol. Geol. Bull., 50, 363-374, 1966.

Smith, D.A., Sealing and nonsealing faults in Gulf Coast Salt Basin, AAPG Bull, 64, 1980.

Snow, D.T., Rock fracture spacings, openings, and porosities, J. Soil Mech. and Found. Div., ASCE, SM 1, 73-91, 1968.

Snow, D.T., Fundamentals and in situ determination of permeability, in Proceedings of symposium on percolation through fissured rock, Int. Soc. Rock Mech. and Int. Assoc. Eng. Geol., G1, 1-6, 1972.

Stesky, R.M., and W.F. Brace, Estimation of frictional stresses on the San Andreas from laboratory measurements, in Proceedings of the Conference on Tectonic Problems of the San Andreas Fault System, Stanford University, 206-214, 1973.

Stevens, P.R., Ground-water problems in the vicinity of Moscow, Latah County, Idaho, U.S. Geol. Surv. Water-Supply Paper 1460-H, 325-357, 1960.

Stone, D.S., Theory of Paleozoic oil and gas accumulation in Big Horn Basin, Wyoming, Amer. Assoc. Petrol. Geol. Bull., 51, 2056-2114, 1967.

Summers, R., K. Winkler, and J. Byerlee, Permeability changes during the flow of water through Westerly Granite at temperatures of 100^{0} - 400^{0} C, J. Geophys. Res., 83, 339-344, 1978.

Thompson, T.F., San Jacinto Tunnel, in Engineering Geology in Southern California, R. Lung and R. Proctor, eds., Assoc. Eng. Geol., Los Angeles Section, p. 105-107, 1966.

Wallace, R.E. and H.T. Morris, Characteristics of faults and shear zones as seen in mines at depths as much as 2.5 km below the surface, in Proceedings of Conference VII: Analysis of Actual Fault Zones in Bedrock, U.S. Geol. Surv. Open File Rep. 79-1239, pp. 74-100, 1979.

Walls, J.D., Permeability mesurements on some selected sandstone samples, Stanford Rock Physics Progress Reports, 7, 57-94, 1979.

Wang, C.Y., W. Lin, and F.T. Wu, Constitution of the San Andreas fault zone at depth, Geophys. Res. Lett., 5, 746-748, 1978.

Ward, L.K., The occurrence, composition, testing, and utilization of underground water in South Australia, and the search for further supplies, South Australia Geol. Surv. Bull., 23, 281 pp., 1946.

Waring, G.A., revised by R.R. Blankenship and R. Bentall, Thermal springs of the United States and other countries of the world - a U.S. Geol. Surv. Prof. Paper 492, 1965.

Wasson, T., Creole Field, Gulf of Mexico, coast of Louisiana, in Structure of Typical American Oil Fields, v. III, Amer. Assoc. Petrol. Geol., 281-298, 1948.

Watkins, J.S. and J.L. Worzel, Serendipity Gas Seep area, south Texas offshore, Amer. Assoc. Petrol. Geol. Bull., 62, 1067-1074, 1978.

Weber, K.J., G. Mandl, W.F. Pilaar, F. Lehner, and R.G. Precious, The role of faults in hydrocarbon migration and trapping in Nigerian growth fault structures, Proceedings of the Offshore Technology Conference, 2643-2653, 1978.

Zoback, M.D. and J.D. Byerlee, Effect of high-pressure deformation on permeability of Ottawa sand, Amer. Assoc. Petrol. Geol. Bull., 60, 1531-1542, 1976.

Zoback, M.D., H. Tsukahara, and S. Hickman, Stress measurements at depth in the vicinity of the San Andreas fault: Implications for the magnitude of shear stress at depth, J. Geophys. Res., 85, 6157-6173, 1980.

Figure Captions

Figure 1 Livermore Valley Ground Water Basin. Faults divide the basin into several distinct groundwater basins.

Figure 2 Structure of the Kala oil and gas field, Baku region, USSR. The contour interval is 10 meters. The distribution of the oil and gas in the Sabunchi series (productive formation of Pliocene age) is shown. The cross faults form separate pools along the axis of the fold (from Levorsen, 1967).

Figure 3 Subsidence over Blue Ridge and Mykawa Oil fields. Note increased subsidence on both sides of surface faults east of Mykawa field (from Kreitler, 1976).

Figure 4 Successful and unsuccessful boreholes in dense slate traversed by a fault zone carrying vein quartz (from Ward, 1946).

Figure 5 Map and section of the Escravos Beach field showing the hydrocarbon fault relationships in a field with multiple-growth faults.

Figure 6 Microscopic view of deformation bands in Entrada Sandstone from Buckskin Spring area. Crushed grains define a zone, about 0.5 mm thick. Displaced siltstone laminae are in upper and lower right corners of the photograph. Crossed nichols. Scale bar 2 mm long.

Figure 7 Detail of small area of Figure 6, showing small grain sizes and poor sorting of material within deformation band.

Figure 8	Grain size distribution of Entrada and Navajo Sandstones and their deformation bands. Grain size is much smaller, and sorting is poorer in the bands than in the original sandstones (from Aydin, 1978).
Figure 9	Series of block diagrams showing sequential development from a single band to a slip surface. (a) Single deformation band. (b) Two insulation bands. (c) A zone of deformation bands. (d) Slip surface developed on left-hand edge of zone (from Aydin and Johnson, 1978).
Figure 10	Microscopic view of a cross-section of crushed sandstone adjacent to a slip surface in Entrada Sandstone. Slip surface is boundary near upper edge of photograph. Strip of highly crushed sandstone next to slip surface is about 1 to 3 mm wide. Remainder of view shows part of the associated zone of deformation bands (from Aydin and Johnson, 1979).
Figure 11	Oblique view of a zone of deformation bands and slip surface, San Rafael Desert, Utah. Dark siltstone and shale beds are offset about 7 m (from Aydin and Johnson, 1978).
Figure 12	Model of petroleum migration based upon observations of fault zones in sandstone.

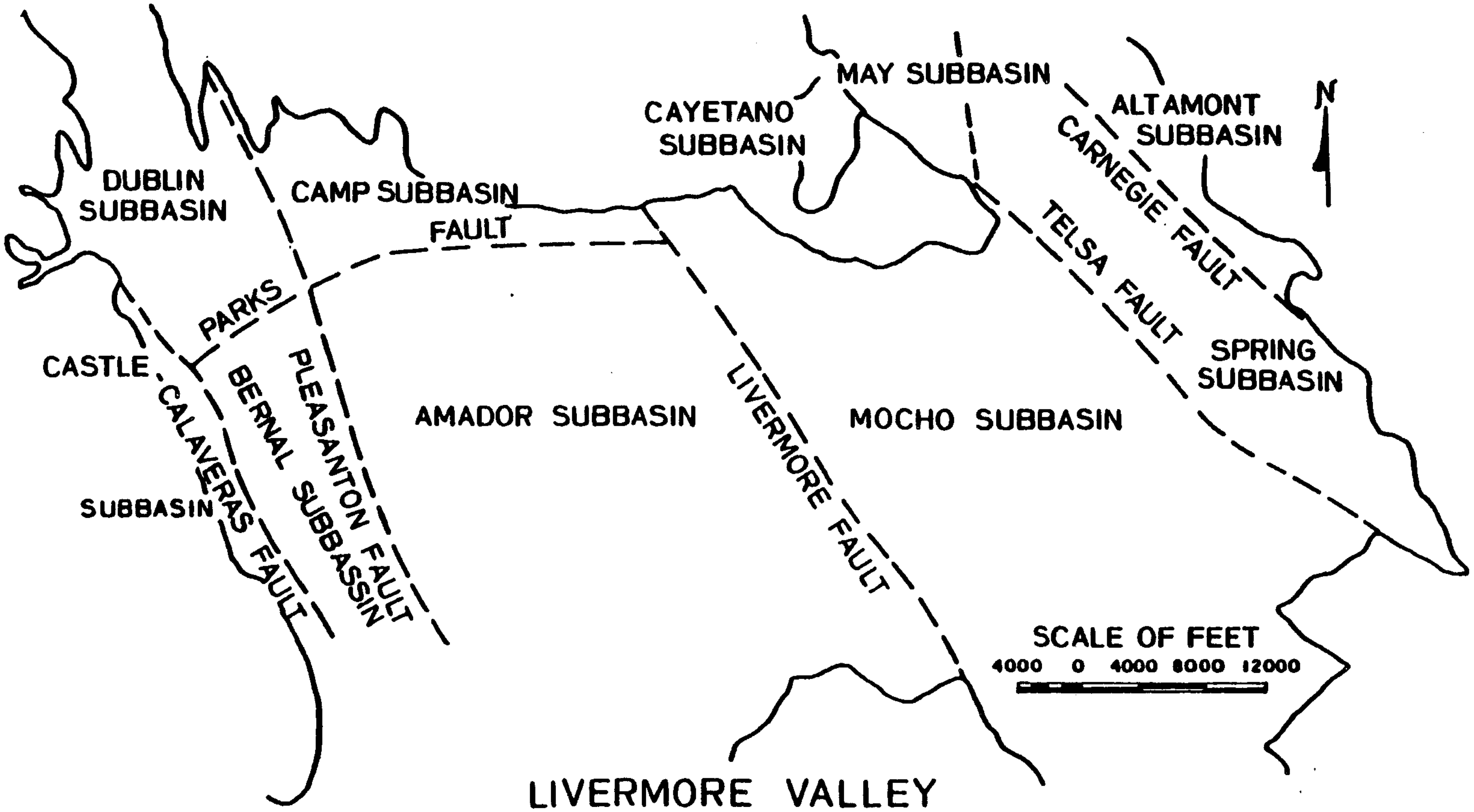

LIVERMORE VALLEY

GROUND WATER BASIN

SHOWING DIVISION BY FAULTS INTO DISTINCT SUBBASINS

FIGURE 1

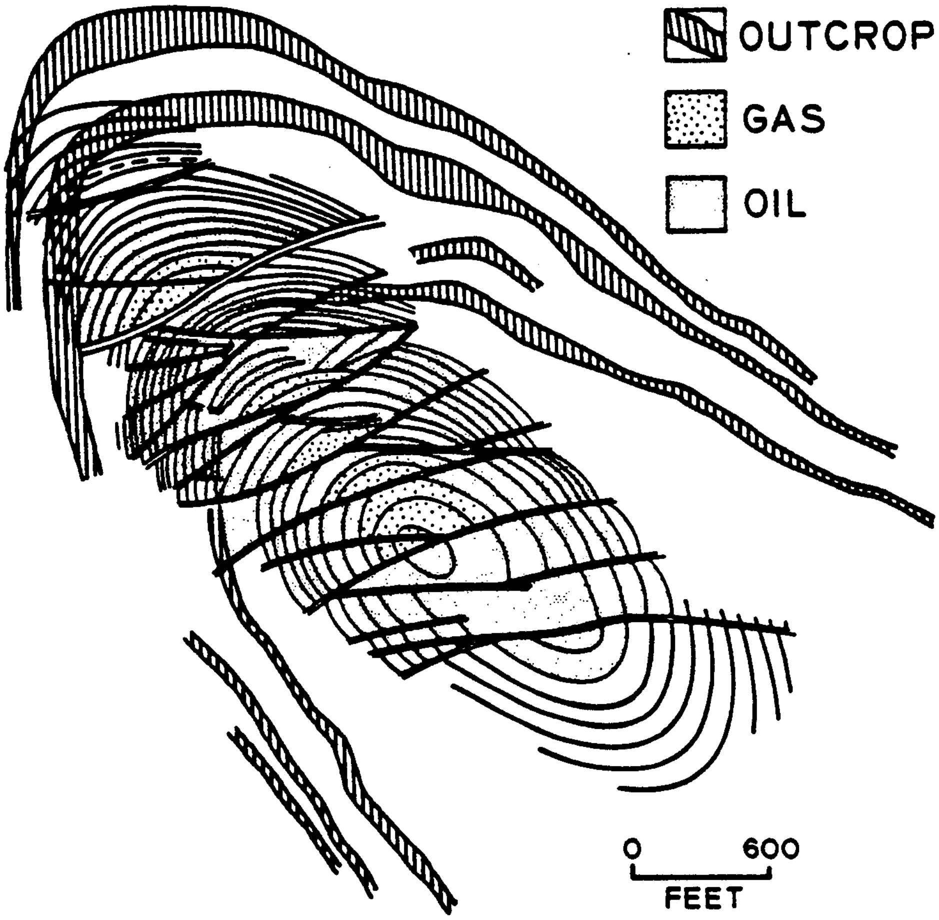

FIGURE 2

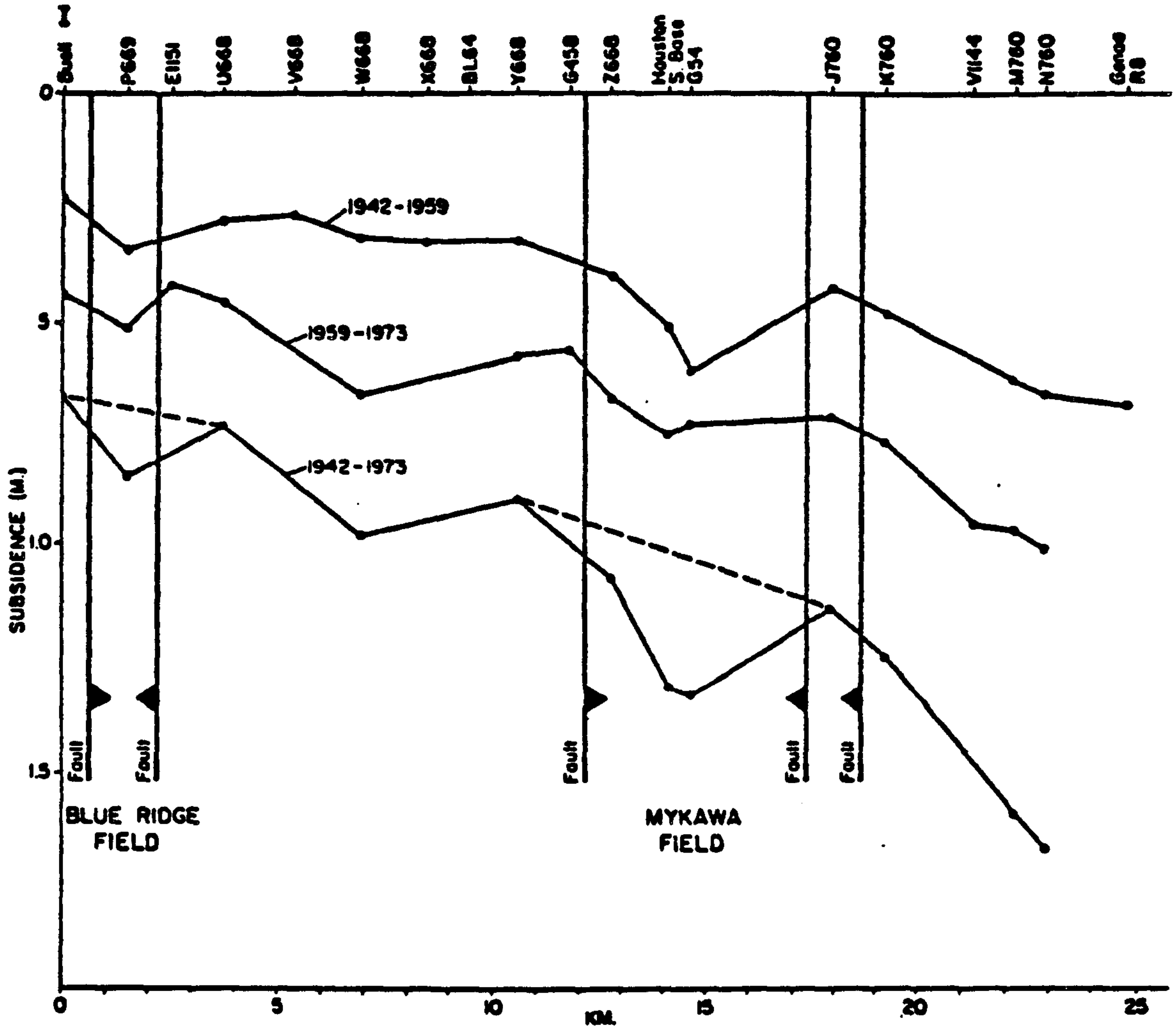
Bull I
P669
E1151
U668
V668
W668
X668
BL64
Y668
G458
Z668
Houston S Base
G54
J760
K760
V1144
M760
N760
Genoa R8
0
.5
1.0
1.5
SUBSIDENCE (M.)
1942-1959
1959-1973
1942-1973
Fault
Fault
Fault
Fault
Fault
BLUE RIDGE FIELD
MYKAWA FIELD
0
5
10
15
20
25
KM.

FIGURE 3

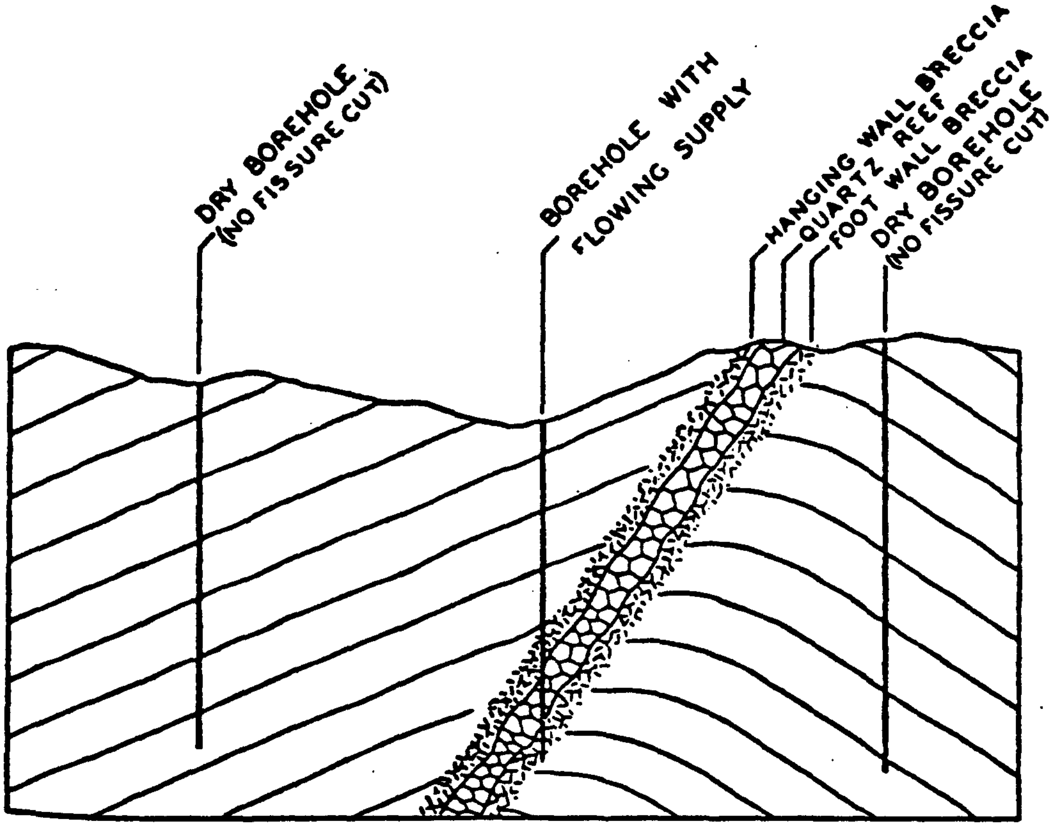
DRY BOREHOLE
(NO FISSURE CUT)
BOREHOLE WITH
FLOWING SUPPLY
HANGING WALL BRECCIA
QUARTZ REEF
FOOT WALL BRECCIA
DRY BOREHOLE
(NO FISSURE CUT)

FIGURE 4

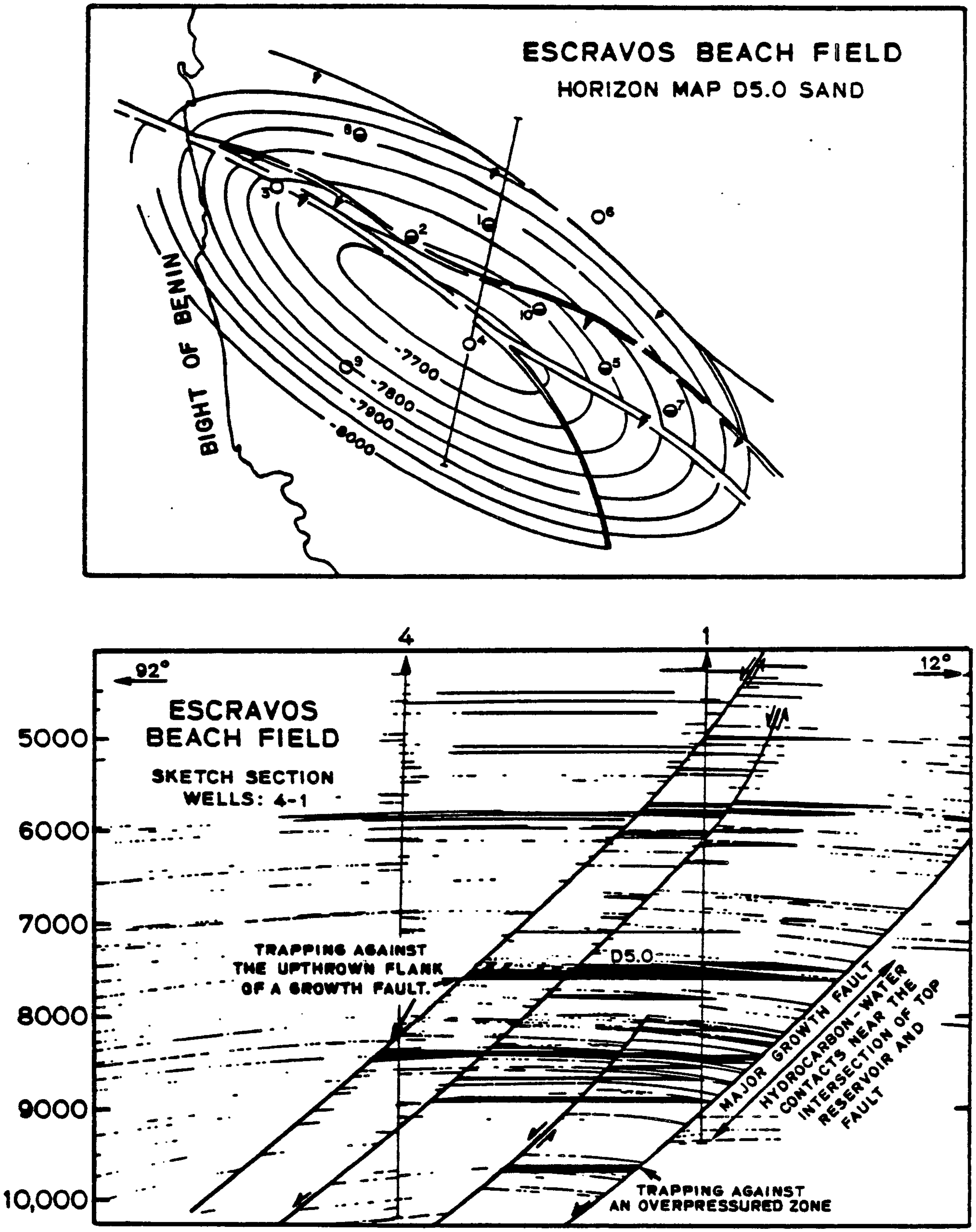
ESCRAVOS BEACH FIELD
HORIZON MAP D5.0 SAND
BIGHT OF BENIN
-7700
-7800
-7900
-8000
1
2
3
4
5
6
7
8
9
10
4
1
92°
12°
ESCRAVOS BEACH FIELD
SKETCH SECTION WELLS: 4-1
5000
6000
7000
8000
9000
10,000
D5.0
TRAPPING AGAINST THE UPTHROWN FLANK OF A GROWTH FAULT.
MAJOR GROWTH FAULT
HYDROCARBON-WATER CONTACTS NEAR THE INTERSECTION OF TOP RESERVOIR AND FAULT
TRAPPING AGAINST AN OVERPRESSURED ZONE

FIGURE 5

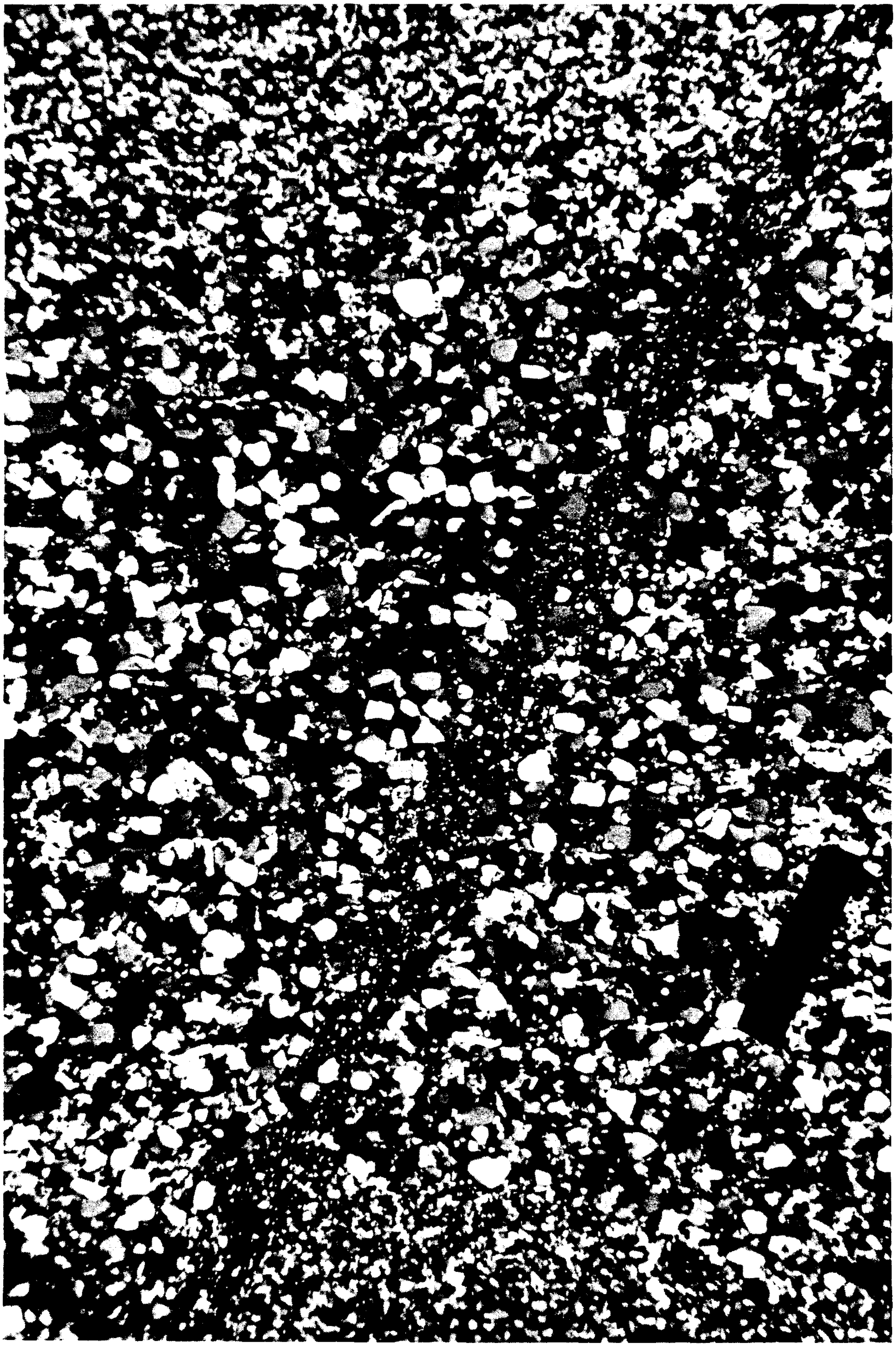

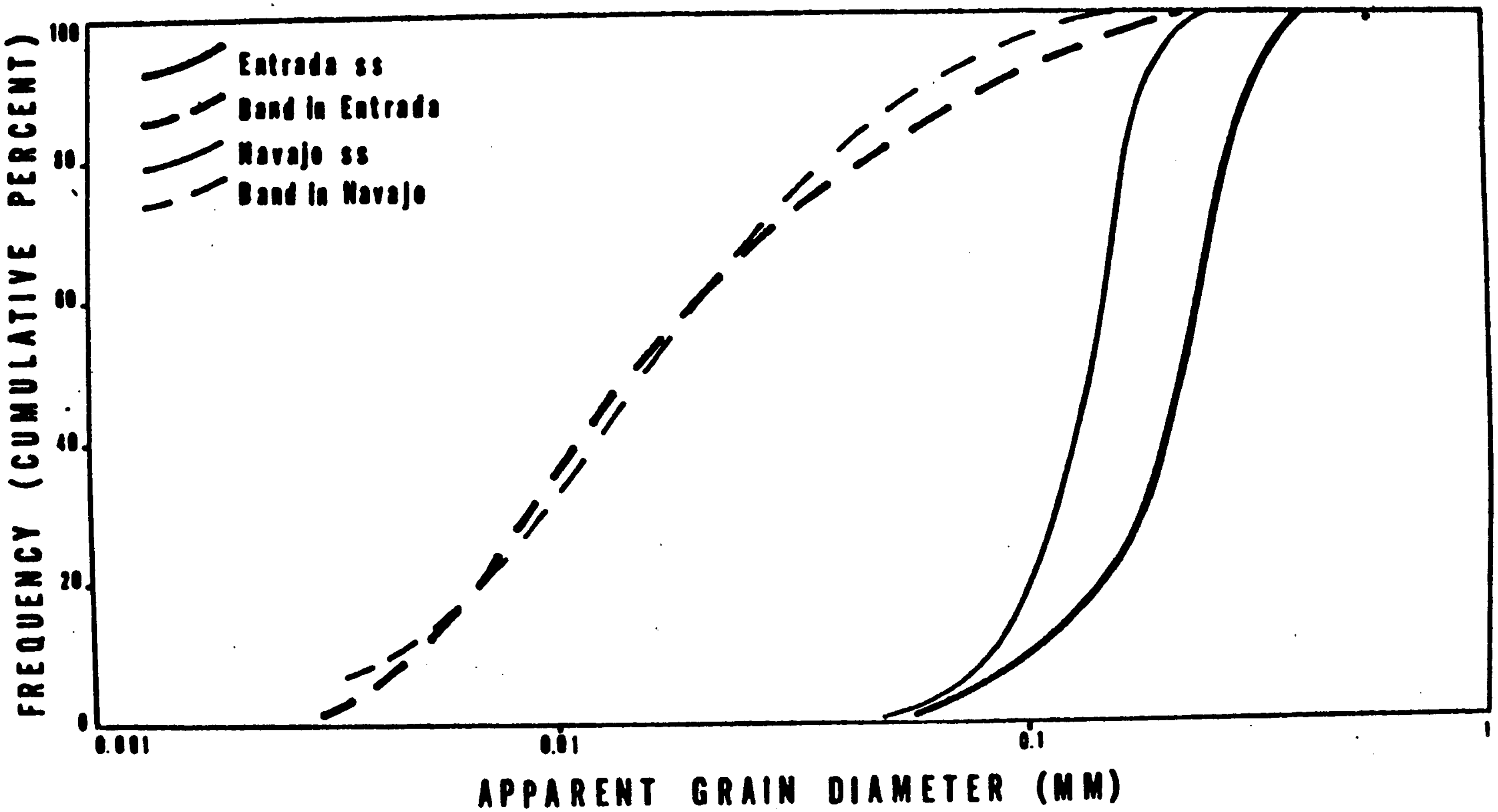
Entrada ss
Band in Entrada
Navajo ss
Band in Navajo
FREQUENCY (CUMULATIVE PERCENT)
100
80
60
40
20
0
0.001
0.01
0.1
1
APPARENT GRAIN DIAMETER (MM)

FIGURE 8

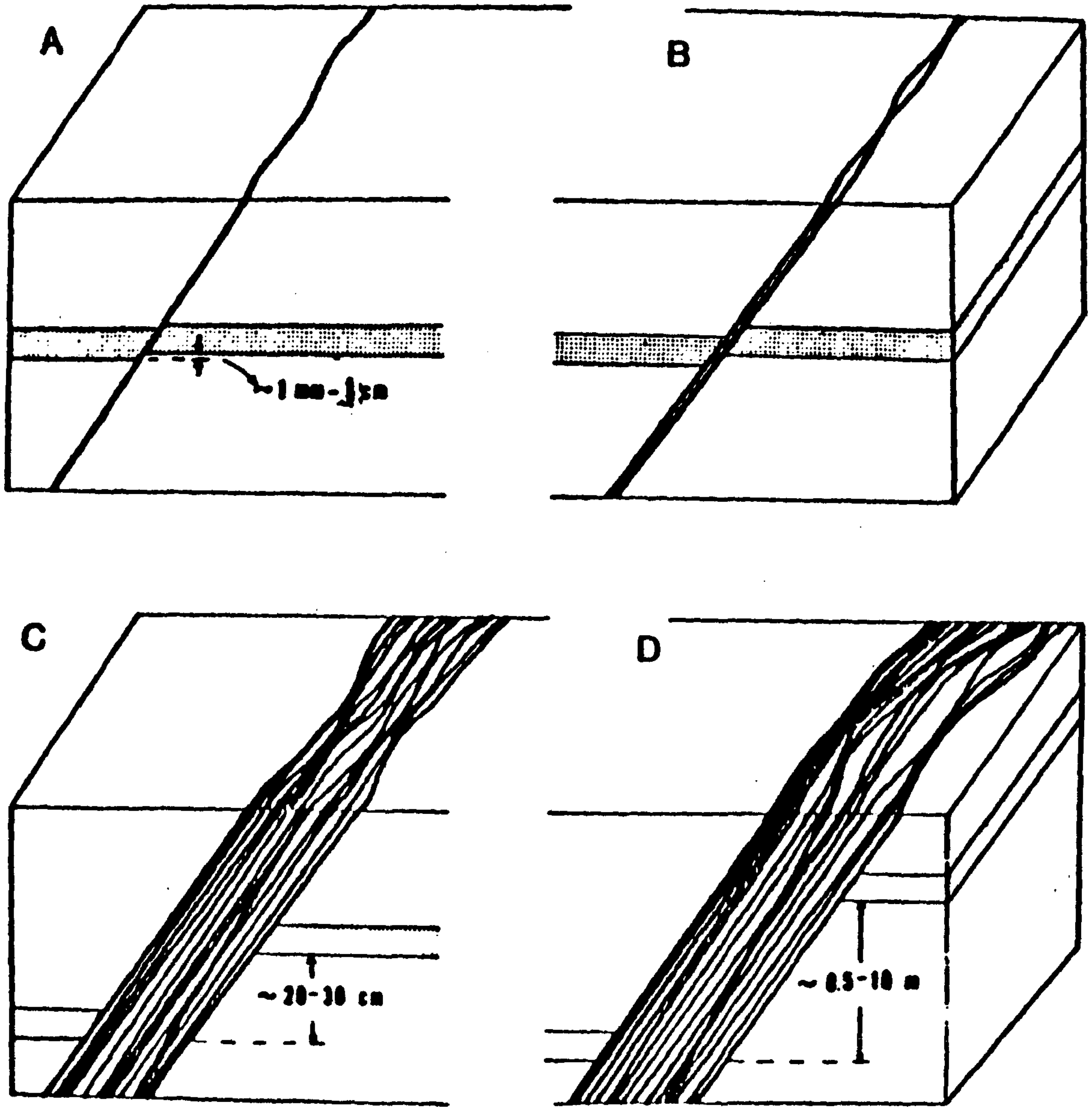

FIGURE 9

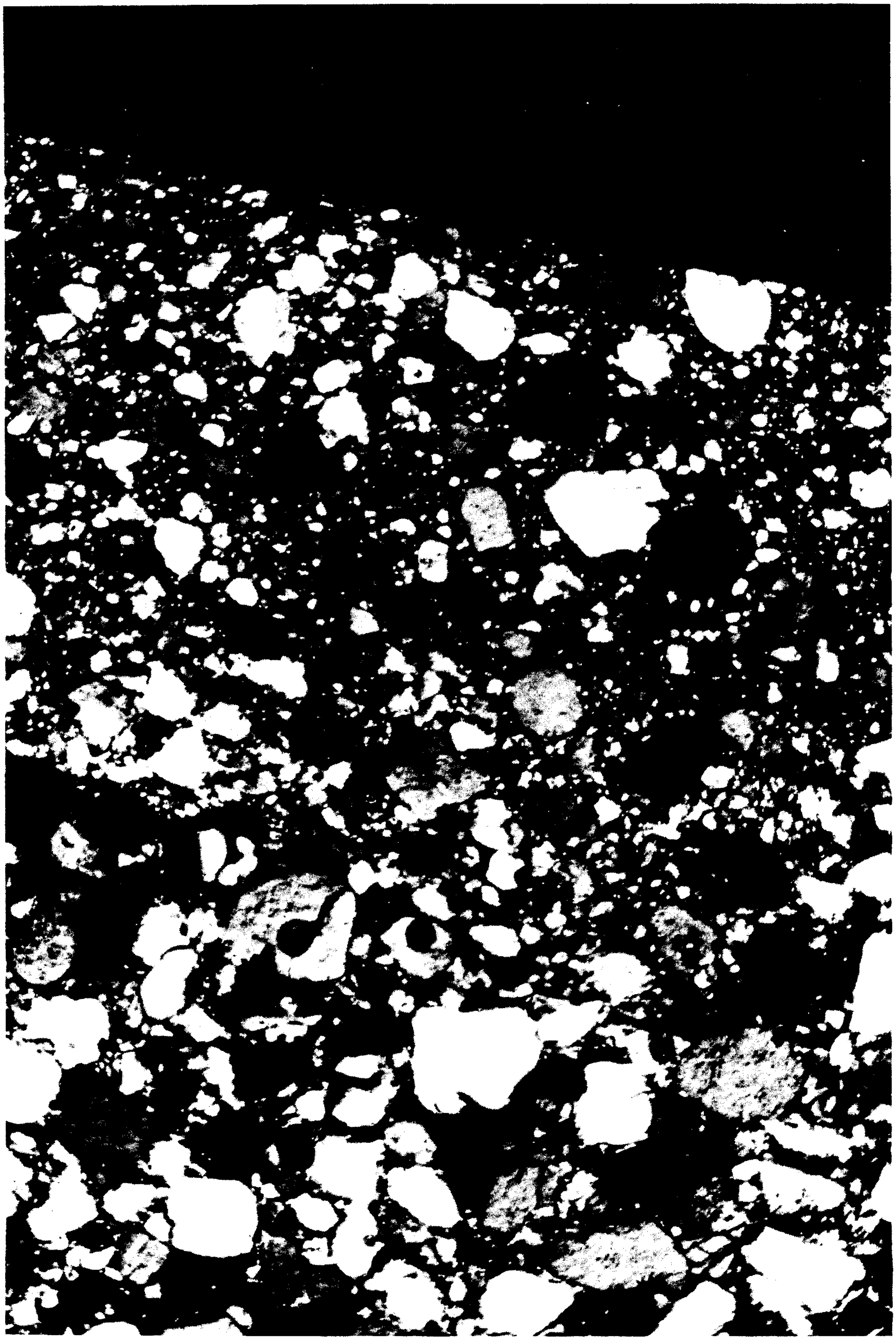

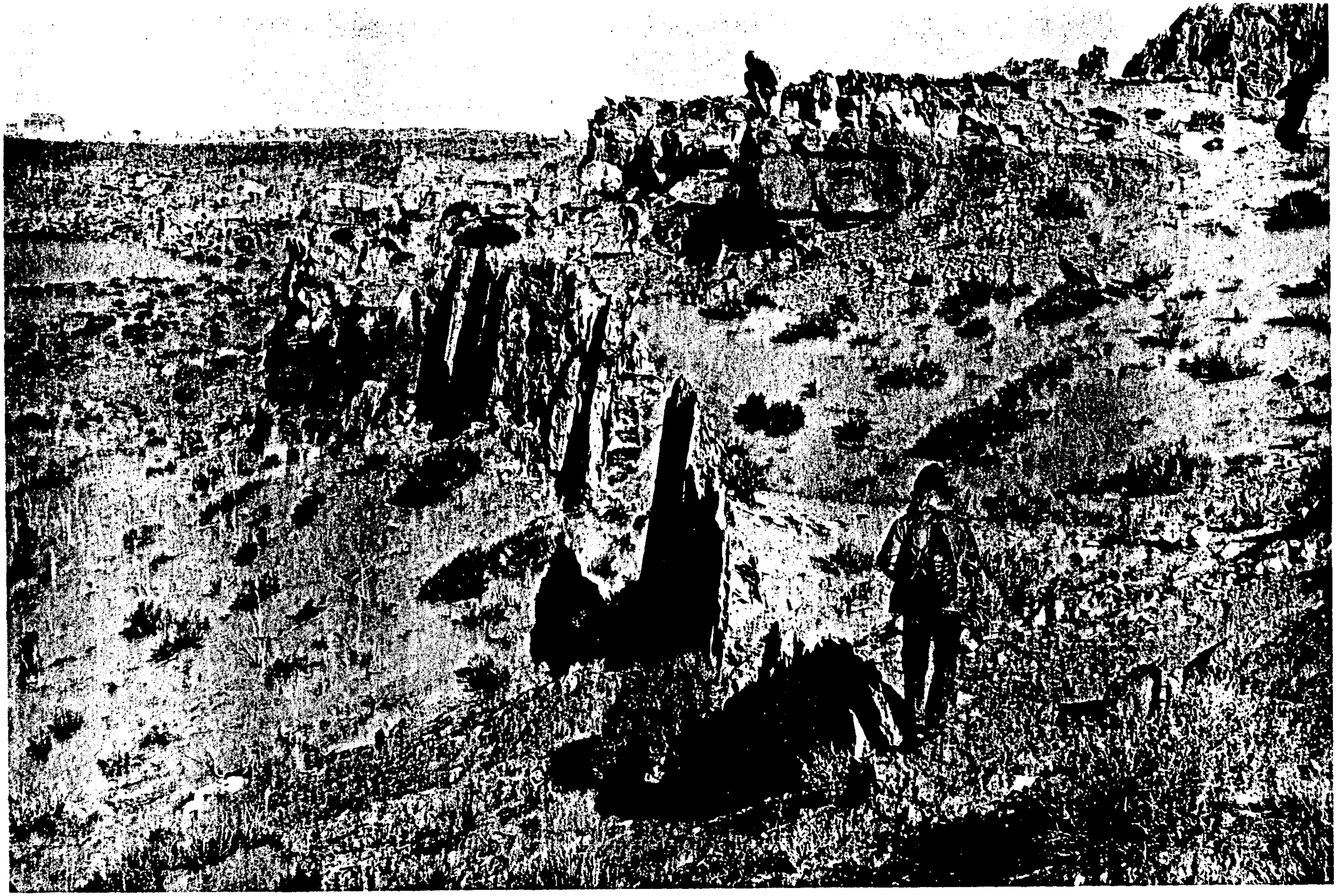

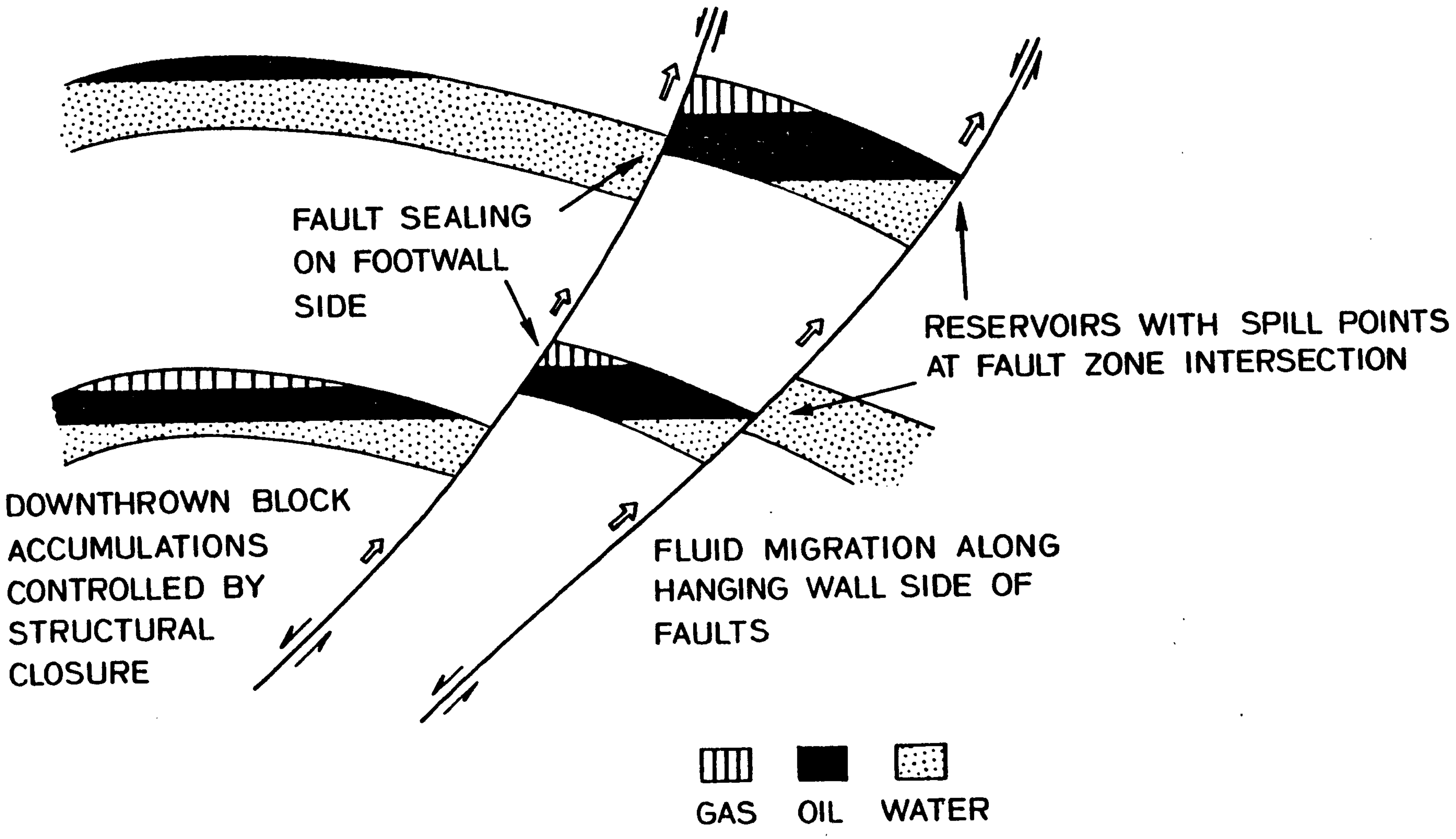
FAULT SEALING
ON FOOTWALL
SIDE
RESERVOIRS WITH SPILL POINTS
AT FAULT ZONE INTERSECTION
DOWNTHROWN BLOCK
ACCUMULATIONS
CONTROLLED BY
STRUCTURAL
CLOSURE
FLUID MIGRATION ALONG
HANGING WALL SIDE OF
FAULTS
GAS
OIL
WATER

FIGURE 12

A PORE SPACE MODEL FOR PERMEABILITY AND BULK MODULUS

ABSTRACT

A network model of pore space is presented in which permeability and bulk modulus at different confining pressures can be calculated. Pores are modeled as straight conduits of circular, ellipitic, or tapered section. The interconnection of these conduits is modeled by emplacing them in regular two-dimensional hexagonal, square, or triangular networks. Flow through each conduit is modeled using Poiseuille's law. Flow through the network is calculated based upon the analogy of fluid flow in Darcy's law to current flow in Ohm's law. An estimate of the effective bulk modulus can be obtained by summing the contributions of the individual pores. The effect of confining pressure on permeability and bulk modulus is determined by the elastic properties associated with the individual pores. For appropriate aspect ratio distributions, the permeability and bulk modulus characteristics of the network model are similar to those found in laboratory experiments. For rocks of moderate porosity, like sandstone, the model predicts that the bulk modulus is most affected by small, low aspect ratio pores, while the permeability is controlled by larger round pores. In contrast, for rocks like granite and tight sandstones, in which there are relatively few round pores, the bulk modulus and the permeability are both affected by easily deformed pores. These relations are observed in experimental data. The success of the model in predicting these bulk modulus and permeability responses indicates that the network theory approach is a promising method for modeling porous media.

INTRODUCTION

What constitutes an adequate model of the pore space of rocks? Rocks are complex, multi-component physical systems. Their responses to physical stimuli are a function of the responses of the individual components, the component interactions, and the structure of the system. In general, the details of the structure of the system and the interaction of its components are not known. Most measurements of the response of porous media to stimuli represent macroscopic averages of processes taking place on the microscopic scale. In order to understand the macroscopic processes, their dependence on the structure and composition of the system, and how they vary under differing conditions of temperature and pressure requires an understanding of the processes on the microscopic scale.

Early pore space studies attempted to relate a single parameter, such as porosity, to measured properties, such as velocity (Wyllie, et al., 1958), resistivity (Wyllie and Spangler, 1952), and permeability (Archie, 1950). The results of these studies showed that general trends may exist between the single parameter and the measured property for a given formation, but, as is shown in Figure 1, direct functional relationships do not exist except for certain simple geometries. Note that in Figure 1, permeabilities in two different sandstones may be of the same order while their porosities differ by 10% or more. It is certain now that single parameter models cannot adequately predict the properties of rocks.

More advanced pore space models, such as the ellipsoidal inclusion model used to predict velocity and moduli properties (e.g. Nur, 1969; Cheng and Toksoz, 1979), and the pore shape - based network models used to predict permeability (e.g. Dullien, 1975), have proven to be reasonably effective. However, almost all of these advanced developments suffer from a fundamental flaw in that they predict only one type of rock response. For example, in the ellipsoidal inclusion model there is no discussion of crack interaction and the model cannot be used to study the permeability or resistivity of a rock. Similarly, permeability models which have been proposed to date are not of use in describing the elastic characteristics of rock. Therefore, even these more advanced models cannot be used to predict rock properties other than those for which they were intended.

A complete pore space model, then, is one which can be used to predict the rock response to any physical stimulus under any prescribed conditions. There are many commonly measured rock and pore space properties such as porosity, density, compressional and shear velocities, permeability, capillarity, resistivity, and grain size. A complete pore space model would give accurate predictions of both the velocity and permeability characteristics of rock, for example, and it would correctly predict the change in both properties with increasing confining pressure or temperature. It has been common in previous model studies to consider each response as separate, but there is increasing evidence, especially from studies of attenuation of elastic waves in saturated and partially saturated media (Winkler and Nur, 1979), that interactions of the various physical components of the system and the factors which control their responses are significant. A more complete pore space model which addresses the different responses of the various components of the physical system is essential to a fuller understanding of the properties of rocks.

Very little work has been done developing models which specifically address more than one type of physical response. To this author's knowledge, Madden (1976) has given the only discussion of a model which may be used to evaluate more than one physical response. In this particular case, Madden made a detailed statistical study of the mixing laws responsible for the observed electrical conductivity properties of rocks (Archie's law) and briefly discussed some of the consequences that the results of this work would indicate for the elastic properties of rock. Due to the complexity of the system studied and the wide range of length scales required (Madden (1976) noted that length scales ranging from about 10^{-9} to 10^{-2} m may be of importance to electrical conduction in rocks) it is not now possible to develop a complete rock model. It is possible, however, to use currently available modeling techniques to investigate the role of pore space structure and distribution on more than one rock property.

In this paper, a model is presented which can be used to investigate the role that pore shape and pore interconnection have on permeability as a function of confining pressure while at the same time an estimate of the bulk modulus as a function of confining pressure is calculated. The ultimate goal of this work is to produce a model which can reasonably predict the properties required to give accurate modulus (or velocity) vs. confining pressure and permeability vs. confining pressure curves for the same rock (typical data shown in Figure 2).

A network theory approach to permeability modeling is used. The conductive elements in the network are chosen to be circular, elliptic, or tapered tubes of given aspect ratio. The flow through these tubes is determined using Poiseuille's law. The pressure differences in the network are found by applying Kirchoff's laws throughout the network. The tube shapes were chosen because, for these particular shapes, the change of tube shape as a function of confining pressure is known (Berg, 1965; Mavko and Nur, 1978). By considering the change in fluid conduction with confining pressure, a model for the variation of permeability with confining pressure is produced. In addition, an approximate calculation of the effective bulk modulus of a porous solid can be made using the tube shapes considered here (Walsh, 1965; Mavko and Nur, 1978). Thus, for a network of elliptic or tapered cracks, it becomes a straightforward computer calculation to find the permeability and bulk modulus as functions of confining pressure. Other factors which are calculated include the porosity and the hydraulic radius, from which the calculated permeability and the permeability predicted using Archie's law may be compared.

THEORETICAL DEVELOPMENT

CALCULATION OF PERMEABILITY

The most promising approach to the study of transport phenomena in porous media is based upon simple network theory. The application of network theory to permeability studies is facilitated by the analogy of fluid flow in Darcy's law to current in Ohm's law. The network theory approach has been used by many, the first attempt to apply it to rock properties (capillarity and permeability) appears to have been made by Fatt (1956 a, b, c). Dullien and his coworkers have had considerable success applying network theory to the study of permeability, resistivity, and capillarity in sandstones (for a review see Dullien, 1979). Simple network theory is also a basis for Madden's (1976) embedded network approach to conductivity modeling.

A network theory approach to permeability modeling is superior to the simple capillary tube or hydraulic radius (Carman-Kozeny) approach (Wyllie and Gregory, 1955) in that flow in more than one dimension is considered and a relatively wide range of element "resistances" and interconnections are possible, thus somewhat better modeling the variable pore sizes and connections of real rock. Both computer models (Rink and Schopper, 1968) and actual constructed resistor networks (Greenberg and Brace, 1969; Shankland and Waff, 1974) have been used to study network characteristics. In these approaches, a distribution of resistances was chosen and the resistive elements were randomly emplaced in the network. The resistance and voltage of the system determine the current flowing, which determines the permeability or conductance of the modeled rock system. Greenberg and Brace (1969) and Shankland and Waff (1974) were interested in changes in rock resistivity as a result of changes in confining pressure. To simulate the effect of increasing confining pressure on the system they randomly removed branches or nodes (depending upon the type of experiment) to simulate a decrease in porosity.

Computer models of networks will be studied in this paper. The networks are created using a pseudo random number generator to specify element location in the grid. The elements are tubes of given section and size. The distribution of tube sizes and aspect ratios can be found using experimental data on the bulk modulus or flow as a constraint. Thus, as in the models of Rink and Schopper (1968) and Shankland and Waff (1974), elements with a given "resistance" distribution are randomly emplaced in the network. The change of permeability with increasing confining pressure is found by calculating the effect of the stress field on each element and then recalculating the permeability for the case of the new, deformed system. In contrast to the approach of Greenberg and Brace (1969) and Shankland and Waff (1974) where each element resistance is unaffected by changing stress and the probability that any element would be removed is uniform, here the magnitude of the resistance and the probability that an element will be removed from the network is completely determined by the shape of the conduit and the elastic properties of the solid once the network has been established.

NETWORK THEORY

A summary of the network theory approach used is presented here, for a more detailed development see Noble (1969) and Peikari (1974).

If we let v_r = voltage drop across the rth branch

R_r = resistance of the rth branch

i_r = current in the rth branch

then Ohm's law states that

$$v_r = R_r i_r \tag{1a}$$

or

$$\underline{v} = \underline{\underline{R}}\,\underline{i} \tag{1b}$$

where

$$\underline{v} = \begin{bmatrix} v_1 \\ \cdot \\ \cdot \\ \cdot \\ v_2 \end{bmatrix} \qquad \underline{i} = \begin{bmatrix} i_1 \\ \cdot \\ \cdot \\ \cdot \\ i_n \end{bmatrix} \qquad \underline{R} = \begin{bmatrix} R_1 & & & & \\ & \cdot & & 0 & \\ & & \cdot & & \\ & 0 & & \cdot & \\ & & & & R_n \end{bmatrix}$$

At each node it is possible to have a voltage or current source. Let V_r and I_r be node voltage and externally applied current at the rth node. Since there are no internal sources, the voltage drop between any two connected nodes must equal the voltage drop across the branch connecting them. Also, from Kirchoff's circuit law, the sum of the currents at any node must be zero. If we assign a reference voltage at one node, $V_0=0$, we may then write out the following equations for all nodes and branches except for the reference node:

$$\underline{v} = \underline{\underline{R}}\,\underline{i} \tag{2}$$

$$\underline{J} = \underline{\underline{A}}\,\underline{i} \tag{3}$$

$$\underline{\underline{A}}^T\,\underline{V} = \underline{v} \tag{4}$$

where

$$\underline{\underline{J}} = \begin{bmatrix} I_1 \\ \cdot \\ \cdot \\ \cdot \\ I_n \end{bmatrix} \qquad \underline{\underline{V}} = \begin{bmatrix} V_1 \\ \cdot \\ \cdot \\ \cdot \\ V_n \end{bmatrix}$$

and $\underline{\underline{A}}$ is an incidence matrix defined by Kirchoff's circuit law:

A_{ij} = 1 when the current in branch j is incident to node i and directed away from it.

= -1 when the current in branch j is incident to node i and directed toward it.

= 0 when branch j is not incident to node i.

In the problem to be considered, $\underline{J}$, $\underline{\underline{A}}$, and $\underline{\underline{R}}$ will be known, and $\underline{v}$, $\underline{i}$, and $\underline{V}$ are unknown. We have three matrix equations in three matrix unknowns. We want to find $\underline{V}$. We start with (3)

$$\underline{J} = \underline{\underline{A}}\,\underline{i}$$

Substituting $\underline{i} = \underline{\underline{R}}^{-1}\,\underline{v}$ from (2) gives

$$\underline{J} = \underline{\underline{A}}\,\underline{\underline{R}}^{-1}\,\underline{v}$$

and from (4) we get

$$\underline{J} = \underline{\underline{A}}\,\underline{\underline{R}}^{-1}\,\underline{\underline{A}}^T\,\underline{V} \tag{5}$$

The problem presented is of the familiar form $\underline{\underline{A}}\,\underline{x} = \underline{b}$, where $\underline{\underline{A}}$ is a n by n matrix, and $\underline{x}$ and $\underline{b}$ are vectors of n elements. Here we may compare $\underline{\underline{A}}$ with $\underline{\underline{A}}\,\underline{\underline{R}}^{-1}\,\underline{\underline{A}}^{T}$, $\underline{x}$ with $\underline{V}$, and $\underline{b}$ with $\underline{J}$. Note that there is one equation for each node. In the problem to be considered, $\underline{J}$ will be known and will have the form $\underline{J} = (1,0,0,\ldots,0)^{T}$. This form of $\underline{J}$ represent a system in which there is one external current source applied, such as is found in a laboratory permeability test, where a fluid source is applied at one end of a sample. The matrix $\underline{\underline{A}}\,\underline{\underline{R}}^{-1}\,\underline{\underline{A}}^{T}$ is known from the network, $\underline{J}$ is known, and $\underline{V}$ is unknown. The problem is then one of solving the system of linear equations for $\underline{V}$. Using this development we solve for the voltage required to have the desired current through the network. The network resistance is found from the voltage difference across te entire network using Ohm's law.

The matrix $\underline{\underline{A}}\,\underline{\underline{R}}^{-1}\,\underline{\underline{A}}^{T}$ is particularly easy to generate for regular networks. For example, a square network has the form shown in Figure 3. The position of the nonzero elements in the matrix can be found directly from the network connections without having to resort to formulating both an $\underline{\underline{A}}$ matrix and an $\underline{\underline{R}}$ matrix and then multiplying matrices. This is done by noting that for the ith row, if there is an element connecting the ith and jth element, the i,jth term is the negative value of the resistance between the two nodes, while the i,ith term is the positive sum of all the resistances incident to the ith node. All other entries in the ith row are 0.

Ohm's law has the form $V = IR$ and Darcy's law has the form $q = K\Delta P/\Delta l$ where q is the volume flow rate per unit area, K is the hydraulic conductivity (which includes permeability and viscosity terms), and $\Delta P/\Delta l$ represents the pressure gradient. For modeling using tubular flow, the quantity q is not convenient. Instead, the volume flow rate, Q, through each tubular section will be considered. Correspondingly, the quantity K is changed to include the area term. Thus, we have $Q = K\Delta P/\Delta l$ as the fluid flow equation to be considered, where all of the information about the solid matrix is to be found in K. Comparing Darcy's law with Ohm's law shows that $K \propto R^{-1}$. Thus the network matrix $\underline{\underline{A}}\,\underline{\underline{R}}^{-1}\underline{\underline{A}}^T$ becomes $\underline{\underline{A}}\,\underline{\underline{K}}\,\underline{\underline{A}}^T$.

Three different network configurations will be considered: hexagonal, square, and triangular (Figure 4). The different topologies of the networks can best be characterized by the number of elements incident to any of the interior nodes (the coordination number). For the hexagonal network, three elements are incident to each interior node, for a square network the number is four, and in the triangular network six elements are incident to each interior node. For the same size network, i.e. for the same number of rows and columns of nodes, the triangular network will have the most elements and the hexagonal network will have the least. All of the networks to be discussed will be two dimensional. The network theory approach is suited to three dimensional analysis in theory, but in practice the storage and computational problems associated with three dimensional networks become prohibitive for all but the smallest networks.

The $\underline{\underline{A}}\,\underline{\underline{K}}\,\underline{\underline{A}}^T$ matrix has certain qualities which make solving the system of equations easier than solving an arbitrary nXn system of equations. Figure 3 shows that the matrix is symmetric and sparse (i.e. it contains a large number of zero entries). The matrix is also banded; for hexagonal and square networks the bandwidth is 2m+1 where m is the number of columns of nodes in the network. The bandwidth for triangular networks is 2m+3. In the initial case of zero confining pressure, the matrix is also positive definite and diagonally dominant. However, after the applied confining pressure reaches a level at which cracks may completely close, it is possible for nodes to be completely isolated. In this case the network becomes singular and care must be taken to avoid numerical complications. The procedure adopted in the case of isolated nodes was to assign to the matrix a diagonal value for that node which would prevent the matrix from becoming singular and would assign a zero pressure value at that node.

There are several possible methods that could have been used to solve the system of equations for the voltage or pressure. Since the matrix is sparse, an iterative process such as the Gauss-Seidel method (Dahlquist and Bjorck, 1969) would prove effective. Rink and Schopper (1968) used Cholesky's method to solve the system for the input voltage only. The method used in this study is based upon the Householder decomposition (Dahlquist and Bjorck, 1969). Using this method, the system of equations is solved to give all of the elements of $\underline{V}$. Thus, in addition to studying the overall permeability of the system, fine scale details of the pressure and flow fields in the system can be analyzed.

The numerical problem can also be looked at from a differential equation viewpoint. Darcy's law can be written as

$$\underline{q} = -\underline{\underline{K}}\ \underline{\nabla}\ P \qquad (6)$$

where q is the volume flow rate per unit area, $\underline{\underline{K}}$ is the hydraulic conductivity (permeability divided by viscosity) and P is the fluid pressure. The gradient of equation (6) is

$$\underline{\nabla}\cdot\underline{q} = -\underline{\nabla}\cdot(\underline{\underline{K}}\ \underline{\nabla}\ P)$$

For steady-state, incompressible fluid flow, the conservation of mass requires that $\underline{\nabla}\cdot\underline{q} = 0$, so that

$$\underline{\nabla}\cdot(\underline{\underline{K}}\ \underline{\nabla}\ P) = 0 \qquad (7)$$

Numerically, this yields a second-difference equation with non-uniform weights. The relation between the network theory and the difference equation developments are quite apparent, particularly for the case of a square network.

PORE SHAPES AND FLUID FLOW AS FUNCTIONS OF CONFINING PRESSURE: CASE OF A SINGLE TUBE

In this section applied-stress flow-rate relations for long, straight conduits of elliptic and tapered cross sections will be developed. Each relation will model flow in a single fracture with aspect ratio α (where $\alpha = b/c$ and c and b are the half length and maximum half width, respectively, of the crack). Deformation will be due to an applied hydrostatic stress, p, with the cracks treated as two-dimensional features in plane strain.

Flow will be modeled for each conduit shape by considering incompressible fluid flow through an "equivalent" elliptical conduit. In doing so, use is made of the conclusion by Lamb (1932, p. 587) that "considerable variations may exist in the section without seriously affecting the discharge, provided the sectional area be unaltered." The fluid pressure gradient will be assumed to be constant and unaffected by the applied stress (drained conditions) in every case considered.

DEVELOPMENT

The equation of an ellipse of half length c_0 and half b_0 is

$$y_e = b_0(1-(x/c_0)^2)^{1/2} \tag{8}$$

and the cross sectional area is

$$A_e = \pi b_0 c_0 \tag{9}$$

For a flat, thin elliptical crack, the length is unaffected by an applied hydrostatic stress while the half width varies as (Berg, 1965):

$$b(p) = b_0(1-\frac{2pc_0(1-\nu^2)}{b_0E} \tag{10a}$$

$$c(p) = c_0 \tag{10b}$$

where p is the applied stress, ν is Poisson's ratio, and E is Young's modulus.

The equation of the simple nonelliptical crack considered here is

$$y_t = b_0(1-(x/c_0)^2)^{3/2} \tag{11}$$

and the cross sectional area is

$$A_t = 3/4 \ \pi \ b_o c_o \tag{12}$$

Mavko and Nur (1978) found that the deformation of such a crack as a result of an applied hydrostatic stress could be described by

$$b(p) = b_o \ \frac{(1-4(1-\nu^2)c_o p)^{3/2}}{3Eb_o} \tag{13a}$$

$$c(p) = c_o \ \frac{(1-4(1-\nu^2)c_o p)^{1/2}}{3Eb_o} \tag{13b}$$

Note that for the nonelliptical crack the length is not constant as a function of applied stress. Figure 5 shows one quadrant of both elliptic and nonelliptic sections.

Fluid flow through a conduit of elliptic cross section is found through a simple modification of Poiseuille's law for flow through circular tubes (Lamb, 1932). The volume flow rate, Q, is given by

$$Q = \frac{P\pi}{4\mu} \ \frac{b^3c^3}{b^2+ c^2} \tag{14}$$

where P is the hydraulic pressure gradient, μ is the viscosity, and b and c are the half width and half length of the ellipse, as before. Using equations (10a,b), and volume flow rate as a function of applied stress for an originally elliptic crack becomes

$$Q_e(p) = Q_{oe}(1-\frac{2pc_o(1-\nu^2)}{b_oE})^3 \tag{15}$$

where

$$Q_{oe} = \frac{P\pi}{4\mu} \ \frac{b_o^3c_o^3}{b_o^2+c_o^2} \tag{16}$$

and in (15) we have used the fact that $b \ll c$. This relation between flow and applied stress is shown in Figure 6 for $\alpha=10^{-3}$, $E=6.8(10^5)$ bars, and $\nu=0.25$. A similar development for cracks of circular section gives

$$Q_c(p) = Q_{oc} r^4 \left(1 - \frac{2p(1-\nu^2)}{E}\right)^4 \tag{17}$$

$$Q_{oc} = \frac{P\pi}{8\mu} \tag{18}$$

The elliptic section used to model flow through tapered cracks must have an area of $3/4\pi bc$. Analysis of equation (14) shows that, for $b \ll c$, the width, b, is the most important parameter in describing the volume flow. Thus, the equivalent ellipse was chosen such that the half width equalled that of the nonelliptic section, while the equivalent half length was 3/4 as long. A look at Figure 7 shows that a nonelliptical section and its "equivalent" ellipse differ mainly for $y < b/4$. Thus, for a tapered crack we have

$$Q_t = \frac{P\pi}{4\mu} \frac{b^3(3/4\ c)^3}{b^2+(3/4\ c)^2}$$

Using equations (13a,b), we have

$$Q_t(p) = Q_{ot}\left(1 - \frac{4pc_o(1-\nu^2)}{3b_oE}\right)^5 \tag{19}$$

where

$$Q_{ot} = \frac{P\pi}{4\mu} \frac{b_o^3(3/4\ c_o)^3}{b_o^2+(3/4\ c_o)^2} \tag{20}$$

and in (19) we have used the fact that $b \ll c$. The relation given by equation (19) is shown in Figure 8 for $\alpha=10^{-3}$, $E=6.8(10^5)$ bars, and $\nu=0.25$.

Figures 9 and 10 illustrate the great sensitivity of the volume flow rate as a function of confining pressure to the aspect ratio. An evaluation of the trends shown in Figures 9 and 10 indicates that flow through circular pores is little affected by changes in confining pressure due to the stiffness of the tube shape.

A different functional relationship between flow rate and applied stress has been found for cracks of elliptic and nonelliptic sections. For an elliptic crack, the relation is a third order polynomial in the pressure, p, while for a nonelliptic crack the relation is a fifth order polynomial. For small p, both relations are approximately linear. The flow rate decreases most rapidly with increasing confining pressure at confining pressures of less than 200 bars.

For an aspect ratio of 10^{-3}, $E=6.8(10^5)$ bars, and $\nu=0.25$, the elliptic crack closes at an applied hydrostatic stress of about 360 bars. At this stress the flow is, of course, zero (Figure 7). The flow has fallen to 50% of the original unstressed value when the applied stress reaches 75 bars, or 20% of the stress required to close the crack. The flow is 10% of the unstressed value when the applied stress of 190 bars, or just over 50% of the closing stress. These values illustrate the fact that the flow rate predicted by this model is a rapidly decreasing function of the applied stress.

A simple nonelliptical crack will close when the applied stress is approximately 540 bars, when $E=6.8(10^5)$ bars, $\nu=0.25$, and $\alpha=10^{-3}$, as above. Analysis of Figure 8 shows that the flow is reduced to 50% of the unstressed value when the applied stress reaches about 70 bars, or 13% of the closing stress, and the flow is reduced to 10% of the unstressed value when the applied stress reaches 200 bars, or 37% of the closing stress. Thus for equal aspect ratios the relative decrease in permeability with applied stress is initially more rapid for the nonelliptical crack. For applied stresses greater than about 150 bars, $Q_t(p)/Q_{ot}$ is greater than $Q_e(p)/Q_{oe}$. It is interesting to note that for confining pressures greater than about 40% of the closing stress for a nonelliptical crack, and 50% of the closing stress for an elliptic crack, the flow is less than 10% of the flow through the original, undeformed conduit.

Figure 11 shows the stress-flow relations for elliptical and nonelliptical cracks of equal aspect ratio and equal initial half widths and lengths. In this case the flow through the tapered crack is less than that through the elliptical crack until the applied stress reaches about 65% of the stress required to close the elliptical crack. For greater applied stresses, flow through the tapered crack is larger, but the net flow is less than 10% of the flow through undeformed cracks.

Figure 12 shows the stress-flow relation for the two crack types when the cross sectional areas are equal and the aspect ratios are equal. For a simple rock model in which the porosity is composed of only such crack shapes, this corresponds to the case of equal porosity. The flow through the tapered crack is larger than the flow through the elliptic crack over the entire range of applied stress.

The case of initially equal permeabilities and aspect ratios is shown in Figure 13. In this case the two curves are practically indistinguishable over the entire range of applied stress. The largest difference occurs at high stresses where the total flow is small.

One point to be noted is that the Poiseuille relation for flow through an elliptic section of small aspect ratio is of the same functional form as that which describes flow between parallel planes (Snow, 1968). In both cases

$$Q \backsim b^3 c$$

Thus, the relations between flow and fracture size for elliptic and nonelliptic sections presented here are consistent with the conventional fracture flow developments based upon the parallel plate fracture model (see Appendix A).

A comparison of equations (15) and (19) with the $Q=K\Delta P/\Delta l$ form of Darcy's law used in the $\underline{\underline{A}}\ \underline{\underline{K}}\ \underline{\underline{A}}^T$ matrix shows that the following relations hold for each tube:

For elliptic cracks $$K(p) = \frac{Q_o}{\Delta P}\left(1 - \frac{2pc_o(1-\nu^2)}{b\ E_o}\right)^3 \qquad (21)$$

For tapered cracks $$K(p) = \frac{Q_o}{\Delta P}\left(1 - \frac{4pc_o(1-\nu^2)}{3b_oE}\right)^5 \qquad (22)$$

where ΔP is now the pressure difference across a given tube in the network. Thus, at each pressure step, a $K(p)$ is calculated for every element to form the $\underline{\underline{A}}\ \underline{\underline{K}}\ \underline{\underline{A}}^T$ matrix required for the pressure (permeability) calculations.

There are several assumptions made in using a conduit flow approach to the network permeability problem. The model calculations assume laminar flow of an incompressible fluid. The equations for fluid flow from Poiseuille's law are strictly valid only in the case of long, uniform conduits. In contrast, in the model the tubes are of finite length, with the length chosen to be greater than the greatest open dimension of the tube. Also, it is possible for tubes of different cross-section to be connected with Poiseuille's law used to describe the flow in each tube. Thus, as noted by Dullien (1979), in the simple network model no account is generally made of the excess viscous dissipation due to convergent-divergent flow in the capillaries. For conduits of circular section and varying diameter, Azzam and Dullien (1976) report that the correct pressure losses, found from a numerical solution of the Navier-Stokes equations, are apparoximately 15% greater than those calculated from Poiseuille's law. Losses due solely to changing the conduit section are expected to be somewhat less than this. No attempt to correct for these factors has been made in this work.

A further assumption concerns the character of the pore space at the nodes. In the calculations the nodes have been assumed to possess a negligible volume and to have an infinite conductivity so as to provide no net contribution to pressure losses in the system. The junction of capillaries of varying shape and size requires that actual pore junctions or nodes have a finite volume. Also, the convergent-divergent flow pattern at these nodes could be complex. The neglect of the contributions of the nodes to the flow, porosity, and elastic response of the network is equivalent to the assumption in electrical network theory that the connections between elements are of infinite conductance with no junction effects.

Since the conduits are assumed to be deformable, it is assumed that the pore pressure gradient across the sample is small. This is consistent with the requirements of laminar flow for Poiseuille's law and Darcy's law, and it means that each capillary tube will be of constant section throughout its length.

CALCULATION OF BULK MODULUS

The calculation of effective elastic moduli in porous materials is, in general, quite difficult. Watt et al. (1976) give a summary of theoretical results. They note that for pore- or crack-containing media, specific geometry models must be considered if numerical results are to be obtained. Pore geometries generally considered are penny shaped cracks (Walsh, 1965), two dimensional cracks of elliptic (Walsh, 1965) or tapered (Mavko and Nur, 1978) section, or ellipsoidal inclusions (Eshelby, 1957).

In this work, the response of the conduits to applied confining pressure has been determined assuming the tubes to be effectively two dimensional features. The contributions of the conduits to the effective bulk modulus is determined using the simple sum approach (Reuss bound), based upon the Betti-Rayleigh reciprocity theorem, as used by Walsh (1965) and Mavko and Nur (1978). This method is strictly valid only for a dilute distribution of non-interacting cracks. Here, however, a relatively dense network of cracks is to be connected so as to provide a through going passage for fluids; thus, there must be some degree of interaction between the various elements. The self-consistent approach (O'Connell and Budiansky, 1974; Korringa et al., 1979) was developed to take crack interaction into account, but there has been some question as to the method of calculation (Bruner, 1976). Also, as shown by Mavko and Nur (1978), the prediction of features such as the bulk modulus under varying confining pressure depends upon the specific crack model used and is thus nonunique. Therefore, considering the simplicity of the model, it is believed that the simple sum approach will provide an adequate indication of the role of the cracks in determining the bulk modulus.

The bulk modulus of a dry rock containing elliptic or tapered cracks can be calculated from the expression

$$\frac{1}{K'} = \frac{1}{K}\left(1 + \frac{2\pi}{3}\frac{(1-\nu^2)}{(1-2\nu)}\sum_{i=1}^{N}\frac{c_i^2 d_i}{V}\right) \qquad (23)$$

where K' is the effective bulk modulus of the porous solid, K is the intrinsic bulk modulus of the rock material, ν is Poisson's ratio, c_i is the semimajor axis length for the ith crack, d_i is the crack length in the third dimension, V is the volume of the rock sample, and the summation is over the total number of cracks in the sample, N. Here, d_i will be constant for all cracks and the volume V will be determined by the size of the network. Since the network models considered are essentially two dimensional, the volume V can be thought of as a thin layer from a larger sample, where the thickness of the layer will be of the same size as the length of a single element.

The stress dependence of the bulk modulus is determined by the stress dependence of c_i. Under hydrostatic confining pressure the variation of c_i at stresses less than the closing stress is

$$c(p) = c_0(1- \frac{1-\nu^2}{E} 2p) \qquad \text{circular section}$$

$$c(p) = c_0 \qquad \text{elliptic section}$$

$$c(p) = c_0(1- \frac{4(-\nu^2)}{3\alpha_0 E} 2p) \qquad \text{tapered section}$$

In particular, note that below the stress required to close an elliptic crack its length remains unchanged. The contribution of elliptic cracks of given initial aspect ratio is constant until the closing stress is reached, at which point the contribution of these cracks to the effective bulk modulus vanishes. The contribution of tapered and circular cracks on the other hand, changes as the confining pressure different aspect ratio distributions are required for each type of crack.

The static saturated bulk modulus, K_s, can be obtained from the dry rock modulus using Gassmann's (1951) relation

$$K_s = K \frac{K'+Q}{K+Q} \tag{24}$$

where

$$Q = K \frac{K_f(K-K')}{\phi(K-K_f)}$$

Here K', K, and K_f are the bulk moduli of the dry porous rock, of the intrinsic rock material, and of the fluid, respectively, and ϕ is the porosity. This result assumes that the pore pressure is uniform everywhere throughout the rock.

Because of the pore geometry chosen (2-D cracks), it is not possible to consider the magnitude and stress dependence of the shear modulus. This is a result of the fact that the cracks have been modeled in opening and closing mode only, with no shear displacement across the crack surface. Therefore, it is not possible to investigate the pressure dependence of the velocities of compressional and shear waves in the rock represented by the network model.

POROSITY AND HYDRAULIC RADIUS

Two additional factors, porosity and hydraulic radius were calculated for the porous medium represented by the network. These two parameters are of importance in many conductivity and permeability studies (e.g. Wyllie and Spangler, 1952; Brace, 1977).

The porosity calculated from the network model should approximate that of the desired rock if the model is to be considered adequate. Porosity can be simply calculated from the known cross-sectional areas and lengths of the individual tubes, and the volume of the layer represented by the network. The network, however, is a two dimensional representation of pore properties. Pseudo-three dimensional porosities were calculated from the two dimensional model by assuming that the medium was homogeneous and isotropic, so that $\phi_{3D} = 1.5\ \phi_{2D}$.

The hydraulic radius of a porous medium is defined as the volume of the interconnected pores divided by their surface area (Bird et al., 1960). Since the conduit shapes were known, it was possible to calculate the hydraulic radius of the two dimensional network using the known cross-section area and perimeter of each element, i.e.

$$R_h = \frac{\sum_{i=1}^{N} A_i}{\sum_{i=1}^{N} P_i}$$

where A_i and P_i are the cross-sectional area and perimeter of the ith element.

Porosity and hydraulic radius are important factors in the empirical relation between porosity and permeability, based upon Archie's law. Wyllie and Spangler (1952) and Brace et al. (1968) found the following relation between fluid flow and electrical conductivity of rock:

$$k = (m^2/k_0)F^{-2}\phi^{-1} \tag{25}$$

where k is permeability, k_0 is a shape factor which can vary between 2 and 3, m is the hydraulic radius, ϕ is porosity, and F is the formation factor, defined as the ratio of the resistivity of a fluid saturated rock to the resistivity of the fluid alone. Archie's law, an empirical relation between the formation factor and porosity which appears to hold for a wide variety of rocks (Brace et al., 1965) is given by

$$F = \phi^{-r} \tag{26}$$

where r is a constant close to 2. If r = 2, combining (25) and (26) gives

$$k = (m^2/k_0)\phi^3 = (m^2/k_0)F^{-1.5} \tag{27}$$

Equation (27) states that the permeability can be calculated once the porosity and hydraulic radius are known. Since both of these factors are calculated in the network model it is possible to compare the permeability calculated directly from the permeability model with that calculated from the porosity and hydraulic radius.

SUMMARY OF COMPUTER OPERATIONS

The sequence of computer operations is shown in the flow chart in Figure 14. There are three major routines in the process: SETUP, MAKEA, and HHOLDER.

The main input parameters describe the network size and the tube size distribution. To describe conduit sizes, distributions of aspect ratio and a length scale for the sections are required. Specifying the aspect ratio and length scale determines the flow, porosity, and all related properties for each conduit. For each aspect ratio a distribution of length scales is possible, and for each length scale a distribution of aspect ratios is possible. Aspect ratios of 10^0, 10^{-1}, 10^{-2}, 10^{-3}, and 10^{-4} were considered here. After specifying the aspect ratio, a length parameter is needed. There are several choices for the length scale, three of those choices are mentioned here.

1) Equality of semiminor axes, b. The case of equal semi-minor axes for each pore shape and aspect ratio is that distribution which would be chosen to satisfy capillary pressure data. The capillary pressure response of a porous medium is controlled by the pore

sizes, as given by Laplace's equation

$$p = \sigma(1/r_{min}+1/r_{max}) = \sigma(1/b+1/c)$$

where p is capillary pressure and σ is surface tension. For a circular conduit, $b = c$, $p = 2\sigma/r$. For aspect ratios of 10^{-1} and smaller, $1/b+1/c \sim 1/b$. Thus, if capillary pressure curves are used to determine pore size distribution, the semiminor axes should be the same for each aspect ratio.

2) Equality of flow. In the case of equal flow through all sections of the same length scale, either b or c would be fixed and the other varied with the aspect ratio. This approach insures that approximately equal volumes of fluid will flow in tubes of every aspect ratio.

Both of these first two approaches have the limitation that the low aspect ratio pores are relatively large. For example, in case (1) above, if $b = 10\ \mu m$ and $\alpha = 10^{-4}$, then $c = 10^5\ \mu m = 10$ cm. Such a large thin pore is not realistic in unfractured rock. The results are only slightly better for case (2). For specific problems, particularly those for which r_{min} is relatively constant and small, either case (1) or (2) would be applicable. However, based upon pore size arguments, case (3), below, was most often used in the examples presented here.

3) Equality of semi-major axes. In this case each c would be constant for all aspect ratios. This choice has the advantage that it keeps low aspect ratio pores from having unrealistic lengths. It has the disadvantage in that the permeabilities and porosity contributions of the low aspect ratio pores are relatively small.

small. Thus, the choice of keeping each c constant for all aspect ratios is made on a pore size argument.

The input parameters into the routine SETUP are thus the network size, the aspect ratio distribution, and the length scale distribution. SETUP uses a pseudo-random number generator to create randomly ordered lists of aspect ratio and length scale. These lists are then used by MAKEA to create the $\underline{\underline{A}}\;\underline{\underline{K}}\;\underline{\underline{A}}^T$ matrix. Additional input parameters into MAKEA are starting and final confining pressures and the size of the confining pressure increment. Using the confining pressure - flow rate equations presented earlier, MAKEA creates the $\underline{\underline{A}}\;\underline{\underline{K}}\;\underline{\underline{A}}^T$ matrix at a given confining pressure. In addition, the porosity, bulk modulus, and hydraulic radius as functions of confining pressure are calculated in MAKEA.

The $\underline{\underline{A}}\;\underline{\underline{K}}\;\underline{\underline{A}}^T$ matrix constructed by MAKEA is used in HHOLDER to solve the system of linear equations for the node pressures. After writing the results, the value of the confining pressure is checked. If this is less than the maximum confining pressure, it is increased by the pressure increment, a new $\underline{\underline{A}}\;\underline{\underline{K}}\;\underline{\underline{A}}^T$ matrix is created for the new confining pressure level, and HHOLDER is again used to solve the system of equations. This process continues until the maximum confining pressure is reached.

RESULTS

NETWORK SIZE AND STRUCTURE

In early work with this network model, basic questions arose as to the effect of network size and element location on the calculated permeability. Also, the response of simple aspect ratio distributions was desired, so that the influence of the aspect ratio distribution and bulk modulus could be understood and rough predictions made of the aspect ratio distribution required to model laboratory measurements of permeability.

The question of optimum network size does not appear to have been answered completely. Networks must be large enough to ensure that the calculated values are representative of network properties in general and not of the specific geometry of the particular network, and they must also be small enough so that the problem is tractable. The size of the networks studied here was 20X25 nodes for square and triangular networks, and 19X25 nodes for hexagonal networks. These network sizes compare favorably with those of the physical and computer generated networks studied by Shankland and Waff (1974). Calculated pressure values for smaller networks were comparable to those for the large networks. Also, detailed analysis of the flow paths through sample networks (see below) indicate that edge and/or size effects are not large. It appears that the 20X25 node and 19X25 node networks studied here were adequate to represent permeability in a porous medium without major size effects.

The effect of element location on the value of the calculated permeability was addressed by considering networks of a given aspect ratio distribution in which the order of element emplacement was varied. This was achived by starting the random number generator with different seeds and constructing differently ordered lists of aspect ratios and semi-major axes. Results of several calculations of the flow of water through each type of network are listed in Table 1. The network considered in each case had 30% of its pores with an aspect ratio of 10^0, 30% with 10^{-1}, 35% with 10^{-2}, and 5% with 10^{-3}. 35% of the semimajor axes were 10 µm in length, 30% were in 18 µm, and 35% were 28 µm in length. The aspect ratio distribution was chosen at random, while the pore sizes were adopted from a table of tube sizes given by Dullien (1979, p. 182) for a Berea sandstone model. The results listed are for the flow through tapered cracks. The permeability behavior of elliptic cracks is similar to that through tapered cracks. Due to the difference in cross-sectional areas, permeability of a network of elliptic conduits is 25-40% higher than that through the same network with tapered cracks. This is consistent with the results found earlier for single conduits.

Note that for networks with approximately the same number of nodes, the triangular network has the most elements, followed by the square network, with the hexagonal network having the fewest elements. It follows that the triangular network would be expected to have the highest permeability (least measured pressure difference across the sample) while the hexagonal network would have the lowest permeability. The results of the sample calculations show this relationship. The standard deviations from the averages reflect the varying flow paths present in each of the randomly generated networks. The standard deviation is largest for the network with the fewest elements, the hexagonal system, and is smallest for the network with the most elements, the triangular system. It might be expected that the standard deviation would be somewhat lower if considerably larger networks were considered, however, as mentioned above, the networks studied here appear to be of adequate size to model the network properties.

It is impossible to avoid the fact that, for a given range of element values, the network topology will affect the magnitude of the calculated permeability. It also follows that this effect is expected to be largest in the network with the lowest coordination number, i.e. the hexagonal system.

Figure 15 shows the dependence of permeability on confining pressure for each of the network types. The elastic constants used were $E = 6.8(10^5)$ bars and $\nu = 0.25$. For each network type curves showing the greatest and least measured confining pressure effect are shown. For each network type the absolute values of permeability may vary by about a factor of three, however, the relative permeability loss with increasing confining pressure is nearly the same for all networks of a given type. The difference in relative permeability loss was smallest for triangular networks, about 2% for this particular aspect ratio distribution, and largest for hexagonal networks, where it was about 5%.

The relative decline in permeability is greatest for hexagonal networks and least for triangular networks. This can again be explained by network topology. Flow through hexagonal networks is more likely to be forced to pass through small, easily deformed conduits ($\alpha < 10^{-1}$) than is flow in square or triangular networks, and thus shows a greater variation with confining pressure.

The effect of varying Young's modulus is shown in Figure 16. The upper data points represent the average permeability decrease for a triangular network with aspect ratio and pore size distributions as in Figure 15, and a Young's modulus of $6.8(10^5)$ bars. The lower points represent the average permeability loss for the same network with Young's modulus equal to $4.8(10^5)$ bars. The network with the lower Young's modulus is distinctly more sensitive to the increase in confining pressure. The difference between the measured values for the two averages increses as the confining pressure increases. Thus, even for a network with predominantly stiff shapes such as this, the magnitude of Young's modulus distinctly affects the permeability loss through its effect on the pore response to confining pressure.

POROSITY AND HYDRAULIC RADIUS

Table 2 contains typical values of calculated porosity for the networks discussed above. For the same size network, the porosity of the triangular network is greatest and that of the hexagonal network is the least. The change of porosity with confining pressure is shown in Figure 17. For these networks in which most of the pore space is in relatively stiff circular or high aspect ratio pores, the porosity loss is very small, less than one percent of the total porosity.

Permeability calculated from the relation $k = \frac{1}{2} m \phi_{2D}^3$ was found to be consistently higher than that calculated from node pressures. For triangular and hexagonal networks, the permeability from the hydraulic radius approach was 30-40% larger than calculated from node pressures, for square networks the excess was about 50%. The hydraulic radius, and the permeability calculated from the hydraulic radius, were generally lower for networks with lower permeabilities. However, in comparing two networks, it was found that the higher network permeability could belong to the network with the lower hydraulic radius permeability.

That there is only a general relation between the actual permeability and that calculated from the hydraulic radius is not unexpected. First, Darcian flow is being modeled, which means that the flow is laminar. As noted by Dullien (1979) and Bird et al. (1960), the hydraulic radius concept is known to be a good approximation to reality only for turbulent flow. To adapt the approach to the laminar flow regime correction factors, including tortuosity, are required. Second, the hydraulic radius approach is fundamentally a one-dimensional approach to fluid flow. As noted by Dengler (1978) and Dullien (1979), the consideration of flow in two and three dimensions changes the corrections required for the hydraulic radius approach, and can invalidate it altogether. In this light, it should be remembered that both the actual permeability and that calculated from the hydraulic radius approach were based upon two-dimensional flow. The addition of a third degree of freedom could change the magnitude of the permeability somewhat, but it is guaranteed to greatly affect the permeability given by the hydraulic radius approach due to the presence of additional pores.

PORE PRESSURE AND FLOW PATHS

Additional insights into network behavior are gained by studying the pore pressure at each node and the fluid flow through each element. If all of the elements were identical, the pore pressure would be constant along each row of nodes and there would be a linear pressure decrease along each column of nodes. With a wide range of element values, this situation is not found. A schematic diagram of node pressures is shown in Figure 18 for a square network of tapered cracks with 30% of the elements circular, 30% with an aspect ratio of 10^{-1}, 20% at 10^{-2}, 15% at 10^{-3}, and 5% at 10^{-4}. Note that there are large areas where the measured pore pressure is more than 10% above or below the pressures predicted from the uniform case. The actual pore pressure distribution is far from uniform. The histogram at the bottom of Figure 18 shows that the range of pressure deviations, defined by

$$\Delta P = P - P_{unif}$$

where P is the measure pore pressure and P_{unif} is the pore pressure for a uniform case, is rather large. The peak of the histogram is centered at a pressure less than zero, indicating that most of the pore volume is at a pore pressure lower than would be expected for the uniform case.

The flow through each tube can be calculated knowing its dimensions and the pressure difference across it. A plot of the flow paths for all tubes through which more than 0.1% of the total flow passes is presented in Figure 19. Most of the flow follows just a few paths. At one level in the middle of the network, 66% of the total flow passes through just one tube. At the inlet end, the greatest concentration of flow in one tube is 36% of the total, while at the outlet end it is 27%. The flow converges and diverges throughout the network. A comparison of the flow paths with tube size reveals that almost 100% of the tubes with greater than 0.1% of the total flow have aspect ratios of 10^0 or 10^{-1}. The flow thus follows the path of least resistance, converging where few tubes at a level are large and diverging when many tubes are large. Note also that there are instances in which the direction of flow is apparently reversed where the flow path skirts high resistance elements.

The network model of flow is considerably different than that predicted by hydraulic radius or bundle of capillary tube models. The magnitude of this difference is indicated by the fact that the flow through this network could be modeled as flow through the network volume in just 18 long capillary tubes with an aspect ratio of 10^{-1} and semimajor axis of 10 µm (as used here). The hydraulic radius and porosity for 18 capillary tubes is less than that for the network as a whole. This example serves as a further demonstration that hydraulic radius and bundle of capillary tube models of fluid flow are not realistic models of flow in more than one dimension.

BULK MODULUS

The bulk modulus calculations are not dependent upon the network topology. As the aspect ratio and length distributions were the same for each of the test cases considered in the permeability section, very little difference in bulk modulus was calculated for each network type. For calculating the effective dry and saturated bulk moduli, the intrinsic bulk modulus was taken to be $4.5(10^5)$ bars ($E = 6.8(10^5)$ bars), ν=0.25, and K_f, the bulk modulus of water, was $2.2(10^4)$ bars. For equal aspect ratio and pore size distribu- tions a triangular network has the lowest effective bulk modulus while a hexagonal matrix has the largest effective bulk modulus. This is a result of the different number of cracks in the systems.

The elastic responses of tapered and elliptic pores are different. Thus, while their permeability behavior as a function of confining pressure is very similar, their effective modulus properties may be different. Table 3 gives the effective dry and saturated bulk moduli for networks with 30% of the pores having an aspect ratio of 10^0, 30% with 10^{-1}, 35% with 10^{-2}, 5% with 10^{-3}, and 35% of the semimajor axes being 10 μm, 30% 18 m, and 35% 28 μm.

Examples of effective bulk moduli as functions of confining pressure for a square network of elliptic and of tapered cracks are shown in Figure 20. For this particular aspect ratio distribution neither the change of effective modulus with confining pressure nor the difference between the tapered and elliptic crack effective modulus is great. This result is due to the fact that most of the pore space is composed of relatively stiff crack shapes. The response of most rocks would require more thin cracks (aspect ratios of 10^{-3}, 10^{-4}, and lower) than are present in this model.

RESPONSE OF SAMPLE ASPECT RATIO DISTRIBUTIONS

In this section the permeability and effective bulk moduli will be examined for the following aspect ratio distributions: 1) all cracks of equal aspect ratio, 2) a uniform distribution of aspect ratios, 3) an aspect ratio distribution with only nearly round pores, and 4) a distribution with only very thin cracks. The purpose of this exercise is to show the range of network responses so that rough predictions of pore aspect ratio distribution can be made as first attempts to fit experimental data. Unless otherwise specified, the results presented will be for tapered cracks with $E = 6.8(10^5)$ bars, $K = 4.5(10^5)$ bars, $\nu = 0.25$, $\mu = .01$ poise, $K_f = 2.2(10^4)$ bars, and $d = 120$ μm.

SINGLE ASPECT RATIO

The case of all of the tubes having the same aspect ratio is rather simple. Due to the equality of the permeabilities in each tube, there will be no flow in the network in the direction perpendicular to the overall pressure gradient. Flow will occur only in the tubes parallel to the direction of flow and the pressure drop will be uniform across the network. The permeability of the network will decrease with increasing confining pressure in exactly the same way that flow through a single element of the same aspect ratio would decrease.

The bulk modulus would increase linearly with increasing confining pressure until the cracks were closed in the case of tapered cracks. For elliptic cracks the effective bulk modulus would be constant at all confining pressures less than that required to close the cracks. At the critical confining pressure there would be a step increase in the bulk modulus from the effective, open crack, modulus to the intrinsic modulus.

UNIFORM ASPECT RATIO DISTRIBUTION

The case of a uniform aspect ratio distribution (20% of the pores having each of the aspect ratios 10^0, 10^{-1}, 10^{-2}, 10^{-3}, and 10^{-4}) is one which could possibly represent a rock with pore space somewhere between that of a sandstone with equidimensional pores and a granite with thin, deformable pores. However, the case better illustrates one of the numerical problems presented by the range of length scales needed for an accurate model. In an earlier section it was shown that the flow through an elliptic section is proportional to b^3c where b and c are the semiminor and semimajor axes of the ellipse, respectively. Using the definition of the aspect ratio, $\alpha = b/c$, the quantity b^3c can be rewritten as α^3c^4. Thus, if c is constant and α ranges from 10^0 to 10^{-4}, there is a range of element permeabilities of 10^{12}. If only a small percentage of elements at either extreme are present in the system, there is a very small probability that there will be numerical problems. However, with a large percentage of very small cracks it becomes very probable that the range in magnitudes of the diagonal entries in the $\underline{\underline{A}}\ \underline{\underline{K}}\ \underline{\underline{A}}^T$ matrix will reach 10^{12}, and numerical instabilities in the solution of the system of linear equations result. These numerical problems in dealing with large element contrasts are one factor which motivated Madden (1976) to develop the embedded network approach. As a result of the numerical problems, no successful computations of randomly created networks with a uniform aspect ratio distribution were obtained.

HIGH ASPECT RATIOS

Tests were run on cases in which 50% of the conduits were circular and 50% had aspect ratios of 10^{-1}. The results are shown in Table 4 and Figures 21 and 22. As expected, the network permeabilities were high. The pore shapes studied are stiff, thus, the small change in effective modulus and the small decrease in permeability with increasing confining pressure are expected. The triangular network was significantly more permeable than either the square or hexagonal networks. Also, the triangular network had the smallest decrease of permeability with confining pressure. This is, again, due to the network topology (increased number of connections at each node and a higher probability of having paths which bypass less permeable elements).

LOW ASPECT RATIOS

Results of tests run with 50% of the pores having an aspect ratio of 10^{-2} and 50% with an aspect ratio of 10^{-3} are shown in Table 5, and sample data are plotted in Figures 23 and 24 for square networks. As expected, the permeabilities are low, smaller by a factor of about 10^{6} than the calculated permeabilities for high aspect ratio conduits. Figure 23 shows the permeability as a function of confining pressure for square networks of both tapered and elliptic section. The bulk modulus data in Figure 24 shows that the initial elastic response of the elliptic cracks is stiffer than that of the tapered cracks, but, as noted in the discussion of single elements, conduits of tapered section close at a higher confining pressure, and thus are open to flow to higher pressures. This conclusion is illustrated in Figure 23.

SUMMARY OF SAMPLE CALCULATIONS

These sample calculations have illustrated the application of network theory to permeability problems and the sensitivity of the approach to the length and shape parameters. it was generally found that for randomly constructed networks, permeability increased with increasing porosity and that small, thin cracks make a small contribution to the total flow when there is a population of larger tubes which form a continuous flow path across the network. The degree of pressure dependence is affected by the proportion of thin cracks in the network. To increase the pressure dependence of permeability, Young's modulus could be decreased or the porosity residing in stiff pores could be decreased. One way by which the porosity residing in stiff pores can be decreased is to change the aspect ratio distribution. It is also possible to do this by changing the individual pore sizes using a different scaling system, as mentioned earlier. Figure 25 shows a sample permeability calculation for a network in which the initial flows were equal for every element. This scaling has the effect of making the thin crack porosity relatively large, i.e., the circular tubes have relatively small cross-sections. This particular scaling may be appropriate for materials like clays or shales. However, if the size of the tubes and contribution of each aspect ratio to the total porosity is fixed, the only way to increase the pressure dependence of the network permeability is to decrease Young's modulus.

The sample network calculations demonstrated that the hexagonal network is relatively sensitive to element location and network topology. Hexagonal networks had the lowest permeability, the greatest relative loss of permeability with increasing confining pressure, the lowest porosity, the highest effective bulk modulus, and the smallest change in effective bulk modulus with pressure. All of these factors are due to the small number of tubes and low coordination number for the hexagonal network. As a result, the hexagonal network is not a good network configuration for modeling most rocks, particularly moderate to high porosity rocks. The square network is better than the hexagonal network for modeling rock pore space due to its increased number of pores and higher coordination number. The square network may be suitable for modeling low to moderate porosity rocks, where the required coordination number is not too high. The best two dimensional network for modeling rock pore space is the triangular network with its relatively large number of elements and its high coordination number. For moderate to high porosity rocks with highly connected flow paths, the triangular network is the only one of the three network types discussed here that should be used. In three dimensional networks, Dullien (1979) has had success using very simple cubic networks to study moderate to high porosity sandstones. Thus, in three dimensions it appears that cubic or tetragonal systems may be adequate.

COMPARISON WITH LABORATORY DATA

Nur (1979) presented a comparison of laboratory permeability, resistivity, and velocity measurements. He compiled the data presented here in Figure 26 in which the inverse of permeability is plotted against velocity. The velocity increases are due solely to increased confining pressure, so that these figures represent some indication of the relative sensitivity of permeability and velocity to pressure. For sandstones (St. Peter, Berea, and Massilon) confining pressure influences velocity much more than permeability. In Westerly granite, there is a large effect observed for both permeability and velocity. The explanation offered by Nur (1979) to explain this behavior is that the permeability changes might be controlled by the stiffest part of the pore space, while velocity changes are controlled by the more easily deformed parts of the pore space. In sandstones the stiffest parts of the pore space are the round pores which have little effect on the change of velocity with confining pressure. In contrast, the easily deformed cracks which control the change of velocity with pressure might not be expected to affect the permeability. On the other hand, there are not many round pores in granite so that both permeability and velocity are controlled by thin cracks, and the pore pressure effect on permeability and velocity is greater.

In this section the explanation given above for permeability and velocity data will be tested using the network theory approach. The rocks to be considered are Berea sandstone and Westerly granite. The aspect ratio spectra used are modified from the work of Cheng and Toksoz (1979), who obtained aspect ratio spectra for ellipsoidal inclusions from the inversion of laboratory seismic velocity experiments. (In using this data, the assumption is made that the dynamic and static moduli behave similarly. Cheng and Toksoz (1979) also made this assumption.) Cheng and Toksoz (1979) also determined the intrinsic moduli from the inversion. The pore sizes for Berea sandstone were derived from a table of pore sizes given in Dullien (1979, p. 182). These values were determined from detailed porosimetry and microscopic measurements. The pore sizes for Westerly granite were derived from a table of crack dimensions compiled by Hadley (1976) from scanning electron microscope data.

Typical laboratory measurements of velocity and permeability as functions of confining pressure for Berea sandstone samples are shown in Figure 27. As noted by Walls (1980) and Jones (1979), the responses vary for different Berea sandstone samples.

Table 6 contains a list of input parameters for the Berea sample modeled here. The results of the calculation of bulk modulus and permeability for a triangular network are shown in Figures 28 and 29. Points for both saturated and dry elliptic and tapered cracks are presented in Figure 28. The overall change in dry and saturated bulk modulus with increasing confining pressure approximates, but is somewhat smaller than, that predicted to produce the compressional velocity increase in the data modeled by Cheng and Toksoz (1979). The initial and final dry and saturated moduli of elliptic and tapered systems are close in magnitude, but the tapered crack network shows a steady increase in modulus from 0 to 400 bars confining pressure, by which time the 10^{-3} aspect ratio cracks have closed, while the elliptic crack network modulus remains constant until the 10^{-3} aspect ratio cracks close.

The steep increase in bulk modulus usually seen at very low confining pressures is not present in the model calculations because no very thin cracks ($\alpha < 10^{-3}$) were included. The large step in the response of the elliptic crack model does not represent real rock response. This jump is a result of the use of only a few discrete aspect ratios rather than a continuous distribution. The bulk modulus data points would lie on a much smoother curve if a continuous spectrum was available; however, the different response of the elliptic and tapered sections illustrate the dependence of the calculated bulk modulus on the crack shape considered.

The initial network permebility (k_0) for this model of Berea sandstone was 594 md. In Figure 29 the model results are plotted along with laboratory results for a Berea sample with k_0 = 382 md (laboratory data courtesy J. Walls). The permeability loss as a function of confining pressure in the model is very close to that actually measured. Considering the relatively good approximation of the magnitude of the permeabilities and the similar behavior as a function of confining pressure, the two dimensional network model appears to give an adequate representation of the permeability and bulk modulus properties of a Berea sandstone sample.

This model was run with the semimajor axes held constant. the flow through the network is primarily through tubes of aspect ratios of 10^0 or 10^{-1}. This follows from the pressure dependence of permeability, and it also follows from the fact that the percentage of pores with aspect ratios greater than 10^{-1} exceeds the critical probability for a triangular matrix (Madden, 1976). Based upon this model calculation, it follows that those pores which most affect the velocity, and low aspect ratio pores, have little effect on the permeability, and those pores which most affect the permeability, the high aspect ratio pores, contribute little to the bulk modulus and velocity increase with confining pressure, as predicted by Nur (1979).

The quantities used in modeling Westerly granite are listed in Table 7. Results of model calculations are shown in Figure 30. The data for bulk modulus are shown for dry and saturated cases for both tapered and elliptic sections. There is a very large increase in the dry moduli and a smaller increase in the saturated moduli. Again, no cracks with an aspect ratio less than 10^{-4} were modeled. Note the large increases in dry bulk moduli as the cracks with aspect ratio of 10^{-4}, fully 80% of the total number of cracks, close at less than 100 bars.

Permeability of the Westerly granite model decreases very rapidly with increasing confining pressure, the permeability becoming zero when the confining pressure reaches about 50 bars. The permeability loss behavior is very much like that for a single crack with an aspect ratio of 10^{-4}. With over 80% of the pores having an aspect ratio of 10^{-4}, it is not probable that a continuous flow path through larger pores will be present in a randomly constructed network. In a system such as this, where one aspect ratio predominates, the velocity and permeability are both affected by the same portion of the pore space. Rocks in which this should occur include granites and shales, that is, in any rock in which the majority of the pore space is composed of easily deformed pores.

Laboratory measurements of permeability in Westerly granite as a function of confining pressure range from 260 nd at a confining pressure of 100 bars to 4 nd at 4 kbars (Brace et al., 1968). These experimental values illustrate one of the limitations of the model development. The model permeability is zero at 50 bars, whereas measured values are nonzero to at least 4 kbars. The model limitations lie with the simple shapes chosen to model the pore space. Models using higher order tapered cracks, $y = b_0(1-(x/c_0)^2)^{m+1/2}$, where m is an integer greater than 2, could possibly give a better match to the Westerly granite data. Such cracks readily deform, as do tapered and elliptic cracks, but they do not completely close at confining pressures which would close a similar tapered or elliptic crack, and thus continue to contribute to permeability (G. Mavko, pers. comm.). Real pores are not smooth cracks of regular section, but are voids of irregular shape and surface. In such a system, parts of the pore space remain open at high pressures due to the increas- ing stiffness of the pores as the irregularities come into contact (Mavko and Nur, 1978; Walsh and Grosenbaugh, 1979). In using pore space models based upon tubes of smooth, regular section, one has to remember that he is using a mathematical tool to look at pore space effects rather than accurately modeling the shape and behavior of actual pores.

SUMMARY AND DISCUSSION

The examples given here show that a network model of pore space can reasonably predict the magnitude and behavior of rock permeability and bulk modulus as functions of confining pressure. The results indicate that for a rock in which much of the pore space consists of stiff, nearly round pores, such as in a sandstone of moderate to high porosity, the permeability response is controlled by the large round pores, while the modulus and velocity responses are determined by small thin pores and pore edges. In contrast, in rocks in which there are few round, stiff pores, such as granite, both the permeability and velocity are controlled by thin, crack-like pores.

Thus, it may be concluded that, in general, the greater the proportion of total porosity that resides in thin cracks, the lower will be the permeability and the greater will be the effect of stress on permeability. This conclusion is supported by laboratory evidence from low permeability (tight) gas sands. Jones and Owens

(1980) and McLatchie et al. (1958) concluded that very low permeability rocks are affected to a greater degree than those having higher levels of permeability. Jones and Owens (1980) also noted that permeability measurements suggest that "apertures controlling flow in tight gas sands may be slit-like rather than round."

Given that the network model reasonably represents the bulk modulus and permeability behavior as functions of confining pressure, what predictions can then be made from laboratory velocity, compressibility, and permeability measurements? From the examples presented here, it can be claimed that a rock sample which has a large increase in bulk modulus with confining pressure will also have a large decrease in permeability with increasing confining pressure. For relatively stiff rocks, the predicted decrease of permeability would be small. The converse should also hold, rocks with large permeability losses with increasing confining pressure should also have relatively large increases in bulk modulus and those with small permeability losses should have small increases in bulk modulus. However, as modulus or velocity data gives no information on the topology of pore space and as the permeability gives virtually no information about the present of thin, easily deformed cracks, there is no direct method available to predict the magnitude of either the modulus or permeability from information about the other.

In the opening of this paper the question of what constitutes an adequate pore space model was asked. The network model presented here is two-dimensional, consists of pores of idealized shape and behavior emplaced in regular, unrealistic connected networks, with only a limited range of length scales represented, and predicts the appropriate behavior of only two quantities. The model presented here is thus neither a complete nor an accurate representation of a porous rock. Considering the complexities, it is probably not possible to develop a completely accurate pore space model. However, the network approach used here does appear to provide the means for constructing an adequate pore space model, one from which many facets of rock behavior can be predicted. In this respect, the network theory approach, particularly in conjunction with the embedded network, or renormalization group, approach of Madden (1976), provides a promising avenue to a better understanding of the role of pore space in physical processes and, from this, the ability to predict a wide range of rock and rock-fluid properties.

This study has been specifically concerned with steady-state flow of an incompressible fluid through a porous medium whose flow paths are represented by a simple two-dimensional network of tubes. There are several further lines of study which are immediately apparent. First, an extension of the approach to three dimensions could be performed. The general form of the mathematics required is the same as for a two-dimensional network, however, the size and complexity of the $\underline{\underline{A}}\,\underline{\underline{K}}\,\underline{\underline{A}}^T$ matrix becomes great for even relatively small 3-D networks. Three dimensional networks should prove more accurate in modeling the flow properties of rocks, and it should prove possible to study anisotropic elastic and flow properties by specifying crack orientations. In this way, rocks, which are generally anisotropic to some degree, could be more fully studied.

Time dependent processes could be studied using a network theory approach. Time-dependent processes in networks are often studied in electrical engineering using Fourier and Laplace transform techniques. One possible time-dependent process that could be studied is fluid-solid interaction due to pressure pulses in either the fluid or the solid. In such a problem the elastic properties of both solid and fluid would have to be considered along with the problem of compressible fluid flow. Another time-dependent process that could be studied is the passage of elastic waves, particularly compressional waves, through a saturated solid. It is possible that some of the elastic energy could be dissipated by inter- or intrapore flow, particularly in the case of partial gas saturation. Nur et al. (1980) present laboratory data which make it clear that solid-fluid interaction plays an important role in attenuation. A network approach to this problem may be of particular importance because, as seen in the case of flow through a network (Figure 18), the pore pressure is not likely to be uniform throughout the system. This nonuniformity would be caused by the variable elastic reponses of the different pore shapes to the stresses setup as the waves move through the solid. Several other processes such as capillarity, diffusivity, and even the chemistry of fluid-solid interactions in stresses systems could eventually be studied.

In conclusion, future efforts in pore space modeling must be increasingly concerned with the interrelation of physical processes and the environment in which they occur. Many of the theoretical developments of elasticity, hydraulics, and electro-magnetism which should be applied to porous medium problems are still too primitive to be completely successful. However, there is active research proceeding on this problem in geophysics, chemical and petroleum engineering, materials science, electrical engineering, mechanics, and geology. Approaches such as network theory and renormalization group theory will become increasingly used as problems involving many elements and length scales are addressed. Advanced mathematical and statistical techniques and an interdisciplinary approach will be the only way in which to develop a fully adequate pore space model for rocks.

REFERENCES

Archie, G.E., Introduction to petrophysics of reservoir rocks, Bull. Amer. Assoc. Petrol. Geol., 34, 943-961, 1950.

Azzam, M.I.S. and F.A.L. Dullien, Calculation of the permeability of porous media from the Navier-Strokes equation, Ind. and Eng. Chem. Fundam., 15, 281-285, 1976.

Berg, C.A., Deformation of fine cracks under high pressure and shear, J. Geophys. Res., 70, 3447, 1965.

Bird, R.B., W.E. Stewart, and E.N. Lightfoot, Transport Phenomena, John Wiley and Sons, Inc., 780 p., 1960.

Brace, W.F., Permeability from resistivity and pore shape, J. Geophys. Res., 82, 3343-3349, 1977.

Brace W.F., J.B. Walsh, and W.T. Frangos, Permeability of granite under high pressure, J. Geophys. Res., 73, 2225-2236, 1968

Bruner, W.M., Comments on 'Seismic velocities in dry and saturated cracked solids' by Richard J. O'Connell and Bernard Budiansky, J. Geophys. Res., 81, 2573-2576, 1976.

Cheng, C.H., and M.N. Toksoz, Inversion of seismic velocities for the pore aspect ration spectrum of rock, J. Geophys. Res., 84, 7533-7543, 1979.

Dahlquist, G. and A. Bjorck, Numerical Methods, Prentice-Hall, Inc., Englewood Cliff, N.J., 574 p.

Dengler, L., Pore structure and permeability in a graywacke sandstone, Stanford Rock Physics Progress Report, 5, 219-237, 1978.

Dullien, F.A.L., New network permeability model of porous media AICHE J., 21, 299-307, 1975.

Dullien, F.A.L., Porous Media, Academic Press, Inc., New York, N.Y., 369 p., 1979.

Eshelby, J.D., The determination of the elastic field of an ellipsoidal inclusion, and related problems, Proc. Roy. Soc. London, Ser. A, 241, 376-396, 1957.

Fatt, I., The network model of porous media I. Capillary pressure characteristics, Trans. AIME, 207, 144-159, 1956.

Fatt, I., The network model of porous media II. Dynamic properties of a single size tube network, Trans. AIME, 207, 160-163, 1956.

Fatt, I., The network model of porous media III. Dynamic properties of networks with tube radius distribution, Trans. AIME, 207, 164-176, 1956.

Gangi, A. F., Variation of whole and fractured porous rock permeability with confining pressure, Int. J. Rock Mech. Min. Sci. Geomech. Abs., 15, 249-257, 1978.

Gassmann, G., Uber die elastizitat poroser Medien, Vierteljahressch. Naturforsch. Ges. Zuerich, 96, 1-21, 1951.

Greenberg, R. J. and W.F. Brace, Archie's law for rocks modeled by simple networks, J. Geophys. Res., 74, 2099-2102, 1969.

Hadley, K., Comparison of calculated and observed crack densities and seismic velocities in Westerly granite, J. Geophys. Res., 81, 3484-3494, 1976.

Jones, F. O. and W.W. Owens, A laboratory study of low permeability gas sands, J. Pet. Tech., 1631-1640, 1980.

Jones, T.D., Some compressional and shear velocities in Berea, Massilon, and St. Peter sandstone, *Stanford Rock Physics Progress Report, 5*, 165-183, 1978.

Korringa, J., R.J.S. Brown, D.D. Thompson, and R.J. Runge, Self-consistent imbedding and the ellipsoidal model for porous rocks, *J. Geophys. Res., 84*, 5591-5598, 1979.

Lamb, H., *Hydrodynamics*, Cambridge University Press, 738 p., 1932.

Madden, T.R., Random networks and mixing laws, *Geophysics*, 41, 1104-1125, 1976.

Mavko, G.M. and A. Nur, The effect of nonelliptical cracks on the compressibility of rocks, *J. Geophys. Res., 83*, 4459-4468, 197

McLatchie, A.S., R.A. Hemstock, and J.W. Young, The effective compressibility of reservoir rock and its effects on permeability, *J. Pet. Tech.*, 49-51, 1958.

Nelson, R.A. and J. Handin, Experimental study of fracture permeability in porous rock, *AAPG Bull., 61*, 227-236, 1977.

Noble, B. *Applied Linear Algebra*, Prentice-Hall, Englewood Cliffs, N.J., 477 p., 1969.

Nur, A., Pore space models and the effects of pressure on the relation between physical properties, *Stanford Rock Physics Progress Report, 7*, 125-141, 1979.

Nur, A. and G. Simmons, The effect of saturation on velocity n low porosity rocks, *Earth Planet. Sci. Lett., 7*, 183-193, 1969.

Nur, A.M., J.D. Walls, K. Winkler, and J. DeVilbiss, Effects of fluid saturation on waves in porous rock and relations to hydraulic permeability, SPEJ, 20, 450-458, 1980.

O'Connell, R.J. and B. Budiansky, Seismic velocities in dry and saturated cracked solids, J. Geophys. Res., 79, 5412-5426, 1974.

Peikari, B. Fundamentals of Network Analysis and Synthesis, Prentice-Hall, Englewood Cliff, N.J., 500 p., 1974.

Rink, M. and J.R. Schopper, Computations of network models of porous media, Geophys. Prospect., 16, 277-294, 1968.

Shankland, T.J. and H.S. Waff, Conductivity in fluid-bearing rocks, J. Geophys. Res., 79, 4863-4868, 1974.

Snow, D.T., Rock fracture spacings, openings and porosities, J. Soil Mech. Foundations Div., ASCE, 94, (SM1) 73-91, 1968.

Walls, J.D., Permeability measurements on some selected sandstone samples, Stanford Rock Physics Progress Report, 7, 57-94, 1979.

Walsh, J.B., The effect of cracks on the compressibility of rock, J. Geophys. Res., 70, 381-389, 1965.

Walsh, J.B. and M.A. Grosenbaugh, A new model for analyzing the effect of fractures on compressibility, J. Geophys. Res., 84, 3532-3536, 1979.

Watt, J.P., G.F. Davis, and R. J. O'Connell, The elastic properties of composite materials, Rev. Geophys. Sp. Phys., 14, 541-563, 1976.

Winkler, K. and A. Nur, Pore fluids and seismic attenuation in rocks, Geophys. Res. Lett., 6, 1-4, 1979.

Witherspoon, P.A., J.S.Y. Wong, K. Iwai, and J.E. Gale, Validity of cubic law for fluid flow in a deformable rock fracture, Technical Information Report No. 23, Swedish-American Cooperative Program in Radioactive Waste Storage in Mined Caverns in Crystalline Rock, Lawrence Berkeley Laboratory, 28 p., 1979.

Wyllie, M.R.J. and A.R. Gregory, Fluid flow through unconsolidated porous aggregates Ind. Eng. Chem., 47, 1379-1388, 1955.

Wyllie, M.R.J., A.R. Gregory, and G.H.F. Gardner, An experimental investigation of factors affecting elastic wave velocities in porous media, Geophysics, 23, 459, 1958.

Wyllie, M.R.J. and M.B. Spangler, Application of electrical resistivity measurements to the problem of fluid flow in porous media, Amer. Assoc. Petrol. Geol. Bull., 36, 359-403, 1952.

TABLE 1. Permeability variation for one aspect ratio distribution

NETWORK	SIZE	NO. ELEMENTS	NO. MEASUREMENTS	AVG. PERM	STANDARD DEVIATION	MINIMUM	MAXIMUM
TRINET	20x25	1451	8	2.17 d	0.56 d	1.12 d	3.47 d
SQNET	20x25	995	8	74.5 md	17.4 md	37.6 md	114.5 md
HEXNET	19x25	719	9	6.60 md	1.34 md	3.24 md	13.4 md

aspect ratio	% of total	semimajor axis	% of total
10^{0}	30	10 µm	35
10^{-1}	30	18 µm	30
10^{-2}	35	28 µm	35
10^{-3}	5		
10^{-4}	0		

element length = 120 µm

viscosity of fluid = 0.01 poise

flow rate = $1 cm^3$/sec

TABLE 2. Network porosity

NETWORK	NO. ELEMENTS	POROSITY
TRINET	1451	12.5
SQNET	995	8.8
HEXNET	719	6.2

aspect ratio	% of total	semimajor axis	% of total
10^{0}	30	10 μm	35
10^{-1}	30	18 μm	30
10^{-2}	35	28 μm	35
10^{-3}	5		
10^{-4}	0		

element length = 120 μm

<u>TABLE 3</u>. Effective bulk moduli for sample networks at 0 and 800 bars confining pressure.

NETWORK	NO. ELEMENTS	TYPE OF ELEMENTS	P_c(bars)	K'(10^5 bars)	K_s(10^5 bars)
TRINET	1451	Elliptic	0	3.26	3.37
		Elliptic	800	3.31	3.40
		Tapered	0	3.26	3.37
		Tapered	800	3.36	3.45
SQNET	995	Elliptic	0	3.67	3.75
		Elliptic	800	3.71	3.78
		Tapered	0	3.67	3.76
		Tapered	800	3.74	3.81
HEXNET	719	Elliptic	0	3.99	4.05
		Elliptic	800	4.01	4.06
		Tapered	0	3.99	4.05
		Tapered	800	4.04	4.09

aspect ratio	% of total	semimajor axis	% of total
10^0	30	10 μm	35
10^{-1}	30	18 μm	30
10^{-2}	35	28 μm	35
10^{-3}	5		
10^{-4}	0		

element length = 120 μm

Young's modulus = $6.8(10^5)$ bars

K = $4.53(10^5)$ bars

TABLE 4. Network calculations for systems with high aspect ratio pores. The results are for networks of tubes of tapered action.

NETWORK	NO. ELEMENTS	P_c(bars)	POROSITY(%)	PERMEABILITY(d)	K'(10^5 bars)	K_s(10^5 bars)
TRINET	1451	0	23.9	858	3.30	3.37
		800	23.7	850	3.31	3.37
SQNET	995	0	14.0	6.51	3.71	3.77
		800	14.0	6.21	3.72	3.77
HEXNET	719	0	8.2	1.66	4.02	4.05
		800	8.1	1.55	4.02	4.06

aspect ratio	% of total	semimajor axis	% of total
10^0	50	10 μm	35
10^{-1}	50	18 μm	30
		28 μm	35

element length = 120 μm

viscosity of fluid = 0.01 poise

flow rate = $1 cm^3$/sec

K = $4.53(10^5)$ bars

TABLE 5. Network calculations for systems with low aspect ratio pores. The results are for networks of tubes of tapered action.

NETWORK	NO. ELEMENTS	P_c(bars)	POROSITY(%)	PERMEABILITY(d)	K'(10^5 bars)	K_s(10^5 bars)
TRINET	1451	0	.18	9 md	3.30	4.39
		800	.12	0	3.92	4.44
SQNET	995	0	.11	10.4 nd	3.71	4.45
		800	.07	0	4.15	4.48
HEXNET	719	0	.08	2.33 nd	4.02	4.48
		800	.06	0	4.30	4.50

aspect ratio	% of total	semimajor axis	% of total
10^{-2}	50	10 µm	35
10^{-3}	50	18 µm	30
		28 µm	35

element length = 120 µm

viscosity of fluid = 0.01 poise

flow rate = $1 cm^3$/sec

K = $4.53(10^5)$ bars

TABLE 6. Berea sandstone model.

NETWORK	NO. ELEMENTS	P_c(bars)	POROSITY(%)	PERMEABILITY(d)	K'(10^5 bars)	K_s(10^5 bars)
TRINET	1451	0	15.6	594 md	2.21	2.33
		800	15.4	534 md	2.47	2.54

aspect ratio	% of total	% porosity	semimajor axis	% of total
10^0	22	85.8	10 μm	35
10^{-1}	35	13.5	18 μm	30
10^{-2}	8	0.2	28 μm	35
10^{-3}	35	0.4		

element length = 110 μm
viscosity of fluid = 0.01 poise
flow rate = $1 cm^3/sec$
K = $3.20(10^5)$ bars

Network calculations for a triangular network of tapered cracks which models Berea sandstone. Aspect ratio distribution modified from distribution found by Cheng and Toksoz (1979), for a Berea sample with 16.3% porosity.

TABLE 7. Westerly granite model.

NETWORK	NO. ELEMENTS	P_c(bars)	POROSITY(%)	PERMEABILITY(d)	K'(10^5 bars)	K_s(10^5 bars)
TRINET	1451	0	0.51	0.78 md	2.46	5.09
		800	0.44	0	5.15	5.38

aspect ratio	% of total	% porosity	semimajor axis	% of total
10^{0}	.3	76.7	1 μm	45
10^{-1}	0	0	5 μm	25
10^{-2}	6.5	17.8	10 μm	30
10^{-3}	12.1	3.3		
10^{-4}	81.1	2.2		

element length = 21 μm
viscosity of fluid = 0.01 poise
flow rate = $1 cm^3$/sec
K = $5.9(10^5)$ bars

Network calculations for a triangular network of tapered cracks which models Westerly granite. Aspect ratio distribution modified from distribution found by Cheng and Toksoz (1979), for a Westerly sample with 0.9% porosity.

Figure Captions

Figure 1 Relation between porosity and permeability in two reservoir rocks; at left the Eocene Upper Wilcox sandstone; at the right the Upper Cretaceous Nacatoch sandstone. For each rock there is a general increase in permeability with an increase in porosity, however, at the same permeability the porosity of the Nacatoch sandstone is 10-15% greater than that of the Wilcox. (from Archie, 1950).

Figure 2 Typical laboratory experimental data for velocity (upper) (Jones, 1978) and permeability (lower) (Nur et al., 1980) as functions of confining pressure.

Figure 3 Example of a small square network with 10 nodes and 18 elements. Four elements are incident at each interior node. V = 0 at node 10. Below is the $\underline{\underline{A}}\,\underline{\underline{K}}\,\underline{\underline{A}}^T$ matrix product for this network. K_{ii} is the positive sum of the elements incident to the ith node (sum of the off diagonal entries in a row or column); i.e. $K_{77}=K_{37}+K_{67}+K_{78}+K_{710}$. Note that the matrix is symmetric and sparse. The matrix retains this general form for all square networks.

Figure 4 Network configurations to be considered. a) square, b) triangular c) hexagonal.

Figure 5	Comparison of elliptical and nonelliptical sections. One quadrant is shown, the axes are normalized half length and half width. Note that the nonelliptical curve is lower than the elliptical curve for all x.
Figure 6	Volume flow rate as a function of applied hydrostatic stress for an elliptic crack. The horizontal axis is applied hydrostatic stress in bars. The vertical axis is normalized flow rate, $Q_e(p)/Q_{oe}$.
Figure 7	Comparison of nonelliptical and equivalent elliptic shapes. One quadrant is shown. The axes are normalized half length and half width. These two curves have the same area. Note that the difference in shape is mainly confined to the region in which $y < b/4$.
Figure 8	Volume flow rate as a function of applied hydrostatic stress for a nonelliptic crack. The horizontal axis is applied hydrostatic stress in bars. The vertical axis is normalized flow rate, $Q_t(p)/Q_{ot}$.
Figure 9	Volume flow rate as a function of applied hydrostatic stress for elliptic cracks with aspect ratios of 10^{-2}, 10^{-3}, and 10^{-4}. The horizontal axis is applied hydrostatic stress in bars. The vertical axis is normalized flow rate for each particular case, $Q_e(p,\alpha)/Q_{oe}(\alpha)$.

Figure 10 Volume flow rate as a function of applied hydrostatic stress for nonelliptic cracks with aspect ratios of 10^{-2}, 10^{-3}, and 10^{-4}. The horizontal axis is applied hydrostatic stress in bars. The vertical axis is normalized flow rate, $Q_t(p,\alpha)/Q_{oe}(\alpha)$.

Figure 11 Volume flow rate as a function of applied hydrostatic stress for elliptic and nonelliptic fractures with equal half length and half width. The horizontal axis is applied hydrostatic stress in bars. The vertical axis is the flow rate relative to the flow through an unstressed elliptic fracture, the curves are $Q_e(p)/Q_{oe}$ and $Q_t(p)/Q_{oe}$. Note that flow through tapered cracks is less than that through elliptic cracks for stresses below about 230 bars, and it is greater above 230 bars.

Figure 12 Volume flow rate as a function of applied hydrostatic stress for elliptic and nonelliptic fractures of equal aspect ratio and cross sectional area. The horizontal axis is applied hydrostatic stress in bars. The vertical axis is flow rate relative to the flow through an unstressed elliptic section, the curves are $Q_e(p)/Q_{oe}$. Note that $Q_t(p)$ is larger than $Q_e(p)$ for all p.

Figure 13	Volume flow rate as a function of applied hydrostatic stress for elliptic and noneliptic fractures of equal aspect ratio and equal initial flow rate. The horizontal axis is applied hydrostatic stress in bars. The vertical axis is the flow rate relative to the flow through an unstressed elliptic section, the curves are $Q_t(p)/Q_{oe}$ and $Q_e(p)/Q_{oe}$. The two curves are nearly identical.
Figure 14	Flow chart for computer operations
Figure 15	Relative permeability loss as a function of confining pressure for hexagonal, square and triangular networks of tapered cracks. 30% of the tubes were circular, 30% had an aspect ratio of 10^{-1}, 35% 10^{-2}, and 5% 10^{-3}. For the same size network, hexagonal networks had the greatest relative loss and the triangular network had the least permeability loss.
Figure 16	Relative permeability loss for triangular networks of tapered cracks with the same aspect ratio distribution as in figure 15. The difference is due to a change of Young's modulus. E is $6.8(10^5)$ bars for the upper points and $4.8(10^5)$ bars for the lower data points.
Figure 17	Porosity as a function of confining pressure for the networks studied in figure 15. The porosity loss is less than 0.1% for this particular distribution of mostly stiff tubes.

Figure 18 Node pressures in a network with 30% of the pores having an aspect ratio of 10^0, 30% 10^{-1}, 20% 10^{-2}, 15% 10^{-3} and 5% 10^{-4}. The pore pressure distribution is not uniform when there is fluid flow through the network. The histogram gives the number of nodes with a given deviation from the pore pressure predicted for the case of uniform flow through the network. The majority of node pressures are lower than predicted from the uniform model.

Figure 19 Map of flow paths through the network considered in figure 18. Tubes through which pass more than 0.1% of the total flow are shown. Direction of flow in each tube is shown with an arrow. The magnitude of the flow is given by line type and weight: light line - 0.1-1%, dashed light line - 1-10%, heavy line - 10-50%, heavy dashed line, > 50%. Flow converges, diverges, and even reverses direction throughout network. Almost all flow occurs in tubes of aspect ratios of 10^0 or 10^{-1}.

Figure 20 Variation of dry and saturated bulk moduli with confining pressure for the networks considered in figures 15 and 17. Results shown are for elliptic (upper) and tapered (lower) cracks. There is a step increase in the bulk modulus of the elliptic crack network at 400 bars as the 10^{-3} aspect ratio pores close. There is relatively little change in modulus for either case, due to the stiff pore shapes.

Figure 21 Permeability vs. confining pressure for networks of tapered cracks with 50% of the tubes having an aspect ratio of 10^0 and 50% with an aspect ratio of 10^{-1}. The permeability loss is relatively small.

Figure 22 Dry and saturated bulk moduli vs. confining pressure for networks of tapered cracks with the same aspect ratio as in figure 21. There is very little change of aspect ratio for round or nearly round pores at these low confining pressures.

Figure 23 Permeability vs. confining pressure for square networks of both tapered and elliptic cracks. 50% of the tubes had a aspect ratio of 10^{-2} and 50% had an aspect ratio of 10^{-3}. The permeability loss is great, flow through the network becomes 0 at 400 bars for the elliptic crack network and 600 bars for the tapered crack network.

Figure 24 Dry and saturated bulk moduli as functions of confining pressure for square networks of tapered (circles and squares) and elliptic (crosses and triangles) cracks. The aspect ratio distribution is as in Figure 23. There is a significant increase in dry bulk modulus, particularly at 400 bars for the elliptic crack network and below 600 bars for the tapered crack network, in both cases this is due to closing of the cracks of 10^{-3} aspect ratio.

Figure 25 Relative permeability loss as a function of confining pressure for a square network with the following aspect ratio distribution: 30% 10^0, 30% 10^{-1}, 20% 10^{-2}, 15% 10^{-3}, 5% 10^{-4}. The tubes had initially equal permeabilities. In this representation the low aspect ratio pores are relatively large. The decrease in the permeability is greater than for the case of equal semimajor axes as the easily deformable tubes initially carry much of the total flow.

Figure 26 Velocity in dry rock vs. the inverse of permeability at various confining pressures from Nur (1978). The increase of velocity and decrease of permeability is due to increased confining pressure. In sandstones, confining pressure affects velocity much more than permeability, while in granite there is a large pressure effect for both permeability and velocity.

Figure 27 Typical laboratory result for Berea sandstone. Velocity measurements from Jones (1978), permeability measurements courtesy J.D. Walls.

Figure 28 Dry and saturated bulk moduli for triangular networks of tapered (circles and squares) and elliptic (crosses and triangles) cracks of a Berea sandstone model. The input values are listed in Table 6. The aspect ratio distribution is adapted from that given by Cheng and

Toksoz (1979). The increase in bulk modulus is slightly below that appropriate for the laboratory data modeled by Cheng and Toksoz. This is due to the fact that no aspect ratios less than 10^{-4} were input into the model.

Figure 29 Model calculations and laboratory results for Berea sandstone (lab results from J.D. Walls.) K_0 for the laboratory sample is 382 md; K_0 from the model calculation is 594 md. The model calculations are for a triangular network of tapered cracks. The permeability declines of the model system closely approximates that of the real rock.

Figure 30 Westerly granite model calculations of permeability and bulk modulus as fractions of confining pressure for triangular networks. Note the change in confining pressure scale in the permeability curve. the bulk modulus data show large increases from 0 to 100 bars as the 10^{-4} aspect ratio pores, 81% of the total, close. Tapered crack data shown with circles and squares, elliptic crack data with crosses and triangles. The network permeability decrease is very much like that of a single conduit with an aspect ratio of 10^{-4}. The permeability is zero by 50 bars of confining pressure. Actual laboratory measurements of permeability in Westerly granite are nonzero a confining pressures of at least 4 kbars.

Figure A1 Comparison of permeability vs. confining pressure curves of Gangi (1978) and for elliptic cracks of aspect ratios of 10^{-3} and $10^{-2.5}$ with data for fracture permeability from Nelson and Handin (1977). The bed-of nails model and the elliptic conduit model are possible alternatives to the parallel plate model for fracture flow.

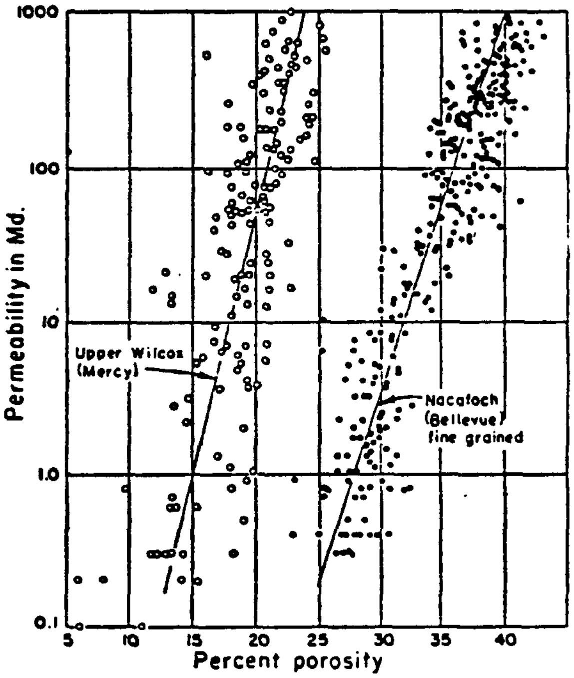
1000
100
10
1.0
0.1
Permeability in Md.
5
10
15
20
25
30
35
40
Percent porosity
Upper Wilcox (Mercy)
Nacatoch (Bellevue) fine grained

FIGURE 1

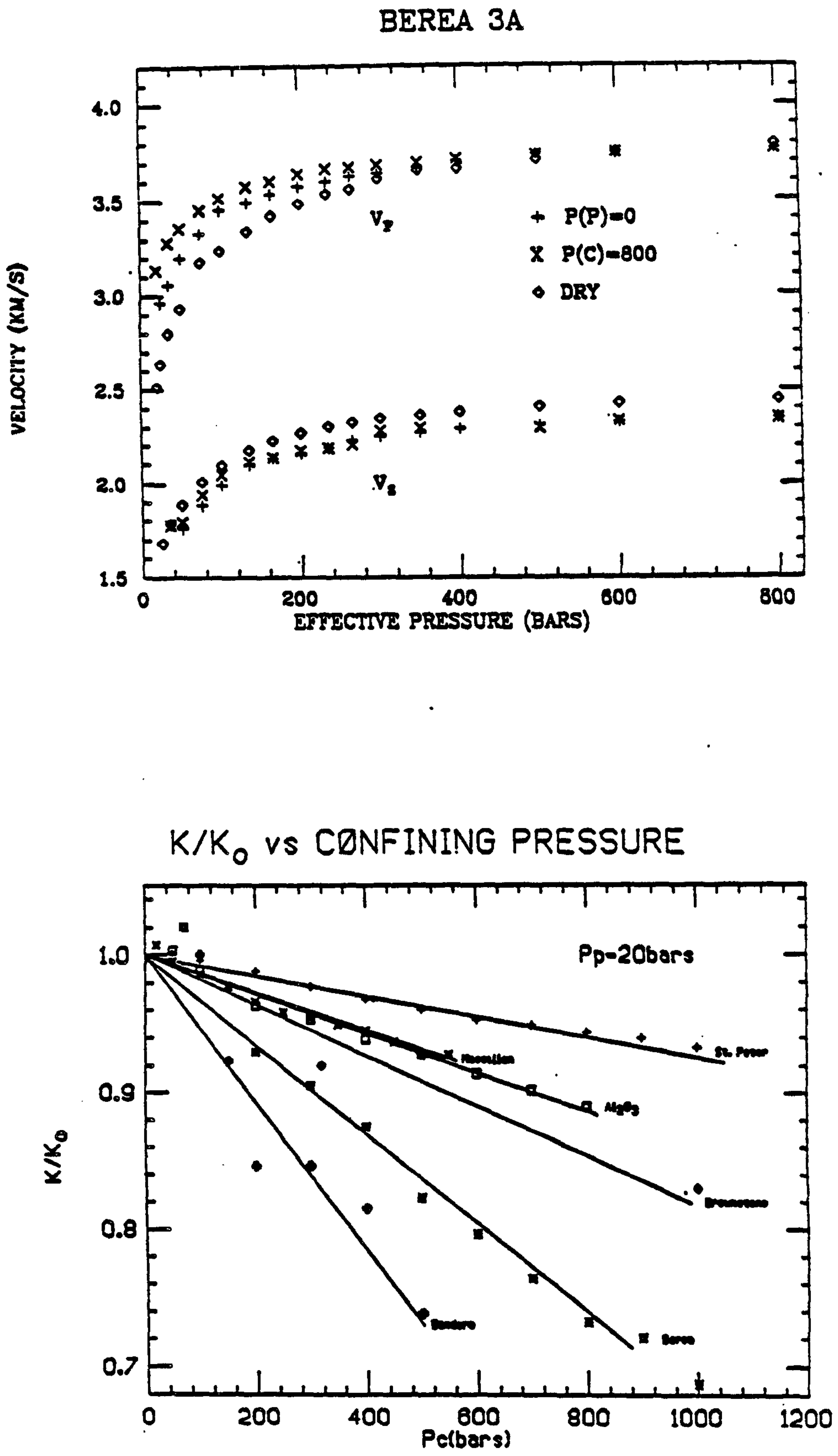
BEREA 3A
VELOCITY (KM/S)
4.0
3.5
3.0
2.5
2.0
1.5
0
200
400
600
800
EFFECTIVE PRESSURE (BARS)
V_P
V_S
+ P(P)=0
X P(C)=800
◇ DRY
K/K$_0$ vs CØNFINING PRESSURE
K/K$_0$
1.0
0.9
0.8
0.7
0
200
400
600
800
1000
1200
Pc(bars)
Pp=20bars
St. Peter
Massillon
Al_2O_3
Brownstone
Bandera
Berea

FIGURE 2

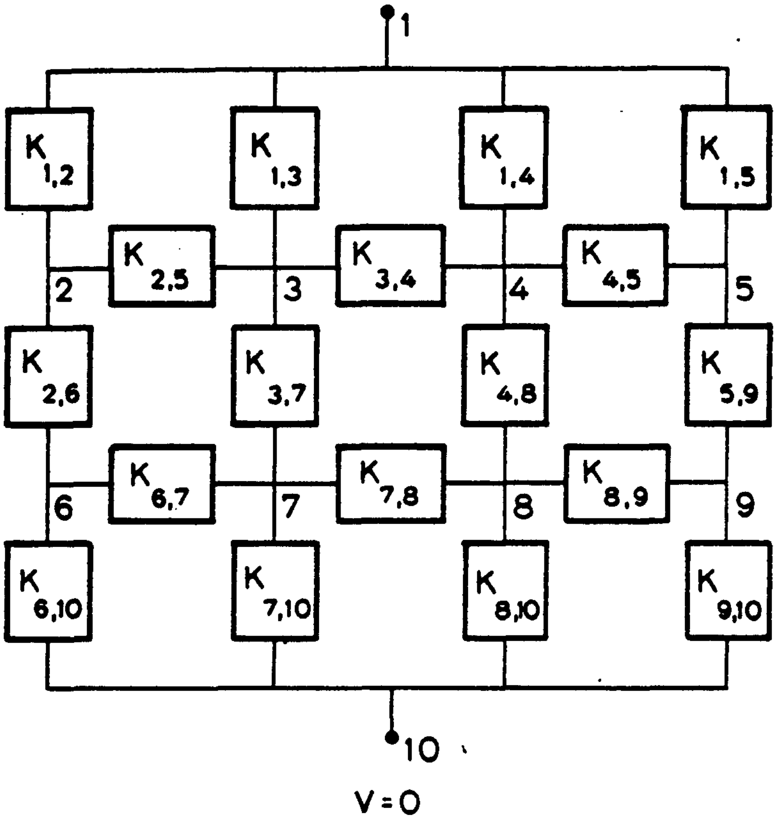

$$\underline{A}\,\underline{K}\,\underline{A}^{T} = \begin{bmatrix} K_{11} & -K_{12} & -K_{13} & -K_{14} & -K_{15} & 0 & 0 & 0 & 0 \\ -K_{12} & K_{22} & -K_{23} & 0 & 0 & -K_{26} & 0 & 0 & 0 \\ -K_{13} & -K_{23} & K_{33} & -K_{34} & 0 & 0 & -K_{37} & 0 & 0 \\ -K_{14} & 0 & -K_{34} & K_{44} & -K_{45} & 0 & 0 & -K_{48} & 0 \\ -K_{15} & 0 & 0 & -K_{45} & K_{55} & 0 & 0 & 0 & -K_{59} \\ 0 & -K_{26} & 0 & 0 & 0 & K_{66} & -K_{67} & 0 & 0 \\ 0 & 0 & -K_{37} & 0 & 0 & -K_{67} & K_{77} & -K_{78} & 0 \\ 0 & 0 & 0 & -K_{48} & 0 & 0 & -K_{78} & K_{88} & -K_{89} \\ 0 & 0 & 0 & 0 & -K_{59} & 0 & 0 & -K_{89} & K_{99} \end{bmatrix}$$

FIGURE 3

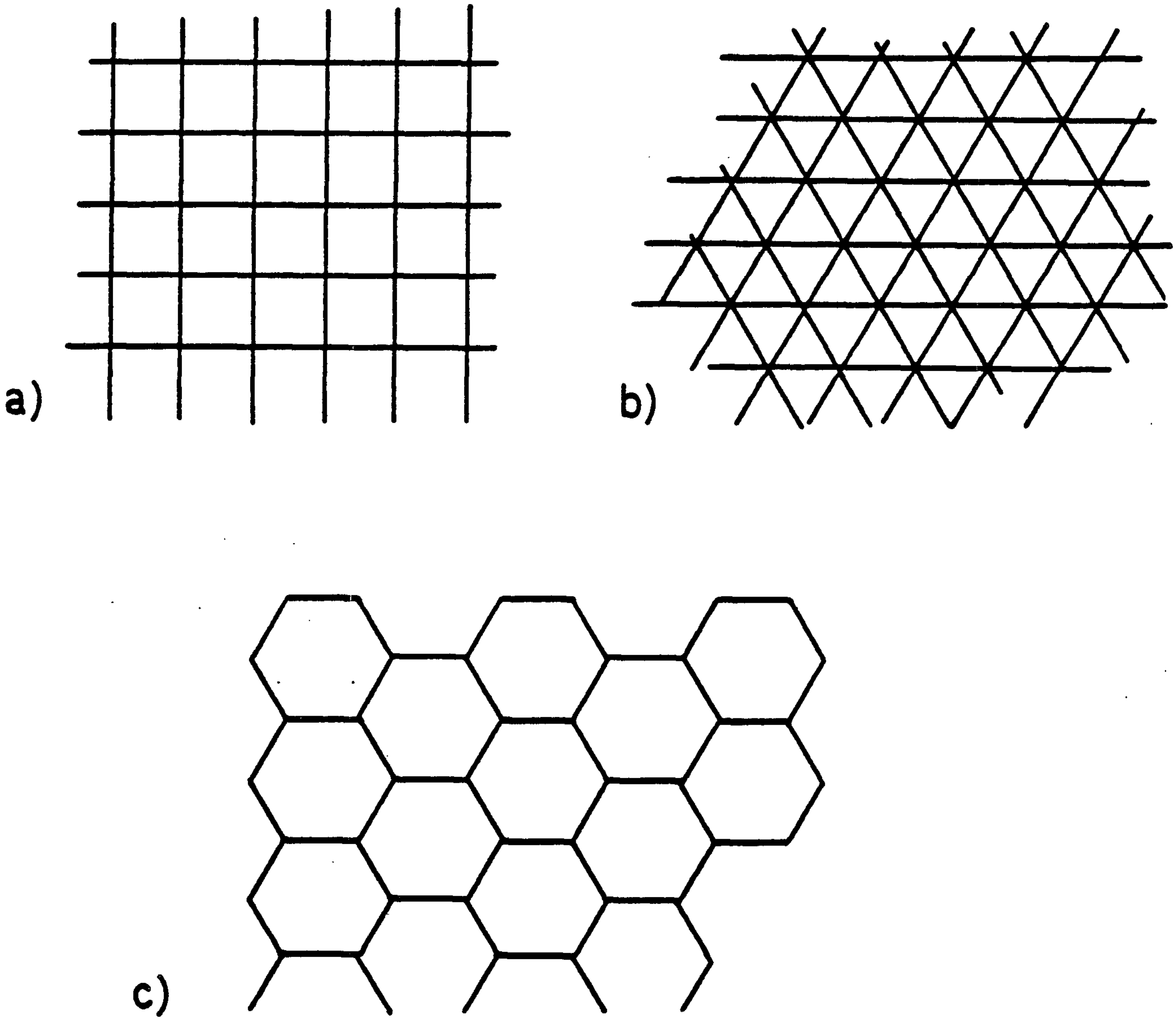

FIGURE 4

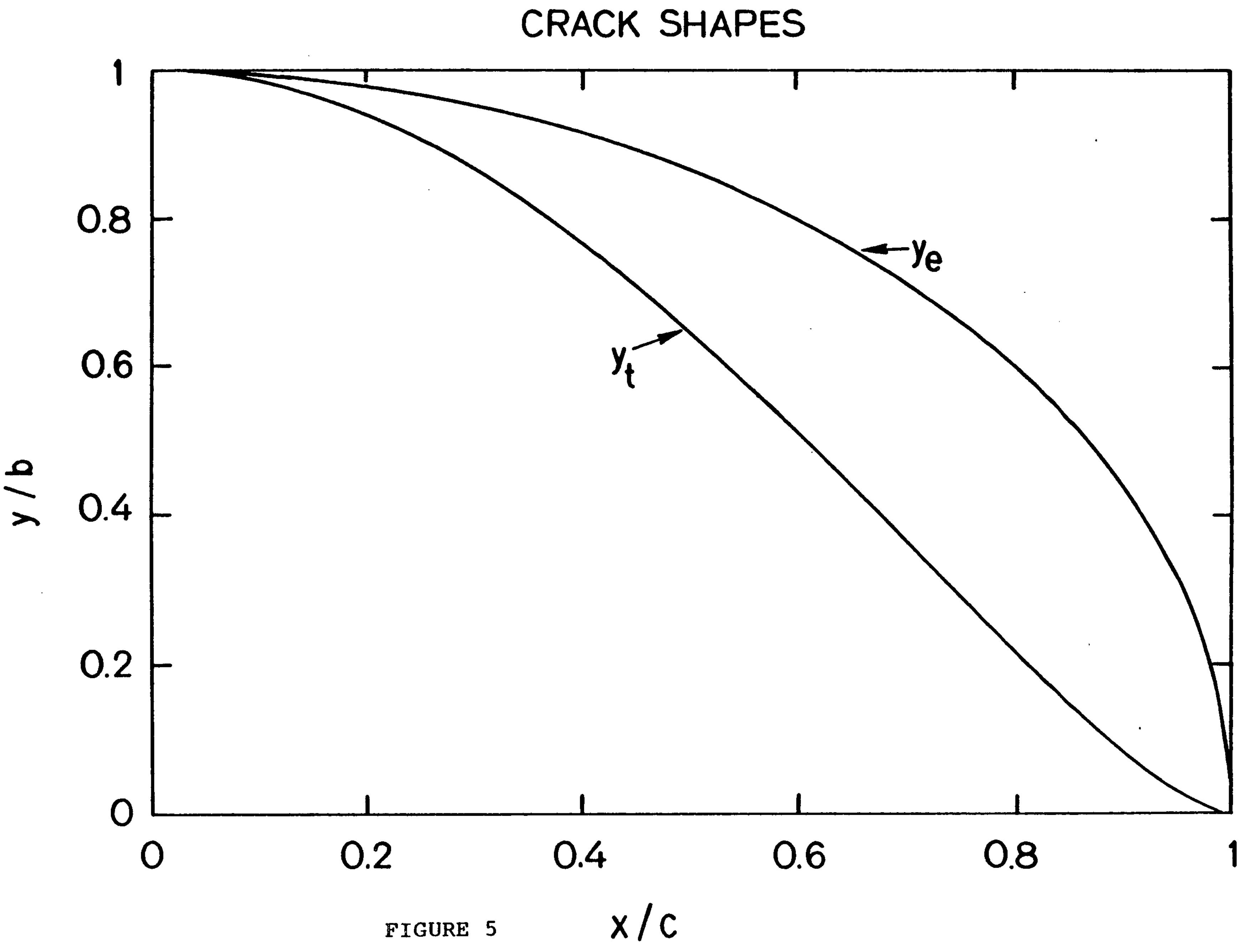

FIGURE 5

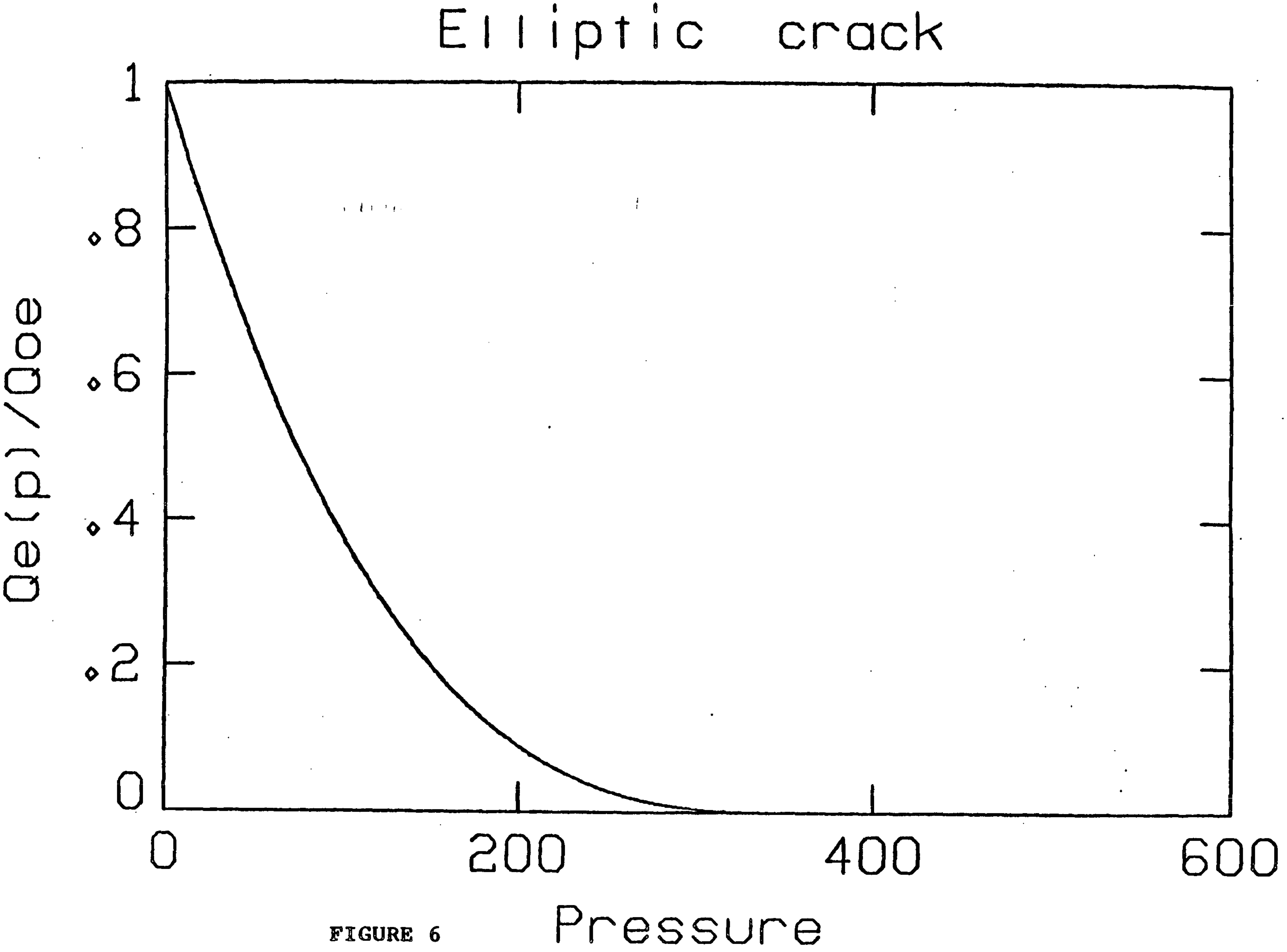

FIGURE 6

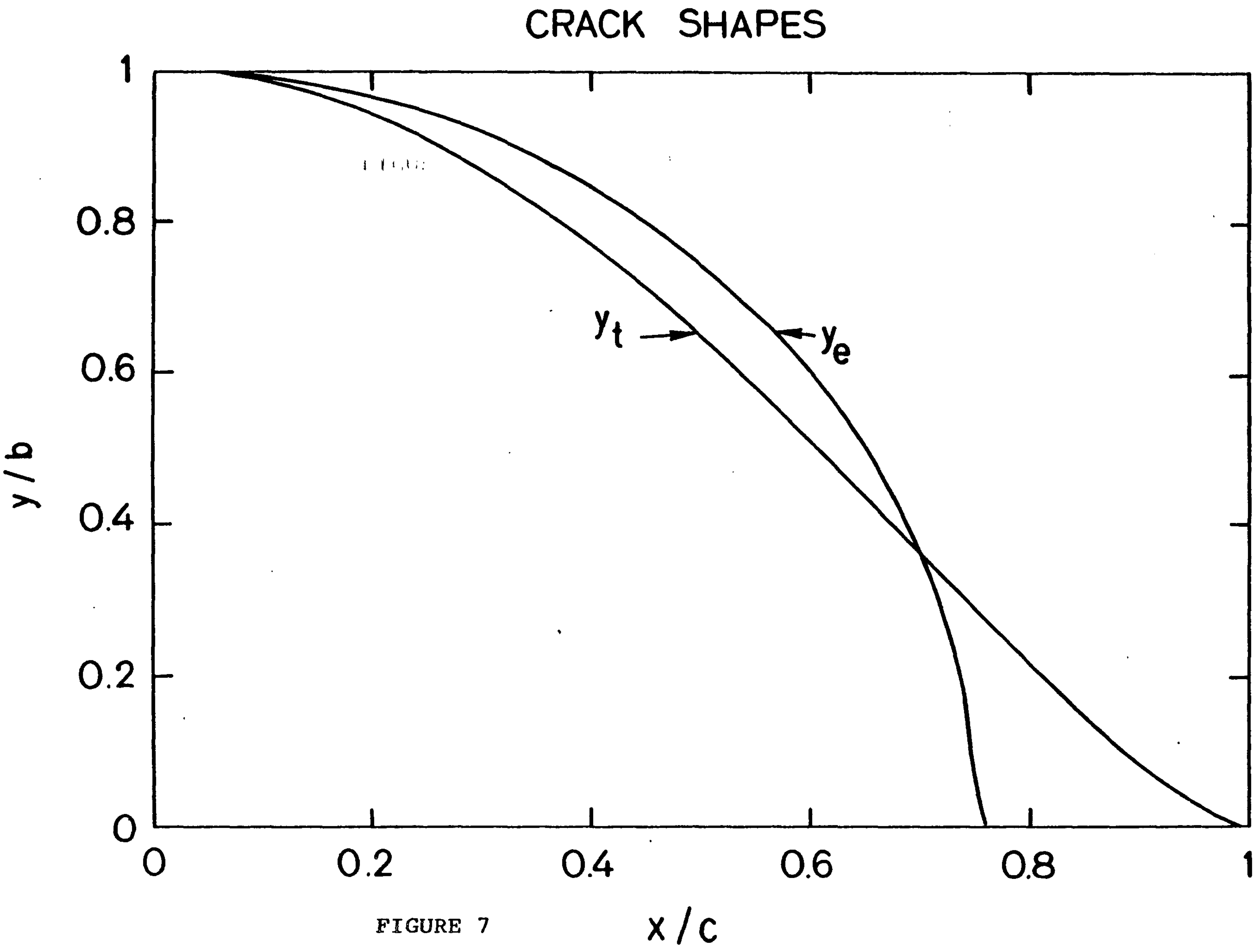

FIGURE 7

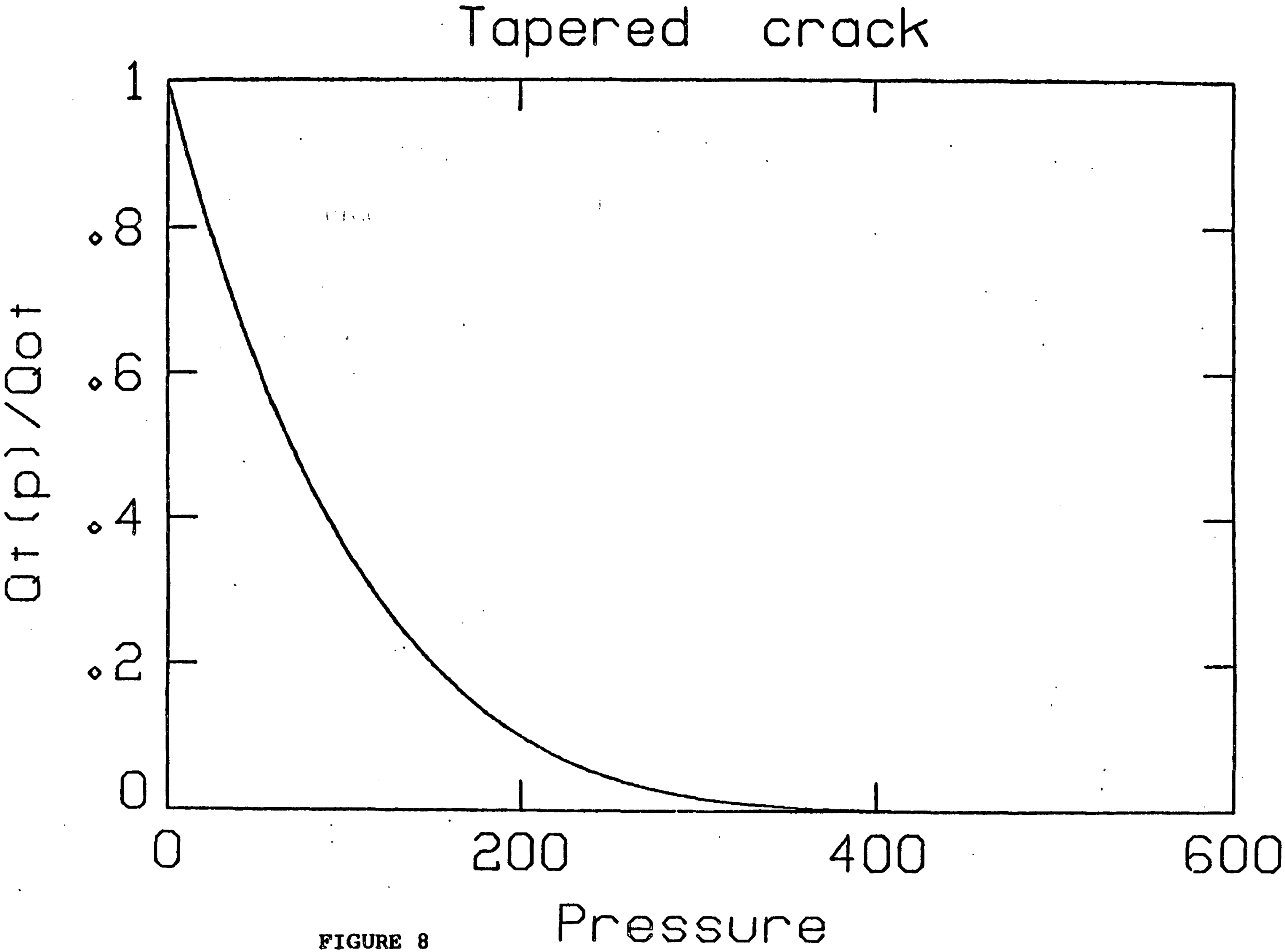

FIGURE 8

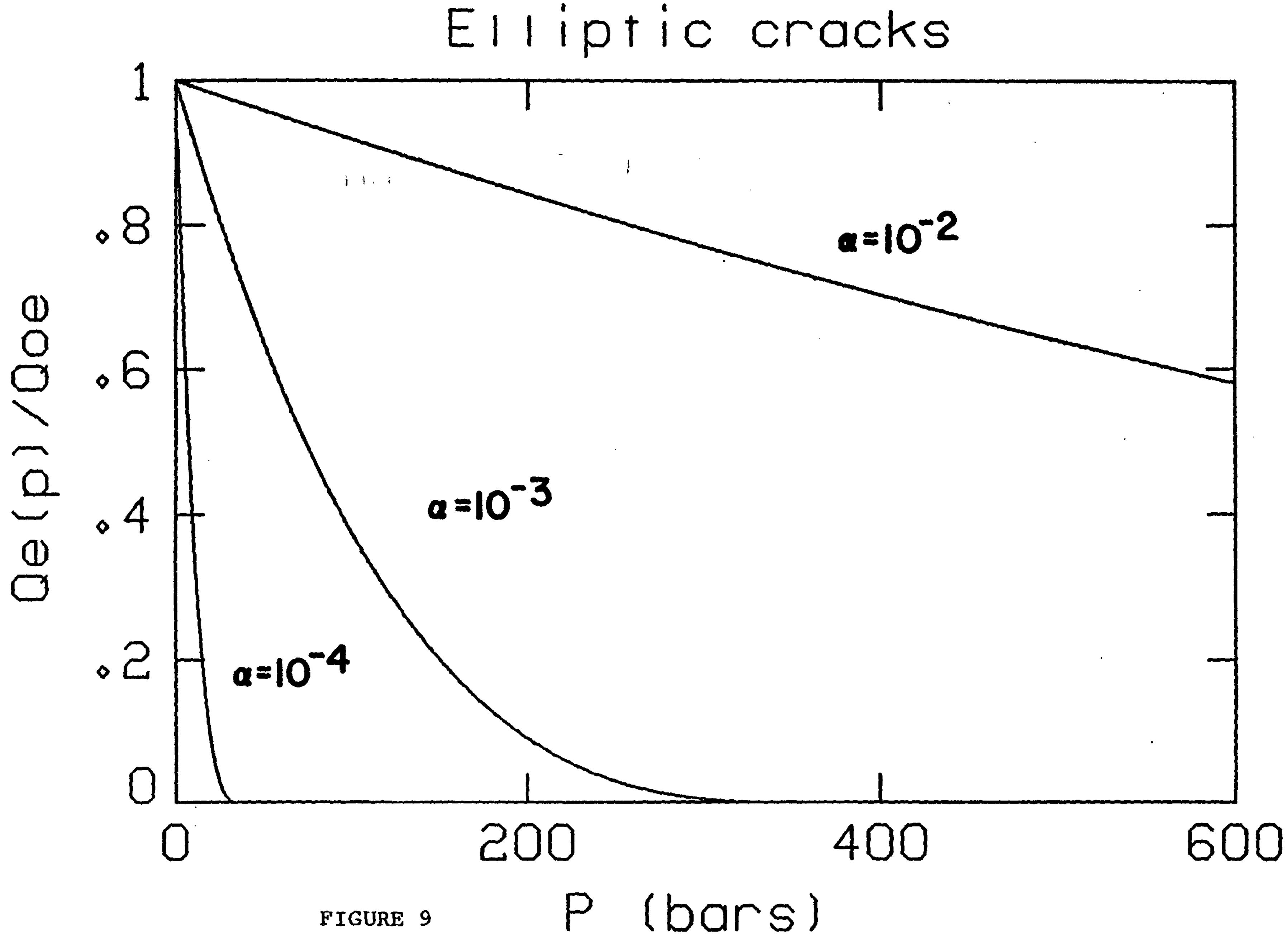
Elliptic cracks
Qe(p)/Qoe
1
.8
.6
.4
.2
0
0
200
400
600
P (bars)
$\alpha=10^{-2}$
$\alpha=10^{-3}$
$\alpha=10^{-4}$

FIGURE 9

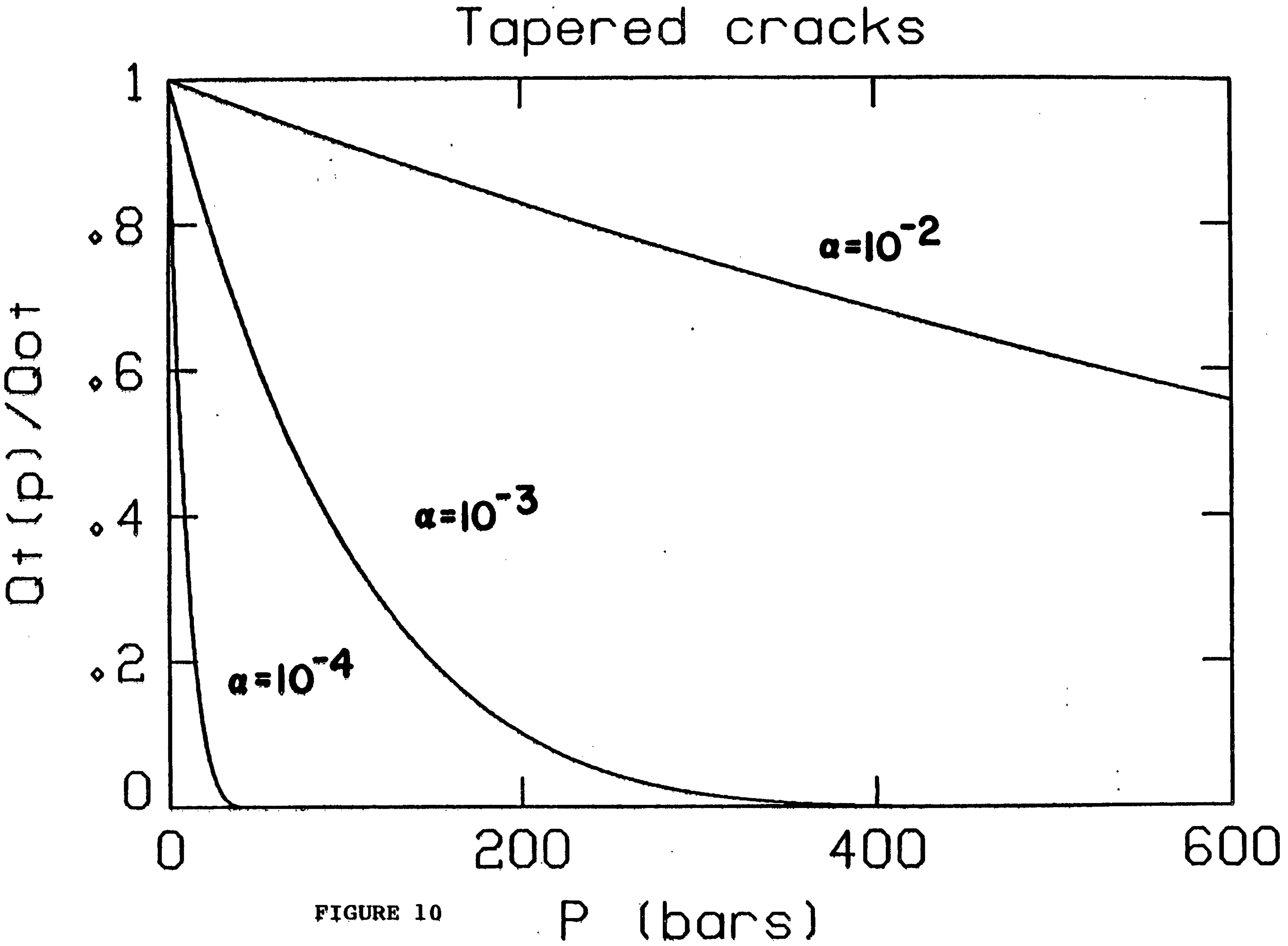
Tapered cracks
Qt(p)/Qot
1
.8
.6
.4
.2
0
0
200
400
600
P (bars)
α=10-2
α=10-3
α=10-4

FIGURE 10

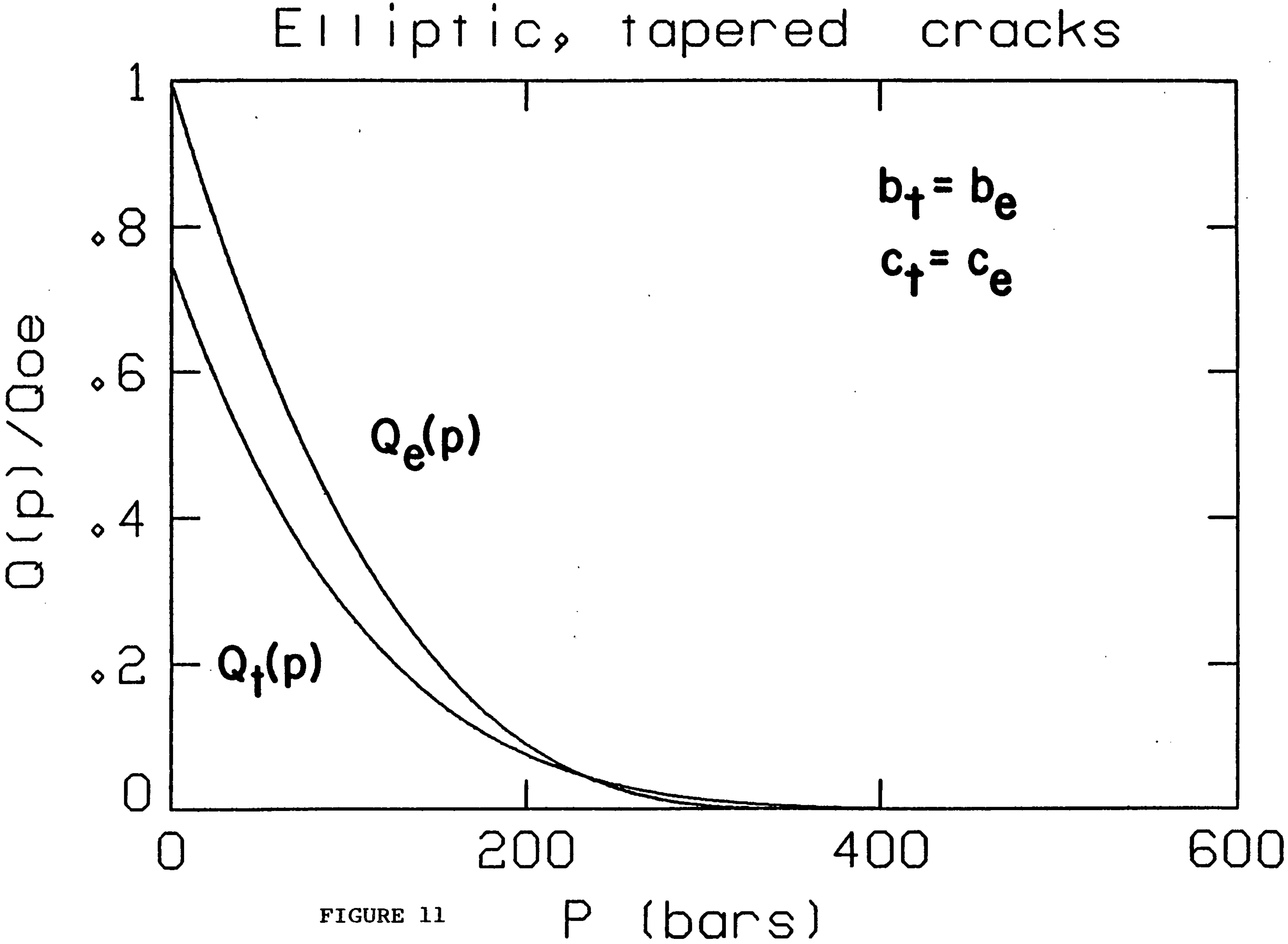
Elliptic, tapered cracks
$b_t = b_e$
$c_t = c_e$
$Q_e(p)$
$Q_t(p)$
Q(p)/Qoe
1
.8
.6
.4
.2
0
0
200
400
600
P (bars)

FIGURE 11

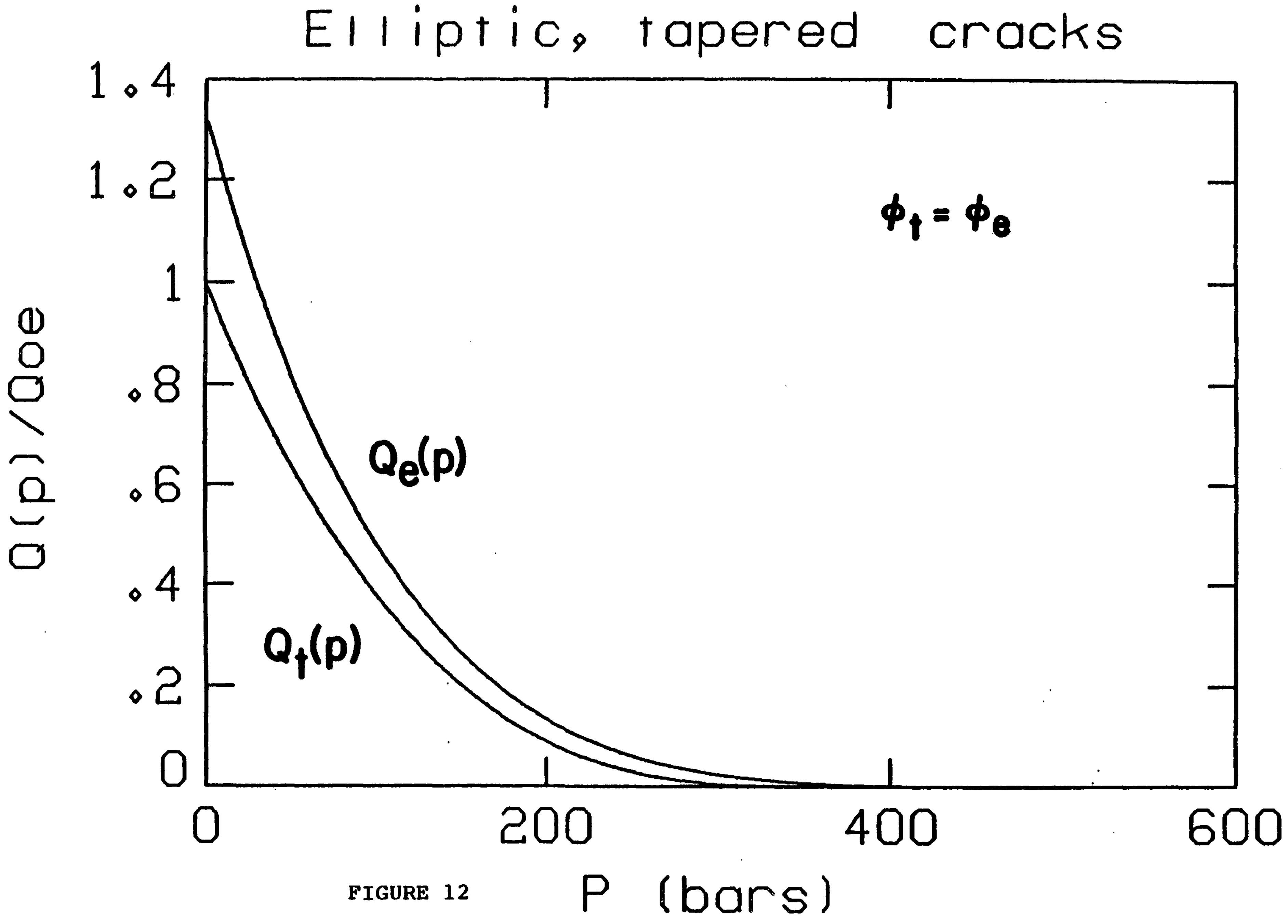
Elliptic, tapered cracks
Q(p)/Qoe
1.4
1.2
1
.8
.6
.4
.2
0
0
200
400
600
P (bars)
$\phi_t = \phi_e$
$Q_e(p)$
$Q_t(p)$

FIGURE 12

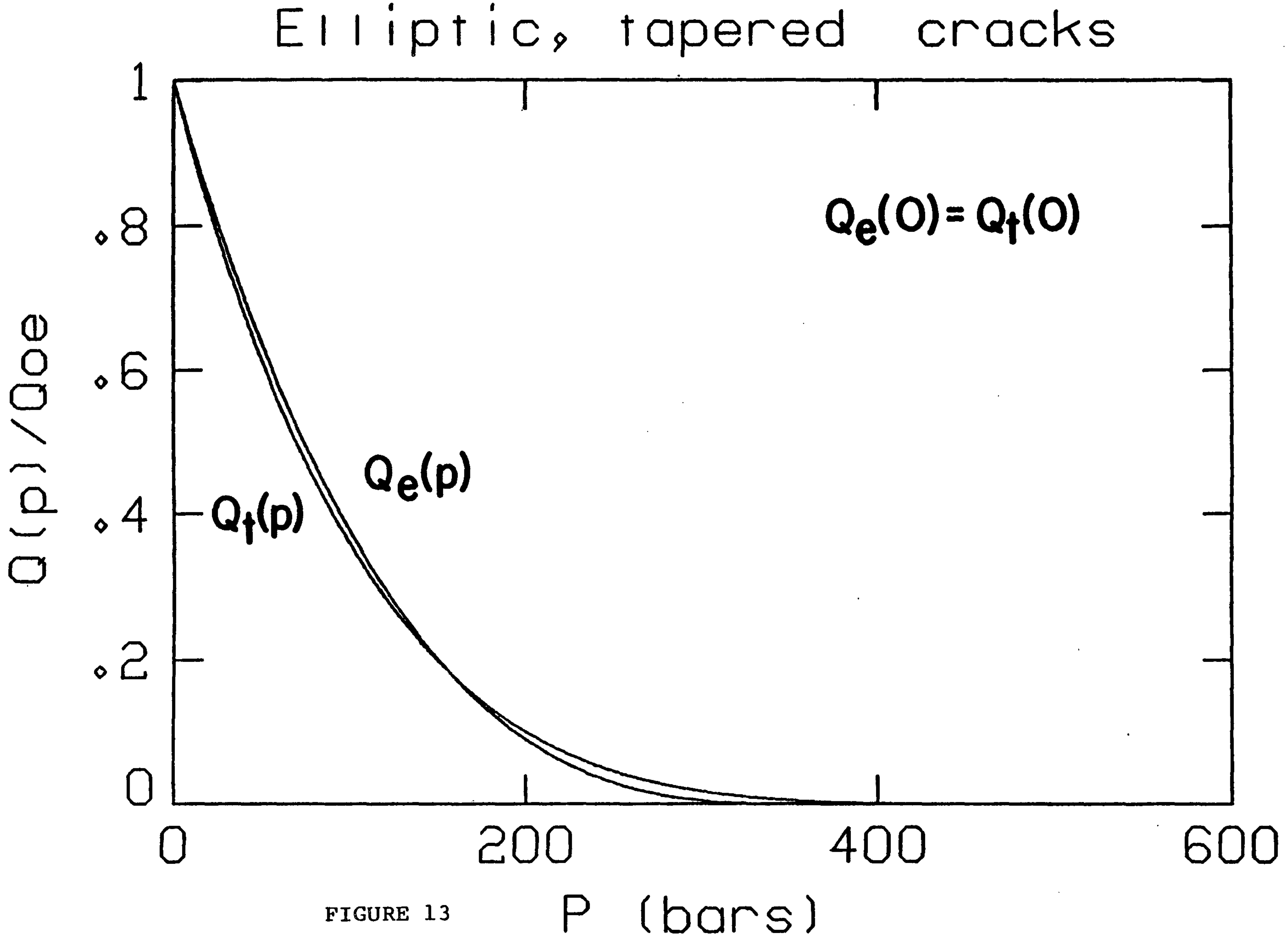
Elliptic, tapered cracks
1
.8
.6
.4
.2
0
Q(p)/Qoe
0
200
400
600
P (bars)
$Q_e(0) = Q_t(0)$
$Q_e(p)$
$Q_t(p)$

FIGURE 13

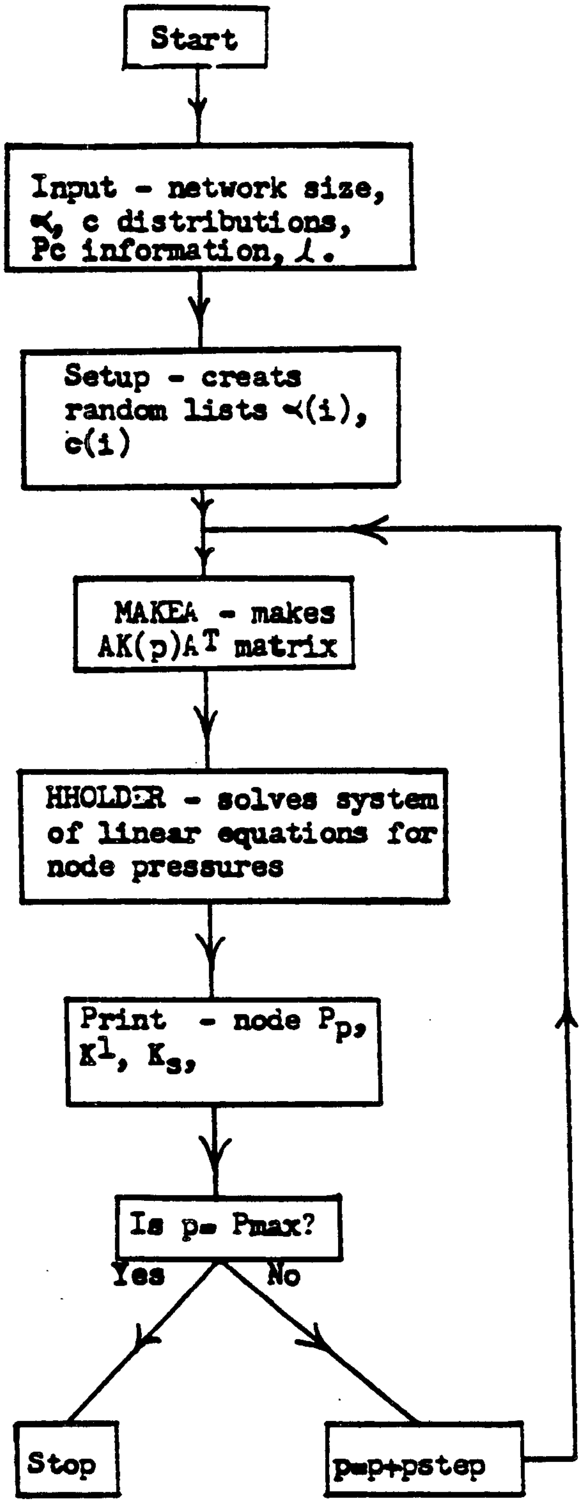
Start
Input - network size, α, c distributions, Pc information, λ.
Setup - creats random lists α(i), c(i)
MAKEA - makes AK(p)A^T matrix
HHOLDER - solves system of linear equations for node pressures
Print - node P$_p$, K^1, K$_s$,
Is p= Pmax?
Yes
No
Stop
p=p+pstep

FIGURE 14

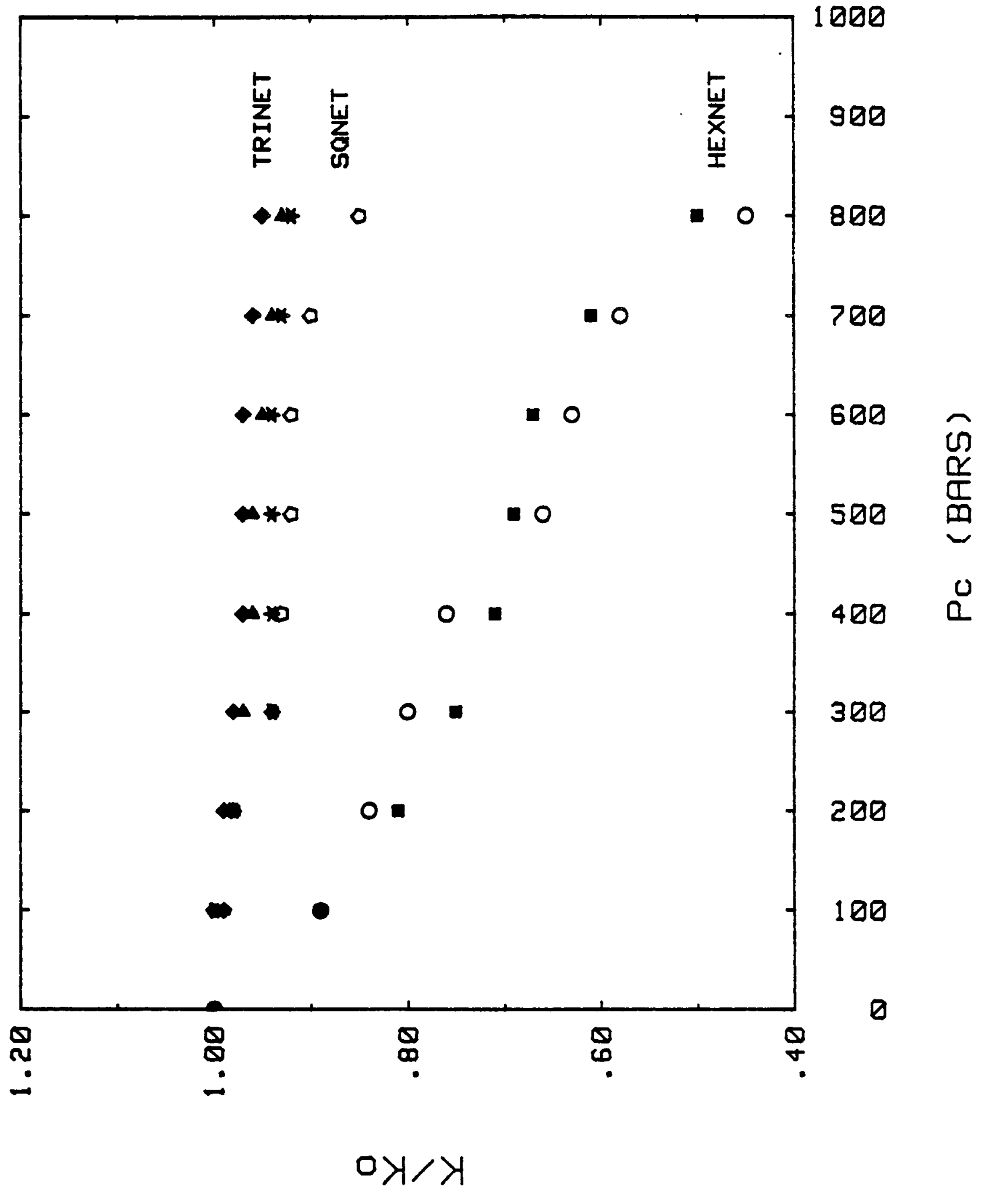
TRINET
SQNET
HEXNET
1.20
1.00
.80
.60
.40
K/Ko
0
100
200
300
400
500
600
700
800
900
1000
Pc (BARS)

FIGURE 15

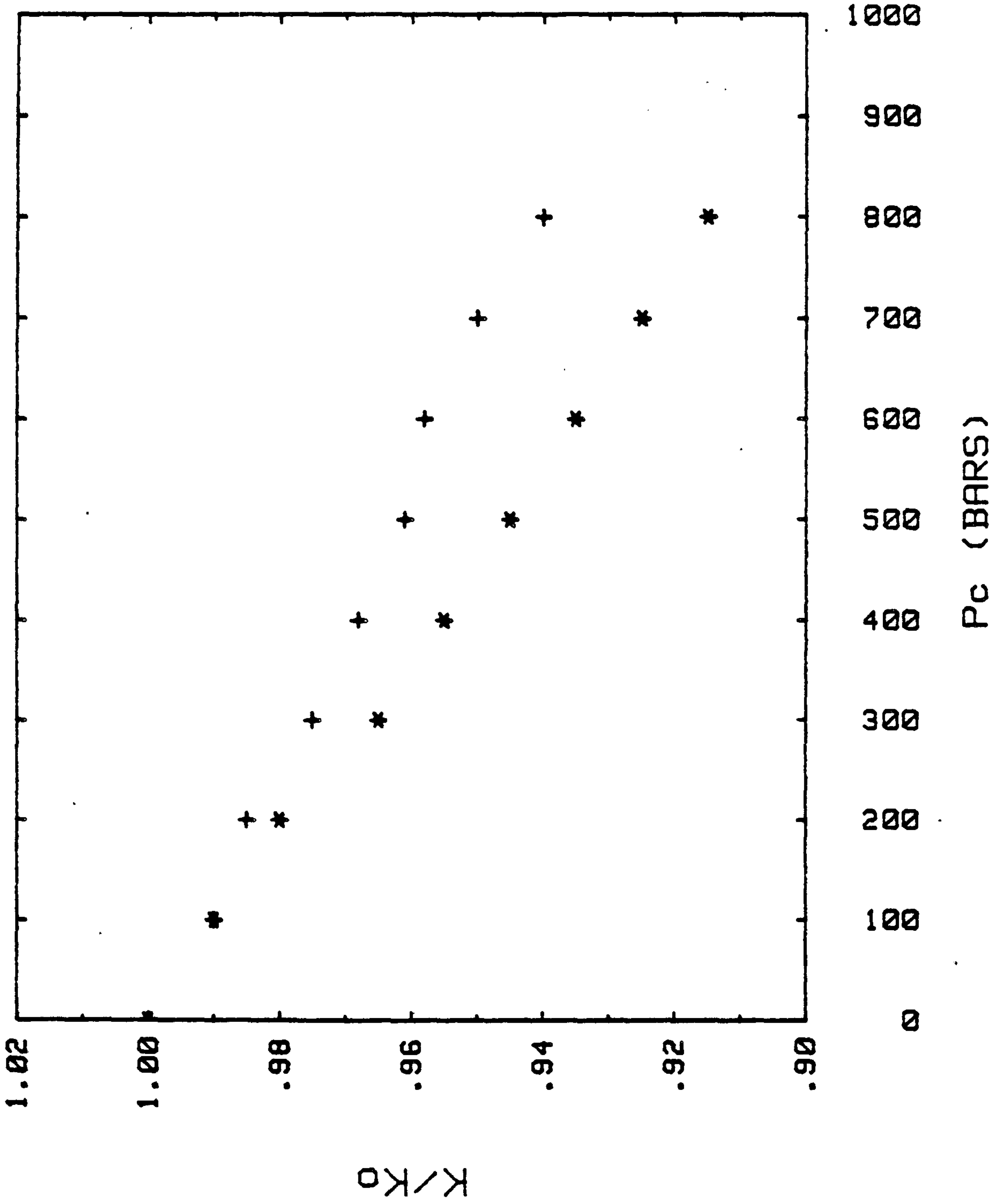
1000
900
800
700
600
500
400
300
200
100
0
Pc (BARS)
1.02
1.00
.98
.96
.94
.92
.90
K/Ko

FIGURE 16

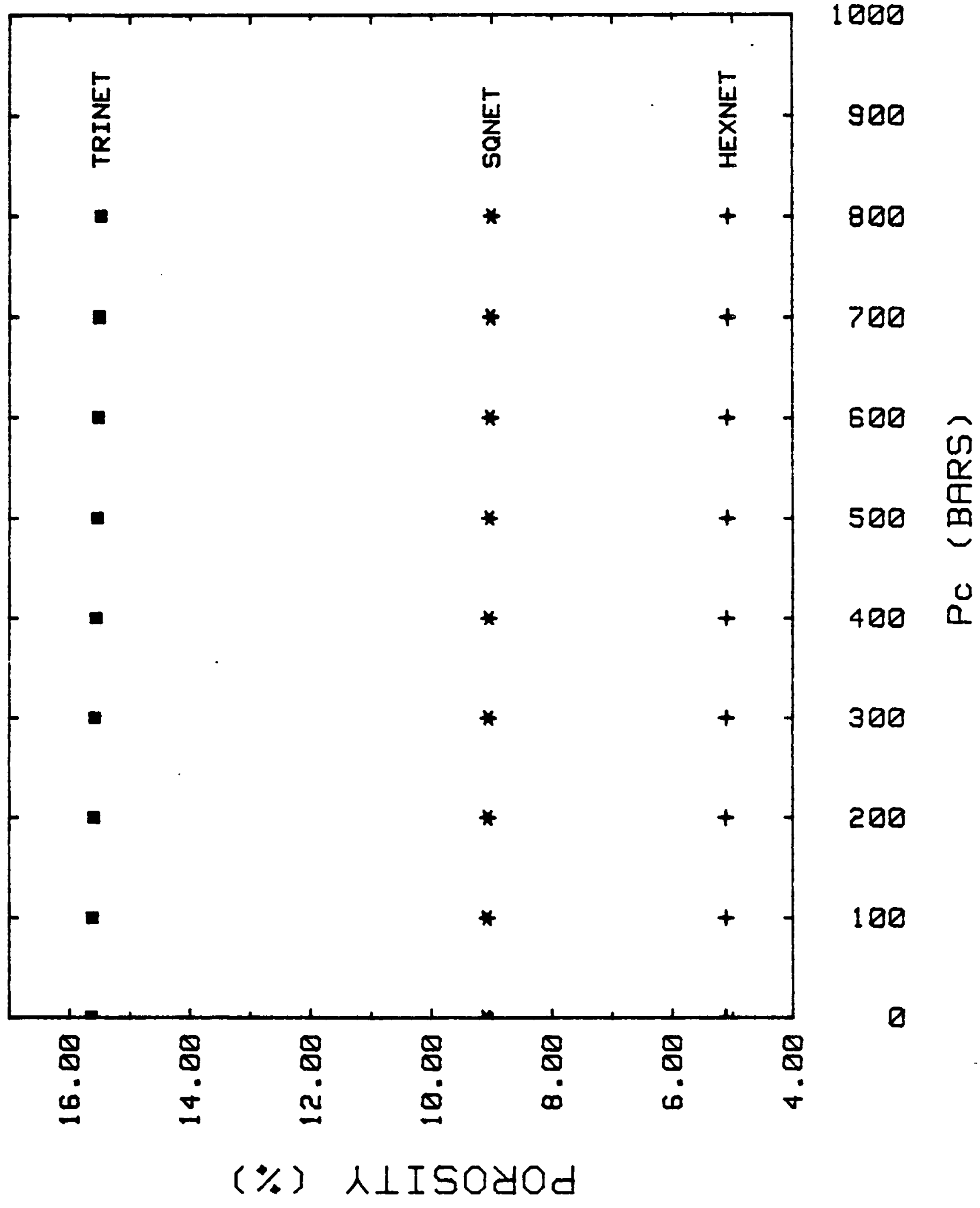
TRINET
SQNET
HEXNET
0
100
200
300
400
500
600
700
800
900
1000
Pc (BARS)
16.00
14.00
12.00
10.00
8.00
6.00
4.00
POROSITY (%)

FIGURE 17

PORE PRESSURE DISTRIBUTION

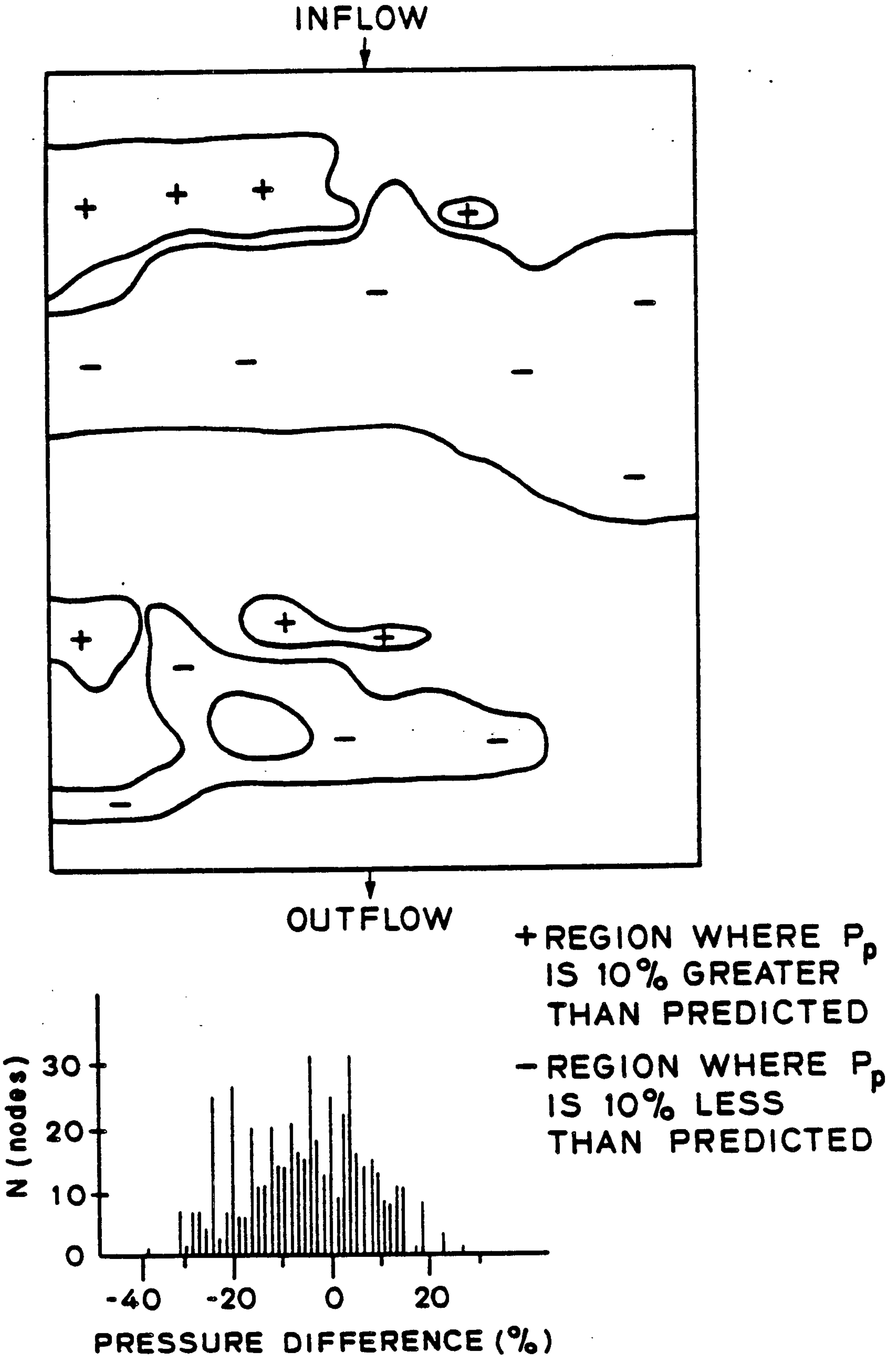

FIGURE 18

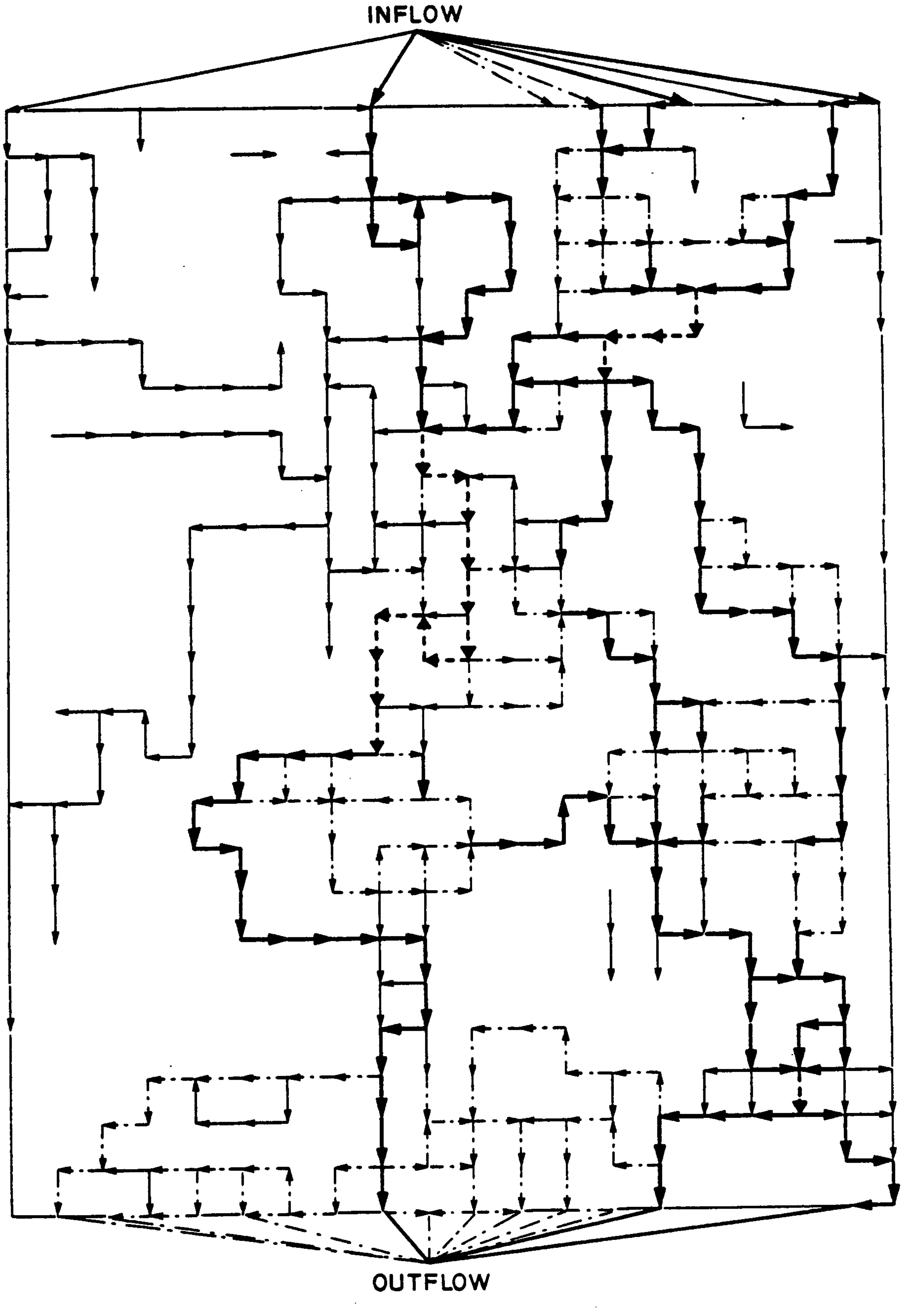

FIGURE 19

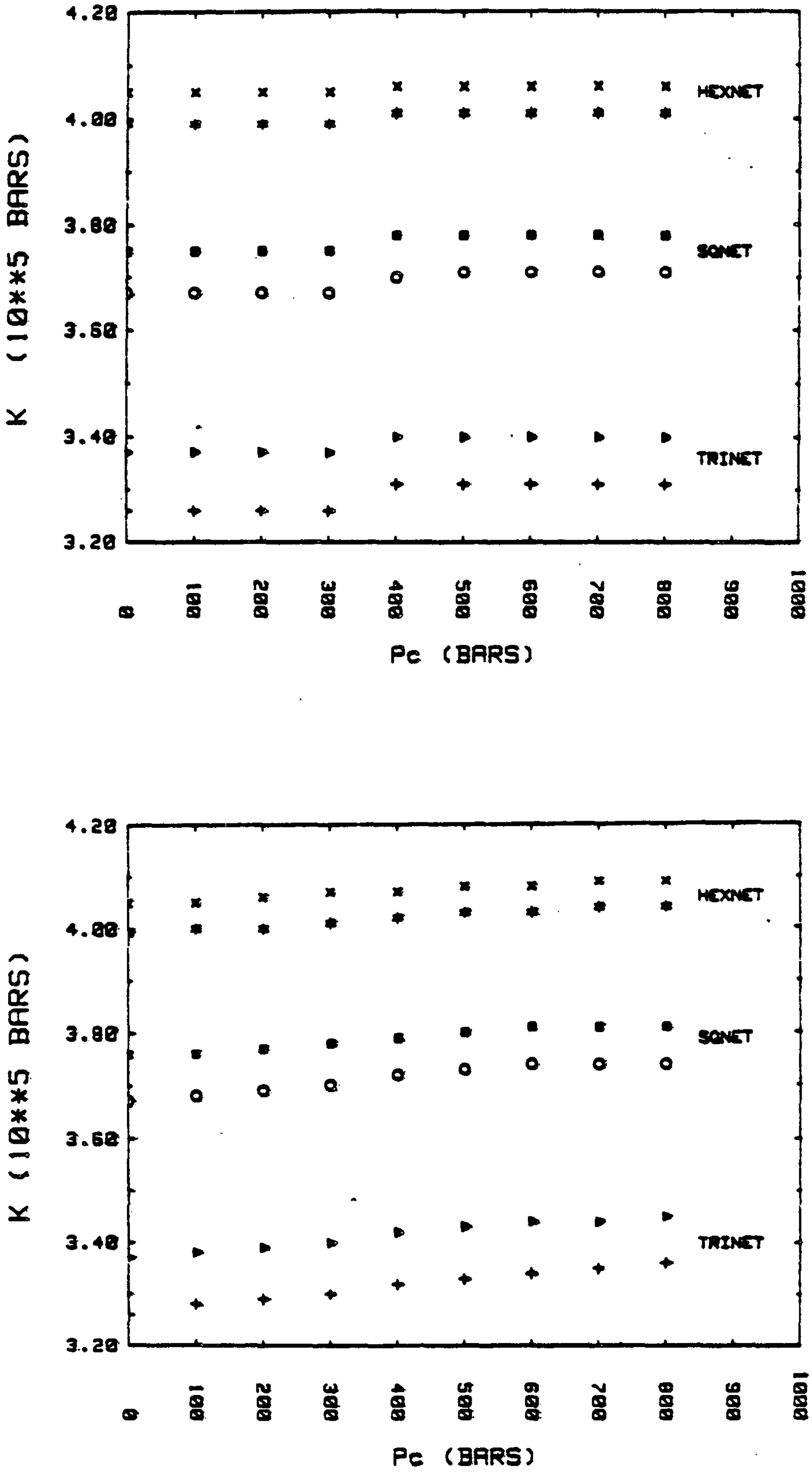
4.20
4.00
3.80
3.60
3.40
3.20
K (10**5 BARS)
HEXNET
SQNET
TRINET
0
100
200
300
400
500
600
700
800
900
1000
Pc (BARS)
4.20
4.00
3.80
3.60
3.40
3.20
K (10**5 BARS)
HEXNET
SQNET
TRINET
0
100
200
300
400
500
600
700
800
900
1000
Pc (BARS)

FIGURE 20

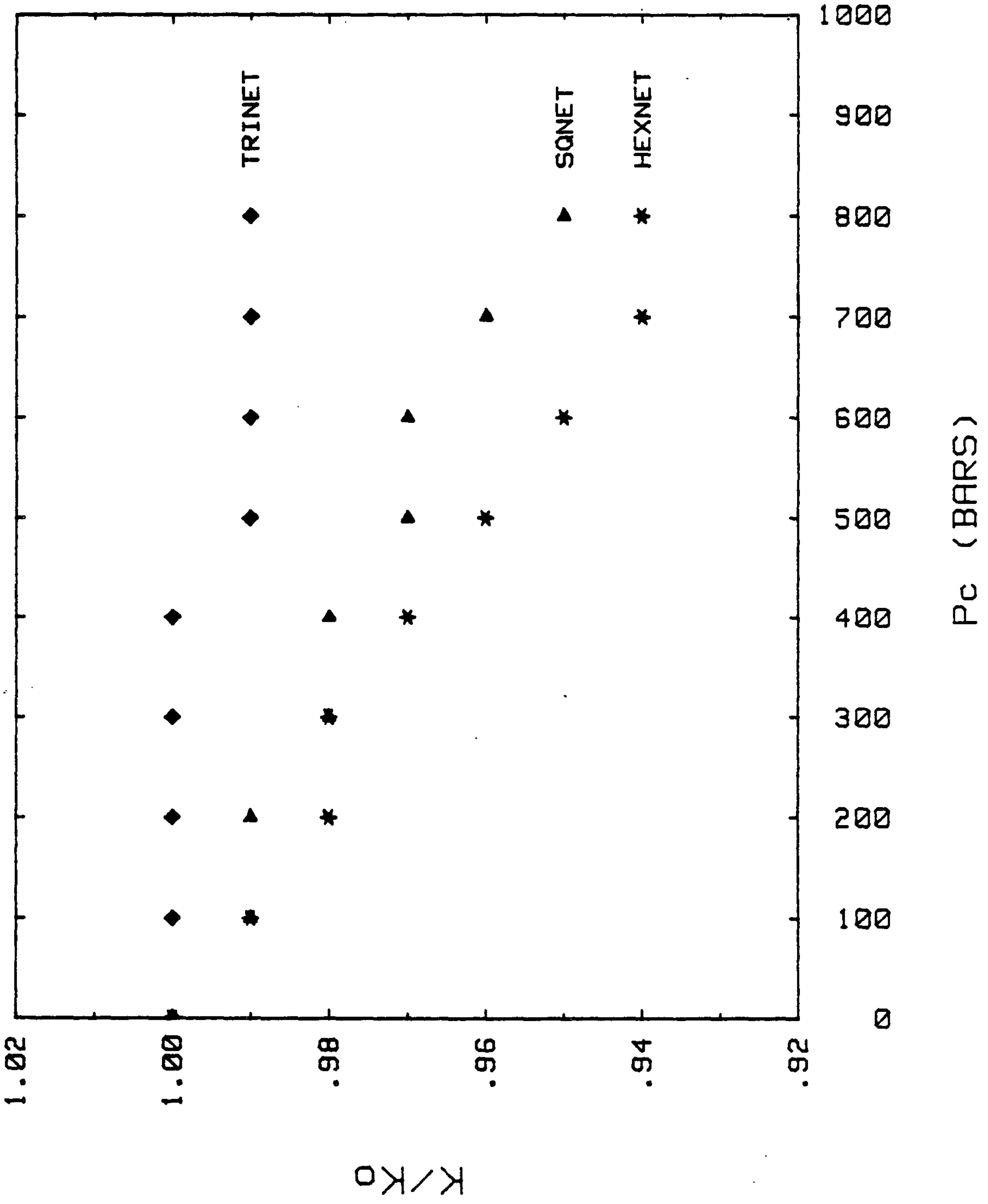
K/Ko
1.02
1.00
.98
.96
.94
.92
Pc (BARS)
0
100
200
300
400
500
600
700
800
900
1000
TRINET
SQNET
HEXNET

FIGURE 21

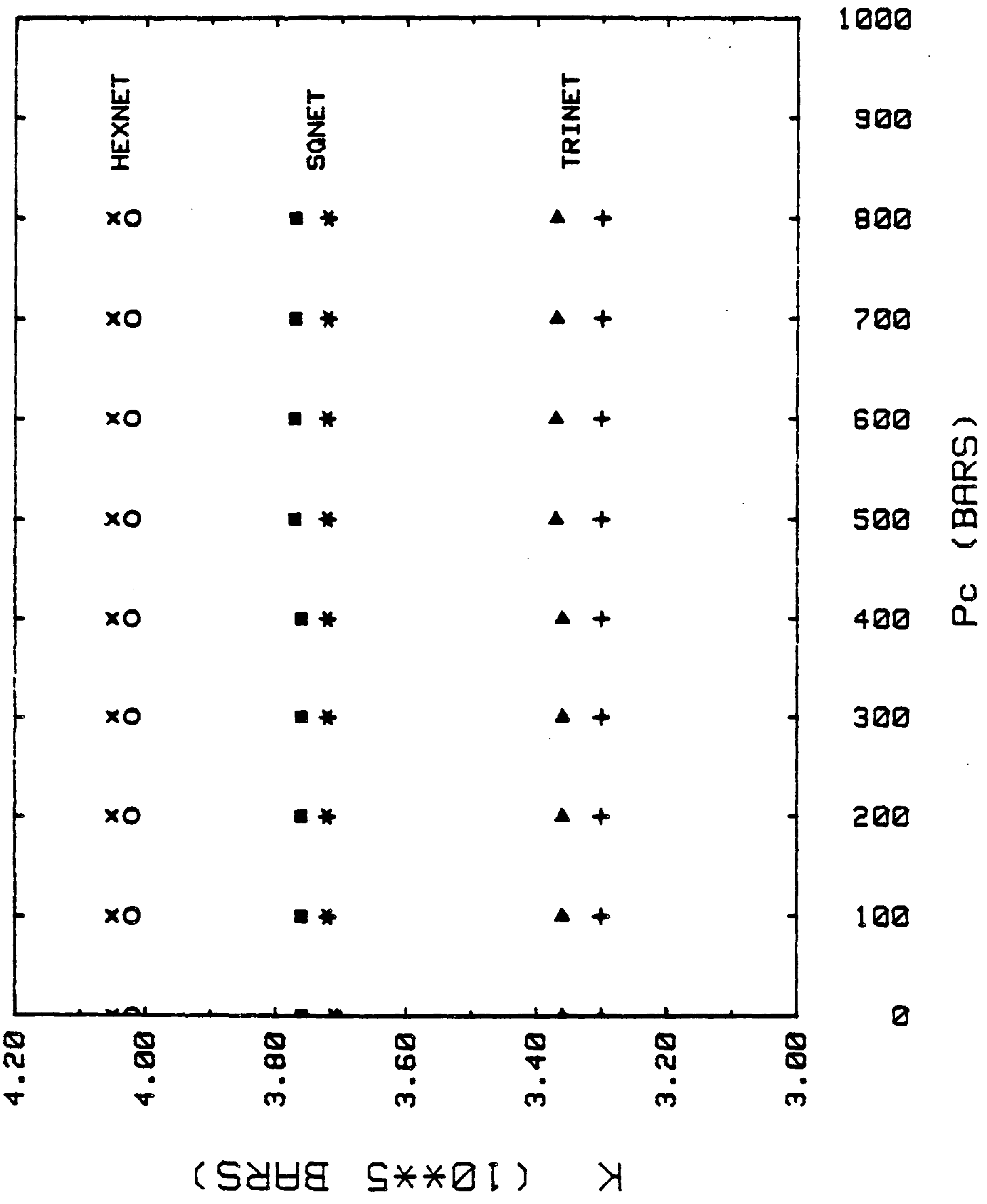
HEXNET
SQNET
TRINET
K (10**5 BARS)
4.20
4.00
3.80
3.60
3.40
3.20
3.00
Pc (BARS)
0
100
200
300
400
500
600
700
800
900
1000

FIGURE 22

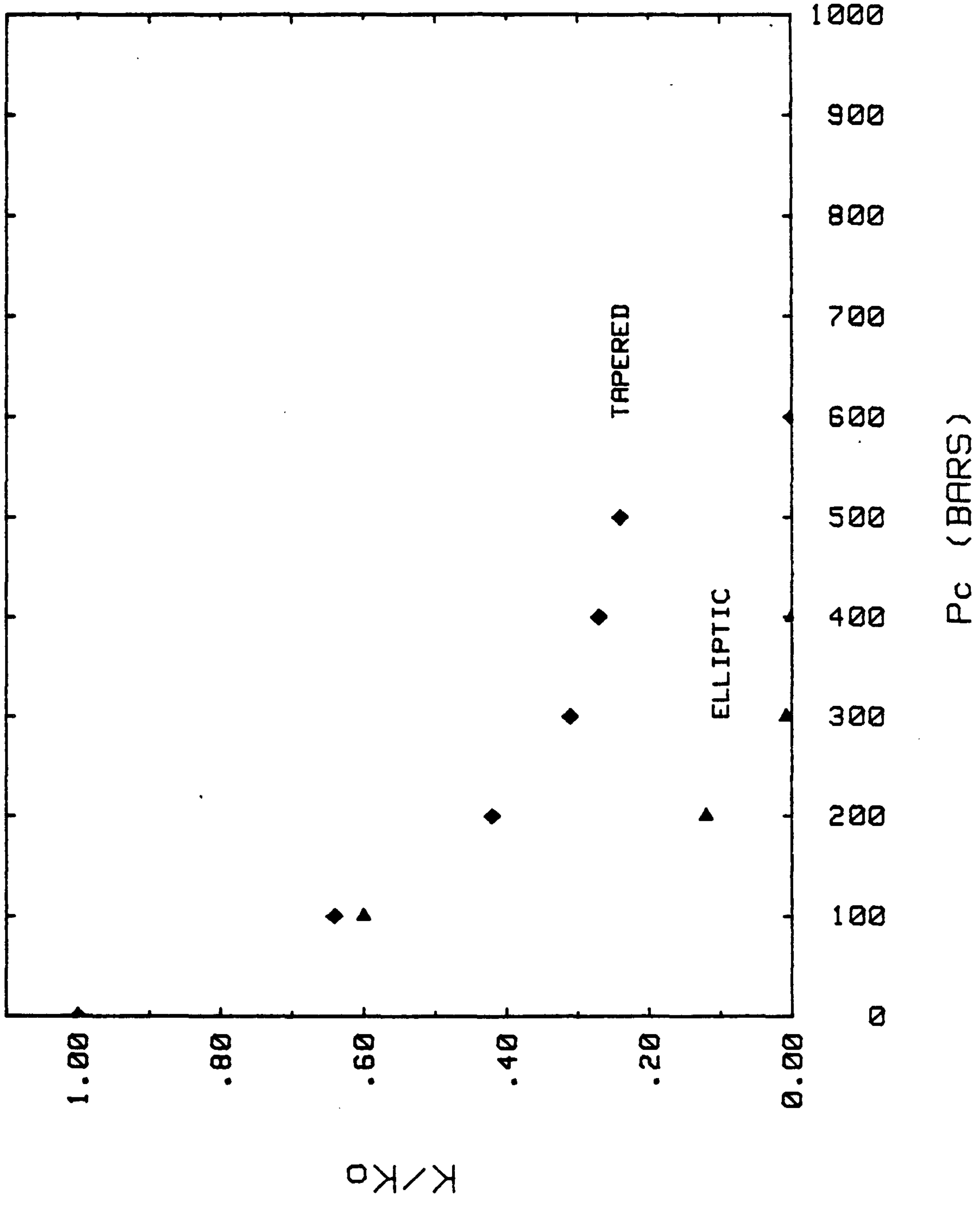
TAPERED
ELLIPTIC
Pc (BARS)
K/Ko
1.00
.80
.60
.40
.20
0.00
0
100
200
300
400
500
600
700
800
900
1000

FIGURE 23

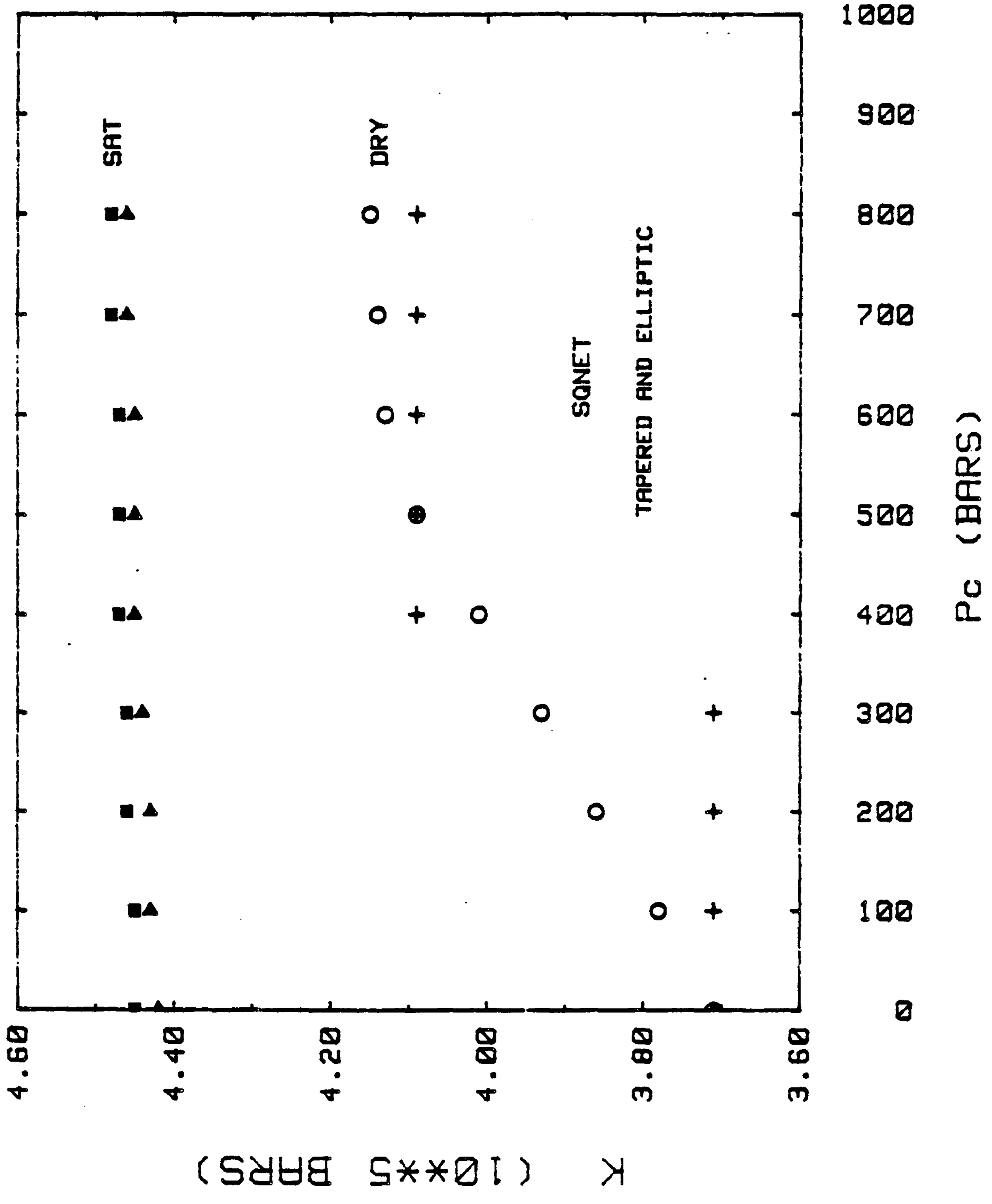
SAT
DRY
SQNET
TAPERED AND ELLIPTIC
0
100
200
300
400
500
600
700
800
900
1000
Pc (BARS)
4.60
4.40
4.20
4.00
3.80
3.60
K (10**5 BARS)

FIGURE 24

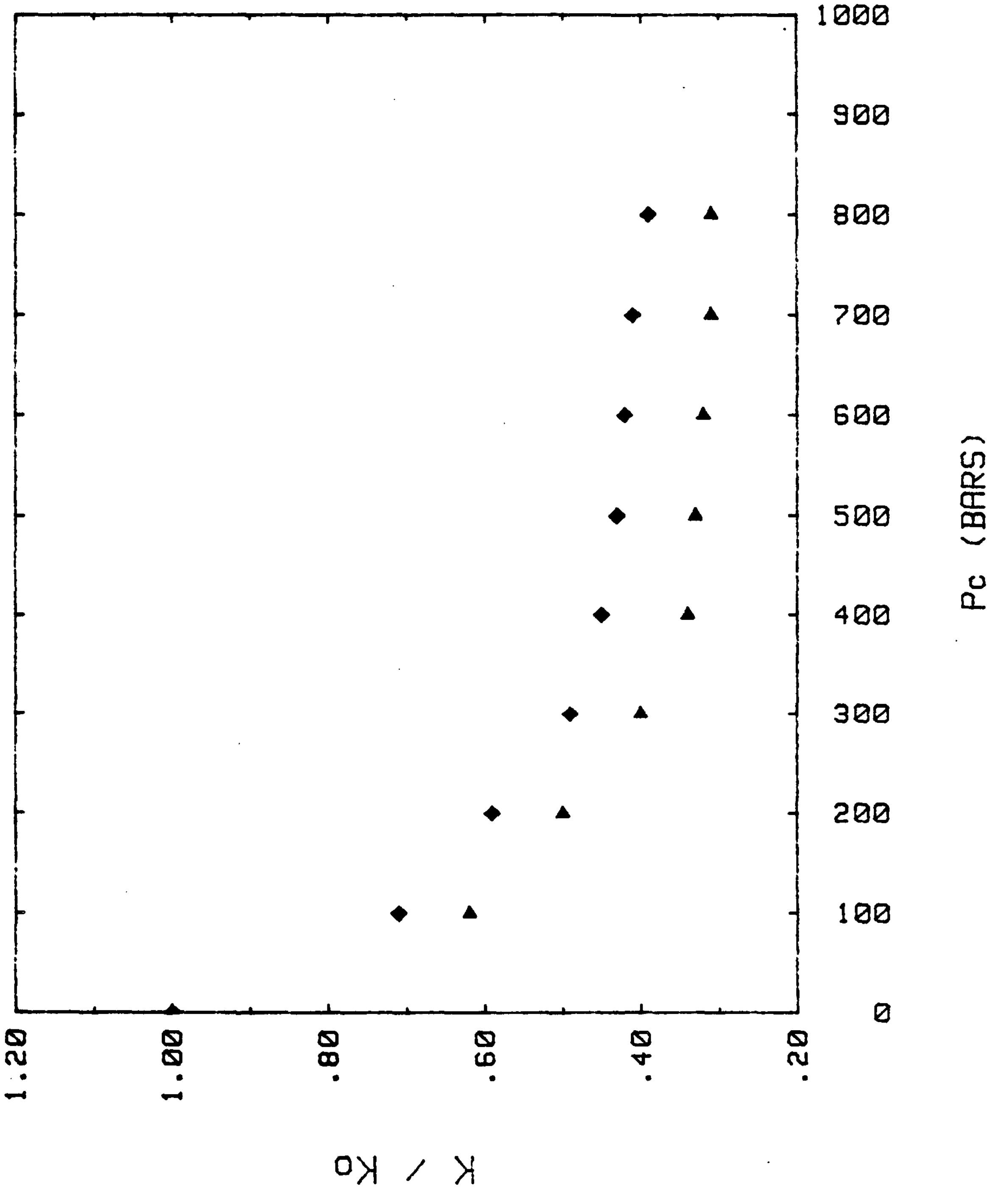
1000
900
800
700
600
500
400
300
200
100
0
Pc (BARS)
1.20
1.00
.80
.60
.40
.20
K / Ko

FIGURE 25

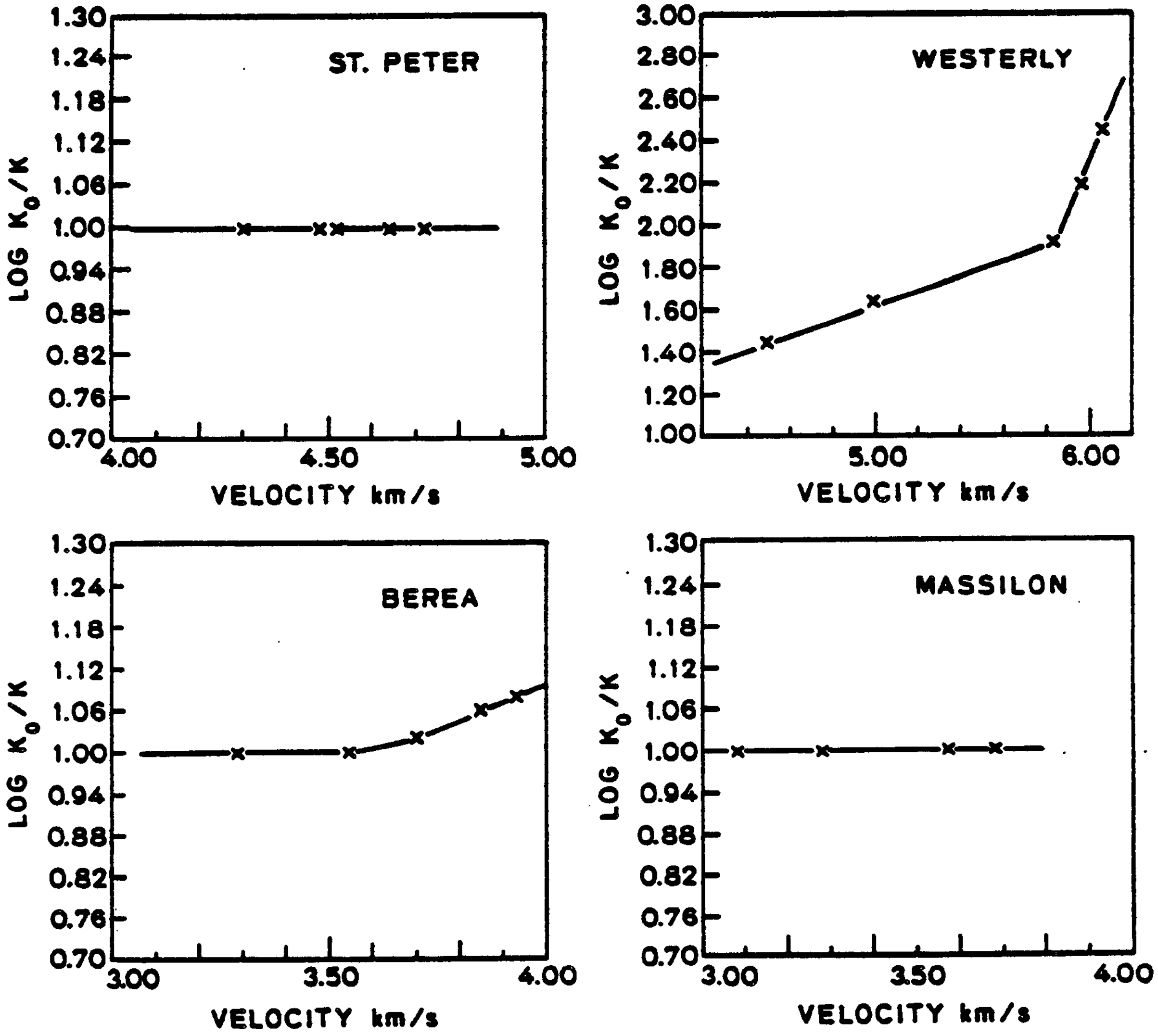
ST. PETER
LOG K₀/K
1.30
1.24
1.18
1.12
1.06
1.00
0.94
0.88
0.82
0.76
0.70
4.00
4.50
5.00
VELOCITY km/s
WESTERLY
LOG K₀/K
3.00
2.80
2.60
2.40
2.20
2.00
1.80
1.60
1.40
1.20
1.00
5.00
6.00
VELOCITY km/s
BEREA
LOG K₀/K
1.30
1.24
1.18
1.12
1.06
1.00
0.94
0.88
0.82
0.76
0.70
3.00
3.50
4.00
VELOCITY km/s
MASSILON
LOG K₀/K
1.30
1.24
1.18
1.12
1.06
1.00
0.94
0.88
0.82
0.76
0.70
3.00
3.50
4.00
VELOCITY km/s

FIGURE 26

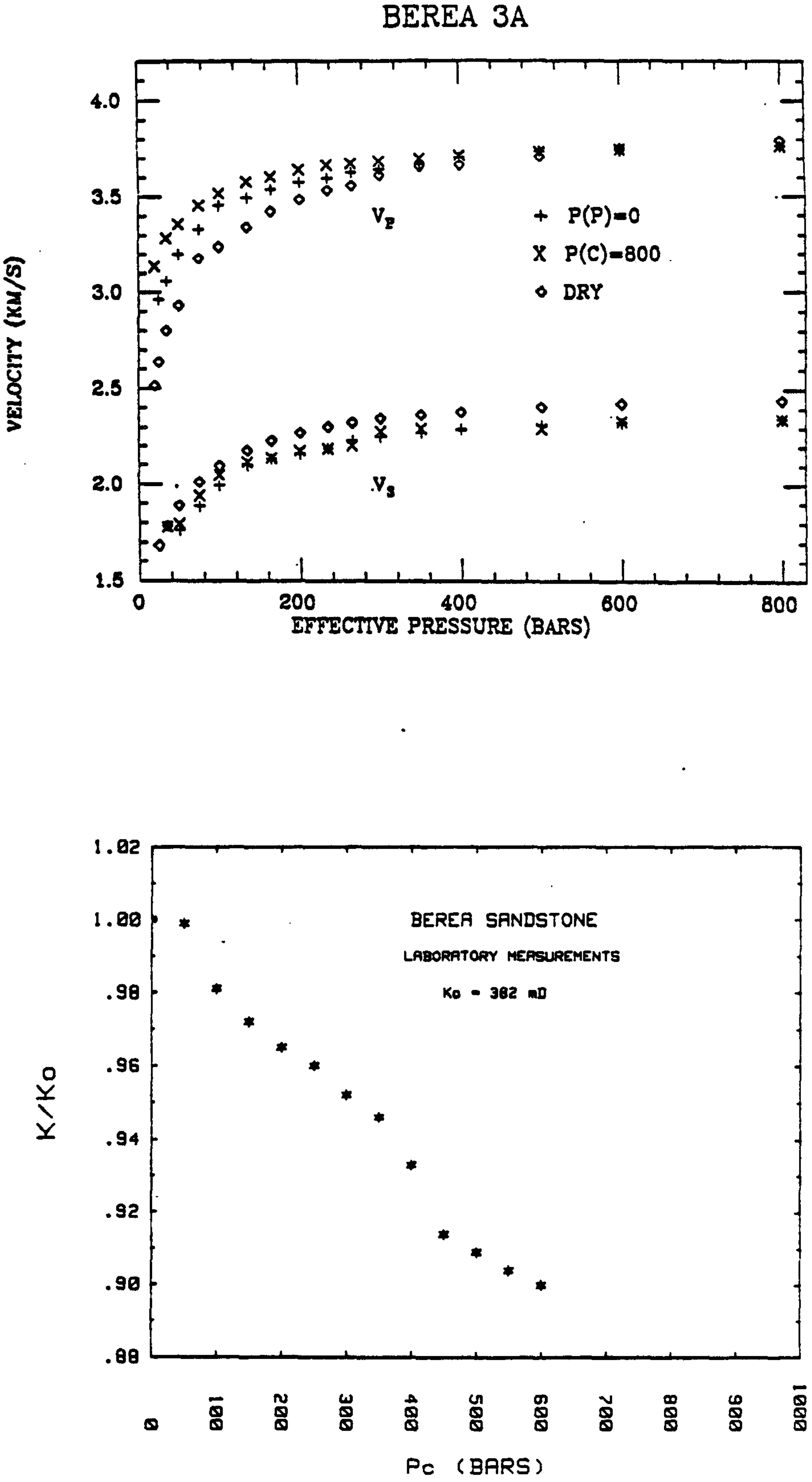
BEREA 3A
VELOCITY (KM/S)
4.0
3.5
3.0
2.5
2.0
1.5
0
200
400
600
800
EFFECTIVE PRESSURE (BARS)
V_P
V_S
+ P(P)=0
X P(C)=800
◇ DRY
K/Ko
1.02
1.00
.98
.96
.94
.92
.90
.88
0
100
200
300
400
500
600
700
800
900
1000
Pc (BARS)
BEREA SANDSTONE
LABORATORY MEASUREMENTS
Ko = 382 mD

FIGURE 27

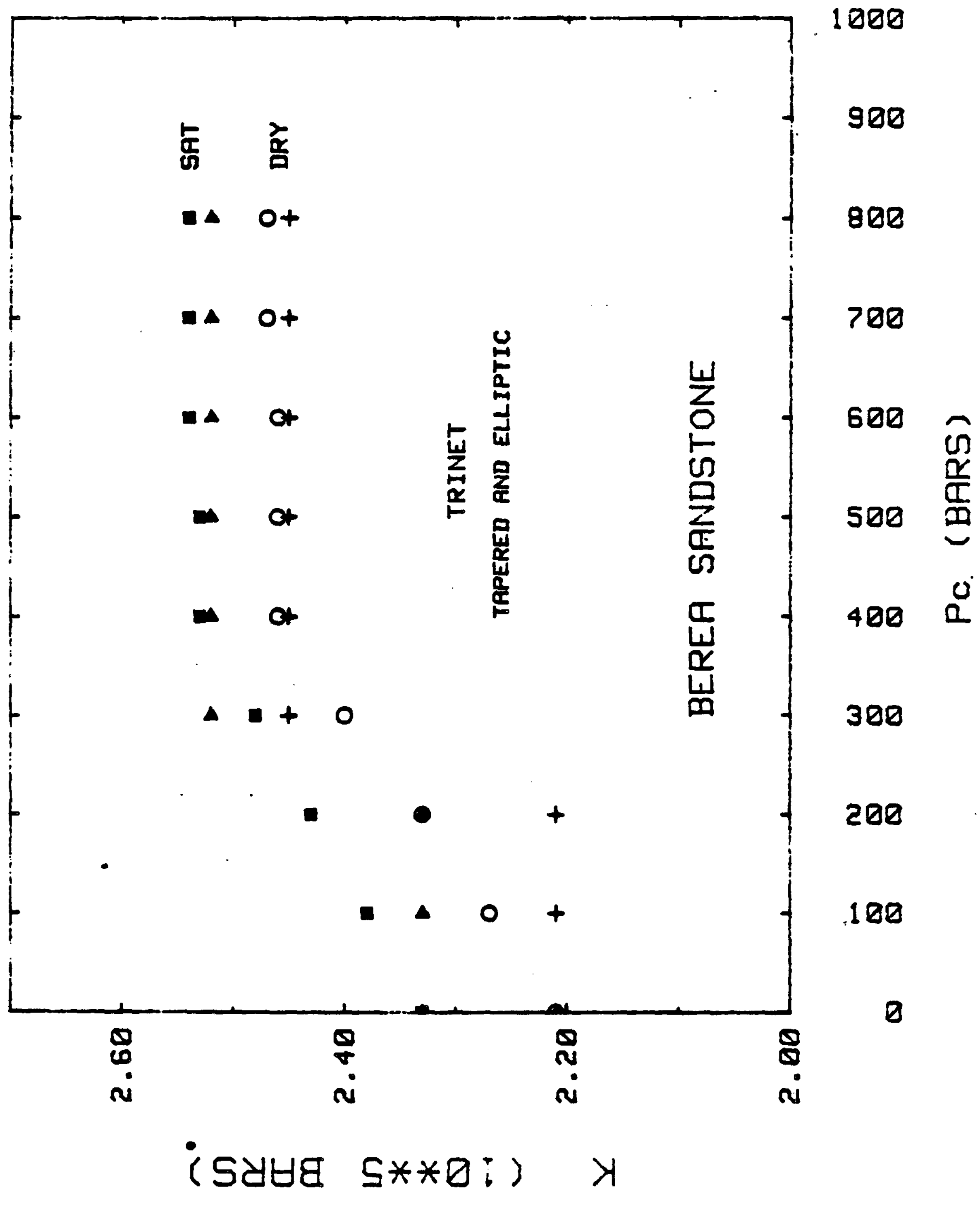
SAT
DRY
TRINET
TAPERED AND ELLIPTIC
BEREA SANDSTONE
Pc (BARS)
0
100
200
300
400
500
600
700
800
900
1000
2.60
2.40
2.20
2.00
K (10**5 BARS)

FIGURE 28

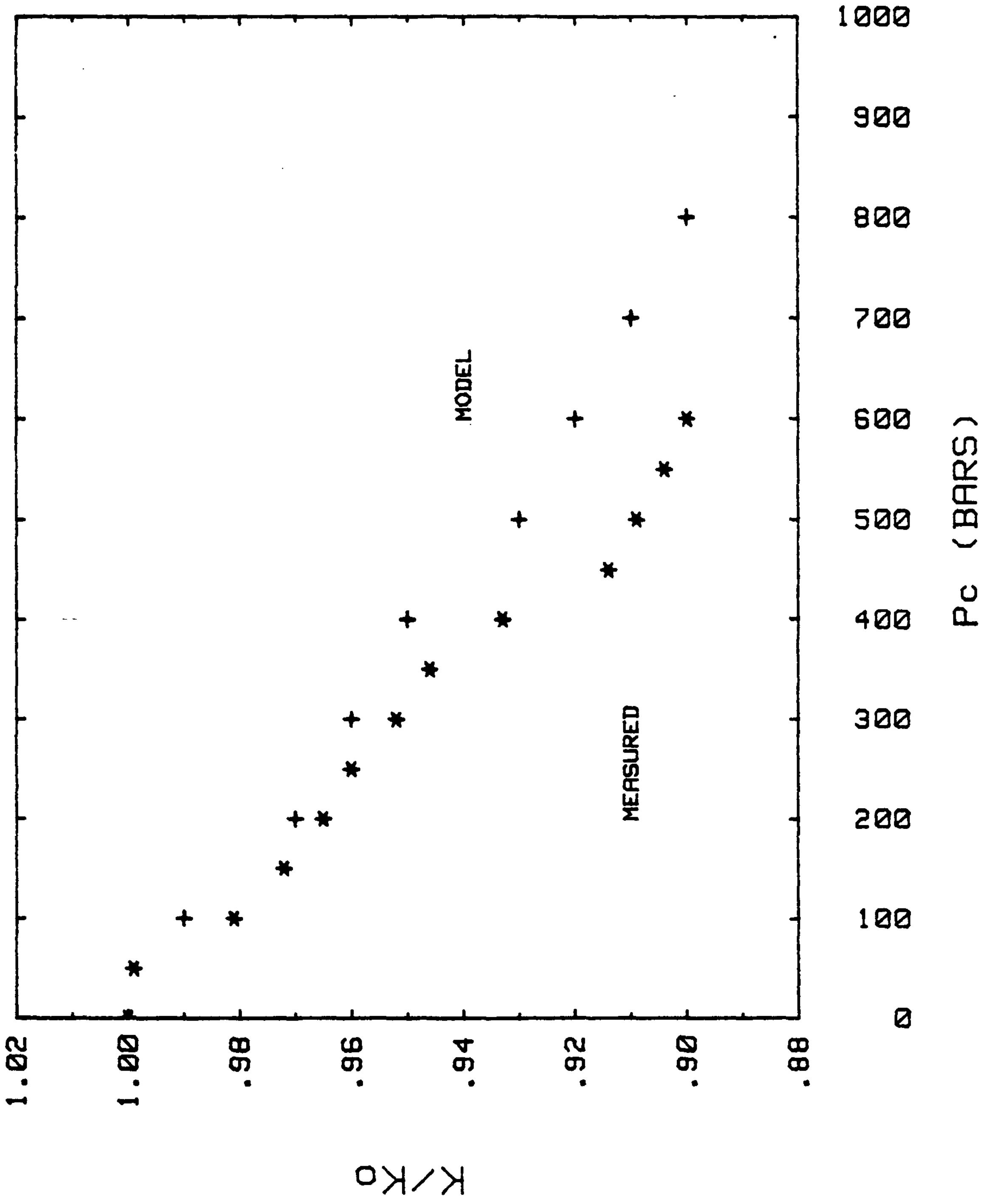
K/Ko
1.02
1.00
.98
.96
.94
.92
.90
.88
Pc (BARS)
0
100
200
300
400
500
600
700
800
900
1000
MODEL
MEASURED

FIGURE 29

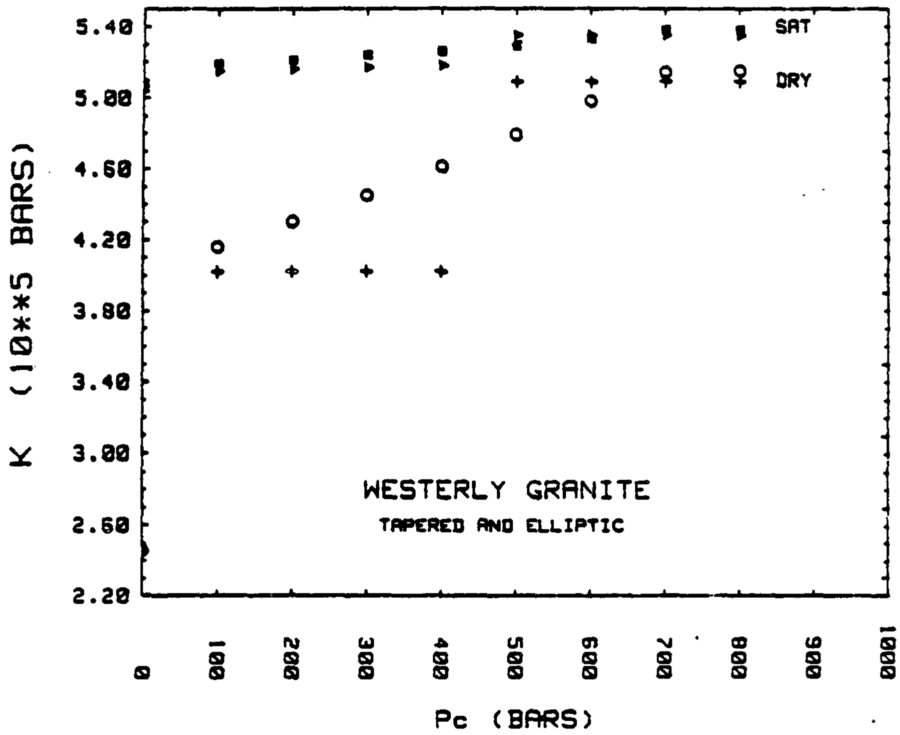
K (10**5 BARS)
5.40
5.00
4.60
4.20
3.80
3.40
3.00
2.60
2.20
SAT
DRY
WESTERLY GRANITE
TAPERED AND ELLIPTIC
0
100
200
300
400
500
600
700
800
900
1000
Pc (BARS)

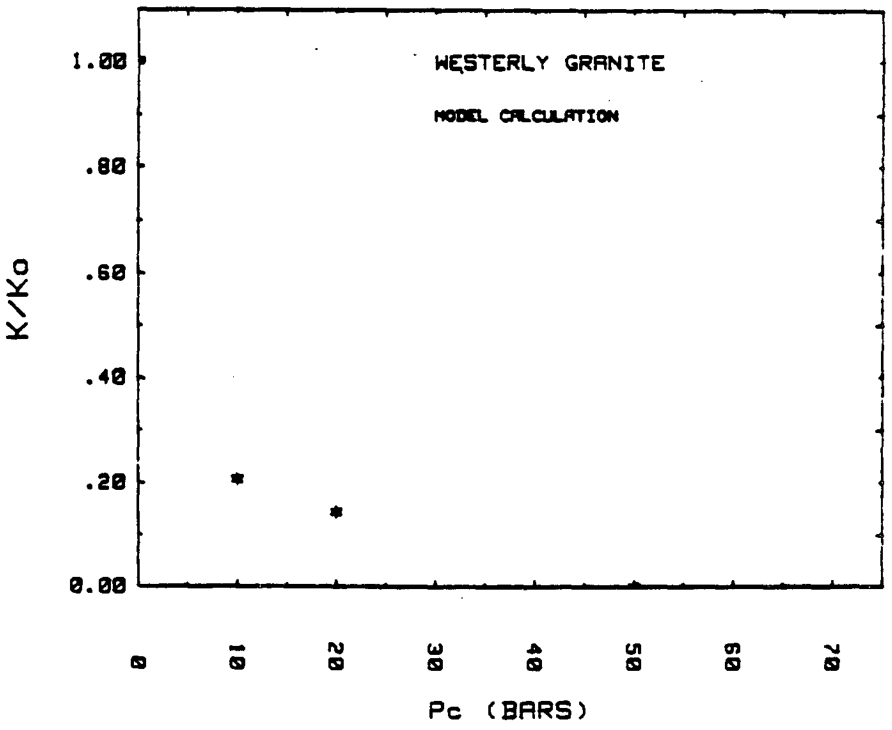
K/Ko
1.00
.80
.60
.40
.20
0.00
WESTERLY GRANITE
MODEL CALCULATION
0
10
20
30
40
50
60
70
Pc (BARS)

FIGURE 30

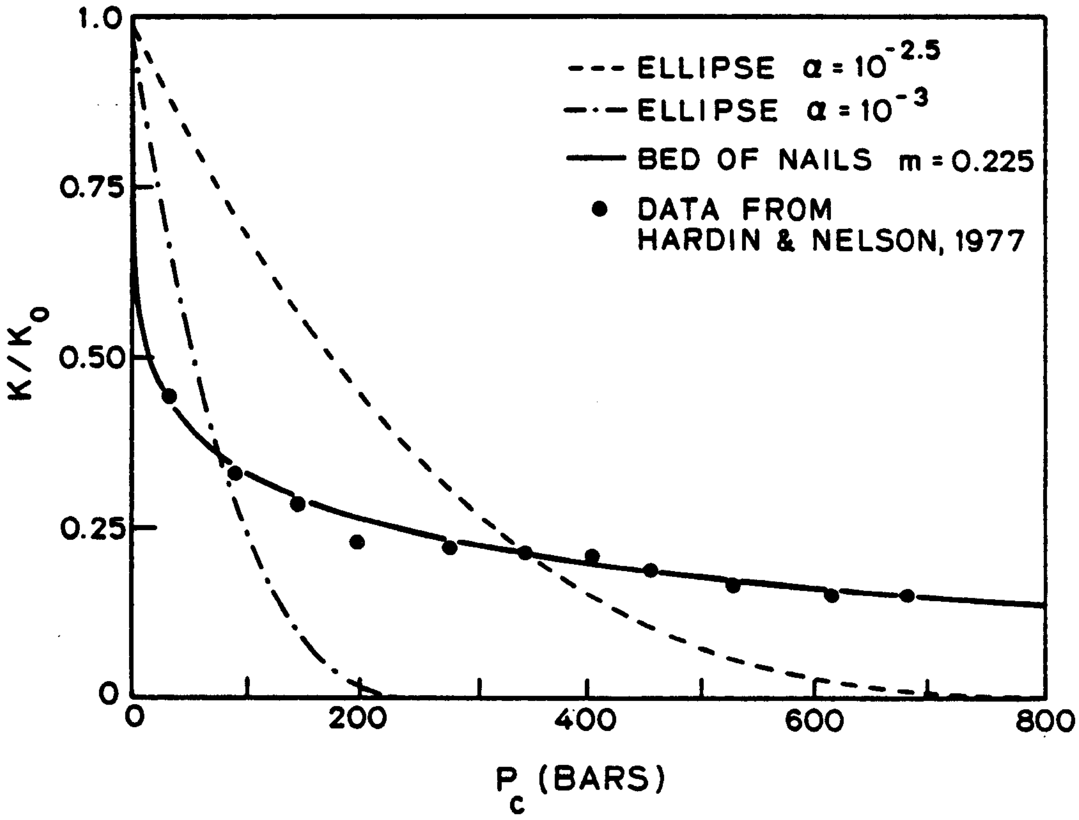
1.0
0.75
0.50
0.25
0
K / K_o
0
200
400
600
800
P_c (BARS)
ELLIPSE α = 10^-2.5
ELLIPSE α = 10^-3
BED OF NAILS m = 0.225
DATA FROM HARDIN & NELSON, 1977

FIGURE A1

APPENDIX A: ELLIPTIC AND TAPERED CRACKS AS MODELS FOR FRACTURE FLOW

Snow (1968) and Witherspoon et al. (1979), among others, have shown that for steady state linear flow between two parallel plates with an aperture of b, the volume flow rate, Q, is given by

$$Q = \frac{b^3 D}{12\mu} \frac{\Delta P}{\Delta l} \qquad (A1)$$

where D is the extent of the fracture normal to the direction of flow and b,μ is the fluid viscosity, and $\Delta P/\Delta l$ is the pressure gradient.

As a comparison, we have seen that the volume flow rate through an elliptic conduit of semimajor axis c and semiminor axis b is given by

$$Q = \frac{\pi}{4\mu} \frac{b^3 c^3}{b^2 + c^2} \frac{\Delta P}{\Delta l} \qquad (A2)$$

If b<<c, this becomes, to a good approximation

$$Q = \frac{\pi}{4} \frac{b^3 c}{\mu} \frac{\Delta P}{\Delta l} \qquad (A3)$$

Equations (A1) and (A3) are both of the form $Q \sim b^3 c \; \Delta P/\Delta l$ and thus may be used to discuss fracture flow. For situations of changing confining pressure, fractures of elliptic or tapered section may more accurately predict variations of fracture flow because, as we have seen, there are solutions to the elasticity problem of the change of conduit shape with confining stress. In contrast, ideal parallel plates are never in contact, so that there is difficulty describing the appropriate constituitive relation. According to the models developed earlier, the flow rate as a function of confining pressure for tapered and elliptic cracks are given by equations (13) and (17). From these equations we get

$$k_e(p) = k_{oe}(1-\frac{2pc(1-\nu^2)}{bE})^3 \qquad (A4)$$

$$k_t(p) = k_{ot}(1-\frac{4pc(1-\nu^2)}{3bE})^5 \qquad (A5)$$

Gangi (1978) used a phenomenological "bed of nails" to model flow through a deformable fracture. For this model he arrived at the relation

$$k(p) = k_o(1-(p/p_1)^m)3 \qquad 0 < m \leq 1 \qquad (A6)$$

where p is confining pressure and p_1 is a constant. For m = 1, (A6) is of the same form as (A4), the expression for elliptic cracks. Figure (A1) shows a comparison of laboratory data on fracture flow in Navajo sandstone acquired by Nelson and Handin (1977), the best fit curve to this data given by Gangi for the bed of nails model, and representative curves from the elliptic crack model. Both of the theoretical curves decay steeply at small confining pressures. However, the confining pressure at which the bed of nails fracture closes is over an order of magnitude larger than that pressure at which either an appropriate elliptic or tapered crack would close.

The fact that the elliptic or tapered crack model permeability will generally become zero at pressures less than is actually observed would imply that the model is applicable primarily where confining stresses are low. If the fracture surface is nonuniform, bringing the two opposing surfaces close together could bring asperities or irregularities into contact. As noted by Mavko and Nur

(1978) and Walsh and Grosenbaugh (1979), this would act to stiffen the crack and make further closing and loss of permeability more difficult. Thus, either the complex irregular crack model considered by Mavko and Nur (1978) and Walsh and Grosenbaugh (1979) or the bed or nails model may provide accurate predictions of fracture permeability as a function of confining pressure, particularly at high confining pressures. This is impossible in the parallel plate model without an empirical constitutive relation.